



HAL
open science

Aciers inoxydables et corrosion localisée : le rôle du molybdène

Thiago Mesquita

► **To cite this version:**

Thiago Mesquita. Aciers inoxydables et corrosion localisée : le rôle du molybdène. Autre. Université de Grenoble, 2012. Français. NNT : 2012GRENI006 . tel-00721758

HAL Id: tel-00721758

<https://theses.hal.science/tel-00721758v1>

Submitted on 30 Jul 2012

HAL is a multi-disciplinary open access archive for the deposit and dissemination of scientific research documents, whether they are published or not. The documents may come from teaching and research institutions in France or abroad, or from public or private research centers.

L'archive ouverte pluridisciplinaire **HAL**, est destinée au dépôt et à la diffusion de documents scientifiques de niveau recherche, publiés ou non, émanant des établissements d'enseignement et de recherche français ou étrangers, des laboratoires publics ou privés.

THÈSE

Pour obtenir le grade de

DOCTEUR DE L'UNIVERSITÉ DE GRENOBLE

Spécialité : **Matériaux, Mécanique, Génie Civil, Electrochimie**

Arrêté ministériel : 7 août 2006

Présentée par

Thiago José MESQUITA

Thèse dirigée par **Ricardo P. NOGUEIRA**

préparée au sein du

- **Centre de recherche UGITECH – France**
- **Laboratoire d'Electrochimie et de Physicochimie des Matériaux et des Interfaces (LEPMI) – France**
- **Laboratoire de Science et Ingénierie des Matériaux et des Procédés (SIMAP) - France**

dans l'École Doctorale « Ingénierie – Matériaux, Mécanique, Environnement, Energétique, Procédés, Production »

Aciers inoxydables et corrosion localisée: le rôle du molybdène

Thèse soutenue publiquement le **02.03.2012**,
devant le jury composé de :

Mme Muriel VERON

Professeur à l'Institut Polytechnique de Grenoble, Présidente

M. Walter J. BOTTA FILHO

Professeur à UFSCar, Rapporteur

M. Thierry CHAUSSADENT

Directeur de Recherche à IFSTTAR, Rapporteur

Mme Nicole KINSMAN

Directrice technique d'IMOA, Examinatrice

Mme Zehbour PANOSSIAN

Directrice de recherche d'IPT, Examinatrice

M. Marc MANTEL

Directeur Centre de Recherche UGITECH, Co-encadrant de thèse

M. Eric CHAUVÉAU

Ingénieur UGITECH, Co-encadrant de thèse

M. Ricardo P. NOGUEIRA

Directeur du LEPMI, Directeur de thèse



PREFACE

This thesis is published to obtain a Ph.D. degree of the Institut National Polytechnique de Grenoble (Grenoble INP/France). Most of the experimental work was carried out at the “Laboratoire d'Electrochimie et de Physicochimie des Matériaux et des Interfaces” (LEPMI Laboratory) from April 2009 to February 2012. The work was undertaken as a part of a CIFRE (“Conventions Industrielles de Formation par la REcherche”) project, named “STAINLESS STEEL IN ALKALINE MEDIA - THE ROLE OF Mo ON PITTING AND CREVICE CORROSION RESISTANCE” under the supervision of Professor Ricardo Pereira Nogueira from Grenoble INP, Dr. Marc Mantel, and Eric Chauveau (*) from Ugitech Company. The project was funded by Ugitech and also the International Molybdenum Association (IMOA).

(*) Present address: CRU – Ugitech, Ugine, France.

ABSTRACT

The use of stainless steels (SS) as concrete reinforcement is becoming increasingly popular in coastal and marine constructions in order to prevent corrosion induced by chloride ions penetrating into the concrete. In these highly aggressive situations, stainless steels have been extensively employed due to their high mechanical and corrosion resistances. However, the influence of Mo addition on pitting corrosion resistance of these steels is not fully understood in alkaline chloride conditions although this element is widely associated to an increasing corrosion resistance in acidic and neutral environments. Therefore, understanding Mo role on corrosion resistance in alkaline conditions is hence of major importance for the setting of optimized alloy compositions. This Ph.D work aims at studying the effect of Mo addition on pitting corrosion properties of austenitic, ferritic and mainly lean duplex stainless steels in alkaline media, which simulates the concrete environment. For these studies not only several different electrochemical techniques such as open circuit potential (OCP), dynamic polarization, zero resistance ammeter (ZRA) and electrochemical impedance spectroscopy (EIS) were used, but also many materials characterizations techniques such as scanning electron microscopy (SEM), X-ray microanalysis (EDX), Thermocalc[®] software simulations and X-ray photoelectron spectroscopy (XPS). The results were discussed with respect to the influence of Mo addition on localized corrosion resistance of both commercial industrial SS (AISI 316L, 304L, 434, 430 and 1.2205 and 1.2304) and highly controlled laboratory ones. These laboratory SS were produced with a well defined chemical composition for which the only difference was the amount of Mo. This allowed us to associate any difference in the corrosion behavior to the Mo content. Finally, as far as the role of Mo is concerned, it will be discussed in terms of pitting corrosion resistance, repassivation kinetics, and passivation properties from acidic to alkaline conditions.

Keywords: Stainless Steels, Molybdenum, Pitting Corrosion, Passivation properties, and Concrete Reinforcement.

ACKNOWLEDGEMENTS

First of all, I would like to convey my sincere thanks to my supervisors Ricardo Pereira Nogueira, Marc Mantel and Eric Chauveau. I am earnestly grateful to them for their enlightening supervision, guidance and perceptive encouragement throughout this research project. I am deeply impressed by their profound knowledge and strict attitude to do research. Without their helpful discussions, this work would not have the shape it has now.

This work would also not have been successfully carried out without the financial and technical support of the project sponsors, which are gratefully acknowledged: The Ugitech Company, “IMOA – International Molybdenum Association”, “INPG – Institut Polytechnique de Grenoble”, and LEPMI – “Laboratoire d'Electrochimie et de Physicochimie des Matériaux et des Interfaces”. Special gratitude is extended to Nicole Kinsman from IMOA, Philippe Mauger from Ugitech, Virginie Roche and Eric Chainet from LEPMI, Pedro Cordoba from “UNED - Universidad Nacional de Educación a Distancia”, Grégory Berthomé and Bernard Baroux from SIMAP/Grenoble laboratory, Bernard Normand from INSA/Lyon Laboratory, Ivan Napoleão Bastos and Marcos Paulo Moura de Carvalho from Universidade do Estado do Rio de Janeiro/Brazil and Zehbour Panossian and Adriana Araujo from IPT/São Paulo Laboratory for their appreciable advice, stimulating discussions and helpful suggestions during the course of this work. I would also like to acknowledge my indebtedness to all my colleagues at the LEPMI laboratory for their valuable assistance in technical and administrative matters.

My sincere appreciations are also expressed to Walter José Botta Filho, Thierry Chaussadent and Muriel Veron for participating in my thesis jury. Their patience and helpful correction and examination of this work are key inputs to the successful conclusions of this project.

Last but not least, I cannot adequately express my gratitude my girlfriend Franklina Vasil, to my mother Maria Augusta A. Mesquita and father Ascendino Mesquita, and to my sister Lilian Carmen Mesquita Dian. I just dedicate this work to them.

Many Thanks to all of you!

Thiago José Mesquita

January, 2012

TABLE OF CONTENTS

<i>Preface</i>	<i>1</i>
<i>Abstract</i>	<i>2</i>
<i>Acknowledgment</i>	<i>3</i>
<i>Table of contents</i>	<i>4</i>
<i>General introduction</i>	<i>7</i>
1. LITERATURE REVIEW	12
1.1. CORROSION OF CONCRETE REINFORCEMENT	12
1.1.1. INTRODUCTION	12
1.1.2. CHLORIDE-INDUCED REBARS CORROSION	13
1.1.3. CARBONATION OF THE POROUS CONCRETE	15
1.1.4. STAINLESS STEELS FOR REINFORCEMENT CONCRETE APPLICATIONS	17
1.2. ROLE OF Mo ADDITION ON CORROSION RESISTANCE OF DIFFERENT SS	19
1.2.1. CORROSION AND PASSIVATION OF PURE MOLYBDENUM	19
1.2.2. INFLUENCE OF Mo ON STAINLESS STEELS PASSIVATION	23
1.2.2.1. ACIDIC CONDITIONS	24
1.2.2.2. NEUTRAL CONDITIONS	28
1.2.2.3. ALKALINE CONDITIONS	29
1.2.2.4. SUMMARY	29
1.2.3. EFFECT OF Mo ON UNIFORM CORROSION OF AUSTENITIC SS	30
1.2.4. EFFECT OF Mo ON PITTING NUCLEATION OF SS	32
1.2.5. ROLE OF Mo ON PITTING PROPAGATION AND REPASSIVATION OF STAINLESS STEELS	39
1.2.6. Mo ADDITION ON DUPLEX STAINLESS STEELS	47
1.3. CONCLUSION	50
1.4. REFERENCES	50
2. EXPERIMENTAL METHODOLOGY	54
2.1. MATERIALS	54
2.1.1. INDUSTRIAL STAINLESS STEELS	54
2.1.2. LABORATORY STAINLESS STEELS	55
2.2. ELECTROCHEMICAL CHARACTERIZATIONS	59
2.2.1. SAMPLES PREPARATION	59
2.2.2. SOLUTION PREPARATION	61
2.2.3. ELECTROCHEMICAL CELL DESCRIPTION	61
2.2.4. ELECTROCHEMICAL EXPERIMENTS	62
2.2.4.1. POTENTIODYNAMIC POLARIZATION	62

2.2.4.2.	ZERO RESISTANCE AMMETER (ZRA)	65
2.2.4.3.	ELECTROCHEMICAL IMPEDANCE SPECTROMETRY	66
2.2.4.3.1.	PRINCIPLE	67
2.3.	SURFACE CHARACTERIZATIONS	68
2.3.1.	SCANNING ELECTRON MICROSCOPY (SEM)	68
2.3.1.1.	SCANNING PROCESS AND IMAGE FORMATION	69
2.3.1.2.	DETECTION OF SECONDARY ELECTRONS	71
2.3.1.3.	DETECTION OF BACKSCATTERED ELECTRONS	71
2.3.1.4.	MEASUREMENTS PROTOCOL	72
2.3.2.	X-RAY PHOTOELECTRON SPECTROSCOPY (XPS)	72
2.3.2.1.	MEASUREMENTS PROTOCOL	74
2.3.2.2.	PEAK IDENTIFICATION	75
2.4.	TRIBO-CORROSION CHARACTERIZATION	78
2.5.	REFERENCES	80
3.	MO EFFECT ON PITTING NUCLEATION AND PROPAGATION – AN INDUSTRIAL AND LABORATORY APPROACH	82
3.1.	INTRODUCTION	82
3.2.	INFLUENCE OF Mo ADITION ON INDUSTRIAL SS	83
3.2.1.	EFFECT OF Mo ADITION ON PITTING POTENTIAL OF INDUSTRIAL SS IN FUNCTION OF pH	83
3.2.2.	Mo EFFECT ON METASTABLE PITS	88
3.3.	EFFECT OF Mo ADITION ON PITTING POTENTIAL OF LABORATORY SS IN FUNCTION OF pH	90
3.4.	INFLUENCE OF Mo ADDITION ON EACH PHASE OF DUPLEX STRUCTURE	97
3.5.	CONCLUSION	103
3.6.	REFERENCES	104
4.	THE INFLUENCE OF Mo ON PITTING REPASSIVATION PROCESS AND MOLYBDATE INHIBITOR BEHAVIORS	106
4.1.	INTRODUCTION	106
4.2.	A COMPARATIVE STUDY OF REPASSIVATION CURRENT TRANSIENTS	107
4.2.1.	THE INFLUENCE OF Mo ADITION ON REPASSIVATION TRANSIENTS IN DIFFERENT pH	107
4.2.2.	Mo EFFECT ON THE REPASSIVATION KINETICS	113
4.2.3.	Mo EFFECT ON EACH PHASE OF DUPLEX SS AFTER MECHA- NICAL DEPASSIVATION	115

4.3.	THE CORROSION INHIBITOR EFFECT OF MOLYBDATES IN FUNCTION OF pH	117
4.4.	CONCLUSION	122
4.5.	REFERENCES	123
5.	THE INFLUENCE OF Mo ON SS PASSIVATION IN ALKALINE “APPLICATIONS”	126
5.1.	INTRODUCTION	126
5.2.	INFLUENCE OF MO ON THE PASSIVE FILM COMPOSITION - AN EX-SITU XPS STUDY IN AIR AND AT pH 7 AND 10 MEDIA	127
5.3.	THE ROLE OF Mo ON THE PASSIVE FILM STABILTY AT DIFFERENT pH	136
5.4.	CONCLUSION	146
5.5.	REFERENCES	147
6.	GENERAL CONCLUSION	150
7.	PERSPECTIVES	155
7.1.	INTRODUCTION	155
7.2.	AN IN-SITU STUDY OF THE ROLE OF MOLYBDENUM ON PASSIVATION OF STAINLESS STEELS	155
7.3.	SS PITTING CORROSION RESISTANCE - THE STUDY OF Mo AND N SYNERGY	156
7.4.	IDEAS FOR DIRECT EXPERIMENTS ON THE POROUS CONCRETE ENVIROMENT	159
8.	RESUME EN FRANÇAIS	162
8.1.	RESUME	162
8.2.	INTRODUCTION	163
8.3.	EFFET DE L’ADDITION DU MO DANS LA RESISTANCE A LA CORRO- SION PAR PIQUES DES ACIERS INOXYDABLES EN FONCTION DU pH	166
8.4.	INFLUENCE DU Mo SUR LA CINETIQUE DE REPASSIVATION DES ACIERS INOX	171
8.5.	ROLE DU Mo SUR LA PASSIVATION DES ACIERS INOX EN MILIEUX ALCALINS	174
8.6.	CONCLUSION	176
8.7.	REFERENCES	179
9.	ANNEXES	182
9.1.	ANNEX 1 – MANUFACTURING OF LABORATORY SS	182
9.2.	ANNEX 2 – SYNCHROTRON PROJECT	183
9.3.	ANNEX 3 – IMPEDANCE AND CPE DISCUSSION	186

GENERAL INTRODUCTION

Steels used as a concrete reinforcement are usually carbon steels or mild steels due to low aggressiveness of the environments where it is currently used and mainly due to their low cost. Stainless steels have not traditionally been widely used as structural materials in building and civil engineering. According to the environment to which the concrete will be exposed (marine environment, place subjected to deicing salt, road pollution...), certain chemical elements like chlorides and carbon dioxide will penetrate and diffuse through the concrete towards the steel reinforcement and thus inducing a significant decrease of pH, which is about 12.5 to 13.5 in a initial state of concrete's life [1].

The corrosion of the reinforcement steels induced by those ions penetrating into the concrete is the main cause of early damage, loss of serviceability and safety of reinforced concrete structures [2]. Therefore, stainless steels have been used to reinforce concrete constructions in USA, Canada, Australia and some European countries in a wide range of applications including highway bridge decks, parapets, retaining walls, underpasses and historic buildings with excellent results [3].

The primary reason for this low use in structural applications is usually the perceived and actual cost of stainless steel, which is directly associated to the price of several alloy elements, mainly nickel and molybdenum. Therefore, developments over the last 20 years, both in available materials and their durability, are now offering a new opportunity for stainless steels to be considered as primary structural materials. The recent metallurgical technology have seen the introduction of low alloyed duplex stainless steels (DSS), often referred to as lean duplex stainless steels. These grades of DSS with low nickel and molybdenum contents, and consequently lower economic impact on concrete structures [4, 5], are characterized by equivalent mechanical strength and toughness compared to conventional duplex grades but lower resistance to localized corrosion, even if their corrosion resistance is comparable to that of austenitic steels like the widely used AISI 304 and 316 grades [4].

The localized corrosion resistance of stainless steels is usually associated with the alloying elements Cr, Mo and N, whereas Ni mainly acts to stabilize the austenite phase [6, 7]. One of the most commonly used expression to the evaluation of corrosion is the so-called pitting resistance equivalent number (PREn) [8]. The PREn is linked to the content of the

three main elements which provide localized corrosion resistance, Cr, Mo and N, each of them weighted based on their influence on pitting corrosion [8, 9].

Even if it is undoubtedly established that the alloying elements effectively play a huge important role in the pitting corrosion resistance of SS, one must consider that the PREn is an empiric expression proposed from an inventory of experimental results obtained under certain specific conditions, mainly in ferric chloride solutions with fixed chloride concentrations [10]. It must hence be noted that its extrapolation to other media must be done carefully, particularly in alkaline environments, as those related to cement and concrete structures. As an example, some recent papers [11-14] pointed out some unexpected results in which, in alkaline conditions, the addition of Mo did not improve the localized corrosion resistance of austenitic grades, in spite of the fact that the PREn predicted a better performance of the Mo-containing grades. This illustrates the lack of knowledge about the mechanism through which Mo affects the corrosion resistance of the bulk material. Therefore, understanding Mo mechanism on corrosion resistance in alkaline media is of major concern to the setting of optimized alloy composition in order to have a good balance between the properties required in these applications and the final cost of the material [12].

In these contexts, the purpose of this Ph.D studies is to investigate the influence of Mo addition in all steps of the pitting corrosion (passivation, pit nucleation, pit propagation and, pit repassivation) for different industrial SS grades, traditional austenitic and ferritic SS and new lean DSS alloys, mainly in alkaline media simulating the porous concrete solution. However, the interest of the study in the aggressive alkaline conditions is not only for concrete reinforcement, but also for several others SS applications such as petrochemical, chemical and alkali industries, paper manufacturing, food processing, etc...

This work started with a literature review (Chapter 1) about reinforcement concrete corrosion, the pure Mo behavior under different media and also about the effect of Mo addition in austenitic, ferritic and duplex SS in which concerns their pitting corrosion resistances. This first step of the thesis helped us to have a better understanding of the already proposed Mo mechanisms and to have new ideas for the experimental methodology used during these works, as will be shown in the Chapter 2.

Then, Mo influence on the localized corrosion resistance of both traditional austenitic SS (AISI 316L and 304L) and new lean austenoferritic duplex SS grades (1.2205 and 1.2304) was investigated in Chapter 3. The preliminary results were discussed by considering the

pitting potential E_{pit} of these alloys in different synthetic electrolyte conditions (from acidic to alkaline environments), by means of dynamic polarization measurements in several pH media. As it will be minutely seen in this thesis, the results indicated an absence of the beneficial effect of Mo in alkaline solutions in the case of austenitic grades, although the presence of Mo promotes a major positive effect for the localized corrosion resistance of duplex SS [11]. These facts brought up the hypothesis that Mo has a stronger influence on the ferrite than on the austenite phase for DSS.

Afterwards, we decided to include the AISI 430 and 434 ferritic SS grades to this work in order to firstly check the Mo effect on the corrosion behavior of each single microstructure (austenitic and ferritic) and then to have a better understanding about what happens when these two structures are mixed in the same material, as in the case of austenoferritic duplex SS. Results showed a positive effect of Mo addition for the ferritic SS even at high temperatures in the alkaline medium (pH 10). These results associated with SEM images and Thermocalc simulations of the DSS microstructure confirmed our indirect evidence of the major effect of Mo on the ferrite phase [11].

As mentioned before, these results were obtained from industrial castings, which present significant compositional differences, and not only in the Mo contents. Even if the results were very interesting and innovative, it was not possible to determine the mechanism of Mo on the localized corrosion in alkaline solutions by using these industrial samples. So, the results and conclusions obtained with these samples had to be hence verified in which concerns the unambiguous role of Mo. Therefore, we decided to manufacture new highly controlled laboratory SS with 0% and 3% of Mo in order to study the real effect of Mo addition on SS pitting corrosion resistance. This allowed us to directly associate the pitting behavior to the Mo alloying and not with Cr, Ni, and N additions. The results of the lab heats showed to be similar to those found for the industrial castings.

Moreover, some hypothesis about the Mo effect on the pitting repassivation claimed by the literature [15-18] could be investigated by using this laboratory heat to perform tribocorrosion experiments as discussed in the 4th chapter. These results showed a better repassivation kinetic for the Mo containing lab SS under acidic condition whereas this beneficial role of Mo was not so evident in alkaline medium. A complementary study of the tribocorrosion measurements was also done by directly adding molybdates, as a corrosion inhibitor, to different solution at several pH. The inhibiting influence of the molybdates also

decreases with the increment of the chloride solution alkalinity confirming then the anomalous behavior of molybdenum seen previously. The interpretation of these data brought up the idea of Mo presence in the passive layer when SS are exposed to alkaline media rather than the formation of Mo-species in the aggressive solution within pit, as already published [15-22] for acidic and neutral media.

Therefore, X-ray Photoelectron Spectroscopy (XPS) technique was used to characterize the passive layer formed on the laboratory SS surfaces under different pH conditions. The focus of these XPS analyses was to verify the presence or absence of oxidized Mo in the protective film. Moreover, the Electrochemical Impedance Spectroscopy (EIS) technique was employed in order to evaluate the Mo role on the oxide film stability from acidic to alkaline media. Both XPS and EIS results are detailed in the chapter 5.

All results are going to be fully described in the following chapters. The role of Mo on pitting corrosion resistance, repassivation kinetics and passivation properties of SS will be discussed in terms of microstructure and also the different Mo contents in the bulk materials, mainly for alkaline condition applications.

REFERENCES

- [1] E. Chauveau, T. Sourisseau, B. Dermelin and M. Mantel, MEDACHS 08, International Conference in Coastal and Marine Environments (2008).
- [2] D. Addari, B. Elsener and A. Rossi, *Electrochimica Acta* 53 (2008) 8078
- [3] C. J. Abbott, *Concrete* 31 (1997) 28.
- [4] G. Gedge, *J. Construc. Steel Research*. 64 (2008) 1194.
- [5] Guidance on the use of stainless steel reinforcement, The Concrete Society, Technical Report 51 (1998).
- [6] F. Zhang, J. Pan, and C. Lin. *Corrosion. Science* 51 (2009) 2130.
- [7] L. Zhang, Y. Jiang, B. Deng, W. Zhang and J. Xu, J. Li. *Materials Characterization* 60 (2009) 1522.
- [8] R.N. Gunn. Abington Publishing, Cambridge England (1999).
- [9] L.F. Garfias-Mesias, J.M. Sykes and C.D.S. Tuck. *Corrosion. Science* 38 (1996) 1319.
- [10] ASTM G48 - 03(2009) - Standard Test Methods for Pitting and Crevice Corrosion Resistance of Stainless Steels and Related Alloys by Use of Ferric Chloride Solution
- [11] T. J. Mesquita, E. Chauveau, M. Mantel, N. Kinsman and R.P. Nogueira. *Materials Chemistry and Physics*, 126 (2011) 602

- [12] A. Bautista, G. Blanco and F. Velasco. *Cement and Concrete Research* 36 (2006) 1922.
- [13] A. Bautista, G. Blanco, F. Velasco, A. Gutiérrez, L. Soriano, F. J. Palomares and H. Takenouti. *Corrosion Science* 51 (2009) 785.
- [14] W.A. Badawy and F.M. Al-Kharafi. *Electrochimica Acta* 44 (1998) 693.
- [15] K. Hashimoto, K. Asami, and K. Teramoto. *Corrosion Science* 19 (1979) 3.
- [16] G.O. Ilevbare, and G.T. Burstein. *Corrosion Science* 45 (2003) 1545.
- [17] M. Kimura, M. Kaneko and N. Ohta, *ISIJ Int* 42 (2002). 1399.
- [18] A. J. Davenport, A. J. Dent, M. Monir, J. A. Hammons, S. M. Ghahari, P. D. Quinn and T. Rayment. *J. Electrochem. Soc.* 158 (2011).
- [19] A. Pardo, M.C. Merino, A.E. Coy, F. Viejo, R. Arrabal and E. Matykina, *Corrosion Science* 50 (2008) 1796.
- [20] R. C. Newman. *Corrosion Science* 25 (1985) 331.
- [21] R. C. Newman. *Corrosion Science* 25 (1985) 341.
- [22] R. C. Newman, and E.M. Franz. *J. Electrochem. Soc.* 131 (1984) 223.

CHAPTER 1

LITERATURE REVIEW

OUTLINE

1. LITERATURE REVIEW	12
1.1. CORROSION OF CONCRETE REINFORCEMENT	12
1.1.1. INTRODUCTION	12
1.1.2. CHLORIDE-INDUCED REBARS CORROSION	13
1.1.3. CARBONATION OF THE POROUS CONCRETE	15
1.1.4. STAINLESS STEELS FOR REINFORCEMENT CONCRETE APPLICATIONS	17
1.2. ROLE OF Mo ADDITION ON CORROSION RESISTANCE OF DIFFERENT SS	19
1.2.1. CORROSION AND PASSIVATION OF PURE MOLYBDE- NUM	19
1.2.2. INFLUENCE OF Mo ON STAINLESS STEELS PASSIVATION	23
1.2.2.1. ACIDIC CONDITIONS	24
1.2.2.2. NEUTRAL CONDITIONS	28
1.2.2.3. ALKALINE CONDITIONS	29
1.2.2.4. SUMMARY	29
1.2.3. EFFECT OF Mo ON UNIFORM CORROSION OF AUSTENITIC SS	30
1.2.4. EFFECT OF Mo ON PITTING NUCLEATION OF SS	32
1.2.5. ROLE OF Mo ON PITTING PROPAGATION AND REPASSIVATION OF STAINLESS STEELS	39
1.2.6. Mo ADDITION ON DUPLEX STAINLESS STEELS	47
1.3. CONCLUSION	50
1.4. REFERENCES	50

1. LITERATURE REVIEW

In this chapter, a state of the art will be done with specific regards on the Mo influence on the pitting corrosion resistance of different SS types and also under several pH conditions. Firstly, the concrete reinforcement corrosion process will be described as this problem is of major importance in our studies, even if alkaline media can be found in others SS “applications”, such as petrochemical, chemical, paper industries, etc... In a second step, references about Mo itself are cited in order to have a better understanding of this element effect as a SS component and finally the Mo mechanisms as an alloying element already reported by the literature will be largely discussed.

The objective of this chapter is to emphasize the need of a better knowledge of the role of Mo as an alloying element in which concerns the corrosion resistance of different stainless steel types, mainly in alkaline media, where data are not as available as in acidic environments. It is worth noticing that the literature about SS corrosion is extremely wide, so that only the most important references associated with the present work will be referenced in this report.

1.1. CORROSION OF CONCRETE REINFORCEMENT

1.1.1. INTRODUCTION

Reinforced concrete deterioration is caused by physical, mechanical and chemical factors and can be induced by external and internal factors to the concrete structure. Physical and chemical deterioration are mostly influenced by climate changes. Consequently the performance of concrete structures will be affected especially in the long term and then the rebar corrosion processes could reduce the concrete lifetime.

Among the deterioration processes, chloride-induced corrosion is the major threat to the durability of marine and coastal concrete structures. Steel reinforcement in concrete is covered by a thin passive layer of oxide that protects it from oxygen and water which may cause corrosion and produce rust. This passive layer can only be maintained at high pH values (i.e. where the pH is greater than 12). The passive layer can be destroyed, during a process known as ‘depassivation’, when chloride ions penetrate the concrete and then accumulate up to a critical level on the surface of steel reinforcement. The corrosion on the

steel surface follows and the corrosion products cause considerable expansion, which can cause internal stress and consequently cracking, spalling or delamination of the concrete.

Carbonation, which is caused essentially by the penetration of atmospheric CO₂ into the concrete, can also accelerate the deterioration of the concrete. It significantly reduces alkalinity of the concrete porous solution and then increases the vulnerability of steel reinforcement to corrosion. The direct consequence of carbonation is shrinkage, but specially a decline in pH, which if left unchecked, will eventually cause corrosion and cracking followed by spalling. So, carbonation can have a considerable impact on durability, especially of above-ground structures and structures exposed to high CO₂ concentrations.

In fact, the deterioration of concrete infrastructure caused by chloride-induced and carbonation-induced corrosion results in considerable economic losses because of a loss of serviceability and an increase in the maintenance required to preserve structural integrity. Moreover, the chloride-induced and carbonation-induced corrosion of concrete infrastructure is directly affected by environmental factors such as temperature and humidity. All these factors – temperature, humidity and CO₂ concentration – will vary as a result of increasing greenhouse gas emissions and climate change. Considering the likelihood of carbon dioxide concentration in atmosphere increase and the consequent increase of temperature, the risk of concrete structural damage may be seriously affected. Another important point for the concrete deterioration is the increase in the number of people and industries moving to coastal regions, and the associated investment in concrete infrastructure in those regions, increases the exposure to further economic losses.

1.1.2. CHLORIDE-INDUCED REBARS CORROSION

Steel bars used as reinforcement in concrete ('rebars') are covered by a thin passive layer of oxide at high pH values (i.e. pH>12 or at a chloride ion content less than a corrosion threshold concentration). When chloride ions concentration reaches a critical level on the surface of steel reinforcement, the protective layer is destroyed [1, 2], which may cause corrosion and produce rust, as shown in Fig. 1.1 a) for an example. This depassivation process can be characterized as a result of electrochemical reactions, as schematically shown by Fig. 1.1 b).

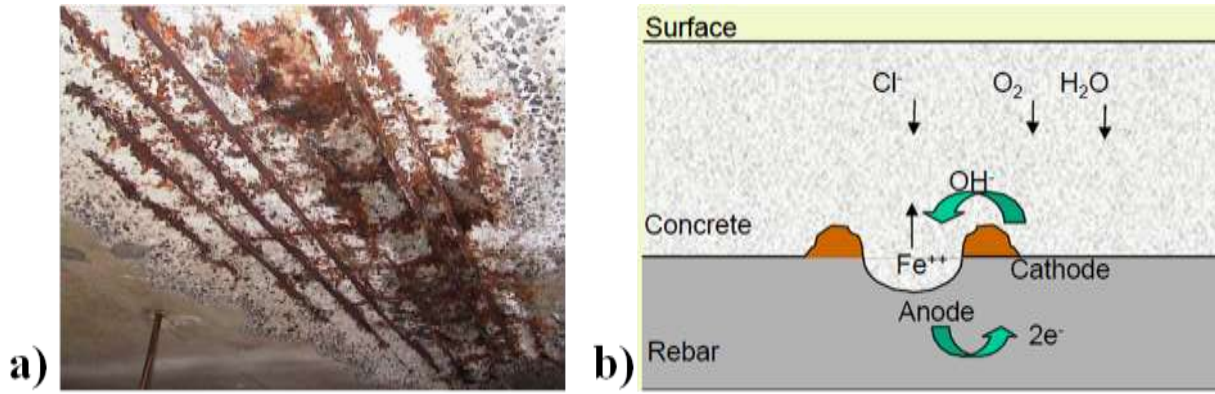


Figure 1.1- a) Corrosion of steel reinforcement in concrete structures; b) Electrochemical reactions at rebar surface induced by chloride penetration [1].

This chloride-induced corrosion at the steel surface involves the following reactions [2]:



The depassivated area becomes an anode, while the passive surface acts as a cathode. At the anode, the reaction mechanism is supposed to be as following:



and the reaction at the cathode is given by:



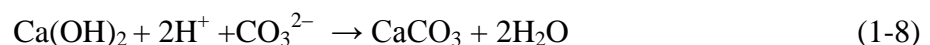
During the corrosion process, two major rust/corrosion products – Fe(OH)_2 (ferrous hydroxide) and Fe(OH)_3 (ferric hydroxide) – are produced [3]. These corrosion products can cause considerable expansion. For example, the volume of Fe(OH)_3 is about four times that of the consumed ferrite. This generates internal stresses and, ultimately, causes cracking, delamination and spalling. The failure process may be further accelerated by external loading.

The chloride-induced corrosion mainly depends on three factors, i.e. Cl^- diffusion coefficient, surface chloride concentration and critical chloride level beyond that corrosion of reinforcement will be initiated. A previous study shows that service life of concrete structure under chloride corrosion attack depends on the cover depth, the diffusion coefficient, chloride

concentration and critical chloride level for the applied rebar [4]. The corrosion process will slow down and may eventually stop when water or oxygen availability is limited. So, depending of the humidity condition, the diffusion of oxygen is restrained to the corrosion area and diminishes the corrosion of the reinforcement whereas a shortage of water in dry concrete also reduces corrosion activity. For determining the rate of chloride penetration into concrete and the resistance of concrete to the penetration of chloride ions, some authors refer to ASTM C1543-02 (2002) and ASTM C1202-97 (1997), respectively [1, 5, 6].

1.1.3. CARBONATION OF THE POROUS CONCRETE

Carbonation in concrete is caused essentially by the penetration of atmospheric CO₂, especially at a relative humidity between 50 and 70% [2]. Carbonation of concrete takes place when the CO₂ from the atmosphere reacts with the alkaline components of concrete, mainly portlandite, and/or with the C—S—H gel (hydrated calcium silicate), resulting in the formation of CaCO₃. The reaction generally leads to a decrease in the pH of the aqueous phase of the concrete pores, from very alkaline values greater than 12 to values below 8. If the reaction reaches the steel reinforcement surface, its passive layer may disappear, exposing the steel surface to corrosion [7]. So, carbon dioxide reacts with Ca(OH)₂ and CaO.SiO₂.nH₂O from the cement, producing calcium carbonate CaCO₃ by the following reactions:



This process reduces the pH of concrete and destroys the passive layer of the concrete reinforcement inducing corrosion of the depassivated metal according to reactions 1-3, 1-4 and 1-5 cited above. The influence of the pH on the Fe stability is clearly presented by the Potential – pH equilibrium (Pourbaix diagram) for iron in the Fig. 1.2. It clearly appears that the stability of oxides is limited to the neutral-alkaline region.

A schematic illustration of the concrete carbonation is presented in the Fig. 1.3 a). A direct consequence of carbonation is shrinkage, but specially a decline at pH down to a critical value, leading to corrosion initiation, which could eventually cause cracking followed

by spalling, as shown in Fig 1.3 b) [8]. Therefore, carbonation is considered a relevant problem for the concrete reinforcement corrosion process.

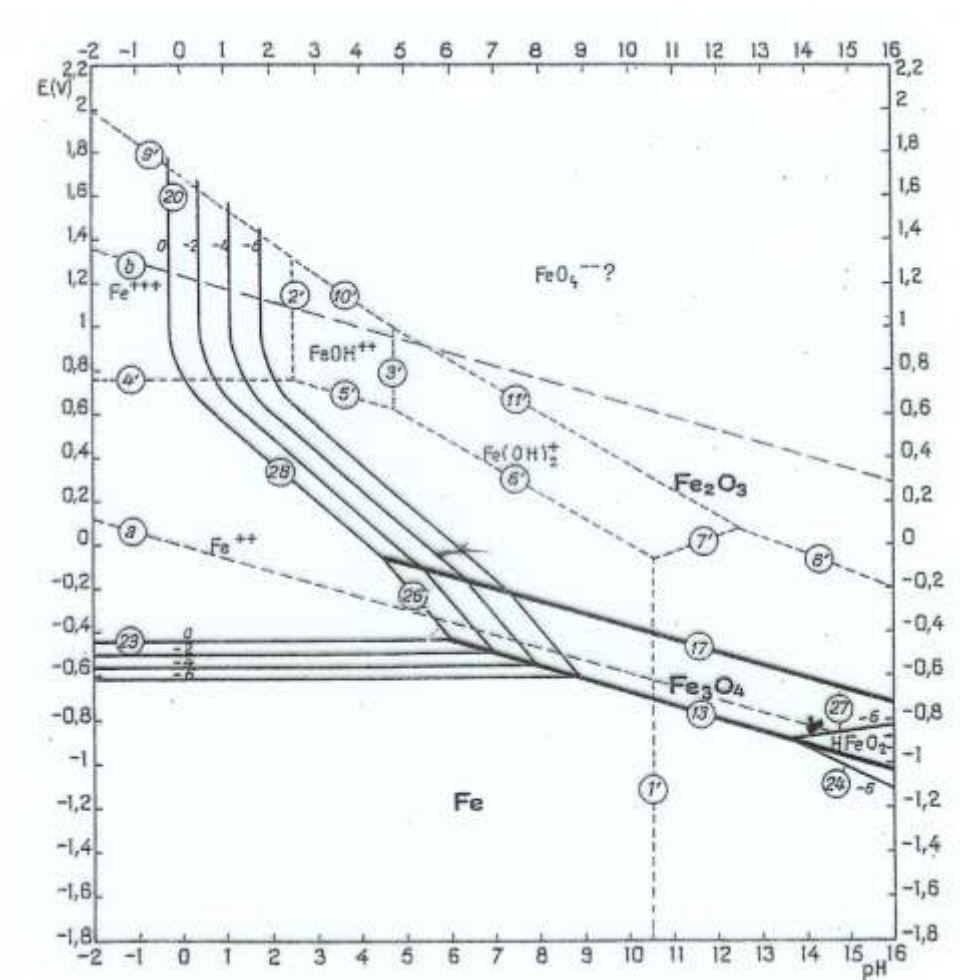


Figure 1.2 - Potential – pH equilibrium (Pourbaix diagram) for iron in water.

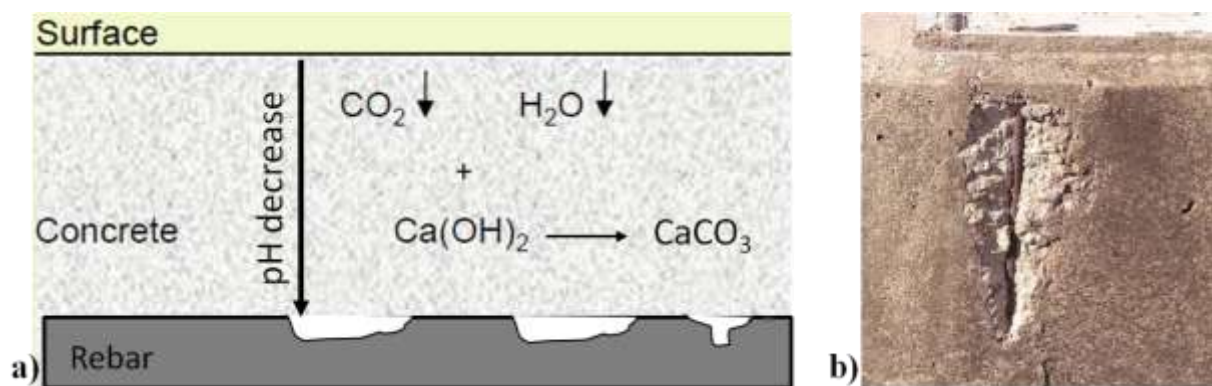


Figure 1.3- a) Representation of the carbonation process in a reinforced concrete; b) example of corrosion and spalling induced by carbonation [1].

1.1.4. STAINLESS STEELS FOR REINFORCEMENT CONCRETE APPLICATIONS

An economic and effective way of eliminating corrosion of reinforcement bars is replacing the widely used carbon steel by any type of stainless steel. *Cramer et al.* [9] reported that stainless steel bars add a 10% premium to the total project costs compared to black iron bars but are expected to reduce cumulative costs by 50% over 120 years of coastal bridge life. In the case of structures with such a long planned service-life, the probability of reaching the reinforcement level by carbonation front within this period is increased [10, 11].

The carbonation process and the chloride ions, which may ingress into the concrete from the outside environment, lead to depassivation of carbon steel as explained before. Therefore, stainless steel is used to make sure that the corrosion resistance of rebars does not limit the service life of the reinforced concrete structure. Ideally, the reinforcement should be resistant against corrosion activation under all conditions that may occur in the structure. In usual atmospheric conditions, the most aggressive environment possible is represented by carbonated concrete pore solution with high concentration of chloride where the content of oxygen is in equilibrium with atmosphere [10].

The corrosion resistance of stainless steel is attributed to the passive, chromium-rich film formed on the surface of the alloy, which is 'self-healing' when damaged. Ferritic stainless steel contains relatively little nickel and has a ferritic microstructure. Its strength is similar to austenitic steel, but ductibility, formability, weldability and corrosion resistance are not as good as for austenitic steel. Martensitic stainless steel may achieve great strength, but its toughness may be inadequate for structural applications. Its relatively low corrosion resistance also limits its use in corrosive environments. Then, for structural engineering, there are two families of alloys of interest: austenitic and mainly duplex stainless steels [1, 11, 12].

In this context, recent developments of low alloy duplex stainless steels (DSS), often referred to as lean duplex steels, increased the variety of steels available to be used as concrete reinforcement bars. These grades of DSS (for example 1.4062, 1.4162, and 1.4362) with low nickel and molybdenum contents, and consequently lower economic impact on concrete structures [11, 13], are characterized by equivalent mechanical strength compared to conventional duplex grades but lower resistance to localized corrosion, even if their corrosion

resistance is comparable to that of austenitic steels like the widely used AISI 304 and 316 grades [11].

As mentioned before, the PREn expression is often used to evaluate corrosion resistance of SS [14, 15]. The PREn linked to the content of the three main elements responsible for providing localized corrosion resistance, Cr, Mo and N, each of them weighted based on its influence on pitting [16, 17] according to the following expression:

$$PREn = \%Cr + 3.3 \times \%Mo + 16 \times \%N \quad (1-9)$$

Even if this equation is highly used as a first approach of pitting corrosion resistance by SS producers and users, it is still an empirical expression proposed from certain specific conditions, mainly in ferric chloride solutions with fixed chloride concentrations [18]. Hence, the pH influence on the pitting corrosion behavior must be carefully understood, particularly in alkaline environments, as those related to cement and concrete structures or paper industries. For example, the addition of Mo did not improve the localized corrosion resistance of austenitic grades as presented in [19-22], in spite of the fact that the PREn predicted a better performance of the Mo-containing grades.

Besides the pH, the PREn expression also neglects the effect of microstructure, surface state, temperature, amount of inclusions and precipitates in the metal microstructure, all of which certainly influences the beneficial role played by the alloying elements on the pitting corrosion resistance [14, 19]. These often forgotten precautions when working with PREn are especially important in the case of DSS, as these alloying elements are not evenly distributed between the two phases, and even more so if heat treatment is not optimized [16] or if it induces the precipitation of deleterious phases such as sigma phase (δ) [23].

Particularly, the influence of Mo addition on the pitting and crevice corrosion mechanism of SS in alkaline media is scarcely investigated in the literature [19, 24] compared to the widely studied neutral and acidic chloride conditions [14, 25-27]. As mentioned before, Mo addition on austenitic SS related anomalous behaviors under high alkaline media [19-22]. The presence of this alloying element did not improve the localized corrosion resistance of austenitic grades. This fact illustrates one of our interest in understanding Mo mechanism on corrosion resistance in alkaline media, which will allow us to optimize the alloy composition in order to have a good balance between the properties required in these applications and the final cost of the material [20].

Therefore, in the following sections, we will describe the state of art about the effect of Mo addition on SS pitting corrosion resistance under different aggressive conditions.

1.2. ROLE OF Mo ADDITION ON CORROSION RESISTANCE OF DIFFERENT SS

1.2.1. CORROSION AND PASSIVATION OF PURE MOLYBDENUM

In this section, we will deal with pure Mo corrosion and its passivation properties in order to help understanding its influence on the corrosion resistance mechanism of stainless steels when it is added used as an alloying element.

Many authors reported that the passive film formed on pure Mo mainly consists of MoO_2 as the passivating species, even though it could change at different conditions [22, 28-31]. However, *in acidic solutions*, MoO_3 was also identified as a constituent of the passive layer beside the MoO_2 . *In alkaline solutions* MoO_3 and $\text{Mo}(\text{OH})_3$ were equally found. Moreover, Mo_2O_5 layers could be present into the Mo passive film in aqueous solutions of different pH in the presence of chloride or sulphate anions [22, 29].

Some authors have unexpectedly concluded that no oxides of molybdenum were formed in 0.1M HCl [28]. Based on Mo electrochemical and XPS data, they have suggested that MoO_3 was only formed in the transpassive region. The potentiodynamic polarization of molybdenum in 0.1M HCl is shown in Fig. 1.4 indicating a passive range between -400 and +100 mV/SCE [28].

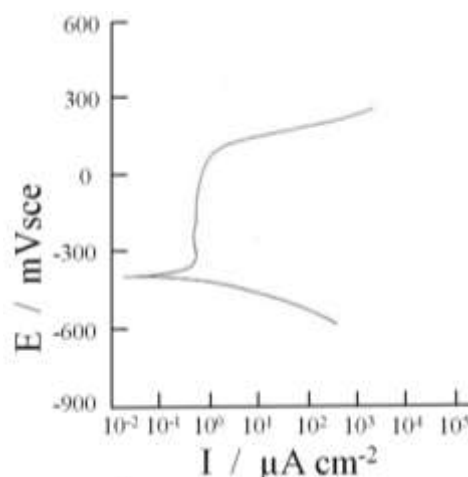
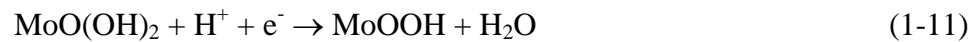


Figure 1.4 - Polarization curve of molybdenum in deaerated 0.1 M HCl solution [3, 28].

The passive film of pure molybdenum presented also a dependence on the solution pH. The stability of the passive film decreases as the pH of the solution increases due to the

formation of the soluble species HMoO_4^- and MoO_4^{2-} [22, 29]. Considering the thermodynamic stability of the different Mo oxides in different aqueous solutions, and the conclusions made by different authors, *Badawy et al.*[22] have proposed the following equilibrium for Molybdenum passive layer in (a) acidic, (b) neutral and (c) alkaline solutions:

(a) In acidic solutions the passive film consists mainly of MoO_2 together with MoO_3 and $\text{Mo}(\text{OH})_3$ [32] which may be reduced according to:



(b) In neutral solutions the reduction reaction may occur by formation of MoO_2 which is more stable [33]:



(c) In basic solutions the oxide MoO_3 is reduced and at the same time oxide film dissolution takes place according to:



These equilibriums for the Molybdenum passive layer are in good agreement with Pourbaix diagram (potential - pH - equilibrium) of the Mo oxides presented in Fig. 1.5 [27, 34].

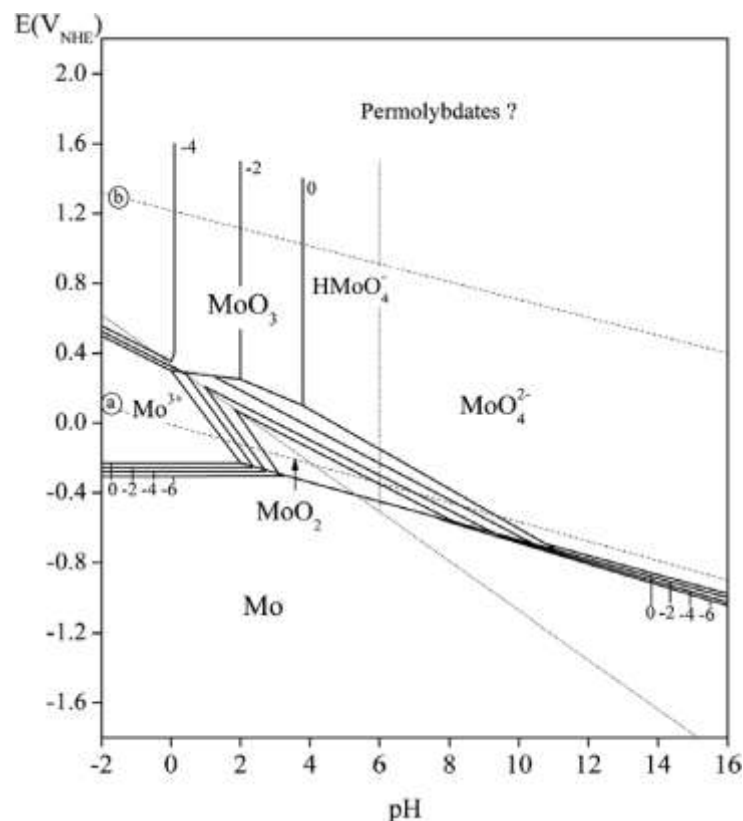


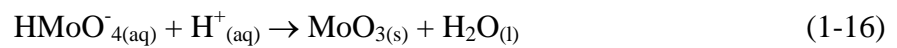
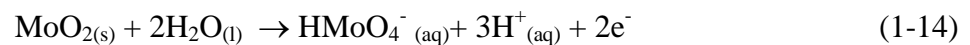
Figure 1.5 - Potential – pH equilibrium for molybdenum system at 25°C [12, 13].

Moreover, *Badawy et al.*[22] reported that the oxide film on Mo is relatively more stable in acidic solutions compared to the neutral and basic solutions based in electrochemical experiments. As could be seen in Table 1.1, there is a good agreement between polarization results and impedance data of the pure Mo after 15 min of electrode immersion in naturally aerated solutions of different pH, because both the polarization resistance and the corrosion potential decrease with pH increase whereas the corrosion current increase [22].

Table 1.1 - Values of the polarization resistance, R_p , corrosion current, I_{corr} , and corrosion potential, E_{corr} (mV_{SCE}), of the molybdenum after 15 min of electrode immersion in naturally aerated solutions of different pH [22].

pH	R_p ($k\Omega\text{ cm}^2$)	i_{corr} ($\mu A\text{ cm}^{-2}$)	E_{corr} (mV)
2	8.780	0.654	-216
7	7.960	1.530	-281
12	7.110	3.390	-539

This behavior was explained on the basis that the main constituent of the passive film is MoO_2 which contains a small ratio of MoO_3 and $Mo(OH)_3$ in *basic solutions* and a small ratio of $MoO(OH)_2$ in *acidic solution* [22]. This is the same of *Y. C. Lu's work* [22, 31, 32, 35], which showed that the passive film formed on Mo in *0.1 M HCl* solution is a compact thin layer constituted of MoO_2 and $MoO(OH)_2$. The transpassive product of pure Mo, however, was a mixture of MoO_2 , $MoO(OH)_2$, Mo_2O_5 and MoO_3 . These oxides are dissolved in aqueous conditions depending on both the potential and the pH of the solution according to the following equilibriums:



Finally, $HMoO_4^-$ was observed as a dissolution product in this acidic medium, which can change the pH of the solution and decrease the corrosion rates.

In another paper, *Halada et al.* [28] have detected also the presence of $MoCl_4$ in the film/electrolyte interface by variable angle Cl_{2p} XPS spectra of passive layer formed on pure Mo in *4M HCl solution*. So, a possible formation of a thin and insoluble Mo oxychloride or

oxyhydroxide chloride complex was reported, as shown in schematic representation of Fig. 1.6.

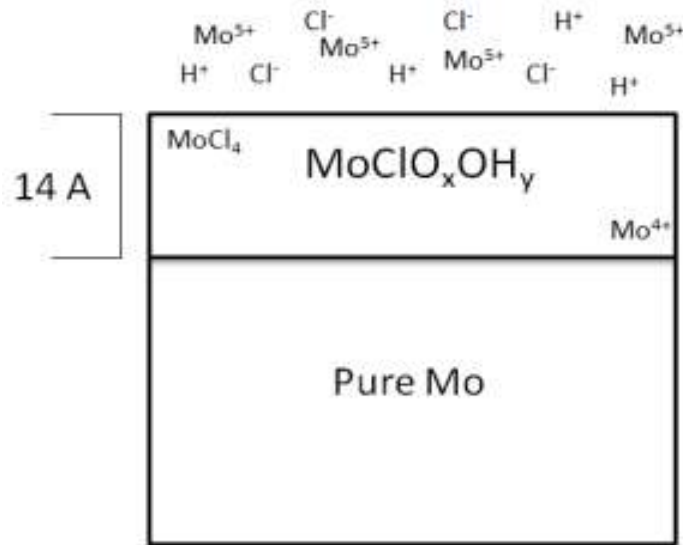


Figure 1.6 - Schematic representation of passive film formed in 4 M HCl on pure Mo proposed by *Halada et al.* [28].

There is a very limited amount of thermodynamic data for the Mo(III) and Mo(IV) oxidation states. In particular, there is a few published information on the properties of Mo(III) ions in aqueous chloride solutions and on the phase equilibrium boundary between Mo(III) and Mo(IV) species (the latter being in the form of solid MoO_2). This boundary is of particular importance for quantifying the behavior of Mo in localized corrosion environments because it delimits the range of conditions under which molybdenum remains completely dissolved in solution in the form of Mo(III) ions. At pH and/or potential values above the Mo(III)/Mo(IV) boundary, Mo(III) species convert to solid MoO_2 , thus imposing a step change in the behavior of corrosion products. In reference [36], the speciation of Mo(III) solutions for a concentration of 0.001 M of total dissolved Mo(III) at 80°C and an ionic strength of 1.0 M (NaCl) have been calculated as shown in Fig. 1.7. In the very low pH which normally correspond to the solution within the active localized corrosion sites, Mo(III) is primarily in the form of the unhydrolyzed ion Mo^{3+} . The amount of the hydrolyzed form of Mo(III) (e.g. MoOH^{2+}) is less than 10% at $\text{pH} < 1$. The hydrolysis becomes increasingly significant as pH increases and, finally, Mo(III) converts to a neutral species $\text{Mo}(\text{OH})_{3\text{aq}}$ at pH above 7. Moreover, depending on the total chloride concentration, the primary Mo(III) species may change from Mo^{3+} to the chloride complex, MoCl^{2+} , as reported in [36].

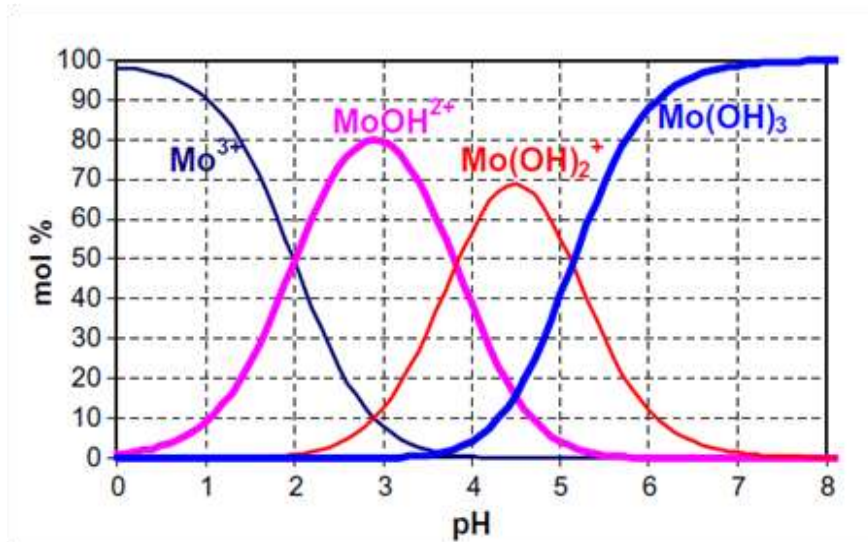


Figure 1.7 - Predicted speciation of Mo(III) in aqueous 0.001 M solutions (NaCl = 1.0 M) at 80 °C as a function of pH [36].

In synthesis from those references about the passivation and corrosion behaviors of pure Mo in different media, we can highlight that:

- The passive layer formed on Mo exposed *in air* consists normally of MoO₃, but when this oxide is exposed to aqueous solutions of different pH the passive film stability changes.
- *In neutral solutions* occurs the reduction reaction of MoO₃ giving MoO₂.
- *In acidic solutions*, the principal constituents of molybdenum passive layer identified by XPS are MoO₃, MoO₂ and hydrated species as MoO(OH)₂ and Mo(OH)₃.
- *In alkaline solution*, the oxides species frequently presents are MoO₃, Mo(OH)₃ and the soluble species like HMoO₄⁻ and MoO₄²⁻. Finally, many authors consider that in aqueous solutions of different pH and in the presence of chloride or sulphate anions the passive film consists mainly of MoO₂, Mo₂O₅, Mo(OH)₃, MoCl²⁺ and MoCl₄[22, 28, 30, 31, 36].

1.2.2. INFLUENCE OF Mo ON STAINLESS STEELS PASSIVATION

The literature review about the corrosion and passivation of pure Mo described in the previous section could help us to understand the mechanisms on the corrosion resistance and the pitting behavior of Mo-alloying stainless steels. As Molybdenum is an important valve metal due to its well known role in improving the corrosion characteristics of SS, a deeper investigation of the literature about Mo addition on different kind of SS will be presented in this section.

It has long been known that Mo additions to Cr and Ni SS improve pitting resistance and also modify the active-passive transition to favor easier passivity and consequently to improve characteristics of the passive film formed [28]. Nevertheless, there exist several studies about the electrochemical behavior of Mo and its role in the improvement of SS corrosion properties in which the presence of this element in the passive film and its influence on pitting corrosion mechanism are discussed [28].

Some authors suggested that Mo is present in the oxide film [31, 37] and they highlighted the importance of neutral species, such as MoO_2 or MoO_3 , in the passivation properties of the oxide film formed on stainless steels while results from some other papers suggest the opposite [27, 37- 39].

By now, the beneficial effect of Mo in the corrosion resistance of SS has been attributed to several factors such as: *an enrichment of Mo in the passive film [40] or in the alloy layer just below the passive film [41], enrichment of Cr in the oxide layer [41] thickening of the passive film and stabilization of the Cr oxides by the presence of Mo^{6+} . It has also been suggested that Mo retards the corrosion process by formation of Mo compounds, by synergistic interaction of Mo ions with other oxides of the passive film [40, 42] and by elimination of the active surface sites through formation of Mo oxides or oxihydroxides in these sites[43, 44].*

Moreover, there are a variety of opinions about the presence and nature of the Mo in the oxide film and also about its behaviors in solutions of different pH. Therefore, Mo influence under acidic, neutral and alkaline conditions will be more accurately discussed in the following sections.

1.2.2.1. ACIDIC CONDITIONS

In general, the role of molybdenum in the corrosion resistance of stainless steels in chloride media is not yet clearly established, although most studies conclude that Mo has a beneficial effect on passivity breakdown and pitting initiation in acid solution [41]. In particular, some authors [26, 41, 43, 45, 46] have studied the influence of Mo alloying additions to the passive layer formation on SS surface in aqueous environments (mainly acidic pH).

Many of them [41, 46] have suggested that the presence of Mo in the stainless steels does not markedly change the composition of the film in acidic media, but the presence of MoO_4^{2-} in the outer part can change the ionic selectivity of the film, promoting the formation of Cr_2O_3 and CrO_3 . The results presented in [46] do not only agree with this assertion, but also highlight the fact that an induced modification of the film could explain the origin of the different Cr distribution along the oxide layers. On the other hand, *Sakashita and Sato* [47] proposed a bipolar model for the passive films where the Mo acts as an adsorbed intermediate that changes the intrinsically anionic selectivity of the outer part of the film into a cationic one, inducing the formation of a dipolar layer which promotes the formation of Cr_2O_3 and CrO_3 . Hence, these results indicate that molybdenum mainly enhances the effect of other passivating species (Cr ones), more than acting directly in the passivation process in *acidic media*.

The authors in [40] associated the increase of the SS passive film thickness with an increase of Mo contents in *acidic solutions*. Moreover, the hexavalent Mo oxides, which were found within the passive film, improved the protective quality of the passive chromium hydroxide film. This type of film should be as compact as the film on Fe-Cr alloys with higher Cr content. Thus, when a compact film is formed on the Mo-containing SS, the transpassive dissolution of alloyed Mo will be inhibited because Mo is fixed in the film. The Mo (VI) oxides which are fixed in the state of solid solution in the film are thought to promote the ability of a Cr (III) oxyhydroxide film to protect the SS from corrosion, since the Mo (VI) oxide is very stable *in acidic solutions with Cl*. Even if the Cr^{3+} content of the passive film is relatively small, a high resistance of the film to pitting could result from a film containing adequate amount of Mo^{6+} in the state of solid solution in the film [40].

Fig. 1.8 illustrates a comparison of the spectra of the Mo $3d_{3/2} - 3d_{5/2}$ levels for the 20Cr-25Ni-5Mo steel, *passivated in 1M HCl at + 0.3V/SCE for 1h*, MoO_3 powder, and a freshly polished sheet of metallic Mo. It can clearly be understood that among the four peaks observed in the spectrum of the 20Cr-25Ni-5Mo steel the peaks at 235.5 and 232.3 eV originate from Mo oxidized at the hexavalent state whereas the peaks at 230.4 and 227.7 eV come from metallic Mo [40].

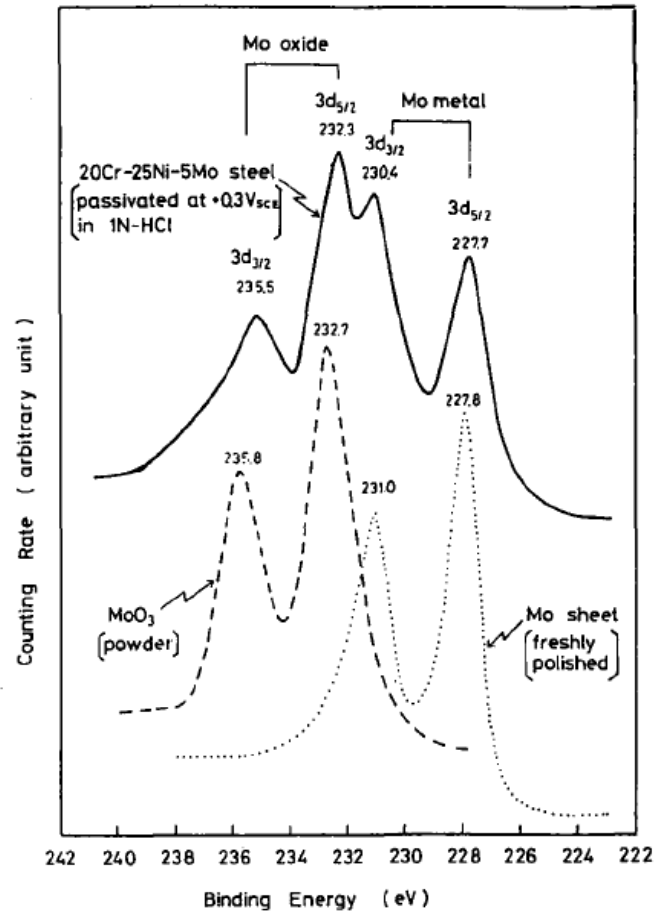


Figure 1.8 – Comparison of the XPS spectra of the Mo $3d_{3/2}$ – $3d_{5/2}$ levels for the 20Cr-25Ni-5Mo steel, MoO_3 powder and freshly polished sheet of metallic Mo [40].

On the other hand, *K. Hashimoto et al.*[48] argued for a deficiency of molybdenum on passive layer of on both 30Cr-2Mo and 30Cr SS as Mo addition did not change the composition and the thickness of passive layer. Nevertheless, they showed that the addition of 2% Mo to 30Cr SS decreases the current density in the passive region two orders of magnitude *in 1M HCl*. They interpreted these beneficial effects of Mo addition to *ferritic stainless steels* in terms of the decrease of the activity of the active surface sites because of Mo through the formation of molybdenum oxy-hydroxide or chromium and iron-molybdate on these sites. This leads to the appearance of homogeneous steels surface and hence to the formation of an uniform passive film.

Another reported effect of Mo is the production of protons which will be drawn towards the solution by the cation selective properties of the outer layer of the passive film, causing then an increase of the proton activity on the surface of SS [35, 49]. The passive films formed on the surface of *Fe19Cr9Ni* and *Fe19Cr9Ni2.5Mo* alloys *in 0.1M HCl* were characterized by AES and variable angle XPS measurements. The result of Mo addition on

Fe19Cr9Ni was the formation of a passive film with an enhanced interfacial barrier film composed mainly of Cr_2O_3 , containing CrO_3 in solid solution which forms a glassy phase. In addition, molybdenum appears to be present as Mo^{4+} and Mo^{6+} identified as hydrated MoO_2 and MoO_4^{2-} , apparently as FeMoO_4 . These authors also proposed that MoO_4^{2-} anions are formed in the solid state along with CrO_4^{2-} , which together are responsible for producing, in 0.1M HCl, a bipolar film consisting of a cation selective outer layer containing CrO_4^{2-} and MoO_4^{2-} and an intrinsically anion selective inner layer. Both of these properties provide greater resistance to break down of passivity in Cl^- ion containing acidic media [35].

In [50], the integrated intensity of molybdenum and chromium in the surface films of 312L SS obtained by GDOES depth profiles plotted as a function of polarization potential *in 2 mol L⁻¹ HCl solution*. (see Fig. 1.9). This intensity was normalized by the integrated intensity of chromium and molybdenum in the air-formed film. Since the integrated intensity is roughly proportional to the amount of these elements in the surface film, this potential dependence should represent the change in the amount of these elements in the surface films as a function of potential. The intensity of molybdenum increases in the active region of -0.18 V vs. Ag/AgCl. The amount of molybdenum is still large at 0 V vs. Ag/AgCl, though this potential is in the passive region of stainless steel. This is probably due to the fact that this potential is still in the passive region of molybdenum. So, the Mo effect on the passive film of SS does not depend only on the exposing solution, but also on the applied potential.

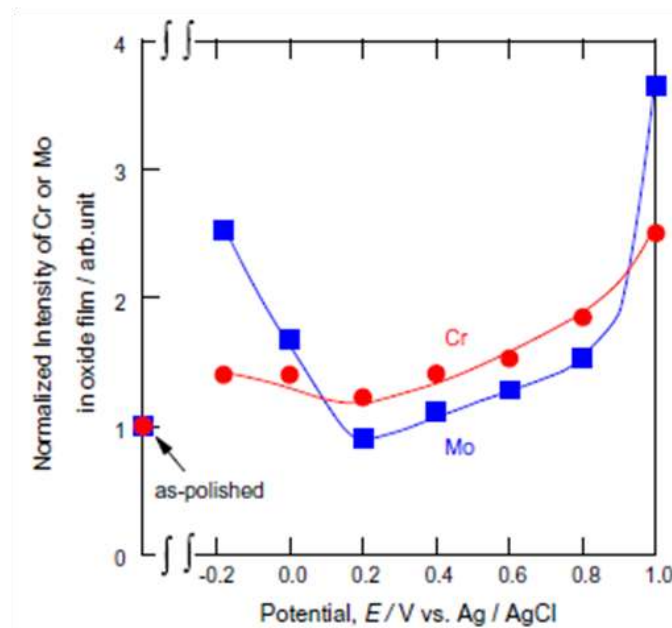


Figure 1.9 - Integrated intensities of chromium and molybdenum in the surface film, normalized by those in the air-formed film, as a function of polarization potential *in 2 mol dm⁻³ HCl solution* [50].

1.2.2.2. NEUTRAL CONDITIONS

M.F. Montemor et al. [43, 51] have shown the presence of Mo in the internal Cr rich layers (Cr_2O_3) formed on austenitic and ferritic SS at hot air (350°C) by Auger and XPS experiments. The presence of Mo in this region results in an enrichment of chromium in the internal region of the film. Although Mo was not a phase forming element, they concluded that the presence of Mo modifies the properties of the oxide film because it could introduce changes in its defect structure. More precisely, Mo decreased the number of acceptors of the p-type Cr oxide and decreased the number of donors in the deep levels of the outer Fe rich oxide layers, which have a n-type semiconductivity, as previously suggested by *Olefjord et al.* in [52].

These last authors, based on XPS study of SS passivated in chloride solutions, suggested that the defects created by Fe^{2+} in the Cr oxide layer were cancelled by those created by Mo^{4+} and Mo^{6+} . Fig. 1.10 shows that the presence of Mo affects the Cr oxide content on the passive film of ferritic and austenitic steels when they are oxidized at 350°C in air. The amount of Cr oxide becomes higher in the presence of Mo (this result was observed for both the commercial and high purity samples) [43].

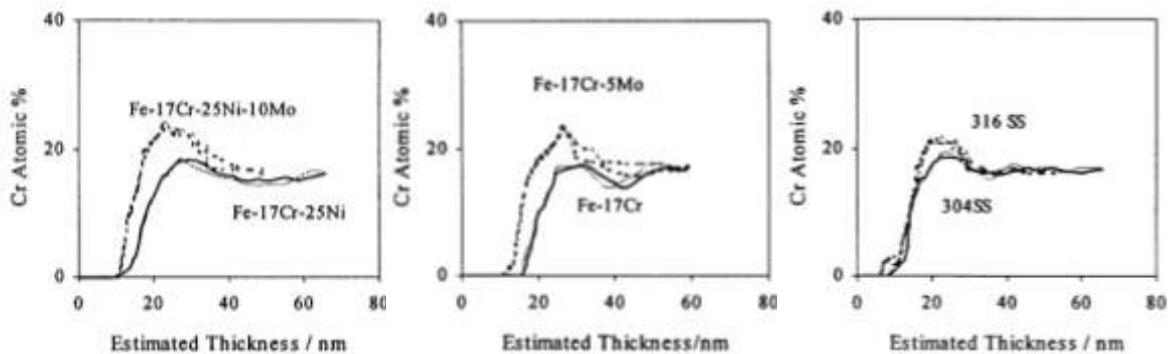


Figure 1.10 - Evolution of the Cr at % obtained from the Auger depth profiles for the high purity alloys and for the commercial alloys oxidized at 350°C in air [43].

By now, the application of synchrotron energy to study SS passivation is not highly used. Nevertheless, *Kimura et al.* [54] reported results about X-ray Absorption Spectroscopy (XAS) measurements at the Mo K edge in pits grown in 1 M LiCl and 1 M LiBr and that showed the appearance of a complex similar to the network of $[\text{MoO}_4(\text{H}_2\text{O})_2]_2$ octahedra; they suggested that the formation of such polymeric networks near the corroding metal interface plays a significant role in the beneficial effect of Mo on the corrosion resistance of SS. Nevertheless, these results are still controversial and not consistent with a very recent X-

ray Absorption Near Edge Structure (XANES) study from *Davenport et al. [55]*, who recorded the presence of Mo(III) species in the solution inside artificial pits formed on an austenitic Mo containing SS (316L).

1.2.2.3. IN ALKALINE CONDITIONS

Passing to alkaline environments, the literature was very scarce. So, in these circumstances, *D. Addari et al. [53]* reported a combined electrochemical and XPS surface analytical investigation on austenitic, ferritic and duplex stainless steels in a simple NaOH solution and also in a more complex alkaline concrete pore medium. These authors concluded that the passive layer of ferritic and duplex SS became enriched in chromium oxy-hydroxide whereas the oxide film became strongly enriched in nickel hydroxide for the austenitic ones.

After 1 day's immersion, the film thickness was $3.6 \pm 0.2 \text{ nm}$ for the ferritic alloy compared to $3.9 \pm 0.2 \text{ nm}$ for the austenitic and duplex stainless steels. The evolution of passive film composition over time in 0.1M NaOH solution generally presented a decrease in iron content whilst an increase in chromium content. The average of passive film composition determined after 1-day immersion in the more complex alkaline solutions is shown at Table 1.2. Finally, these authors [53] indicated that Mo is present both as oxy-hydroxide in the passive film and as metallic molybdenum at the interface of passive layer and the bulk material of the Fe22Cr6Ni2Mo DSS in these alkaline conditions.

Table 1.2- Average passive film composition of the three alloys studied in [55] after immersion for 24 h in alkaline solutions without chloride ions.

Alloy	Fe ox	Cr ox	Ni ox	Mo ox
Fe15Cr	55	45	–	–
Fe18Cr10Ni	43	46	15	–
Fe22Cr6Ni2Mo	38	55	4	4

1.2.2.4. SUMMARY

Thus, by the references cited in the section 1.2.2., we could bring out the following important points:

- The oxide films formed in air at high temperature on the ferritic and austenitic SS are composed by an external iron oxide region and an inner chromium oxide region. The internal region reveals the presence of Mo and moreover Mo addition induces an

enrichment of chromium oxide within the film, but the film thickness is practically independent of the presence and content of Mo.

- *In HCl solution*, the passive films of the Mo-containing Cr-Ni steels (austenitic grades) consist of complex oxy-hydroxide containing Cr^{3+} , Fe^{3+} , Ni^{3+} and Mo^{6+} . Moreover, Mo contents and also the film thickness increases almost linearly with increasing of Mo content on the bulk composition. For this material, the Cr and Mo content on the passive layer presented a dependence on the applied potential. However, for the ferritic stainless steels (30Cr-2Mo) the passive film formed in *1M HCl* consist mainly of chromium oxy-hydroxide.
- *In 1M NaOH solution*, the effect of Mo in the formation of the passive films on austenitic SS point out to the stabilizing effect of the molybdates on the surface of the film, enhancing the formation of a thin layer with a higher Cr/Fe ratio. Finally, the duplex stainless steel (EN 1.4462) present molybdenum as oxy-hydroxide in the passive film and as metallic Mo at the interface with roughly the bulk composition after *24h immersed in 0.1NaOH solution without Cl*.

1.2.3. EFFECT OF Mo ON UNIFORM CORROSION OF AUSTENITIC STAINLESS STEELS

The comprehension on the Mo effect on general corrosion of austenitic SS could help us to understand its influence on pitting properties, so that it's worth discussing the results presented by *Pardo et al.* [26] about the *Mo mechanism on the general corrosion process of austenitic SS in high acidic solutions (30 wt.% H_2SO_4)*.

Firstly, these authors proposed that the passive layer of the AISI 304 was completely dissolved when the specimen gets in contact with the sulphuric acid medium, and then the solution turns to dark green color, which is typical from the Cr(III) species dissolution. The same effect but to a lesser extent was observed for AISI 316. The higher stability of the passive layer of the AISI 316 should be possibly related to the higher amount of Mo(VI) within it. This step of the general corrosion could be seen on Fig. 1.11 a).

In the following step, the unprotected bulk material is exposed to aggressive media and suffers general corrosion attack (Fig. 1.11 b)). Consequently, the solution is enriched in

Cr^{3+} , Fe^{2+} , Ni^{2+} and Mn^{2+} species, whereas the material surface is enriched in Mo^{6+} according to XPS results (Fig. 1.11 c)). In the final step, molybdenum forms an inert and semi-protective layer of MoO_3 (according to Pourbaix diagram for Mo species presented Fig. 1.5) which inhibits the general corrosion process as illustrated in Fig. 1.11 d) [26].

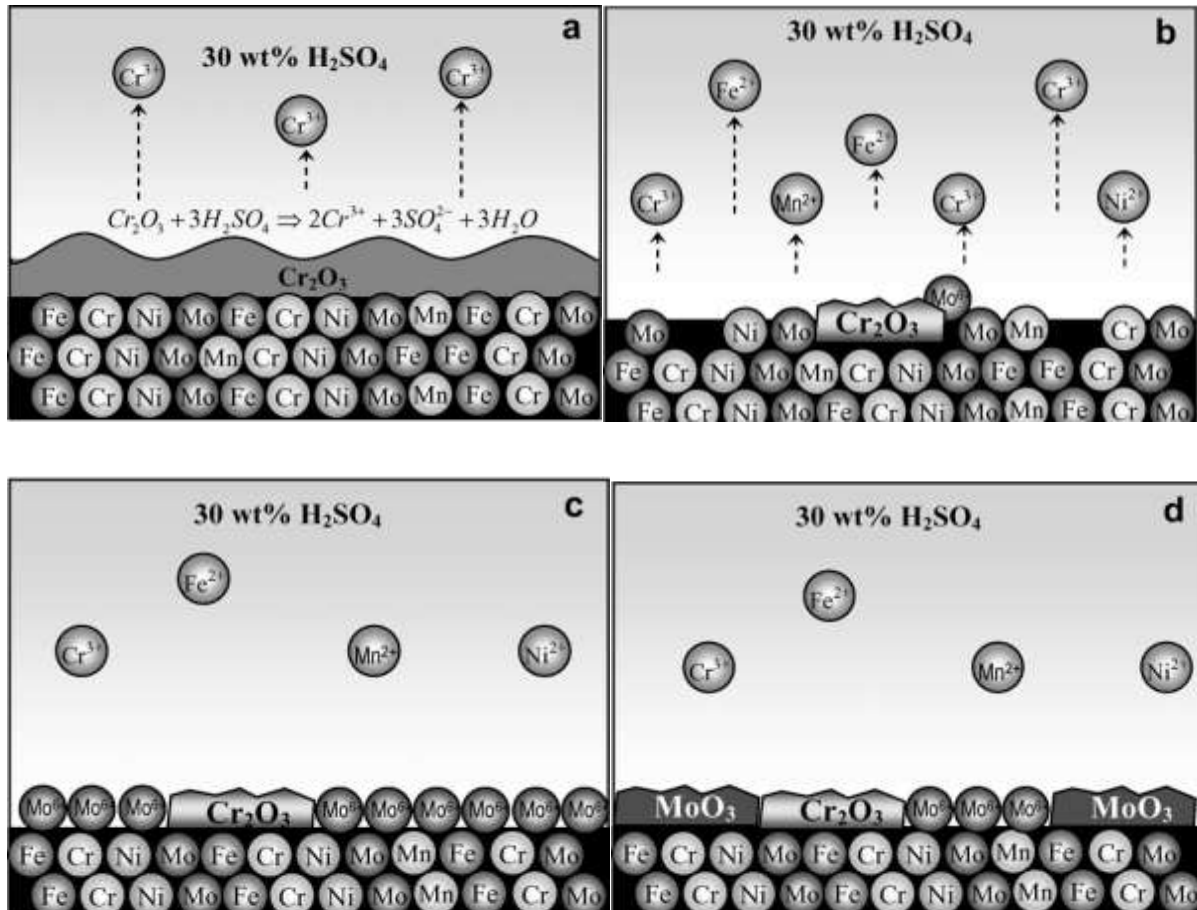


Figure 1.11 - Corrosion mechanism proposed by A. Pardo *et al.*: **a)** passive layer dissolution; **b)** metal cation dissolution; **c)** Mo^{6+} enrichment on the surface material and **d)** formation of MoO_3 oxide layer [26].

Furthermore, the analyses of XPS spectra showed in Fig. 1.12 revealed the presence of Mo^{6+} (probably MoO_3) in the outer region of the passive film, and Mo in metallic state at the film/metal interface for austenitic SS with more than 2wt.% Mo on the bulk composition [26]. So, this formation of a molybdenum-rich oxide stable film in the active region of SS in 30 wt. % H_2SO_4 medium, can act as an effective barrier against the diffusion of species through the film and, therefore, decrease the dissolution rate.

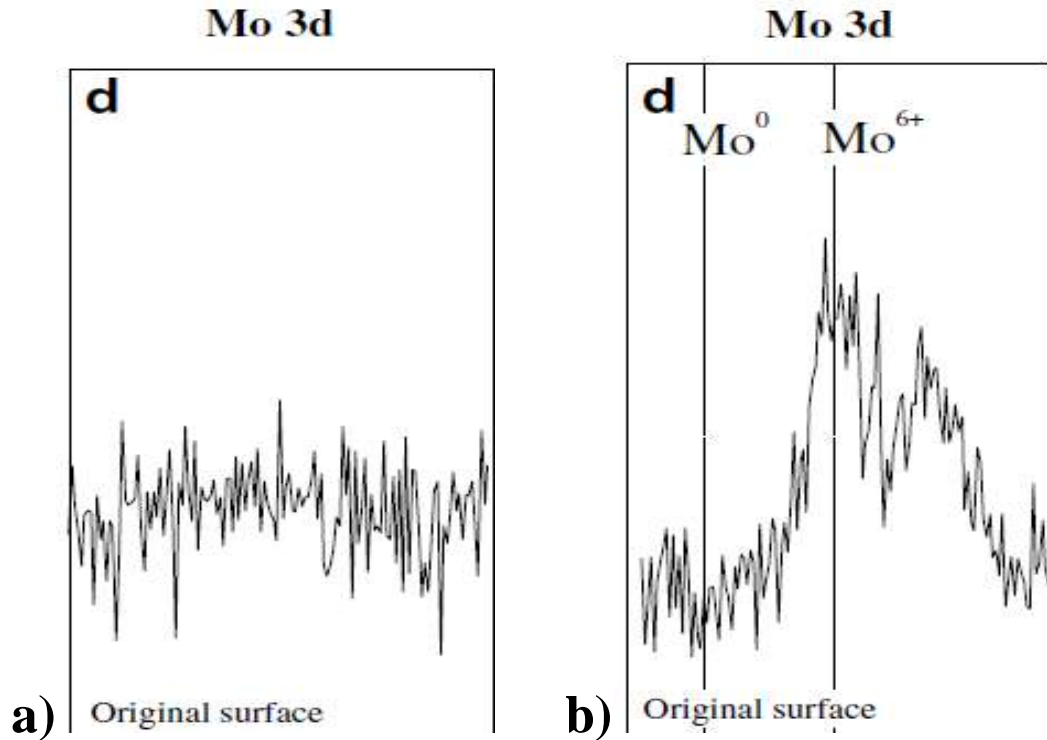


Figure 1.12 - XPS spectra of *Mo 3 d* ionization of the surface for the as received austenitic SS specimen with (a) 0.29%Mo and (b) 2.1%Mo after 9 days in 30 wt.%H₂SO₄ at 25°C [26].

These researchers conclude that Mo seems to play a dual role in the improvement of the general corrosion resistance of the stainless steels by 1°) modification of passive film composition, and 2°) modification of active dissolution by formation of insoluble oxides [26].

1.2.4. EFFECT OF Mo ON PITTING NUCLEATION OF STAINLESS STEELS

The mechanism of pitting attack of stainless steel has been divided into three consecutive steps: initiation (metastable propagation), stable propagation of pits and repassivation. The initiation step mainly corresponds to a local breakdown of the passivation (oxide layer) in presence of aggressive anions in the environment, for example Cl⁻. The corrosion rate is increased by the fact that the environment produced by the corrosion reaction itself is even more aggressive. However, at the earlier stages of pit propagation, if the pits are still very small, they can be repassivated spontaneously; this stage is often referred to as metastable pit

Then, the initiation and propagation of pits can be considered separately, with the initiation stage involving breakdown of the passive film and the development of an

aggressive local chemistry at the corroding site, whilst propagation involves the continued stable growth of the corroding area. Perhaps the most commonly measured quantity in pitting studies is the *pitting potential* (E_{pit}), above of which stable pitting is discernible for a specific alloy and environment. E_{pit} was at first defined as the highest potential at which pits could *repassivate*, but the later observation of short lived pitting events at lower potentials (metastable pitting), shows that E_{pit} is the potential above which pits can stably propagate [56].

Then, some of the many suggestions offered as to how Mo enhances pitting corrosion resistance in SS include:

- 1) the improvement of the bounds in the oxide film [31, 37]. Effect on initiation/nucleation steps.
- 2) the elimination of active sites by the formation of Mo complex such as Mo oxyhydroxides and MoCl_3 [37, 48]. In others words, the Mo effect on metastable propagation and stable pit growth.
- 3) And, by now, the most understood explanation for the Mo effect in SS is the fact that Mo improves the repassivation behavior or the deactivation of growing pits by the formation of molybdates within the pit environments [27, 53, 57], which means the positive influence of Mo on propagation and repassivation of stable and metastable pits.

In this section, we will then introduce some mechanisms about Mo effect on the pitting corrosion initiation, propagation, and repassivation already proposed in the literature for different alloys in several environments.

Firstly, the studies done by *Ilevbare and al.* [37, 58] explained the possible action of Mo on nucleation and metastable pitting of *austenitic SS in deaerated 0.1M HCl (pH=1)*. Since these constitute the embryonic stage of a growing pit, the probability associated with the successful generation of these events will affect the onset of stable pitting. The pit nucleation studies were therefore associated with very small currents ranging from a few picoamperes to a maximum of 350 picoamperes. Fig. 1.13 shows the current transients obtained from the polarization of AISI 316. There is a current overload at the beginning of this experiment because the digital voltmeter was set to measure currents not exceeding 350 pA in order to obtain a good resolution of small nucleation events. The frequency of events is highest immediately after the period of current overload.

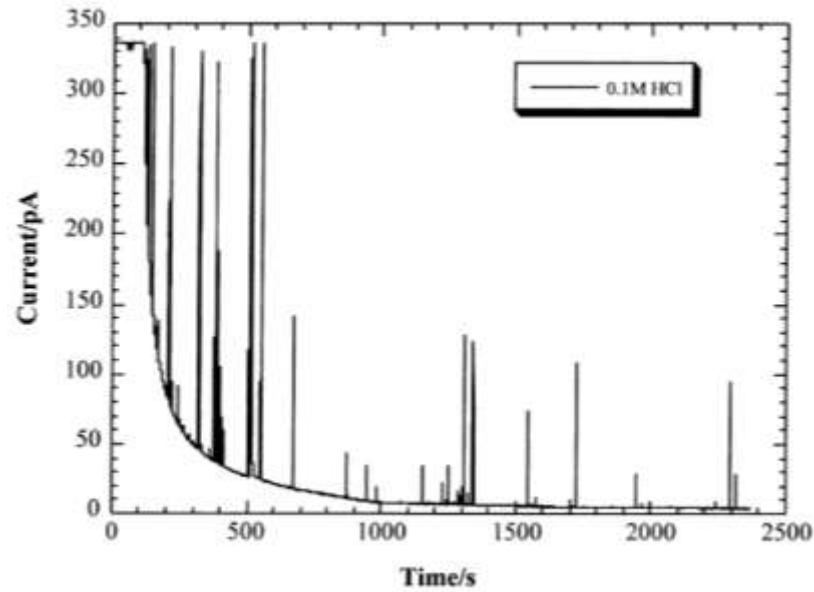


Figure 1.13 - Current transient of SS316GF (cross-sectional area $2 \times 10^{-5} \text{ cm}^2$) in *deaerated* 0.1M HCl for 2370s at 0.2 V (SCE) [37].

Fig. 1.14 a) and b) show two types of nucleation events that were identified in [37]. Fig. 1.14 a) shows a current transient representing single nucleation events (type 1) which indicate a very sharp rise in current followed by an equally fast fall. Fig. 1.14 b) shows a sharp rise (in this illustration preceded by two small nucleation) followed by a gentle partial current decay which further proceeded into a current rise which reaches another peak after a few seconds before complete repassivation sets in (type 2). This second type of events has rarely been observed.

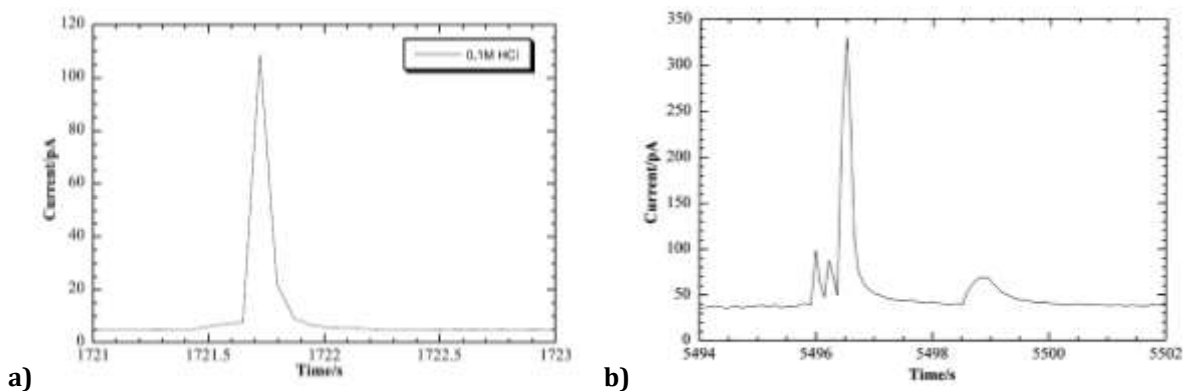


Figure 1.14 – a) Current transients type 1 b) nucleation events type 2 on *AISI 316* (cross-sectional area $2 \times 10^{-5} \text{ cm}^2$) in 0.1 M HCl at 0.2 V (SCE) [37].

The studies of these peak heights (current) indicate a distribution of the nucleation for AISI 304 and 316 which is depicted in Fig. 1.15. This graph shows the percentage of the total number of events calculated from 10 and 15 runs for AISI 304 and 316, respectively. The heights of the events are grouped logarithmically using 1/3 decade intervals. The groups

include (in pA) **A**: 1.6 ± 3.4 ; **B**: 3.4 ± 7.4 ; **C**: 7.4 ± 16 ; **D**: 16 ± 34.5 ; **E**: 34.5 ± 74.3 ; **F**: 74.3 ± 160 and **G**: >160 . The last range **G**, should read 160 ± 344.7 , but it is open ended to cater for all the peaks which have been cut-off by the upper current limit. There is an exponential decay in the number of nucleation events as the current range increases for both metals. The percentage of the events at the current ranges **E**, **F** and **G** are much higher for 304 than for the 316 SS compared to the smaller events in ranges **A** and **B** meaning that a greater proportion of larger events are nucleated on 304 than on 316 SS. This is also consistent with the greater reactivity of SS304. The proportion of events in **G** for 304 SS is much higher than in the previous range, **F**. This is probably because **G** represents more than a 1/3 decade interval; hence, the exponential decay is believed to be consistent as long as the current range does not increase.

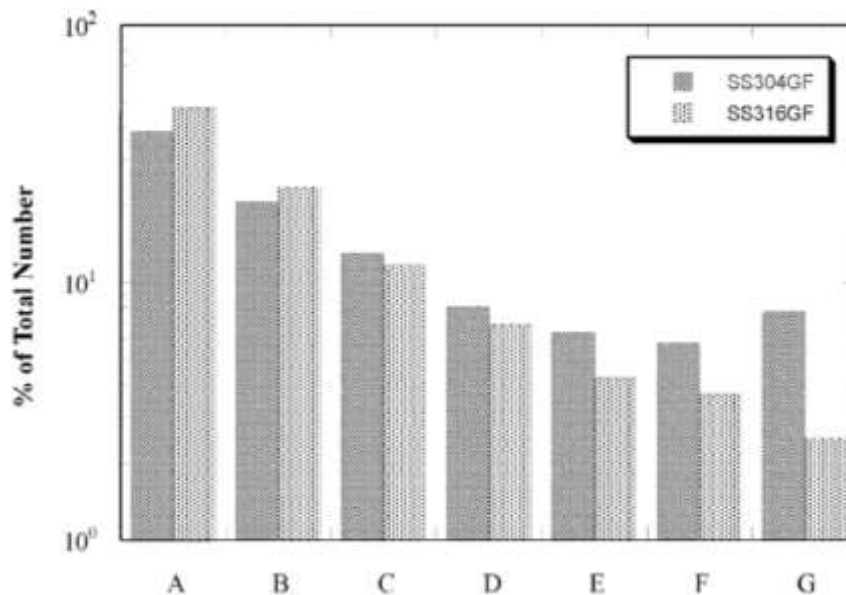


Figure 1.15 - Height distribution of nucleation in deaerated 0.1 M HCl at 0.2 V (SCE) during 2370 s on AISI 304 and 316 [37].

The lower height distribution of nucleation transients for AISI 316 compared to 304 suggests that the Cl^- ions find it more difficult to penetrate the oxide film implying an improvement in its corrosion properties, or that the character of the sites of pit nucleation have been chemically altered so that the dissolution of inclusions become more difficult in the AISI 316 steels. It would be due to the presence of Mo in 316 composition since Mo would therefore be present in the inclusions as sulphides (especially at the inclusion/metal interface) which are insoluble even in acidified Cl^- solutions. The suggestion that Mo sulphides are formed is reasonable since Mo has similar chemical properties to Cr and complex sulphides of the type $(\text{Cr}, \text{Mn})_x\text{S}$ and simpler ones like CrS have been discovered

[59]. Then, these authors [37] concluded about the current transient studies that nucleation step which occurred on AISI 304 compared to those on AISI 316 grew to much higher currents and were more numerous thus increasing the probability of metastable pit propagation. **They suggested that either simple or complex insoluble molybdates are formed with the metal cations within the pits of AISI 316 when Mo from the bulk composition are dissolved and passes to the solution** [37, 58].

Molybdates usually form complexes in *highly acidic environments* like that in the pits, according to the reference [41]. This study investigated the surfaces of *austenitic Mo-containing* alloys in *chloride media* and observed the formation of large islands in which the atomic structure indicates that the Cl^- ions were incorporated. **So, these authors concluded that those islands are composed of molybdenum chlorides. With this idea they proposed a mechanism schemed, as shown in the Fig. 1.16, to explain the different structures observed on alloy surfaces at the nanoscopic scale.**

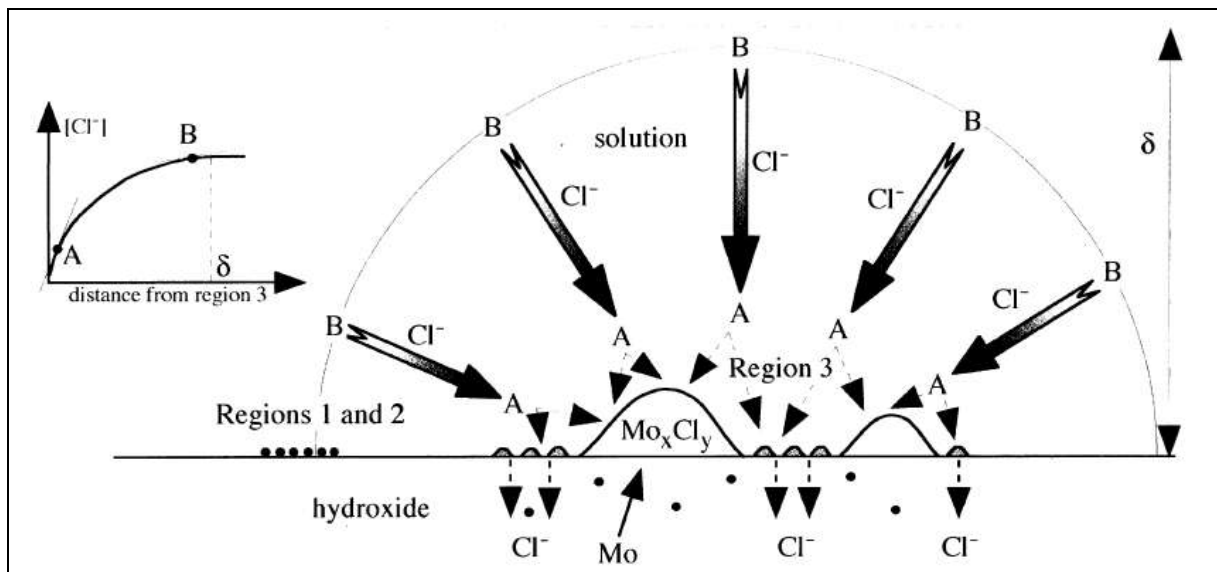


Figure 1.16 – Schematic diagram of mechanisms leading to a localization of Cl^- penetration in relation with formation of islands of molybdenum chlorides *for austenitic SS at acidic media* [41].

This mechanism consists in:

- At the onset, Cl^- concentration in solution is uniform. Chloride located in the near vicinity of the passive film/solution interface (point A in Fig. 1.16) and which are good candidates for penetration into the passive film are consumed for island formation by bonding with molybdates and impurities. Considering the size (about 200 nm) and density of islands, a large amount of Cl^- is concerned. A high gradient appears between points A and B and Cl^-

flow through a layer with a high kinetic of diffusion. Once island formation is achieved, a Cl^- free layer exists between points A and B as the greater part of the Cl^- is already bound by the island growth processes, so that the adsorption and penetration of Cl^- into the passive film are then limited by the diffusion of Cl^- , which is now low. The alloy is then protected against Cl^- aggression. However, a small part of the Cl^- present in region 2 is absorbed into the hydroxide during island formation. The island formation has thus two beneficial effects on Cl^- aggression: it reduces regions where Cl^- is absorbed to regions 2 and in these regions it limits the amount of absorbed Cl^- . This mechanism of Mo action in acidic media is very interesting and these authors always observed islands on the 316 L surface whereas it was never found on the 304 L surface.

In another reference [60], the authors indicated that the metastable pitting potential transients consist of four successive stages (see Fig. 1.17) for stainless steels. These stages are attributed [61] respectively to (1) pit initiation, (2) growth start, (3) growth end and (4) pit repassivation. At the opposite, other authors [62] believe that step (4) rather corresponds to the discharge of the interface capacity on the repassivated surface, at least for slow cathodic reactions as oxygen evolution.

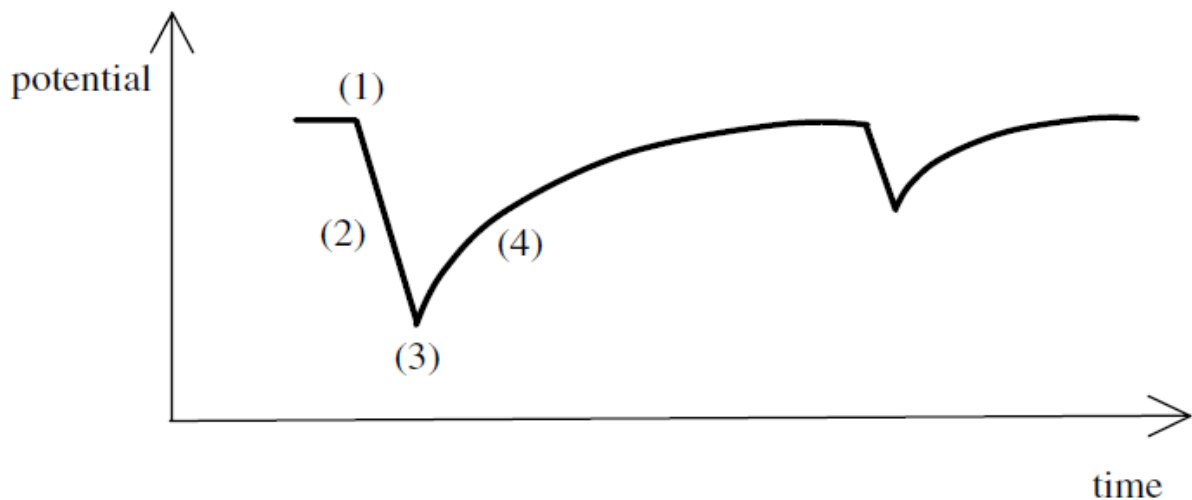


Figure 1.17 - Schematic representation of the potential vs. time variations during metastable pitting. Four successive steps are observed [60].

From ZRA (Zero Resistance Ammeter) analyzes with AISI 304 and 430 SS done in [60], clear differences of the nucleation transients for ferritic and austenitic SS appear. Fig. 1.18 exhibits the parabolic intensity transient type for AISI 430 but nearly triangular ones for AISI 304.

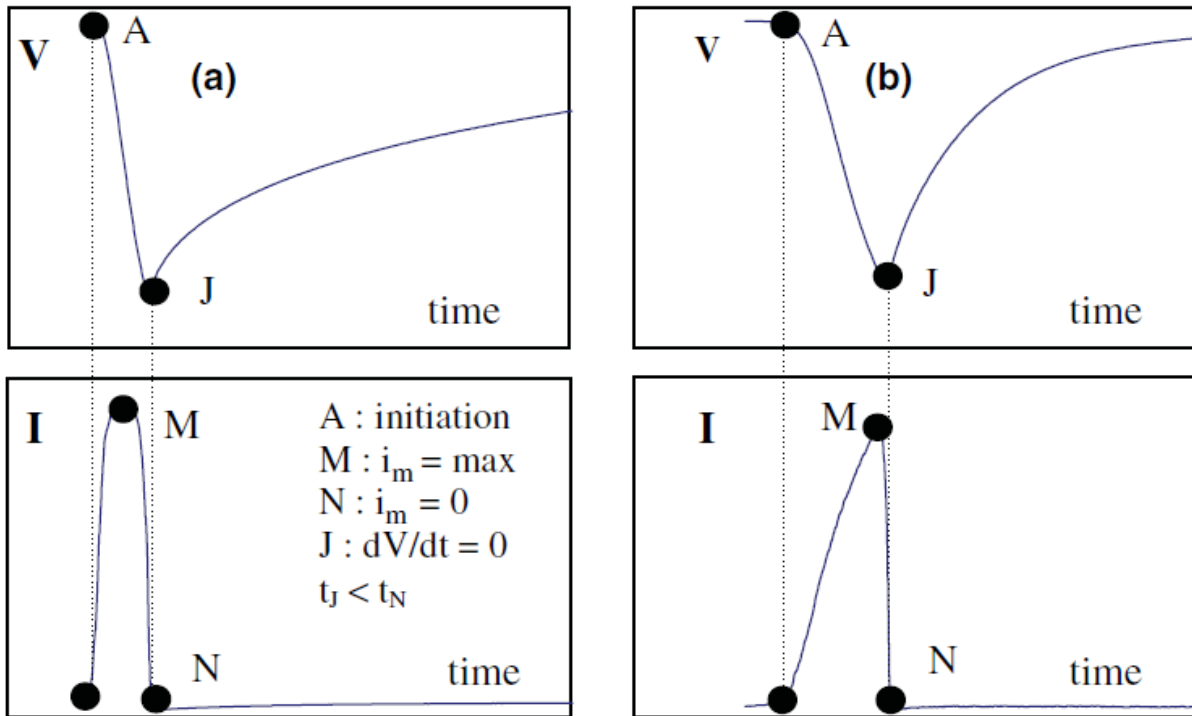


Figure 1.18 - Typical potential and current transients obtained for (a) Fe16Cr in $0.02M NaCl + 2 \times 10^{-4} M FeCl_3$ and for (b) Fe18Cr9Ni in $1M NaCl + 2 \times 10^{-4} M FeCl_3$ [60].

These authors [60] concluded that the last stage of metastable pitting (stage (4) in Fig. 1.17) is not the repassivation but the discharge of the surface capacity. This fact was explained by the intensity transients decreases from the maximum point to zero slightly after the potential minimum (from point M to point N in Fig. 1.18 (b), for example). However, the point N corresponds to the pit repassivation and the final potential increase corresponds rather to the discharge of the interfacial capacitance by the cathodic reaction (reduction of Fe^{3+} to Fe^{2+}) as suggested by *Isaac et al.* [62].

According to the references presented above, the presence of Mo as an alloying element in SS reduces the occurrence of both nucleation and propagation of metastable pits. Moreover, the extent of growth these events achieve is reduced and the attainment of stable pit growth is made more difficult in the presence of Mo. **Thus, the role of Mo for the first step of the pitting corrosion (nucleation of pits) is: to decrease the nucleation pit probability and the formation of the metastable pits. Consequently, this element could have also an important effect on the shape of the current transient, as shown above in Fig.1.18 for the Nickel addition.**

1.2.5. ROLE OF Mo ON PITTING PROPAGATION AND REPASSIVATION OF STAINLESS STEELS

As mentioned before, the stage of pitting corrosion propagation is reached when spontaneous repassivation is not possible [27, 37, 56, 63, 64]. Then almost all of the mechanisms proposed for the Mo action in the propagation pitting corrosion step on stainless steels turn around the presence of Mo in the passive oxide film, even though the presence of Mo in the oxide film of stainless steels is still keenly debated in the literature. However, *Pardo et al* [27] reported that Mo addition enhances the pitting corrosion resistance of austenitic SS studied in the neutral pH containing 3.5 wt.% NaCl, since this element presence reduces progressively the corrosion rate, increasing critical pitting temperature (CPT) values and ennobling both E_{pit} (pitting potential) and E_{corr} (corrosion potential). In other words, the AISI 316 SS are more resistant to stable pitting than AISI 304 ones in this medium. This is consistent with early findings which reported that the pitting resistance of Mo-containing SS is superior to that of non-Mo-containing ones [27, 37]. This behavior could be seen in Fig. 1.19, which indicates that Mo additions shifted slightly the corrosion potential (E_{corr}) to more noble values and increased the pitting corrosion resistance, determined by the pitting potential (E_{pit}). On the other hand, concerning Mn additions, their effect was detrimental, resulting in reduction of both E_{corr} and E_{pit} , and in increase of the corrosion current density [27]. So, sometimes the negative Mn effect could hide the positive influence of Mo for the pitting corrosion resistance.

There are same hypothesis about the influence of inclusions on the SS corrosion properties, for example: the inclusions supporting an important effect at the stages of metastability and growth of pits. Recent studies reveal that during MnS dissolution a decrease of pH occurs and these region are the precursor sites for pitting attack, *Stewart and Williams* [65], confirmed that these inclusions dominated the pit nucleation sites. On the other hand, *T.L. Sudesh et al.* [64] indicate that the sulphide inclusion may not be the only cause of pit initiation because they observed the pitting corrosion in very low sulphur containing austenitic SS. Therefore, it must be kept in mind that the metallurgical difference in the SS could mislead the interpretation of the corrosion results. In our case, the presence of MnS inclusion on the stainless steels microstructure are precursor sites for pitting attack [64, 65].

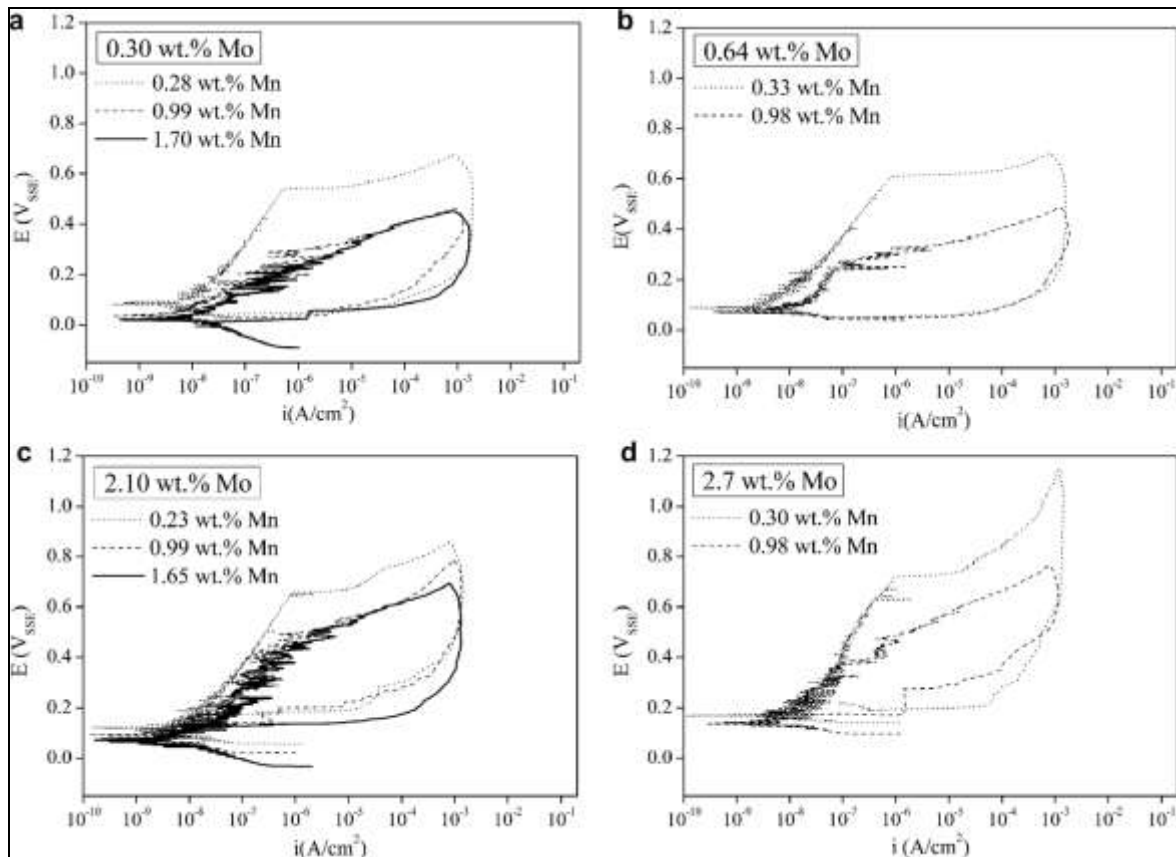


Figure 1.19 - Cyclic polarization curves obtained as a function of Mn and Mo content on *austenitic SS after exposure in 3.5 wt.% NaCl solution* for 1 h at 22°C: (a) 0.30 wt.% Mo; (b) 0.64 wt.% Mo; (c) 2.10 wt.% Mo and (d) 2.7 wt.% Mo. The reference electrode utilized was Ag/AgCl [27].

Finally, *Pardo et al. [27] have proposed an interesting three stage mechanism in an attempt to clarify how both Mn and Mo participate in pitting corrosion behavior of the most common austenitic SS (AISI 304 and 316) in aerated 3.5wt% NaCl solution,* investigating the role of sulphides inclusion as initiators of pitting corrosion, and the changes of repassivation properties due to the presence of Mo as alloying element for SS. The three stages of this mechanism are:

First Stage. Partial dissolution of MnS: According to Pourbaix diagrams [33], in neutral chloride environments and within the passivity region of stainless steels, MnS inclusions are thermodynamically unstable and tend to dissolve. During their dissolution, the bare surface of the steel is revealed, starting the localized attack in this area as shown in Fig. 1.20 [27].

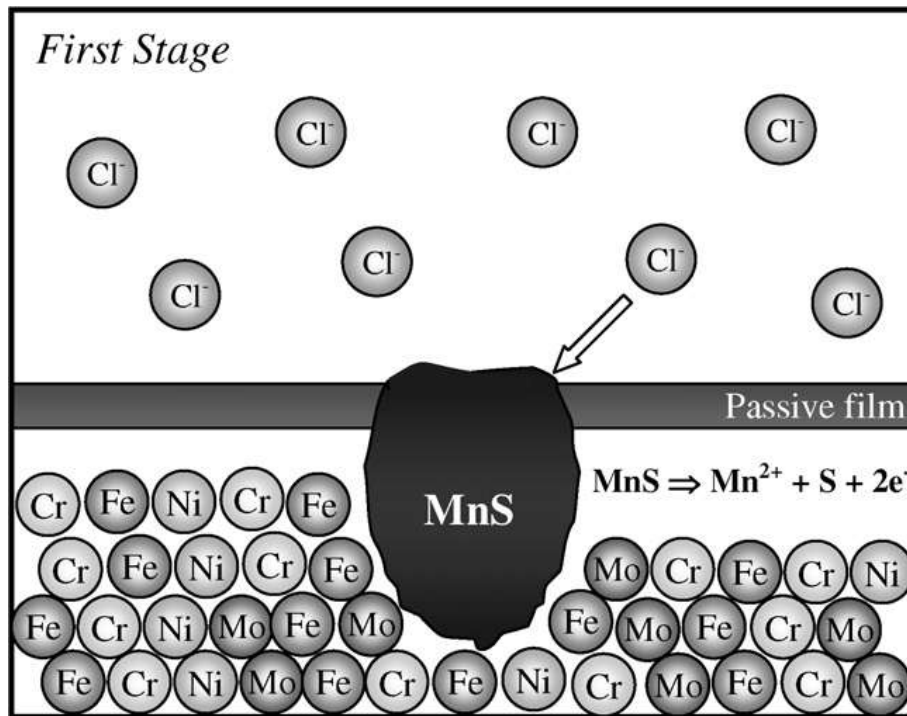


Figure 1.20 - Partial dissolution of MnS. First step of *Pardo et al* mechanism [27].

Second Stage. Dissolution of the matrix alloy elements: The following step is the dissolution of the bulk material, which results in the generation of cationic species of the alloy elements such as Fe^{2+} , Ni^{2+} , Cr^{3+} but, particularly Mo^{3+} as illustrated in Fig. 1.21. Further hydrolysis reaction of these species favors the local drop of pH from neutral toward acidic values [27].

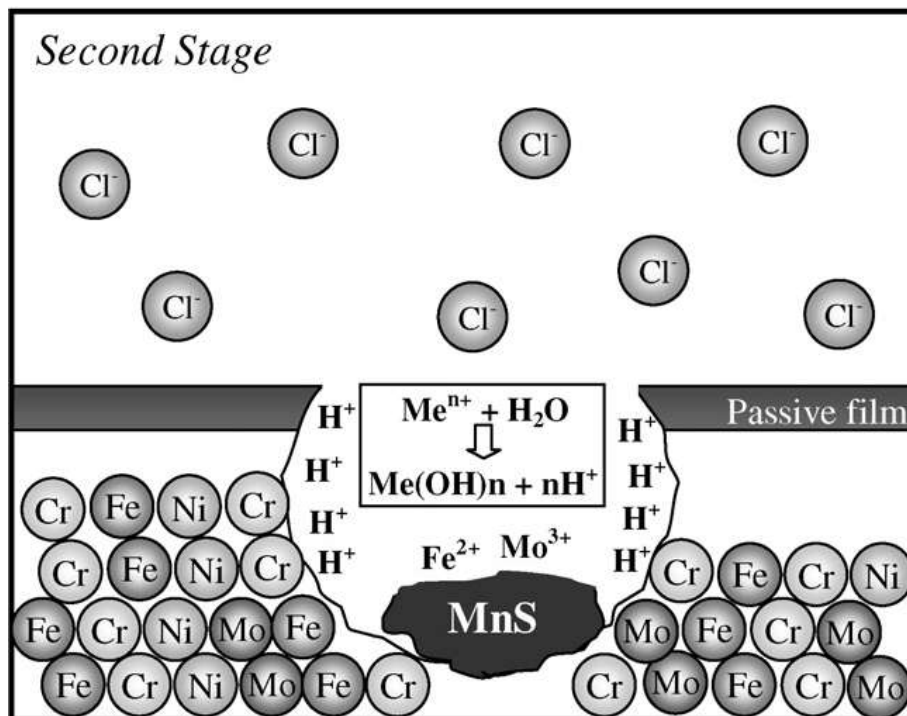


Figure 1.21 - Dissolution of the matrix alloy elements [27].

Third Stage. Formation of molybdenum oxides: In most of the cases, under these conditions, i.e. low pH and high potential values, Mo^{3+} species are oxidized and then molybdenum achieves its highest oxidation state, Mo(VI). In this oxidation state, Mo can easily react to form highly stable and insoluble compounds such as FeMoO_4 , but generally MoO_3 (see Pourbaix diagram – Fig. 1.5), which partially or entirely cover the pit wall, as demonstrated in Fig. 1.22. As a result, pits at this metastable stage are repassivated and the probability of achieving their stable stage is reduced [27]. It is worth noticing, however, that these authors did not investigate the effect of S species within the pits in this step of the pitting corrosion.

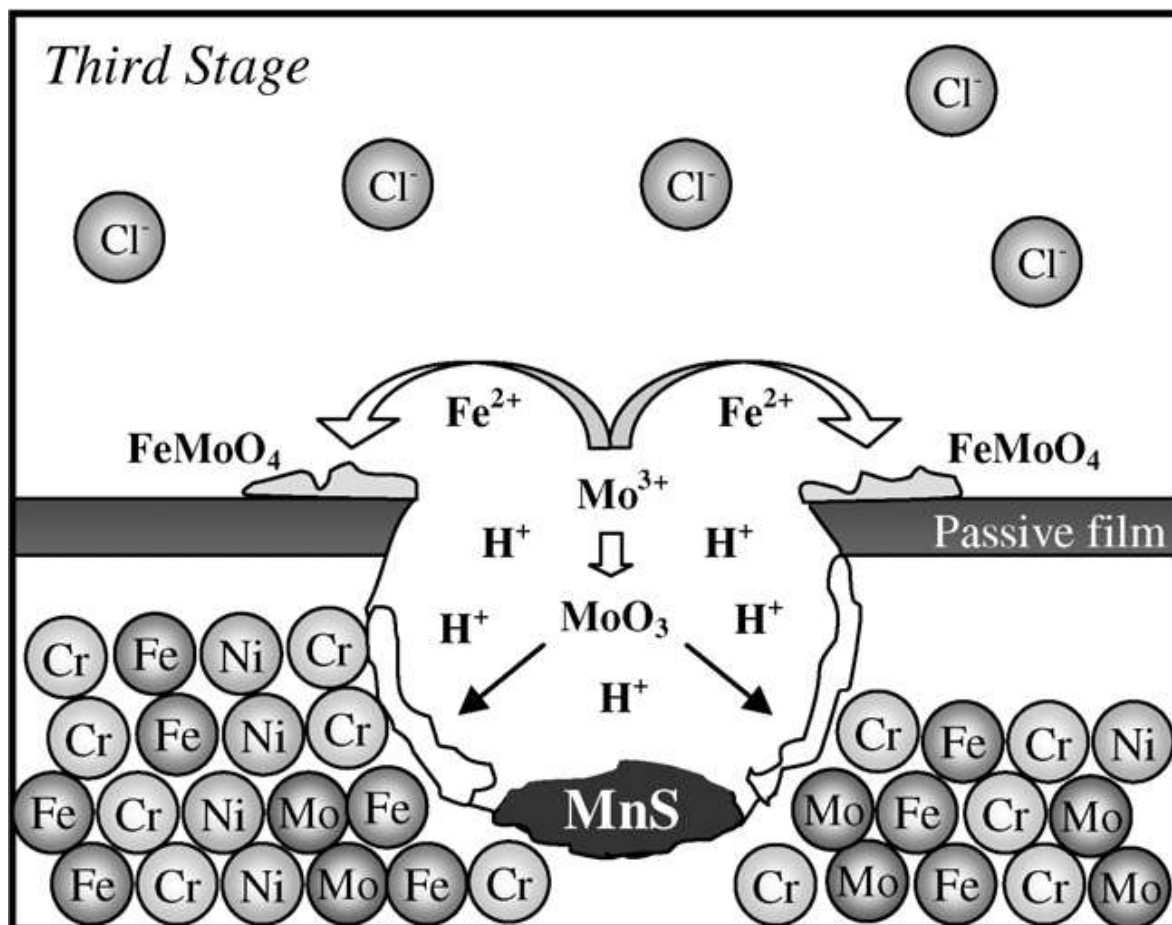


Figure 1.22 - Formation of molybdenum oxides. Third step of Pardo's mechanism [27].

The presence of molybdenum oxides on pit walls of *austenitic SS (with 2.75%Mo) in chloride solutions* was observed by Scanner Electron Microscopy (SEM) as illustrated in Fig. 1.23 [27]. This image confirms the hypothesis of Mo oxides to promote the repassivation process and decrease the localized attack at neutral conditions. Accordingly, others results from SEM analyses [27] indicated that for the austenitic SS with 2.1 wt.% Mo, the pitting corrosion attack was notably reduced compared to specimens with only 0.29 wt.% Mo. These results are in very good agreement with the mechanism described above.

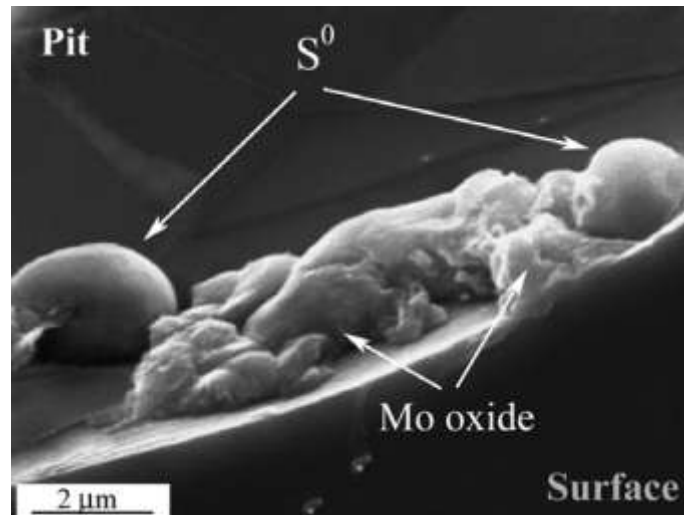


Figure 1.23 - SEM analysis of a pit formed in the *austenitic SS with 2.75% Mo content polarized in 3.5 wt.% NaCl solution until a potential value close to E_{pit}* [27].

The results presented above are very consistent with the works done by *Lemaitre et al.* [66], who reported that the influence of Mo additions is as a simply shift E_{pit} up to nobler values, about +100mV for 1% Mo containing ferritic steel and the 2% Mo containing austenitic steel in aerated corrosive medium of NaCl at room temperature and neutral pH. The molybdenum improves the resistance to local breakdown of the passive film in both steels, but the mechanism is probably not the same for each case. Fig. 1.24 shows the relation between E_{pit} and chloride concentration for ferritic SS (AISI 430 and AISI 434) and for austenitic ones (AISI 304 and AISI 316). The results indicate a noticeable influence of metallic structure (α and γ) on the pitting potential, higher for the austenitic alloys. This fact can be explained by whether the different Ni content in these metals and the austenitic transformation [66].

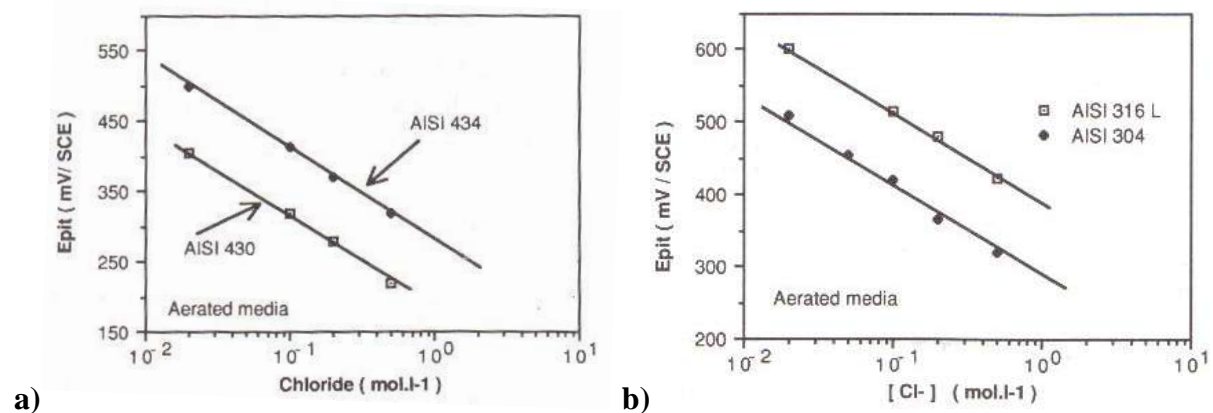


Figure 1.24 – **a)** Pitting potential for ferritic SS (AISI 430 and AISI 434); **b)** Pitting potential for austenitic SS (AISI 304 and AISI 316L) [66].

These results are also in good agreement with those published by *M. Kaneko and H.S. Isaacs [67]*, whom supported the idea that additions of Mo resulted in a dramatic increase in the E_{pit} . Fig. 1.25 a) shows the pitting potential increase with Mo alloying to Fe–18%Cr–x%Mo ferritic alloys and b) for Fe 18%Cr-12-15%Ni-x%Mo austenitic alloys in 1M LiCl and 1M LiBr solutions. The pitting potential clearly increased for ferritic stainless steels when the Mo contents increased. On the other hand, in the case of austenitic grades, Mo clear effect was found in LiCl and almost constant values were obtained in LiBr. These results emphasize the proposal of a possible different mechanism of Mo for the ferritic and then for austenitic structures.

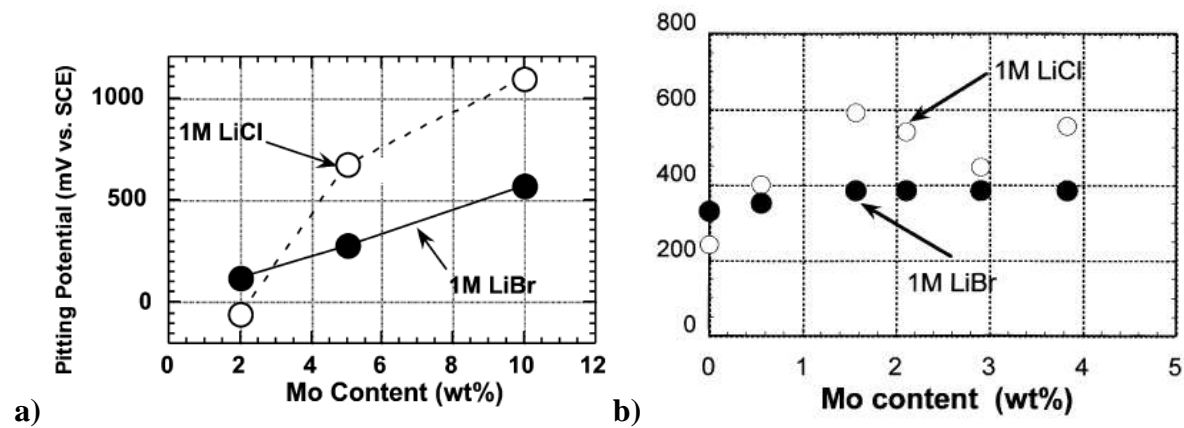


Figure 1.25 – Effect of Mo concentration on the pitting potential of **a)** Fe-18%Cr-Mo ferritic alloys and **b)** 18%Cr-12-15%Ni-x%Mo austenitic alloys in 1M LiCl and 1M LiBr [67].

However, the studies done by *A. Bautista et al. [20]* demonstrated an absence of positive role of Mo on the E_{pit} of austenitic SS in alkaline conditions. These authors compared the corrosion resistance of low-Ni 204Cu SS with that of more traditional austenitic SS such as 304, 316 and 316Ti using polarization tests which were carried out in simulated carbonated and non-carbonated pore concrete solutions with different chloride concentrations. Even if they were not investigating the Mo influence, we can observe its behavior by simply comparing the 304SS with 316 SS. So, **the absence of a positive effect of Mo is clearly observed in Fig. 1.26**.

Moreover, in order to evaluate the general corrosion susceptibility of these materials in carbonated media, these authors presented the potential values needed to reach predetermined anodic intensities (10^{-6} and 10^{-5} A cm⁻²) in simulated carbonated and non-carbonated pore concrete solutions since previous research [68] have demonstrated that corrosion intensities higher than 10^{-6} A cm⁻² should be considered highly dangerous. These corrosion intensities would consume a structure's service life in less than 10 years, even

though the major corrosion authors use $100 \mu\text{A cm}^{-2}$ as the current density to determine the pitting potential [26, 27, 66, 67, 69]. Thus, in Fig. 1.27, the strength of the corrosion cells necessary to reach the current intensity of $10^{-6} \text{ A cm}^{-2}$ is higher for 304 compared to 316, except in media without chlorides. Considering higher corrosion intensities, $10^{-5} \text{ A cm}^{-2}$, this unexpected behavior of Mo addition is even more evident. **Therefore, it is possible to conclude that for very aggressive media (carbonated and highly chloride contamination) the behavior of 304 should be as good as that of 316 type.**

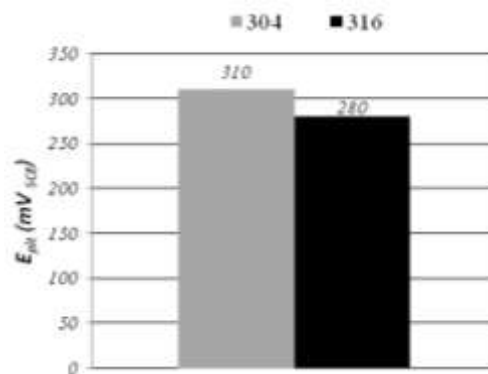


Figure 1.26 - Influence of Mo addition on E_{pit} of austenitic stainless steel determined from the polarization curves recorded in carbonated, saturated $\text{Ca}(\text{OH})_2$ solutions with 1% NaCl [20].

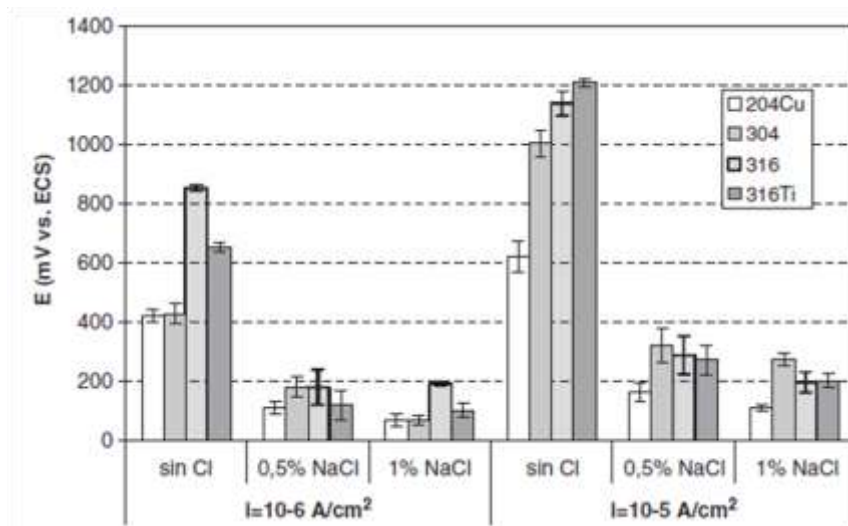


Figure 1.27 - Potentials at predetermined values of current density (10^{-6} and $10^{-5} \text{ A cm}^{-2}$) are reached for SS in carbonated, saturated $\text{Ca}(\text{OH})_2$ solutions with different NaCl concentrations.

These anomalous behaviors of Mo on alkaline media were also reported in [70], where the effect of pH (2–12) on the electrochemical properties of the austenitic SS (AISI

304L and AISI 316L) in 0.5 M Na_2CO_3 were investigated. These authors described that E_{pit} increases linearly with pH value according to the following empirical linear expression:

$$E_{pit} = a + b \times \text{pH} \quad (1.18)$$

where a and b are constants. The value of b is 91 mV for SS 304L and 69.6 mV for 316L. In these results, the pitting potential of 304L increased faster than E_{pit} of 316L when the pH raises. Unfortunately, the authors did not specified the values for constant a . However, from Fig. 1.28, it was possible to estimate this constant a which is higher for 316L than 304L SS, which means a beneficial effect of Mo in acidic conditions. **In this way, we can conclude from [70] that: - in acidic CO_3^{2-} containing solutions (2 - 4) the pitting corrosion resistance is a little better for 316L than 304L stainless steel. With the pH increase (8 - 12), however, the results were inverted, and the 304L became a bit more resistant compared to 316L.**

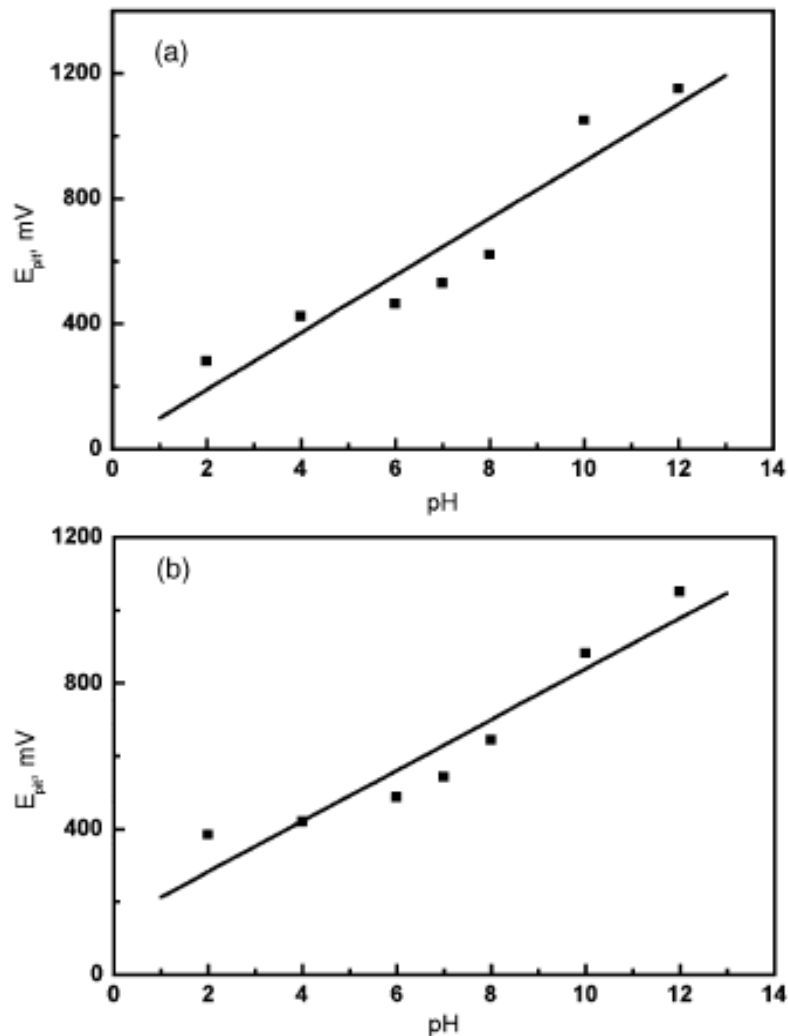


Figure 1.28 - Pitting potential (E_{pit}) as functions of pH of 0.5 M Na_2CO_3 solution for (a) 304L SS and (b) 316L SS [70].

1.2.6. Mo ADDITION ON DUPLEX STAINLESS STEELS (DSS)

Particularly, the influence of Mo addition on the pitting and crevice corrosion mechanism of duplex SS *in alkaline media* is scarcely investigated in the literature [24, 68, 71, 72] compared to the widely studied neutral and acidic chloride conditions [14, 15, 25-27]. Nevertheless, in a very recent paper, *Alvarez et al.* [73] studied the corrosion behavior of two corrugated lean duplex stainless steels (2001 and 2304). Results have been analyzed not only in terms of the overall corrosion resistance but also considering the influence of the microstructure on the corroded surface morphology as shown in Fig 1.29. The role of Mo is evoked and pointed out to be positive and mostly associated to the ferrite phase for the 2205 DSS. As Mo is a ferritizer element (i.e., it could tend to be localized in the ferrite and therefore it may probably increase the corrosion resistance of this phase). In this sense, the lower Mo content of 2304 could explain why ferrite in this material corrodes during their tests shown in Fig. 1.29, while the whole material remains fully immune in 2205.

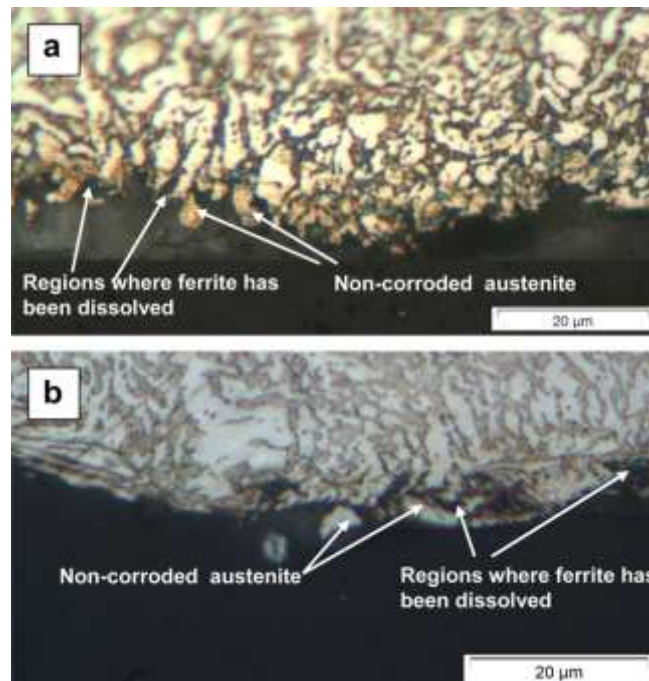


Figure 1.29 - Images showing the selective corrosion of the *lean duplex 2304* after the polarization curves (a) *in non-carbonated solution with chlorides* and (b) *in carbonated solution with chlorides*. The metallographic attack has colored ferrite phase in dark and austenite phase in light [73].

In another paper, *Deng et al.* [74] investigated the critical pitting temperature (CPT) and critical repassivation temperature (T_r) for two kinds of duplex SS in *1M NaCl solution* at

a potential of 750 mV/SCE (see Fig. 1.30). These experiments showed that the value of CPT for UNS S32750 was higher than that of UNS S31803, indicating a higher pitting resistance for UNS S32750. Moreover, It is also noted that the value of ΔT ($CPT - Tr$) for UNS S32750 was 17°C, which was lower than that of UNS S31803 ($\Delta T = 23.1^\circ\text{C}$), demonstrating that the UNS S32750 has better repassivation ability.

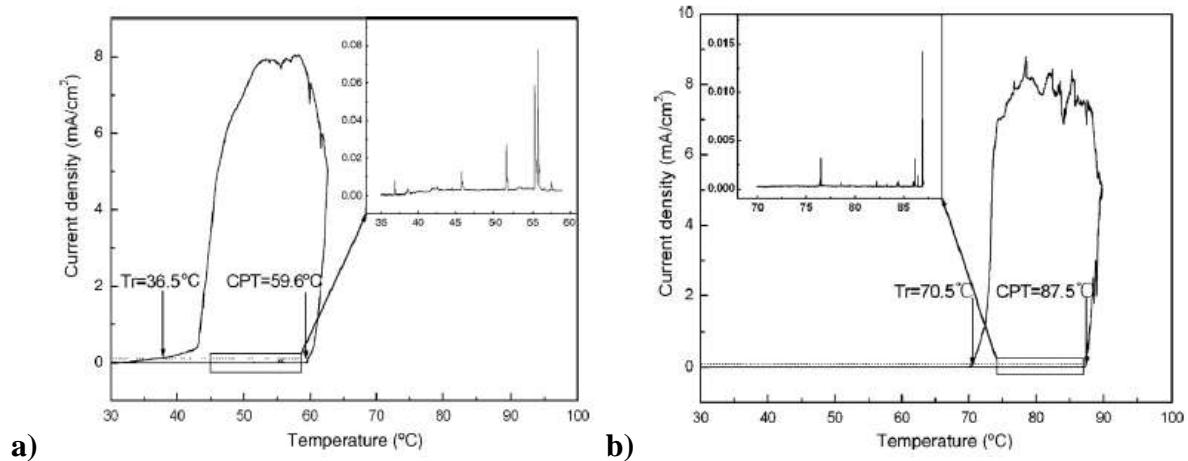


Figure 1.30 - Cyclic thermammogram of (a) UNS S31803 and (b) UNS S32750 in 1M NaCl at a potential of 750 mV [74].

These results were explained by correlating pitting corrosion resistance with the PREn of the weaker phase of each alloy. PREn values, calculated with the expression 1-9, for each phase and also for the global alloys are described in Table 1.3 [74].

Table 1.3 - The chemical composition (wt.%) and PREn of the two phases in UNS S31803 and UNS S32750 [74].

Materials	Phase	Cr	Ni	Mo	N	PREn
UNS S31803	Austenite	20.86	6.65	2.43	0.38	34.96
	Ferrite	23.86	4.36	3.51	0.05	36.24
	Both phases	22.46	5.39	3.11	0.18	35.60
UNS S32750	Austenite	23.23	8.21	2.81	0.47	40.02
	Ferrite	26.45	5.48	4.16	0.05	40.98
	Both phases	25.15	6.74	3.43	0.27	40.49

An important effect of alloying elements such as Cr, Mo, and N was found to both austenite and ferrite phases for these two different DSS. Figs. 1.31 (a) and (b) show the metastable pits formed on the etched surface of UNS S31803 and UNS S32750 below the CPT, respectively. This kind of metastable pits was more occluded with a dimension of $\approx 2\mu\text{m}$, which is consistent with the results found by *Moayed and Newman* at [75]. These metastable pits were preferentially formed in the austenite phase, especially near the grain boundary. The lower pitting resistance for austenite indicated by lower PREn values and the

higher Mo content on the ferrite could be responsible for this fact (see Table 1.3). Figs. 1.31 (c) and (d) demonstrated the stable pits formed on the etched surface of UNS S31803 and UNS S32750 above CPT analyzed, respectively. As expected, pits firstly grew in the austenite grain and kept getting removal of austenite phase until they reached the ferrite phase, indicating that pitting propagation was restrained by ferrite phase. The locations marked by the black circle in Fig. 1.31 (c) clearly reflect the information about selective corrosion of austenite in UNS S31803. However, the stable pits formed on UNS S32750 tended to have a rough interior surface, dish-shaped profiles, without any remnant ferrite phases over the pits, revealed by Fig. 1.31 (d). As expected, the pit growth was also restrained by ferrite phase at the periphery of the pit reflected by the black circle in Fig. 1.31 (d) [74].

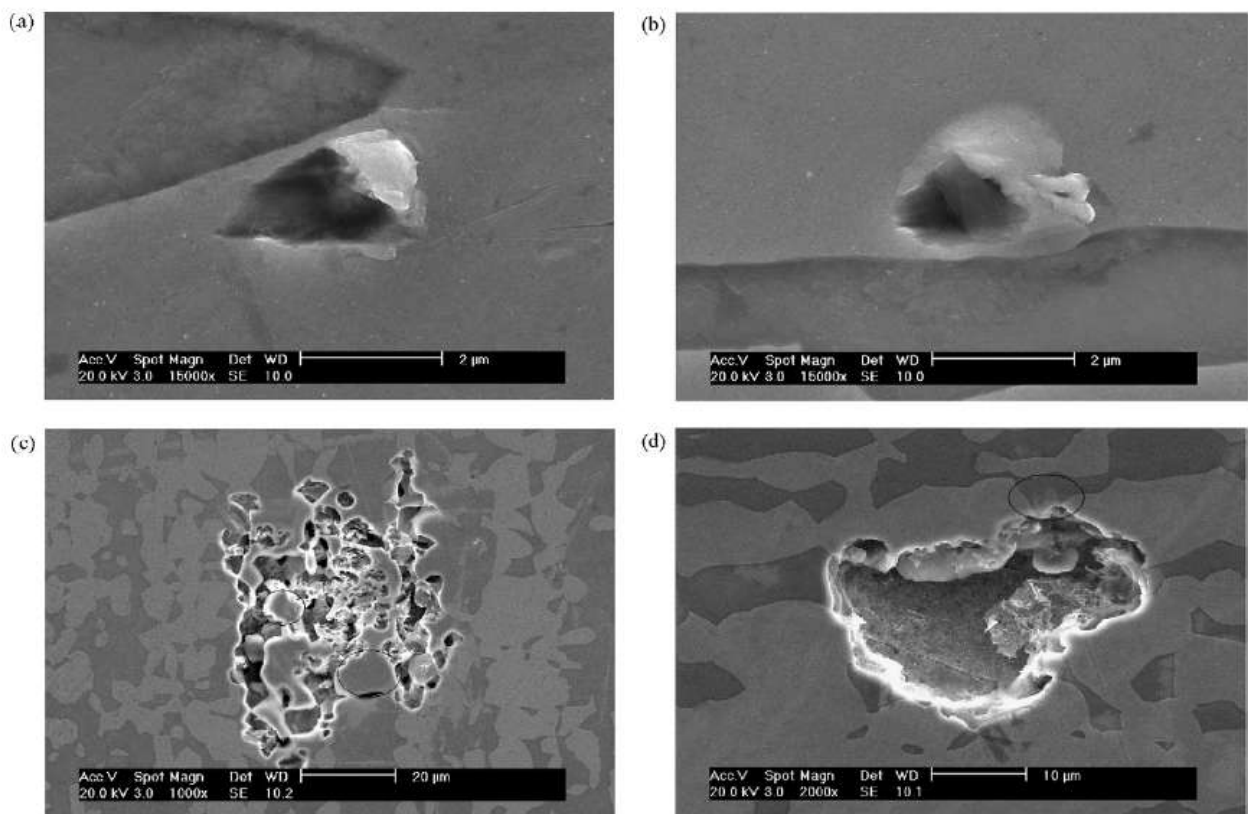


Figure 1.31 – SEM morphologies of pits formed during the cyclic thermammetry test at 750 mV/SCE in 1M NaCl: **(a)** metastable pit formed on UNS S31803, **(b)** metastable pit formed on UNS S32750, **(c)** stable pit formed on UNS S31803 and **(d)** stable pit formed on UNS S32750 [74].

From those references[14, 15, 24-27, 68, 71-74], *we can extract an important information about a possible different influence of Mo for each phase of a duplex structure, which seems to be stronger for the ferrite phase compared to the austenite one.*

1.3. CONCLUSION

The positive role of Mo in acidic media can be considered as generally accepted. In the case of alkaline media, however, the role of Mo is much less studied. Moreover, some authors claimed to unexpected behavior of Mo containing SS grades under aggressive alkaline media such as pore concrete solutions in the presence of Cl^- , as presented above.

Then, in the present work, the behavior of different Mo-containing and Mo-free austenitic, ferritic and duplex stainless steels exposed to chloride rich alkaline media will be characterized. Furthermore, the main objective of this Ph.D thesis is to investigate the role of Mo and determine its mechanism of action in which concerns the corrosion resistance of different stainless steel types, mainly in alkaline media, where data is not as available as in acidic environments. These high alkaline conditions are particularly relevant to coastal or off shore rebar applications or alkali and paper industries.

1.4. REFERENCES

- [1] X. Wang, M. Nguyen, M. G. Stewart, M. Syme, A. Leitch, “*Analysis of Climate Change Impacts on the Deterioration of Concrete Infrastructure – Part 1: Mechanisms, Practices, Modelling and Simulations – A review*”. – Published by CSIRO, 2010: p. ISBN 9780 (2010)
- [2] A. M. Neville, “*Properties of Concrete*”- 4th Edition, Pearson Education Limited, England (2008).
- [3] P. Thoft-Christensen, “*What happens with reinforced concrete structures when the reinforcement corrodes? In Maintaining the Safety of Deteriorating Civil Infrastructures*”- 2nd International Workshop in Life-Cycle Cost Analysis and Design of Civil Infrastructure Systems
- [4] R. P. Khatri and V. Sirivivatnanon, *Cement and Concrete Research* 34 (2004) 745.
- [5] ASTM C1543-02 (2002) – Standard Test Method for Determining the Penetration of Chloride Ion into Concrete by Ponding. American Society for Testing and Materials.
- [6] ASTM C1202-97 (1997) – Standard Test Method for Electrical Indication of Concrete Ability to Resist Chloride Ion Penetration. American Society for Testing and Materials.
- [7] I. Galan, C. Andrade, P. Mora and M. A. Sanjuan. *Environ. Sci. Technol.* 44 (2010) 3181
- [8] D.W.S. Ho and R.K. Lewis. *Cement and Concrete Research* 17 (1987) 489.
- [9] S.D. Cramer, B. S. Covino Jr, S. J. Bullard, G. R. Holcomb, J. H. Russell, F. J. Nelson, H. M. Laylor and S. M. Soltesz. *Cement and Concrete Composites* 24 (2002) 101.
- [10] M. Kouril, P. Novák, and M. Bojko. *Cement and Concrete Research* 40 (2010) 431.

- [11] G. Gedge, *J. Construc. Steel Research*. 64 (2008) 1194.
- [12] A. Knudsen, F. M. Jensen, O. Klinghoffer, and T. Skovsgaard, “*Cost-effective Enhancement of Durability of Concrete Structures by Intelligent Use of Stainless Steel*”. Conference on Corrosions and Rehabilitation of reinforced Concrete Structure, Florida, December 8-11, 1998.
- [13] “*Guidance on the use of stainless steel reinforcement*”, The Concrete Society, Technical Report 51 (1998).
- [14] L. Zhang, Y. Jiang, B. Deng, W. Zhang and J. Xu, J. Li. *Materials Characterization* 60 (2009) 1522.
- [15] F. Zhang, J. Pan, and C. Lin. *Corrosion. Science* 51 (2009) 2130.
- [16] R.N. Gunn. Abington Publishing, Cambridge England (1999).
- [17] L.F. Garfias-Mesias, J.M. Sykes and C.D.S. Tuck. *Corrosion. Science* 38 (1996) 1319.
- [18] ASTM G48 – 03(2009) – Standard Test Methods for Pitting and Crevice Corrosion Resistance of Stainless Steels and Related Alloys by Use of Ferric Chloride Solution
- [19] T. J. Mesquita, E. Chauveau, M. Mantel, N. Kinsman and R.P. Nogueira. *Materials Chemistry and Physics*, 126 (2011) 602
- [20] A. Bautista, , G. Blanco and F. Velasco. *Cement and Concrete Research* 36 (2006) 1922.
- [21] A. Bautista, G. Blanco, F. Velasco, A. Gutiérrez, L. Soriano, F. J. Palomares and H. Takenouti. *Corrosion. Science* 51 (2009) 785.
- [22] W.A. Badawy and F.M. Al-Kharafi. *Electrochimica Acta* 44 (1998) 693.
- [23] I. N. Bastos, S. M. Tavares, F. Dalard and R.P. Nogueira. *Scripta Materialia* 57 (2007) 913.
- [24] E. Chauveau, T. Sourisseau, B. Dermelin and M. Mantel, MEDACHS 08, International Conference in Coastal and Marine Environments (2008).
- [25] L. Zhang, Y. Jiang, B. Deng, W. Zhang, J. Xu and J. Li, *Electrochimica Acta* 54 (2009) 5387.
- [26] A. Pardo, M.C. Merino, A.E. Coy, F. Viejo, R. Arrabal and E. Matykina, *Corrosion Science* 50 (2008) 780.
- [27] A. Pardo, M.C. Merino, A.E. Coy, F. Viejo, R. Arrabal and E. Matykina, *Corrosion Science* 50 (2008) 1796.
- [28] G. P. Halada, C. R. Clayton and H. Herman. *J. Electrochem. Soc.* 142 (1995) 74.
- [29] Y. Wu, R. C. Ni, H. Z. Hua and A. Pourbaix. *Corrosion Science* 24 (1984) 691.
- [30] M. Ürgen, U. Stolz, and R. Kirchheim. *Corrosion Science* 30 (1990) 377.

- [31] Y.C. Lu, And C.R. Clayton. Corrosion Science 29 (1989) 927.
- [32] A.A. Pozdeeva, E.I. Antonovskaya, and A.M. Sukhotin. Corrosion Science 6 (1966) 149.
- [33] M. Pourbaix, *Atlas of Electrochemical Equilibria in Aqueous Solutions*. NACE, CEBELCOR, (1974).
- [34] W.J. Tobler, and S. Virtanen. Corrosion Science 48 (2006) 1585.
- [35] Y.C. Lu, And C.R. Clayton. J. Electrochem. Soc. 133 (1986) 2465.
- [36] P. Wang, L. L. Wilson, D. J. Wesolowski, J. Rosenqvist, A. Anderko. Corrosion Science 52 (2010) 1625.
- [37] G.O. Ilevbare, and G.T. Burstein, Corrosion Science 43 (2001) 485.
- [38] J.N. Wanklyn. Corrosion Science 21 (1981) 211.
- [39] A. E. Yaniv, J. B. Lumsden., and R. W. Staehle. J. Electrochem. Soc. 124 (1977) 490.
- [40] K. Sugimoto, Y. Sawada, Corros. Sci. 17 (1977) 425.
- [41] V. Vignal, J.M. Olive, and D. Desjardins. Corrosion Science 41 (1999) 869.
- [42] E. Akiyama, A. Kawashima, K. Asami, K. Hashimoto. Corrosion Science 38 (1996) 1281.
- [43] M.F. Montemor, A. Simões, M.G.S. Ferreira, M. Da Cunha Belo, Corros. Sci. 41 (1999) 17.
- [44] A. H. Zimmerman, M. R. Martinelli, M. C. Janecki, C. C. Badcock. J. Electrochem. Soc. 129 (1982) 289.
- [45] R.F.A. Jargelius-Petterson, B.G.Pound. J. Electrochem. Soc. 145 (1998) 1462.
- [46] C.M. Abreu, M. J. Cristóbal, R. Losada, X. R. Nóvoa, G. Pena, M. C. Pérez. Electrochimica Acta 49 (2004) 3049.
- [47] M. Sakashita, N. Sato, and R.P. Frankenthal, J. Kruger (Eds.), Passivity of Metals, Corrosion Monograph Series, The Electrochemical Society, Princeton, USA, 1978: p. p. 479.
- [48] K. Hashimoto, K. Asami, and K. Teramoto. Corrosion Science 19 (1979) 3.
- [49] K. Sugimoto, and Y. Sawada, Corrosion Nace 32 (1976) 347.
- [50] M. Uemura, T.Yamamoto, K. Fushimi, Y. Aoki, K. Shimizu, and H. Habazaki. Corrosion Science 21 (2009) 1554.
- [51] L. Freire, M. J. Carmezim, M. G. S. Ferreira, M. F. Montemor, Electrochimica Acta 56 (2011) 5280.
- [52] I. Olefjord, B. Brox, and A. U. Jelvestam. J. Electrochem. Soc. 132 (1985) 2854.

- [53] D. Addari, B. Elsener and A. Rossi, *Electrochimica Acta* 53 (2008) 8078
- [54] M. Kimura, M. Kaneko and N. Ohta, *ISIJ Int* 42 (2002). 1399.
- [55] A. J. Davenport, A. J. Dent, M. Monir, J. A. Hammons, S. M. Ghahari, P. D. Quinn and T. Raymentb. *J. Electrochem. Soc.* 158 (2011).
- [56] N.J. Laycock, and R.C. Newman. *Corrosion Science* 39 (1997) 1771.
- [57] L. Wegrelius, F. Falkenberg., and I. Olefjord, *J. Electrochem. Soc.* 146 (1999) 1397.
- [58] G.O. Ilevbare, and G.T. Burstein. *Corrosion Science* 45 (2003) 1545.
- [59] S.P. Mattin, S.P. and G.T. Burstein, *Philos. Mag. Lett.* 76 (1997) 341.
- [60] G. Berthomé, B. Malki, and B. Baroux, *Corrosion Science* 48 (2006) 2432.
- [61] M. Hashimoto, S. Miyajima, and T. Murata, *Corrosion Science* 33 (1992) 885.
- [62] Y. Ishikawa and H. S. Isaacs. *J. Electrochem. Soc.* 132 (1985) 1288.
- [63] R. Qvarfort, *Corrosion Science* 40. 40 (1998) 215.
- [64] L. Sudesh, L. Wijesinghe and D. J. Blackwood. *Corrosion Science* 49 (2007) 1755.
- [65] J. Stewart, and D.E. Williams. *Corrosion Science* 33 (1992) 457
- [66] C. Lemaitre, A. A. Moneim, R. Djoudjou, B. Baroux and G. Beranger. *Corrosion Science* 34 (1993) 1913.
- [67] M. Kaneko, and H.S. Isaacs. *Corrosion Science* 44 (2002) 1825.
- [68] J. A. González, E. Otero, S. Feliu, A. Bautista, E. Ramírez, P. Rodríguez, W. López. *Magazine of concrete Research* 50 (1998) 189.
- [69] H. Baba, T. Kodama, and Y. Katada. *Corrosion Science* 44 (2002) 2393.
- [70] S.A.M Refaey, F. Taha, and A.M.A. El-Malak. *Applied Surface Science* 242 (2005) 114.
- [71] T. J. Mesquita, E. Chauveau, Marc Mantel, Nicole Kinsman and Ricardo. 61st Annual Meeting of the International Society of Electrochemistry, 2010.
- [72] G. Blanco, A. Bautista, and H. Takenouti. *Cement and Concrete Composites* 28, (2006) 212.
- [73] S.M. Alvarez, A. Bautista and F. Velasco, *Corros. Sci.* 53 (2011) 1748.
- [74] B. Deng, Y. Jiang, J. Gong, C. Zhong, J. Gao and J. Li, *Electrochimica Acta* 53 (2008) 5220.
- [75] M.H Moayed, and R.C. Newman. *Corrosion Science* 48 (2006) 1004.

CHAPTER 2

EXPERIMENTAL METHODOLOGY

OUTLINE

2. EXPERIMENTAL METHODOLOGY	54
2.1. MATERIALS	54
2.1.1. INDUSTRIAL STAINLESS STEELS	54
2.1.2. LABORATORY STAINLESS STEELS	55
2.2. ELECTROCHEMICAL CHARACTERIZATIONS	59
2.2.1. SAMPLE PREPARATION	59
2.2.2. SOLUTION PREPARATION	61
2.2.3. ELECTROCHEMICAL CELL DESCRIPTION	61
2.2.4. ELECTROCHEMICAL EXPERIMENTS	62
2.2.4.1. POTENTIODYNAMIC POLARIZATION	62
2.2.4.2. ZERO RESISTANCE AMMETER (ZRA)	65
2.2.4.3. ELECTROCHEMICAL IMPEDANCE SPECTROMETRY (EIS)	66
2.2.4.3.1. PRINCIPLE	67
2.3. SURFACE CHARACTERIZATIONS	68
2.3.1. SCANNING ELECTRON MICROSCOPY (SEM)	68
2.3.1.1. SCANNING PROCESS AND IMAGE FORMATION	69
2.3.1.2. DETECTION OF SECONDARY ELECTRONS	71
2.3.1.3. DETECTION OF BACKSCATTERED ELECTRONS	71
2.3.1.4. MEASUREMENTS PROTOCOL	72
2.3.2. X-RAY PHOTOELECTRON SPECTROSCOPY (XPS)	72
2.3.2.1. MEASUREMENTS PROTOCOL	74
2.3.2.2. PEAK IDENTIFICATION	75
2.4. TRIBO-CORROSION CHARACTERIZATION	78
2.5. REFERENCES	80

2. EXPERIMENTAL METHODOLOGY

In this section, the materials and the electrochemical experiment procedures as well as surface characterization measurements used during our investigations about the role of molybdenum on pitting corrosion of stainless steels will be described. To come out this work, two families of SS were used: the traditional industrial grades (austenitics: AISI 304L (EN 1.4307) and 316L (EN 1.4404); ferritics: 430 (EN 1.4016) and 434 (EN 1.4113); and duplex: 2304 (EN 1.4362) and 2205 (EN 1.4462)) and also highly controlled composition SS (referred to as laboratory materials). Several experiments, such as Anodic Polarization, Electrochemical Impedance Spectroscopy (EIS), Zero Resistance Ammeter (ZRA), Electrochemical noise, Optical Microscopy, Scanning Electron Microscopy (SEM), and X-ray Photoelectron Spectroscopy (XPS), were carried out with both traditional and laboratory alloys in order to better characterize the Mo role on stainless steels for alkaline applications. Materials and experiments used in this study will be described in the following sections.

2.1. MATERIALS

2.1.1. INDUSTRIAL STAINLESS STEELS

In this work, three different classes of industrial stainless steels (Austenitic, Ferritic and Duplex) were studied. The AISI 430 and AISI 434 are ferritics SS, AISI 304L and AISI 316L are austenitic SS, and finally, the 2304 and 2205 are Duplex ones (austenoferritics). The 434, 316L and 2205 steels respectively contain 0.92wt.%Mo, 2.172wt.%Mo and 2.78wt.%Mo, whereas the others three SS, 430, 304L and 2304, are Mo free alloys with 0.05wt.%Mo, 0.21wt.%Mo and 0.277wt.%Mo, respectively. These materials have been provided by “UGITECH company” and their whole composition is given in Table 2.1. Moreover, this Table presents the PREn values for each material calculated using the *equation 1-9*. As our main objective is to study the effect of Mo addition on SS used as concrete reinforcements, all samples were cut out from annealed industrial draw wires, which are normally employed in this kind of application.

Table 2.1 – Chemical composition of industrial stainless steels provided by UGITECH.

Industrial Material	Elements (wt. %)											
	C	Si	Mn	Ni	Cr	Mo	Cu	N	Co	S*	PREn	
Austenitic	304L	0.02	0.49	0.60	11.12	18.29	0.21	0.31	0.03	0.00	9	19.46
	316L	0.01	0.49	0.73	11.08	16.89	2.17	0.48	0.03	0.25	10	24.53
Ferritic	430	0.01	0.31	0.30	0.29	16.16	0.05	0.10	0.03	0.02	5	16.80
	434	0.03	0.39	0.39	0.45	16.17	0.92	0.12	0.05	0.03	23	20.01
Duplex	2304	0.02	0.41	1.09	4.02	22.30	0.28	0.30	0.15	0.13	4	25.62
	2205	0.02	0.4	1.61	5.45	22.91	2.78	0.22	0.15	0.07	3	34.48

*S ppm

2.1.2. LABORATORY STAINLESS STEELS

Although the major composition difference between the two grades of each industrial steel family is the Mo content, these materials also present some small variations in the concentration of others elements (for example Mn, Ni and Cr, as shown in the Table 2.1). These differences in the chemical composition could have a non-negligible influence on the pitting corrosion resistance of these alloys and then mislead our analysis about the real role of Mo on corrosion properties of SS in the alkaline situation. Therefore, we decided to prepare laboratory SS in the UGITECH research center based on the industrial steels, but with a well defined chemical composition. The only difference between these new alloys will be the presence or absence of Mo. These new materials were called “laboratory alloys” and their final chemical compositions are presented in Table 2.2. For this new configuration of samples, 4 austenitic SS (with 0, 1, 2, and 3%wt Mo), 2 ferritic SS (with 0 and 3%wt Mo), and 2 duplex SS (with 0 and 3%wt Mo) were produced. As for the industrial SS, the PREn values for the lab alloys were calculated by *equation 1-9 as shown in Table 2.2.*

All laboratory heats were hot forged, hot rolled, annealed and then cold rolled to have homogeneous samples such as a similar grain size for instance. All details of this process could be found in annex 1. The specimens were sampled from the laboratory cold rolling boards in the disk form (thickness 2mm x diameter 15mm).

In order to simplify the writing and reading of this thesis report, the lab alloy samples will be named by using their chemical composition values for the main SS alloying elements, Chromium (Cr), Nickel (Ni) and Molybdenum (Mo). For example, if the material contains

18wt% of Cr, 12wt% of Ni and 3wt% of Mo, it will be named 18Cr12Ni3Mo, which represents an austenitic SS (Cr+Ni) with 3% of Mo.

Table 2.2 – Chemical composition of laboratory stainless steels fabricated by UGITECH research center.

	Laboratory Material	Elements (wt. %)									
		C	Si	Mn	Ni	Cr	Mo	N	Al	S*	PREn
Austenitic	18Cr12Ni	0.025	0.594	1.012	12.067	17.999	0.004	0.023	0.0033	13	18.38
	18Cr12Ni1Mo	0.028	0.513	0.990	12.060	17.859	1.000	0.024	0.0031	13	21.54
	18Cr12Ni2Mo	0.020	0.515	1.048	12.080	17.879	1.968	0.019	0.0032	12	24.68
	18Cr12Ni3Mo	0.028	0.571	1.018	11.995	18.003	2.989	0.029	0.0036	15	28.33
Ferritic	18Cr	0.028	0.492	1.056	0.003	18.108	0.004	0.029	0.0024	15	18.59
	18Cr3Mo	0.029	0.533	1.076	0.005	18.018	3.01	0.028	0.0023	14	28.399
Duplex	23Cr4.6Ni	0.029	0.58	1.031	4.569	22.968	0.015	0.175	0.0024	12	25.82
	23Cr4.6Ni3Mo	0.029	0.559	0.981	4.56	22.97	3.004	0.186	0.003	13	35.86

*S ppm

The microstructures of all laboratory heats were analyzed with traditional metallographic methods. Fig. 2.1 and 2.2 show the microstructure of austenitic castings, 18Cr12Ni and 18Cr12Ni3Mo, respectively, in different regions of the samples (edge and center). Fig. 2.1 a) and b) show the edge of 18Cr12Ni sample where the austenitic grains are much hammer-hardened and also a difference between the grain deformation direction of edge and center sample. The same metallographic morphologies were found for 18Cr12Ni3Mo samples. Looking now to higher magnification at the center of 18Cr12Ni samples, Fig. 2.1 c) and d), the presence of few inclusions inside of the austenitic grains could be observed in small amounts.

For 18Cr12Ni3Mo, however, a greater quantity of inclusion and/or oxide and also precipitation of secondary ferrite within grains appears as clearly shown in Fig. 2.2. The secondary ferrite was precipitated in an aligned form at the center of 18Cr12Ni3Mo grain probably in the Mo enriched zones. This secondary ferrite precipitation is associated with the higher Mo content (3 wt%) because this element is a well known to induce ferrite formation

in SS metallurgy [1-3]. Any traces of intragranular precipitation was observed for the austenitic lab.

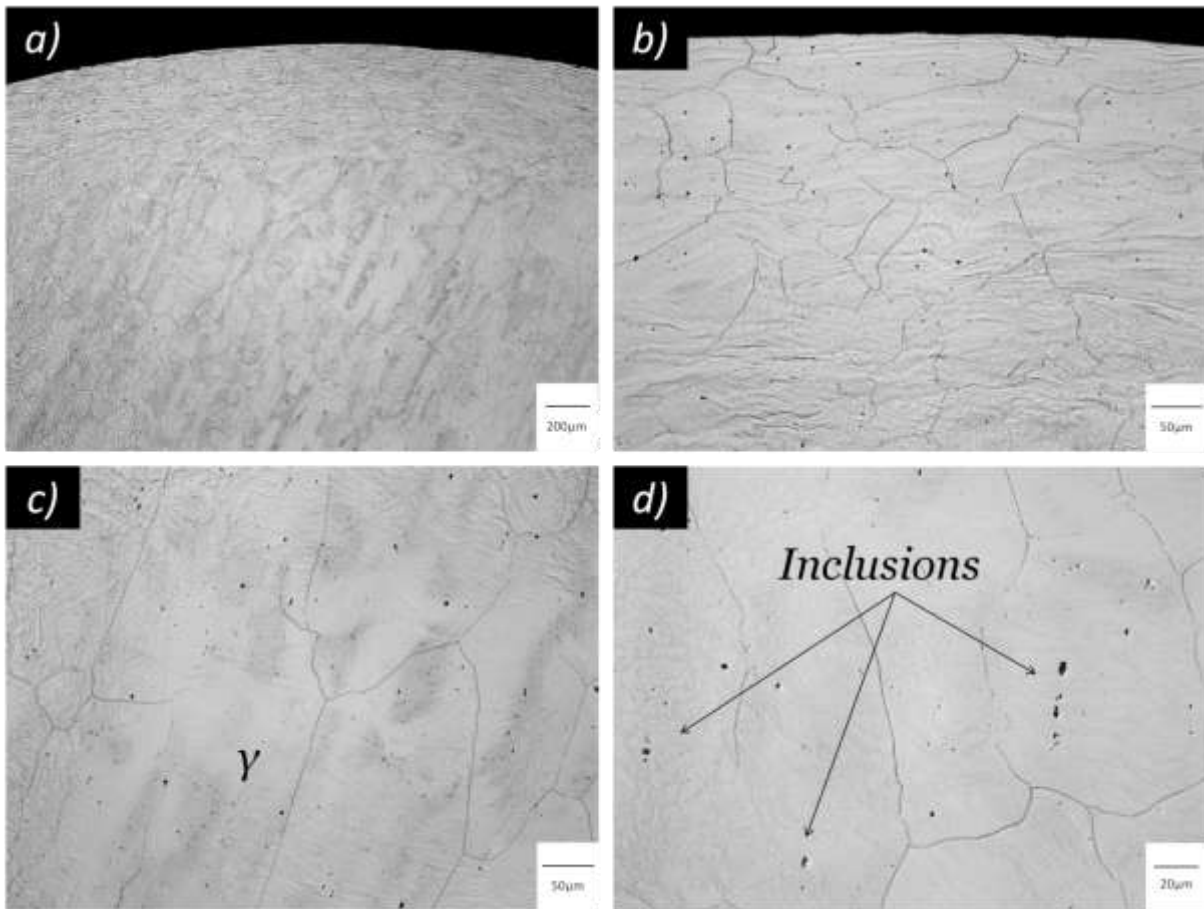


Figure 2.1 - Metallographic images of 18Cr12Ni heat at different zones and zooms: from the edge of the sample at **a)** 50x and **b)** 200x and from the center of the sample at **c)** 200x and **d)** 500x. NaOH solution was used to make the electrochemical etching of the sample.

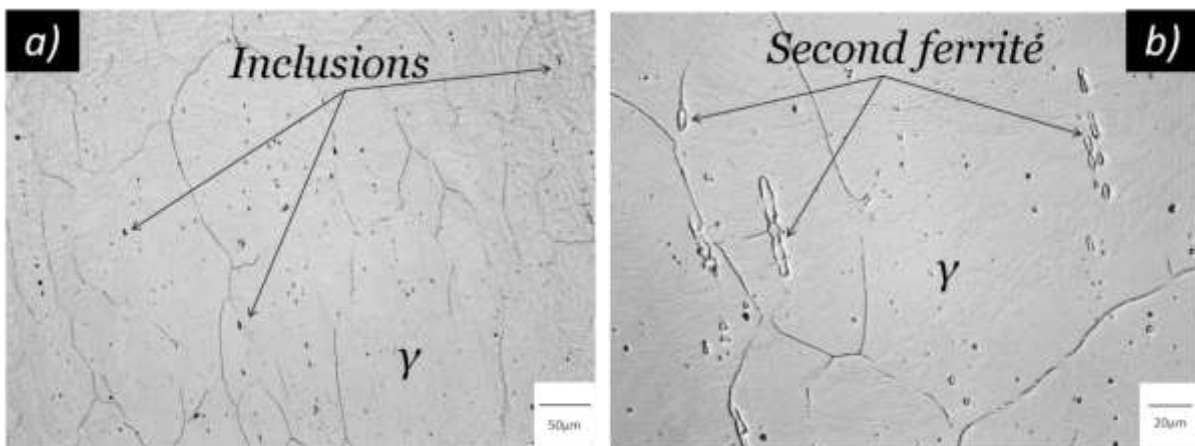


Figure 2.2 - Metallographic images of laboratory Mo containing austenitic heat at different magnifications at from the center of the sample **a)** 200x and **b)** 500x. NaOH solution was used to make the electrochemical etching of this sample

Fig. 2.3 shows the metallographic images from ferritics lab alloys, a) and b) pictures depict 18Cr SS whereas c) and d) correspond to 18Cr3Mo. As for the austenitic lab SS, pictures were taken at both the edge and the center of samples. Once again, we could clearly see the difference between the grain deformations on the extreme edge (Fig. 2.3 a) and c)) and the centre of the samples (Figs. 2.3 b) and d)). In other words, the edge's samples were more hammer-hardened. Moreover, in the absence of Mo, the ferritic lab SS exhibited a bigger amount of precipitates and oxides, distributed overall microstructure. In the presence of Mo, however, we observed those precipitates especially at the grain boundaries as shown in Fig. 2.3 d). So, for these materials, the precipitations were intergranular and intragranular.

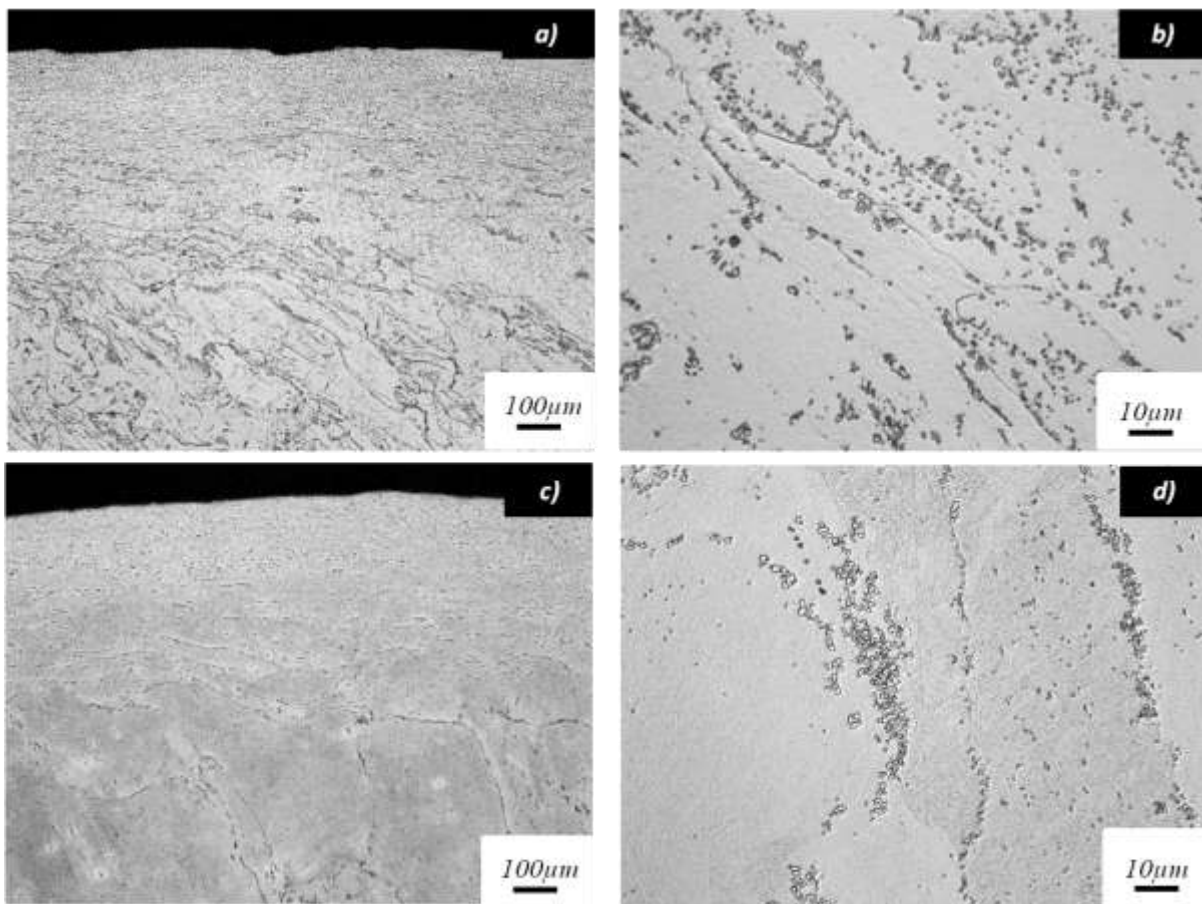


Figure 2.3 - Metallographic images of **a)** and **b)** Mo free lab ferritic heat and **c)** and **d)** Mo containing ferritic lab SS at different zones and zooms.

At last, the duplex lab SS were analyzed. The same differences with respect to the grains deformation on the edge and center of the sample highlighted for austenitic and ferritic were also checked for the duplex alloys. Fig. 2.4 a) and b) illustrate the typical microstructures of 23Cr4.6Ni and 23Cr4.6Ni3Mo SS, respectively. In these pictures, it's easy to observe the influence of Mo on the amount of each phase (ferrite α and austenite γ). The

percentages of each phase were estimated in the presence and absence of Mo by using imaging analyzer software. Thus, 10 different zones were investigated for each material and then the average results were: 39.11% of ferrite and 61.89% of austenite for 23Cr4.6Ni whereas 23Cr4.6Ni3Mo contains 53.18% of ferrite and 46.82% of austenite. To summarize, Mo stabilizes the ferrite phase and then increases α contents in the duplex microstructure (darker gray in Fig 2.4). These materials contain very few precipitates and/or oxides in their microstructures.

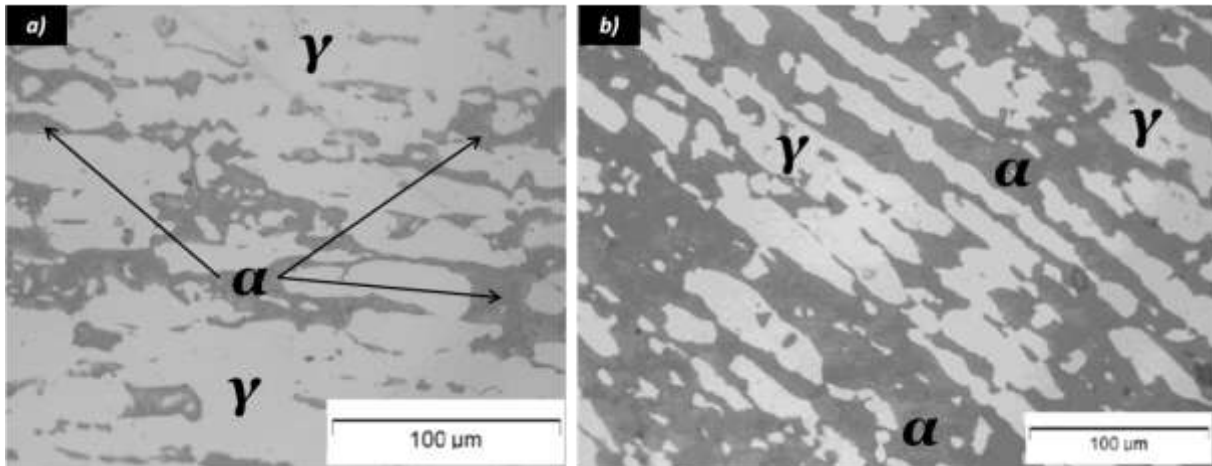


Figure 2.4 - Metallographic pictures of lab duplexes SS in a) absence of Mo and b) presence of Mo on the bulk composition. The effect of Mo on each phase distribution is clearly observed comparing those pictures.

2.2. ELECTROCHEMICAL CHARACTERIZATIONS

In this section, the electrochemical methods used in this work will be minutely described. Firstly, the sample and solution preparations will be presented and then the electrochemical measurements.

2.2.1. SAMPLES PREPARATION

For industrial heats, all specimens were cut out at a length of 50mm from the commercial draw wires and the initial diameters were: 6.55mm, 5.60mm, 5.6mm, 5.8mm, 8.7mm and 5.6mm for the 434, 430, 316L, 304L, 2205 and 2304, respectively. The cylindrical exterior surfaces were wet mechanically polished using SiC paper from grade 80 to grade 1200. The polishing process normally reduces the initial sample diameter to a final diameter D_f . So, the equation 2-1 was used to determinate the working surface limits (length L) in order to have always the same exposed area ($S = 2.5 \text{ cm}^2$). The exposed area is limited by an EPOXY resin (PRO EPOXY – Pattex – ACIER). After resin application, all specimens are air-aged at the

room temperature for 24 hours before performing of electrochemical measurement. Fig. 2.5 illustrates a schematic representation of the samples from the industrial materials after preparation for electrochemical experiments.

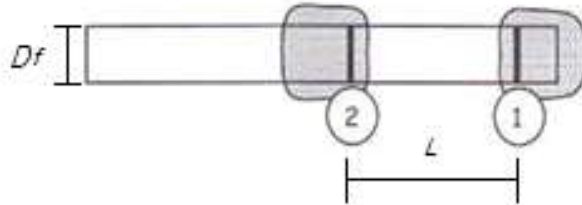


Figure 2.5 - Schematic illustration of industrial Stainless steels specimen after the mechanical polishing preparation. The wiredrawing deformation direction was studied.

The length L between the traces utilized for resin application was calculated with the expression (2-1):

$$L = \frac{2.5}{\pi \times D_f} \quad (2-1)$$

For laboratory heats, the specimens have a disk shape with 1.5 cm and 2 mm as diameter and thickness, respectively. The samples were embedded with an acrylic resin after connecting a small copper wire in order to have a good electrical contact to perform the electrochemical experiments. Fig. 2.6 illustrates a typical laboratory SS sample preparation. Finally, this procedure provided a working surface of 1.77 cm² as only one side of the SS disk were exposed.

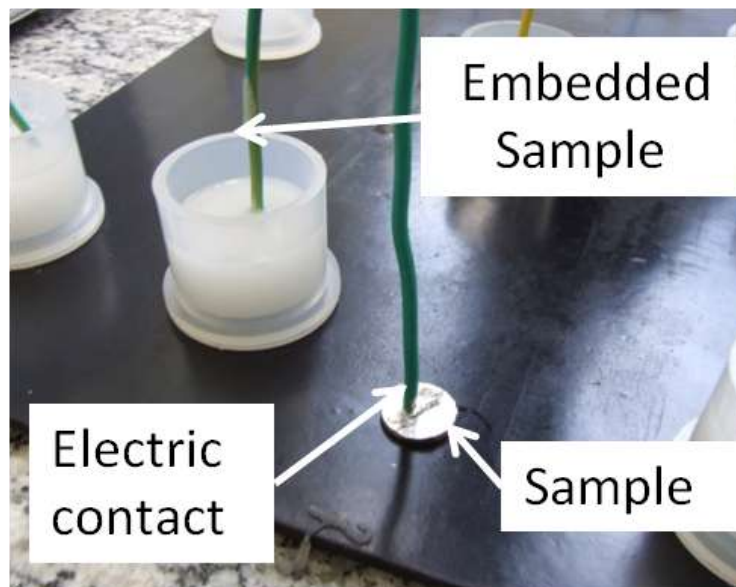


Figure 2.6 - Laboratory stainless steels specimens during the preparation for electrochemical experiments. The rolling deformation direction was evaluated.

2.2.2. SOLUTION PREPARATION

Highly pure chemical compounds and deionized water were used to prepare the corrosive solutions. The different aggressive media were the following:

- 1) Alkaline medium simulating concrete pore solutions with a pH close to 10 ($0.025 \text{ M NaHCO}_3 + 0.025 \text{ M Na}_2\text{CO}_3 + 35 \text{ g/L NaCl (21 g/L Cl}^-)$) at 25°C , 50°C and 75°C temperatures. Chloride concentration was very similar as those found in seawater.
- 2) Alkaline media simulating pore concrete solutions with a pH higher than 12 ($0.025 \text{ M NaHCO}_3 + 0.025 \text{ M Na}_2\text{CO}_3 + 21 \text{ g/L Cl}^- + X \text{ M NaOH}$) at 25°C . NaOH was used to increase the pH of the solution and simulate the first steps of the concrete hardening.
- 3) Neutral sodium chloride aqueous solution, $35 \text{ g/L NaCl (21 g/L Cl}^-)$. The pH of our deionised water used to prepare this medium was about 6.6. This pH was considered neutral for our experiments.
- 4) Acidic chloride media with a pH between 4 and 0.5, various quantity of HCl + 35 g/L NaCl . The pH was set up at 4 by adding a droplets of HCl (0.0001 M HCl) and at 0.5 by adding 5 M HCl .
- 5) Molybdate media - These solutions have the same composition of the media 1), or 2), or 3) or 4) described before, except that they contain an additional 0.1 M of Na_2MoO_4 .

All media were carefully aerated by air bubbling during 1 hour before immersing the sample in the solution. The solutions were always changed after each experiment in order to eliminate all contamination provided by the previous tested sample dissolution.

2.2.3. ELECTROCHEMICAL CELL DESCRIPTION

For the electrochemical measurements a 150 mL three-electrode cell was utilized, in which the working electrode was the tested material and the counter and reference electrodes were platinum (Pt) and saturated calomel electrode (SCE), respectively. The SCE reference electrode presents a potential of 0.241 V with respect to standard hydrogen electrode. Fig. 2.7 illustrates the electrodes and the cell assembly.

Another important detail about this electrochemical cell is the fact that it has a double glass wall which allows water circulation to control the temperature of the solution inside the cell. This water flow is controlled by a thermostat so that the temperature of experiments could be monitored from room temperature to 90°C . For our experiments, three different

temperatures (25, 50 and 75°C) were investigated for the first measurements. Afterwards, the temperature was fixed at 25°C as it appeared that Mo effect was not depending on T.

The electrolytes, presented in section 2.2.2., were aerated with atmospheric air during one hour by using a single air-pump. This procedure provides the oxygen saturation of these solutions.

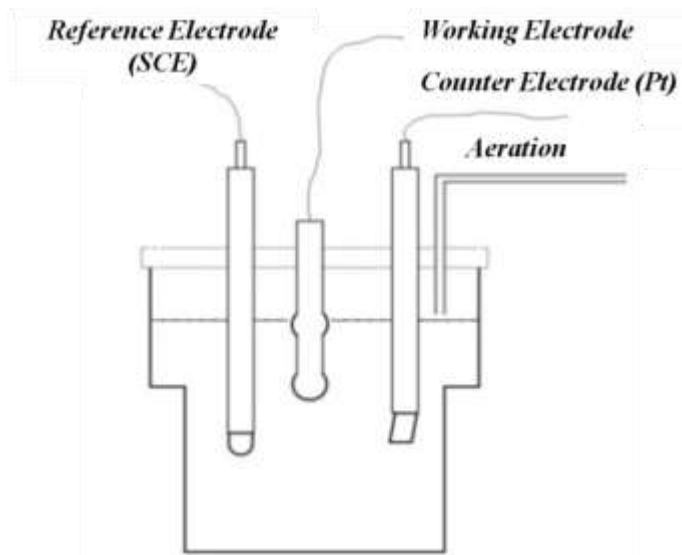


Figure 2.7 - Three – electrode cell description.

2.2.4. ELECTROCHEMICAL EXPERIMENTS

In this section, the electrochemical experiments will be summarized. These techniques provided some important information about the corrosion and passivation properties of industrial and laboratory SS in different pH conditions.

2.2.4.1. POTENTIODYNAMIC POLARIZATION

Polarization method such as potentiodynamic polarization and cyclic polarization, are often used for laboratory corrosion testing. These techniques can provide significant useful information regarding the corrosion mechanism, corrosion rate and susceptibility of specific materials to corrosion in determined environments. Polarization methods involve the control of the potential (E), which is scanned at 1 mV s^{-1} in the present case, along the desired range: around the corrosion potential, in the anodic and/or cathodic domains. The resulting current (I) is monitored as a function of time (t) or potential. If the working surface is known, it is possible to estimate the current density (J), normally given in A cm^{-2} .

For our works the potentiodynamic polarization measurements were used as this experiment is often used to evaluate pitting susceptibility of SS. This kind of polarization is a

destructive method in which the shape of the polarization curve indicates the type of corrosion (general and pitting). Particularly, the existence of the hysteresis in the return scan of the polarization is often associated with pitting, while the size of the loop is often related to the amount of pitting.

A typical potentiodynamic polarization curve is illustrated in Fig. 2.8. As it can be seen in that curve the scan starts from point **1** and progress in the positive potential direction, anodic scan, until the current density reaches $100\mu\text{A cm}^{-2}$. (point **3**) The scan direction is then reversed and process in the negative or cathodic direction until point **4**. There are a number of notable features on the curve, for example: - the open circuit potential (E_{ocp}) or corrosion potential (E_{corr}) is determined by the point **2** in Fig. 2.8. At this potential the sum of anodic and cathodic reaction rates on the electrode surface is theoretically zero and as a result, the measured current density will be close to zero. Then, as the potential increases in the anodic direction, we move into region **A**, which is normally the active zone, where the metal oxidation is the dominant reaction until passive current density is achieved on zone **B**, which is called the passive region. In our example, there is not a clear activation zone because the SS was already passive at E_{corr} . Passing to the region **C**, some spikes on the polarization curve could be observed, this behavior is being normally associated with a quick depassivation and repassivation of the passive layer, which are so-called metastable pits phenomena.

Once the potential reached a sufficiently high anodic value, sometimes termed the breakdown potential, the current density rapidly increases (region **D**). This increase may be due to a number of phenomena, depending on the alloy/environment combination. In our example presented in Fig. 2.8, we have a SS in a chloride electrolyte so that this sudden increase in J is associated to pitting corrosion (localized breakdown of passivity), while for others materials, it may be due to the transpassive dissolution. Furthermore, for some alloys, typically those with a very protective oxide, the sudden increase in current is due to the oxygen evolution, as these materials do not suffer any corrosion attack.

Finally, when the value of current density reaches $100\mu\text{A cm}^{-2}$, the polarization is reversed in the cathodic way in order to study the repassivation tendency of our materials. If an alloy easily repassivates, the current density decreases rapidly after the scan rate reversal and then this alloy will be once again in the passivation domain (point **4**). On the other hand, if the material could not repassivate the current density will still remain high causing the

pitting propagation and strong corrosion of the material. When the surface of the tested material do not present corrosion attack after the polarization measurements, the increase on the current density should have the same shape for scan and scan-back curves, which characterizes the oxygen evolution.

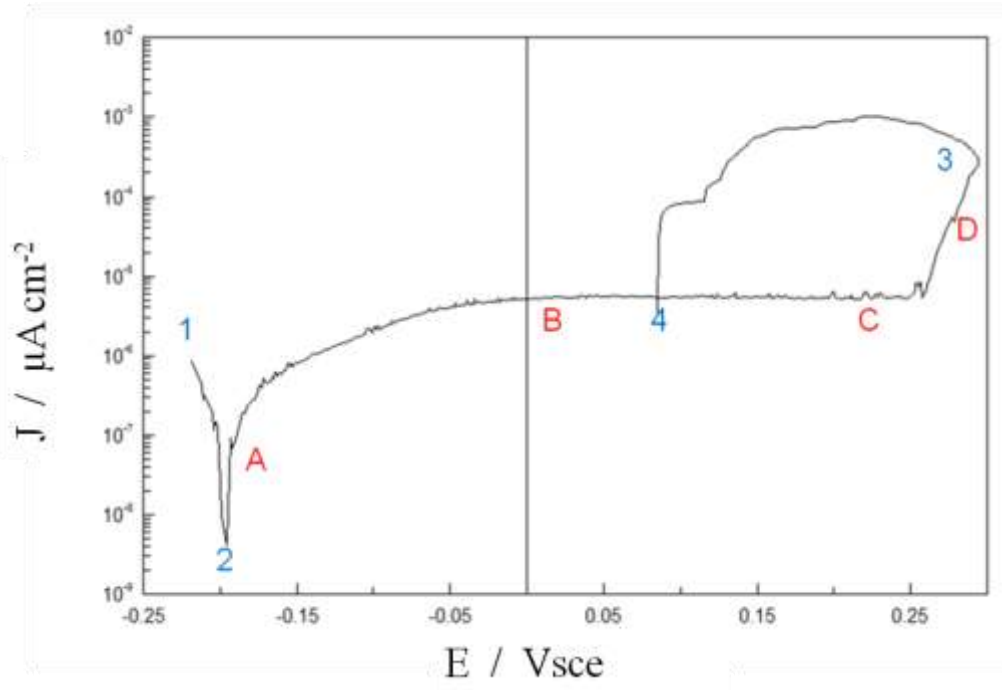


Figure 2.8 - A typical cyclic polarization curve for a stainless steel at salt water (35g/L NaCl).

The parameters fixed during the potentiodynamic polarization measurements with our materials were:

- 1 hour of potential stabilization at OCP potential in the electrolyte before starting the polarization;
- Polarization starts at -0,03Vsce against E_{corr} ;
- Polarization was reversed at current density of $100\mu\text{A cm}^{-2}$ (scanned back to the corrosion potential). This current density was chosen because it is widely used in the literature [4-8] to determine the pitting potential E_{pit} ;
- Potential Scan Rate was 1mVs^{-1} ;

It must be emphasized here that the reverse scan procedure was only qualitatively employed in this present work. Indeed, although largely used, this technique is controversial and intrinsically irreproducible. This is effectively a major drawback — unfortunately almost always disregarded — which is related to the fact that the shape and amplitude of the reverse scan is totally depending on what happened in the forward one. The increase of the current,

even if it can be undoubtedly ascribed to the onset of pits and the film breaking down, is in fact related to the shape and number of events and none of this under the control neither accessible to the operator. One should not forget that the polarization curve is plotted as current density reported to the Euclidian macroscopic surface. Up from the moment pits are formed, we simply do not know what is the actual active surface that delivers the total measured current. This kind of protocol is hence very ambiguous and at least totally misleading. This is why in the present work, we kept this protocol, but only in a very qualitative approach.

A SI 1287 Electrochemical Interface (potentiostat/galvanostat SOLARTRON, Schlumberger) was used to perform these electrochemical polarization experiments. The software used to control the potentiostat was CORRWARE 2 whereas CORRVIEW 2 and ORIGIN 8 software were employed to analyze the data.

2.2.4.2. ZERO RESISTANCE AMMETER (ZRA)

A zero resistance ammeter (ZRA) is a current to voltage converter that produces a voltage output proportional to the current flowing while imposing a 'zero' voltage drop to the external circuit. In corrosion tests, the ZRA is typically used to measure the galvanic coupling current between two dissimilar electrodes. An interesting application is when the coupling current between two nominally identical electrodes is measured. If both electrodes were identical then very little coupling current would flow. In real situations these electrodes will always be slightly different, one being more anodic or cathodic than the other and a small coupling current will exist.

Fig. 2.9 presents a schematic representation of the experimental set-up with two identical working electrodes connected through a ZRA system [9]. Our ZRA electrochemical experiments consist in two identical working electrodes connected through a low impedance ammeter, and a standard calomel reference electrode (SCE), which let us simultaneously measure the current intensity and potential variations in open circuit or upon polarization. During corrosion measurements, the data-sampling rate was 1000 Hz which gives a sufficient resolution. The frequency of measurements could be decreased if necessary. The objective of this kind of experiments is to measure the current and potential transients when the metastable pits nucleate and repassivate. Then, interpreting these data, we could have some ideas about the role of Mo on the first step of pitting corrosion, the passivity breakdown and recovering.

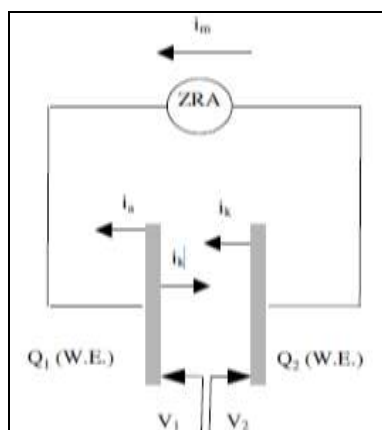


Figure 2.9 - Schematic representation of the experimental set-up with two identical working electrodes connected through a low resistance ammeter (ZRA) [9].

The device used to perform these measurements was a PCI4/750 potentiostat/Galvanostat – Gamry Instruments, Inc., which was driven by the data acquisition processing software ESA400- Electrochemical Signal Analyzer.

2.2.4.3. ELECTROCHEMICAL IMPEDANCE SPECTROSCOPY (EIS)

Electrochemical Impedance Spectroscopy EIS has been successfully applied to the study of corrosion systems for thirty years and has been proven to be a powerful and accurate method to estimate corrosion rates and passivation properties. One of the main advantages of this technique in corrosion domain is to access the charge transfer resistance or polarization resistance, proportional to the corrosion rate at the monitored interface. EIS results usually have to be interpreted with the help of a complex model of the interface or equivalent circuits. Another important advantage of EIS over other laboratory techniques is the possibility of using very small amplitude signals without significantly disturbing the system during measurement. To make an EIS measurement, a small amplitude voltage signal, usually between 5 and 20 mV, is applied to a specimen over a range of frequencies of 0.001 Hz to 100,000 Hz. The EIS instrument records the real and imaginary components of the impedance response of the system. Depending upon the shape of the EIS spectrum, a model circuit or circuit description code is used to simulate the interface behavior and initial circuit parameters are assumed and input by the operator. Besides, EIS is a very sensitive technique and it must be used with great care. This may be connected with the fact that existing literature reviews papers about EIS are very often difficult to understand by non-specialists and, frequently, they do not show the entire mathematical developments of equations connecting the impedance with the physico-chemical parameters. It should be stressed that

EIS cannot give all the answers about a corrosion system, but it is a complementary technique to others methods. So, the electrochemical impedance spectroscopy is a non-stationary technique that allows extract and analyze phenomena more or less coupled, such as transport of reactive species in solution, adsorption of reactive species on an electrode and interfacial electrochemical and chemical reactions [10]. It is used in areas of research areas such as batteries [11-13], corrosion [14-16], the electrochemical deposition [17, 18], semiconductors [19-21] or corrosion inhibitors [22, 23]. Using this technique remains essential in the context of our study because thanks to it, we should be able to identify the mode of action of various compounds on our materials and also evaluate the passive layer stability in our electrolytes.

2.2.4.3.1. PRINCIPLE

The impedance concept is a generalization of Ohm's law to the study of ac circuits. Impedance, symbolized by Z , measures the tendency of a circuit to resist to the passage of an alternating electrical current, and is expressed as:

$$Z = \frac{V_{ac}}{I_{ac}} \tag{2-2}$$

It depends on the frequency of signals V_{ac} and I_{ac} .

EIS consists of measuring the impedance of an electrochemical system subjected to a low amplitude sinusoidal voltage (ΔE) and with variable frequency:

$$\Delta E(t) = |\Delta E| \exp(j\omega t) \tag{2-3}$$

Where: ω is the angular frequency ($\omega = 2 \pi f$, f is frequency in Hertz), and $|\Delta E|$ is the excitation amplitude. This amplitude is chosen to approximate a linear behavior of the studied system as shown in Fig. 2.10. Particularly for metallic systems, this amplitude $|\Delta E|$ is generally about 10 mV.

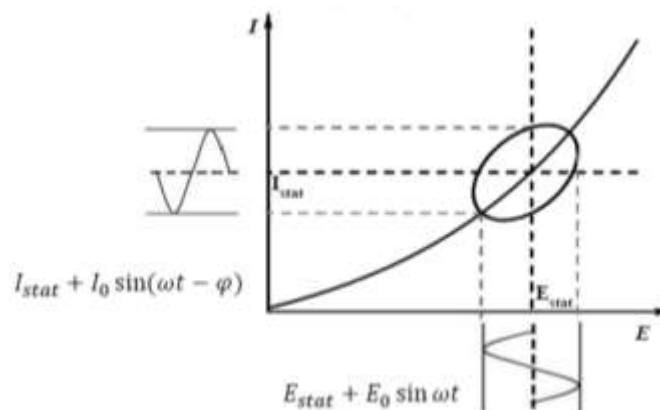


Figure 2.10 - Analysis of a non-linearized system by using small perturbations in potential.

The system's response to this disturbance (ΔE) is a sinusoidal current (ΔI) with the same angular frequency, such as:

$$\Delta I(t) = I_0 \sin(\omega t - \varphi) \quad (2-4)$$

Where: φ is the phase shift on ac relative to potential and $|\Delta I|$ is the current amplitude. Then, *Euler relations* are used in order to simplify the calculation of Z passing to complex notation, which gives:

$$\left. \begin{array}{l} \overline{\Delta E(t)} = E_0 \exp(j\omega t) \\ \overline{\Delta I(t)} = I_0 \exp(j\omega t - \varphi) \end{array} \right\} Z(\omega) = \frac{\overline{\Delta E(t)}}{\overline{\Delta I(t)}} = \frac{E_0}{I_0} \exp(j\varphi) = |Z| \exp(j\varphi) \quad (2-5)$$

Where: j is the complex number ($j^2 = -1$), Z is a complex number with real part Z_{Re} and an imaginary part Z_{Im} . Thus, impedance modulus $|Z|$ and its argument φ are given by:

$$|Z| = \frac{|\Delta E|}{|\Delta I|} = \sqrt{Z_{Re}^2 + Z_{Im}^2} \quad \text{and} \quad \varphi = \text{Arc tan} \left(\frac{Z_{Im}}{Z_{Re}} \right) \quad (2-6)$$

For our experiments, a SI 1287 Electrochemical Interface (potentiostat/galvanostat SOLARTRON, Schlumberger) coupled with a frequency response analyser 1250 ou 1260 was used to perform the electrochemical impedance experiments. The software used to control the potentiostat was CORWARE 2/Zplot and to analyze the data ZVIEW 2, ZSimpWin and ORIGIN 8 were used. The following set up was used to perform the electrochemical impedance measurements:

- DC potential: 0 vs OCP
- AC amplitude: 10 mV
- Initial Frequency: 5000 Hz
- Final Frequency: 0.01Hz

2.3. SURFACE CHARACTERIZATIONS

2.3.1. SCANNING ELECTRON MICROSCOPE (SEM)

The scanning electron microscope (SEM) is a type of electron microscope that images the sample surface by scanning it with a high-energy beam of electrons in a faster scan pattern. The electrons interact with the atoms constituting the sample and produces signals that contain information about the sample's surface topography, composition and other properties such as electrical conductivity.

The types of signals produced by a SEM include secondary electrons (SE), back-scattered electrons (BSE), characteristic X-rays, light (cathodoluminescence), specimen current and transmitted electrons. Secondary electron detectors are common in all SEMs, but it is rare that a single machine would have detectors for all possible signals. The signals result from interactions of the electron beam with atoms at or near the surface of the sample. In the most common or standard detection mode, secondary electron imaging or SEI, the SEM can produce very high-resolution images of a sample surface, revealing details about less than 1 to 5 nm in size. Due to the very narrow electron beam, SEM micrographs have a large depth of field yielding a characteristic three-dimensional appearance useful for understanding the surface structure of a sample. A wide range of magnifications is possible, from about 10 times (about equivalent to that of a powerful hand-lens) to more than 500,000 times, about 250 times the magnification limit of the best light microscopes. Back-scattered electrons (BSE) are beam electrons that are reflected from the sample by elastic scattering. BSE are often used in analytical SEM along with the spectra made from the characteristic X-rays. As the intensity of the BSE signal is strongly related to the atomic number (Z) of the specimen, BSE images can provide information about the distribution of different elements in the sample. For the same reason, BSE imaging can image the different phases of a Duplex Stainless Steel. Characteristic X-rays are emitted when the electron beam removes an inner shell electron from the sample, causing a higher energy electron to fill the shell and release energy. These characteristic X-rays are used to identify the composition and measure the abundance of elements in the sample.

2.3.1.1. SCANNING PROCESS AND IMAGE FORMATION

In a typical SEM, an electron beam is thermionically emitted from an electron gun fitted with a tungsten filament cathode. Tungsten is usually used in thermionic electron guns because it has the highest melting point and lowest vapour pressure of all metals, thereby allowing it to be heated for electron emission, and because of its low cost. Other types of electron emitters include lanthanum hexaboride (LaB₆) cathodes, which can be used in a standard tungsten filament SEM if the vacuum system is upgraded and field emission guns (FEG), which may be of the cold-cathode type using tungsten single crystal emitters or the thermally-assisted Schottky type, using emitters of zirconium oxide.

The electron beam, which typically has an energy ranging from 0.5 keV to 40 keV, is focused by one or two condenser lenses to a spot about 0.4 nm to 5 nm in diameter [24]. The

beam passes through pairs of scanning coils or pairs of deflector plates in the electron column, typically in the final lens, which deflect the beam in the x and y axes so that it scans in a raster fashion over a rectangular area of the sample surface [24].

When the primary electron beam interacts with the sample, the electrons lose energy by repeated random scattering and absorption within a teardrop-shaped volume of the specimen known as the interaction volume, which extends from less than 100 nm to around 5 μm into the surface. The size of the interaction volume depends on the electron's landing energy, the atomic number of the specimen and the specimen's density. The energy exchange between the electron beam and the sample results in the reflection of high-energy electrons by elastic scattering, emission of secondary electrons by inelastic scattering and the emission of electromagnetic radiation, each of which can be detected by specialized detectors. The beam current absorbed by the specimen can also be detected and used to create images of the distribution of specimen current. Electronic amplifiers of various types are used to amplify the signals which are displayed as variations in brightness on a cathode ray tube. The raster scanning of the CRT display is synchronised with that of the beam on the specimen in the microscope, and the resulting image is therefore a distribution map of the intensity of the signal being emitted from the scanned area of the specimen. The image may be captured by photography from a high resolution cathode ray tube, but in modern machines is digitally captured and displayed on a computer monitor and saved to a computer's hard disk. Fig. 2.11 illustrates a schematic diagram of a SEM.

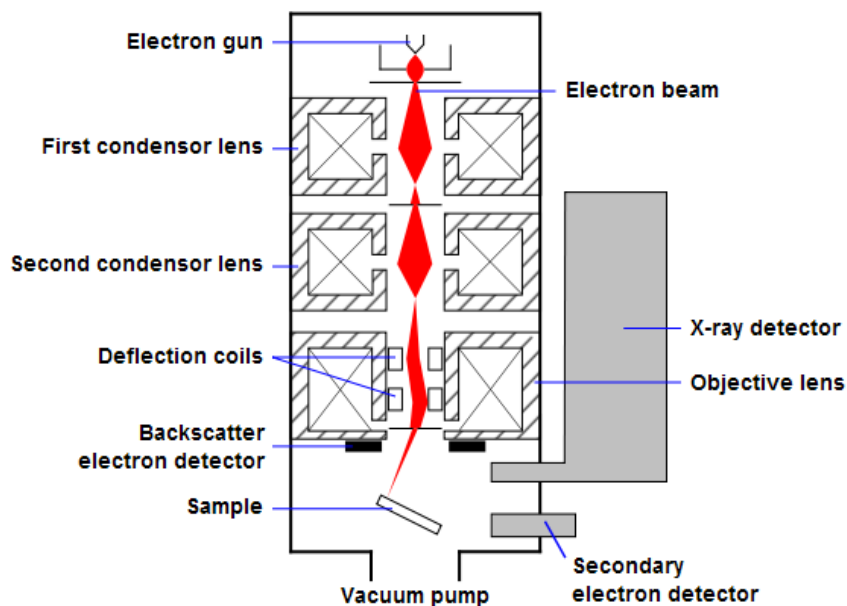


Figure 2.11 - Schematic diagram of an SEM.

2.3.1.2. DETECTION OF SECONDARY ELECTRONS

The most common imaging mode collects low-energy (<50 eV) secondary electrons that are ejected from the k-orbitals of the specimen atoms by inelastic scattering interactions with beam electrons. Due to their low energy, these electrons originate within a few nanometers from the sample surface [24]. The electrons are detected by an Everhart-Thornley detector [25] which is a type of scintillator-photomultiplier system. The secondary electrons are first collected by attracting them towards an electrically-biased grid at about +400 V, and then further accelerated towards a phosphor or scintillator positively biased to about +2,000 V. The accelerated secondary electrons are now sufficiently energetic to cause the scintillator to emit flashes of light (cathodoluminescence) which are conducted to a photomultiplier outside the SEM column via a light pipe and a window in the wall of the specimen chamber. The amplified electrical signal output by the photomultiplier is displayed as a two-dimensional intensity distribution that can be viewed and photographed on an analogue video display, or subjected to analog-to-digital conversion and displayed and saved as a digital image. This process relies on a raster-scanned primary beam. The brightness of the signal depends on the number of secondary electrons reaching the detector. If the beam enters the sample perpendicular to the surface, then the activated region is uniform about the axis of the beam and a certain number of electrons "escape" from within the sample. As the angle of incidence increases, the "escape" distance of one side of the beam will decrease, and more secondary electrons will be emitted. Thus steep surfaces and edges tend to be brighter than flat surfaces, which results in images with a well-defined, three-dimensional appearance. Using this technique, image resolution less than 0.5 nm is possible [25].

2.3.1.3. DETECTION OF BACKSCATTERED ELECTRONS

Backscattered electrons (BSE) consist of high-energy electrons originating in the electron beam that are reflected or back-scattered out of the specimen interaction volume by elastic scattering interactions with specimen atoms. Since heavy elements (high atomic number) backscatter electrons more strongly than light elements (low atomic number), and thus appear brighter in the image, BSE are used to detect contrast between areas with different chemical compositions [24]. The Everhart-Thornley detector, which is normally positioned to one side of the specimen, is inefficient for the detection of backscattered electrons because few such electrons are emitted in the solid angle subtended by the detector, and because the positively

biased detection grid has little ability to attract the higher energy BSE electrons. Dedicated backscattered electron detectors are positioned above the sample in a "doughnut" type arrangement, concentric with the electron beam, maximising the solid angle of collection. BSE detectors are usually either of scintillator or semiconductor types. When all parts of the detector are used to collect electrons symmetrically about the beam, atomic number contrast is produced. However, strong topographic contrast is produced by collecting back-scattered electrons from one side above the specimen using an asymmetrical, directional BSE detector; the resulting contrast appears as illumination of the topography from that side. Semiconductor detectors can be made in radial segments that can be switched in or out to control the type of contrast produced and its directionality.

Backscattered electrons can also be employed to form electron backscatter diffraction (EBSD) image that can be used to determine the crystallographic orientation of the specimen.

2.3.1.4. MEASUREMENTS PROTOCOL

The SEM was used in this work in order to observe the topography of stainless steel surfaces and also the pit morphology after different corrosion attacks. For this purpose an electron acceleration voltage of 20 KV was applied. The morphology and topography graph of samples were studied by secondary electrons, the chemical compositions of each phase of the duplex structure were determined by using EDX - WDX spectra acquired backscattered electrons.

The apparatus used was a LEO Stereoscan 440, equipped with an EDX analysis.

2.3.2. X-RAY PHOTOELECTRON SPECTROSCOPY (XPS)

X-ray photoelectron spectroscopy (XPS), which is also known as an abbreviation for Electron Spectroscopy for Chemical Analysis (ESCA), is a quantitative spectroscopic technique that measures the elemental composition, empirical formula, chemical state and electronic state of the elements that exist within a thin layer (~10nm) in the material surface. XPS spectra are obtained by irradiating a material with a X-rays beam while a simultaneously measuring of the kinetic energy and number of electrons that escape from the top 1 to 10 nm of the material being analyzed (see Fig. 2.12). XPS requires ultra high vacuum (UHV) conditions.

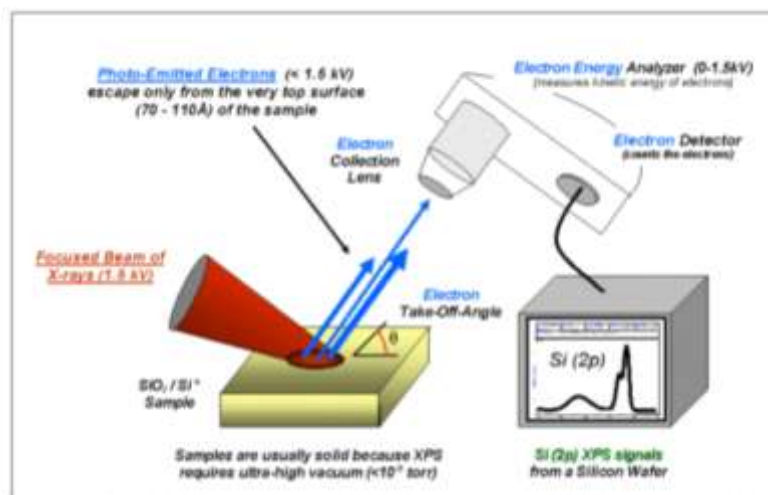


Figure 2.12 - Schematic illustration of the XPS analyses.

As XPS is a surface chemical analysis technique, it can be used to analyze the surface chemistry of a material in its "as received" state, or after some treatment, for example: fracturing, cutting or scraping in air or UHV to expose the bulk chemistry, ion beam etching to clean off some contamination of the surface, exposure to heat to study the changes due to heating, exposure to reactive gases or solutions, exposure to ion beam implant, exposure to ultraviolet light.

XPS detects all elements with an atomic number (Z) of 3 (lithium) and above. It cannot detect hydrogen ($Z = 1$) or helium ($Z = 2$) because the diameter of these orbitals is so small, reducing the catch probability to almost zero. Detection limits for most of elements are in the parts per thousand ranges. Detection limits of parts per million (ppm) are possible, but require specific conditions: concentration at top surface or very long collection time (overnight experiment).

Nowadays, XPS is routinely used to analyze inorganic compounds, metal alloys, semiconductors, polymers, elements, catalysts, glasses, ceramics, paints, papers, inks, woods, plant parts, make-up, teeth, bones, medical implants, bio-materials, viscous oils, glues, ion modified materials and many others. XPS especially provides information about:

- elemental composition of the surface (top 1–10 nm usually);
- empirical formula of pure materials;
- elements that contaminate a surface;
- chemical or electronic state of each element in the surface;
- uniformity of elemental composition across the top surface (or line profiling or mapping);

- uniformity of elemental composition as a function of ion beam etching (or depth profiling);

As an energy of a particular X-ray wavelength is known, the electron binding energy of each of the emitted electrons can be determined by using an equation that is based on the work of Ernest Rutherford (1914):

$$E_{\text{binding}} = E_{\text{photon}} - (E_{\text{kinetic}} + \phi) \quad (2-7)$$

where E_{binding} is the binding energy (BE) of the electron, E_{photon} is the energy of the X-ray photons being used, E_{kinetic} is the kinetic energy of the electron as measured by the instrument and ϕ is the work function of the spectrometer (not the material). Fig. 2.13 shows a typical XPS spectrum of our lab austenitic 18Cr12Ni3Mo after a passivation period of 3 weeks on air.

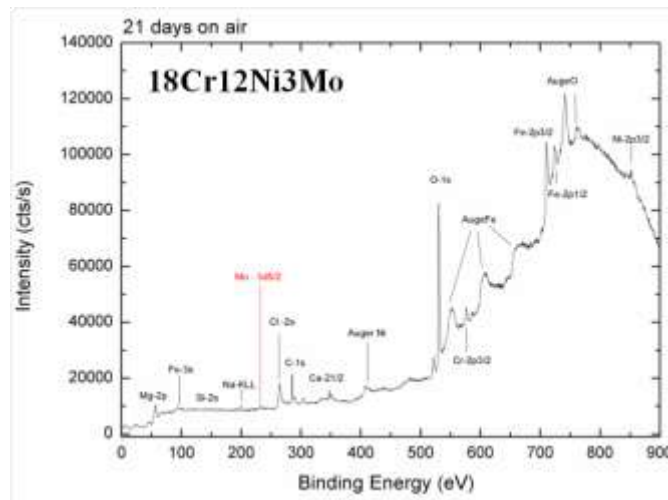


Figure 2.13 - Typical XPS spectrum of the passive film formed on the lab austenitic SS surface (18Cr12Ni3Mo) after aging on the air during 21 days.

2.3.2.1. MEASUREMENTS PROTOCOL

The device used, type of XR3E2 Vacuum Generators, widely described by *Vittoz et al.* [26], consists of a spherical analysis chamber located in a mobile support samples, an X-ray source, analyzer, electron gun and an ion gun, not used in this work. The analysis pressure was approximately 10⁻¹⁰ mbar in the chamber; this pressure was achieved using an ion pump coupled to a titanium sublimation pump.

The mobile support allows the sample movements along the three axes X, Y and Z, but also rotations around axes Z and X. Thus, it is possible by varying the angle α between the

analyzer and the studied surface from 30° to 90° degrees to adjust the depth of passive film investigation according to the relation $d = 3 \lambda \sin(\alpha)$, where λ means free path average photoelectrons. An angle of 90° corresponds to the maximum depth probed is about 6-9 nm, while a 30° angle gives an even more superficial analysis of 2-3 nm (for $\lambda \approx 1.7$ nm). All analysis were performed with both angular values to have better understanding of oxide film structure.

The X-ray source was an anode dual aluminum / magnesium temperature-regulated and for whose the working voltage applied to the filament is fixed at 15 kV for a current of 20 mA. We have used a X-ray source with the best resolution, the K line of magnesium, which have an energy of 1253.6 eV and a maximum half width of 0.7 eV lower than the one for aluminum. This source is not quite monochromatic, remote satellite peaks around the main peak 9eV could appear.

The electron analyzer, type hemispherical capacitor (CLAM2), operates on him in "constant energy" through the input optical delay or accelerates electrons. This conventional mode of using provides a constant energy resolution of the peaks over the entire energy range studied, but there is an effect of reducing the analyzer transmission when the kinetic energy increases. The optimal energy transit, chosen as the best compromise between a sufficient signal and an acceptable resolution, was set at 30 eV. The detector at the analyzer exit is equipped with an electron multiplier type "Channeltron", which amplifies the incoming electron current by a factor of 108.

So, once the desired surface treatment is achieved, the sample is introduced into the chamber where the pumping is immediately started. After transfer into the analysis chamber and calibration, a general spectrum of acquisition (between 0 and 1000 eV binding energy as shown in Fig. 2.13) and then those of located zones around the remarkable peaks C 1s, O 1s, Fe 2p_{3/2}, Cr 2p_{3/2}, Ni 2p_{3/2} and Mo 3d_{5/2} were analysed. The software "Spectrum-Imagum" designed by R & D International was used to obtain the spectra and to treat the XPS data. The spectra show a general resolution of 0.5 eV, while the localized spectra were obtained with a resolution of 0.1 eV.

2.3.2.2. PEAK IDENTIFICATION

The detailed spectra obtained for stainless steel or oxides are generally divided into several sub-peaks suggesting the coexistence of several species. The binding energy values

used in these works are provided from the combined study of bibliographic data and analysis models oxides. In this review, the energies are referenced to C 1s peak of aliphatic carbon at 285.0 eV and located the decomposition characteristics related to steel AISI 304 from the *Vittoz's works* [26]. This decomposition is performed after subtracting the continuous background by Shirley method conventionally used.

➤ **Decomposition of the signal Cr 2p 3 / 2**

The spectra of the signal from Cr 2p_{3/2} are decomposed into two sub-aggregate peaks corresponding to a share of photoelectrons from the metal matrix and secondly to those present in the oxide film. Most authors agree to localize the peak associated with the chromium oxide Cr₂O₃ form shifted by 2.5 eV towards high energy compared with the Cr metal peak [27-30]. These data, listed in Table 2.3, coincide with the calibrations performed to the chromium oxides used models. It's worth noting that the presence of hydroxides species is difficult to be detected because of the proximity of the peaks oxides and hydroxides and also by the disturbing phenomena of spin. In this case, we prefer to study the oxygen signal in which the distinction oxide / hydroxide is easier to be done.

Table 2.3 - Characteristics of the elementary peaks used in the decomposition of the overall signal Cr 2p_{3/2}.

	Cr ^o	Cr ₂ O ₃	Cr (OH) ₃
Energy E_L (eV)	574.1 ± 0.1	576.6 ± 0.2	577 ± 0.2
LMH (eV)	1.8 ± 0.1	3.0 ± 0.2	-
Dissymmetry	15 %	-	-
Report L / G	-	10 %	10 %

➤ **Decomposition of the signal Fe 2p 3 / 2**

As for the Cr 2p 3/2 signal, the signal Fe 2p_{3/2} is divided broadly into two sub-peaks corresponding to a share of photoelectrons from the metal matrix and secondly to those present in the oxide film. However, the decomposition of the sub-peak oxide were more difficult because of the possible coexistence of species Fe³⁺ and Fe²⁺. This phenomenon is due to the presence in the passive layer of goethite FeOOH, of Haematite Fe₂O₃, magnetite Fe₃O₄ and/or wustite FeO. Indeed, results from the literature show that if the Fe³⁺ species are thermodynamically stable under the analysis conditions then, it is more difficult to obtain reference values of the state of Fe²⁺ from standard substances (Fe₃O₄, FeO) unstable at room temperature [31, 32].

Nevertheless, it was noticed that the Fe 2p_{3/2} peaks associated with Fe³⁺ (Fe₂O₃, FeOOH) are accompanied by a satellite peak of shake-up type shifted about 8eV for high binding energies, while FeO oxides show a satellite peak at 6eV corresponding to the principal oxide peak. In the case of Fe₃O₄ species, no traces of this satellite peak type was detected [27, 33].

For these reasons, the identification of the iron oxidation was rather carried out using a semi-quantitative approach due to the total oxide peak displacement and also to the existence of satellite peaks. Furthermore, the differentiation between the oxide and hydroxide iron was performed from oxygen peak, like in the studies of chromium peak. All tabulated values used in this work are listed in Table 2.4.

Table 2.4 - Characteristics of the elementary peaks used in the decomposition of the overall signal Fe 2p 3 / 2.

	Fe ^o	FeO	Fe ₃ O ₄	Fe ₂ O ₃	FeOOH
Energy E_L (eV)	707.0 ± 0.2	709.9 ± 0.2	708.4 ± 0.2	710.9 ± 0.2	711.3 ± 0.3
LMH (eV)	1.6 ± 0.1				
Dissymmetry	20 %				
Satellite Peak(eV)		715.9 ± 0.2		718.9 ± 0.2	718.9 ± 0.2

➤ **Decomposition of the signal O 1s**

The O 1s signal received from XPS analysis mainly comes from four distinct families of species, generally included in the oxidized metals surface. There are those related to the hydrocarbon contamination layer (carbon / oxygen) [34], water physisorbed, the hydroxides (M-OH), and oxides (MO). The bending energies for O 1s sub-peaks decomposition are listed in Table 2.5.

The analysis of this signal provides a primarily information on the degree of hydroxylation of oxides (report of M-OH / MO_x sub-peak). However, this approach does not distinguish whether the metal M is associated oxides or hydroxides, because of the proximity of their corresponding binding energies.

Table 2.5 - Characteristics of the elementary peaks used in the decomposition of the overall signal O1s.

	H ₂ O	C-O, C=O	M-OH	M-O
Energy E_L (eV)	533.3 ± 0.1	532.6 ± 0.1	531.5 ± 0.2	530.1 ± 0.2
LMH (eV)	1.8 ± 0.1	1.8 ± 0.1	1.7 ± 0.1	1.7 ± 0.1
Report L / G	10 %	10 %	10 %	10 %

It should be noted that some peaks such as molybdenum Mo 3d 5/2 peak, observed in Mo containing alloys, are not listed here. They will be shown in the chapters describing their observations. Thus, from these tabulated values and following the traditional equation of XPS analyses, it is possible to decompose all the peaks and determine their intensity, which are linked to the total atomic concentration of each alloying element. Consequently, an estimation of the passive layer composition could be done. In addition, the thickness of oxidized layers on the surface of the SS could be calculated.

2.4. TRIBO-CORROSION CHARACTERIZATION

Tribocorrosion is a material degradation process due to the combined effect of corrosion and wear [35]. The name tribocorrosion expresses the underlying disciplines of tribology and corrosion. Tribology concerns the study of friction, lubrication and wear (its name comes from the Greek "tribo" meaning to rub) and corrosion refers to the chemical and electrochemical interactions between a material, usually a metal, and its environment. Corrosion may accelerate wear and wear may accelerate corrosion [36]. Both phenomena, as well as fretting corrosion (which results from small amplitude oscillations between contacting surfaces) fall into the broader category of tribocorrosion. Erosion-corrosion is another tribocorrosion phenomenon involving mechanical and chemical effects: impacting particles or fluids erode a solid surface by abrasion, chipping or fatigue while the surface corrodes [37].

Tribocorrosion techniques were used in this work in order to study the effect of Mo on the repassivation kinetics of SS under different pH conditions. It is well known that SS get their corrosion resistance from the presence at the surface of a thin oxide film, called the passive film, which acts as a protective barrier between the metal and the environment [38]. Nevertheless, SS can not only provide an excellent corrosion protection thanks to the passive layer formation but thanks to its spontaneously self-healing properties. Therefore, our idea was to use tribocorrosion measurement to locally destroy the passive layer and simultaneously measure the current and potential transients by using electrochemical noise equipment. Fig. 2.14 presents **a)** the tribometer employed for these experiments, **b)** the tribocorrosion cell and, **c)** the samples after the scratch test.

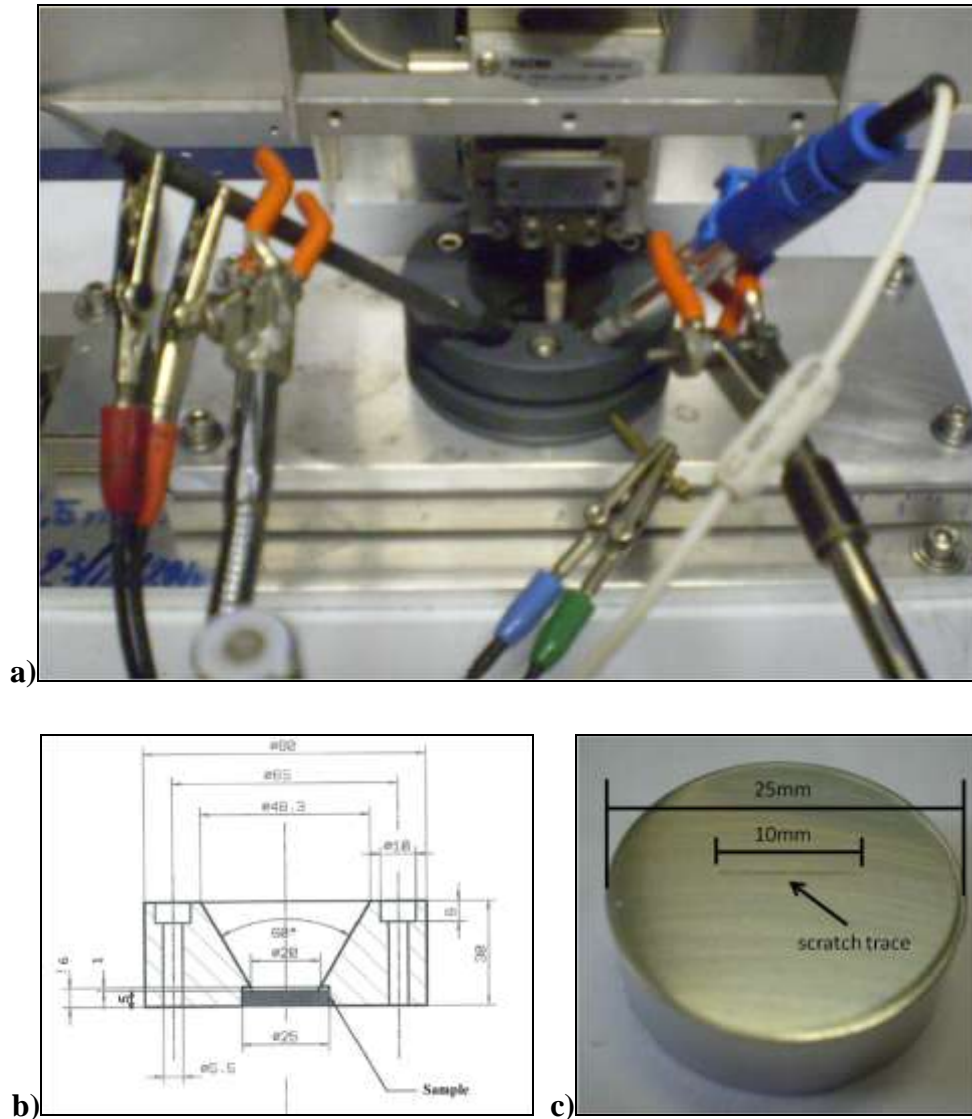


Figure 2.14 - a) Tribometer experiment, **b)** the tribocorrosion cell description and, **c)** the SS samples after the scratch test.

All tribological tests are performed using a reciprocating motion tribometer from Falex Company. These experiments were done in association with INSA laboratory under supervision of Prof. Bernard NORMAND. Samples have a working surface of 10.17 cm² and the counter body is a 6 mm diameter corundum pin ($E = 380$ GPa and $\nu = 0.25$) with a curvature radius of 100 mm. Roughness is controlled by polishing with SiC emery paper up to grade 4000 on a special holder. The stroke length and sliding velocity were fixed to 10 mm and 50 mm/s, respectively, with a trapezoidal motion type. Holding times are set as 100 s for the forward and the backward motions. A 10 N nominal pressure was selected for all tests during 10 cycles and the coefficient of friction is noted COF. Electrochemical experiments were performed at the same time by using a GAMRY REF600 potentiostat and a classical

three cell experiment, where the working electrodes were composed by SS lab alloys, a saturated calomel electrode (SCE) as a reference electrode and a graphite disc as a counter electrode. During friction, the potential was fixed at the open circuit potential or corrosion potential (E_{corr}). Data are recorded at the frequency of 1000 Hz to get a good accuracy on current and potential values during the transient caused by the mechanical passivity breakdown.

2.5. REFERENCES

- [1] F. Zhang, J. Pan, and C. Lin. Corrosion. Science 51 (2009) 2130.
- [2] L. Zhang, Y. Jiang, B. Deng, W. Zhang and J. Xu, J. Li. Materials Characterization 60 (2009) 1522.
- [3] R.N. Gunn. Abington Publishing, Cambridge England (1999).
- [4] A. Pardo, M.C. Merino, A.E. Coy, F.Viejo, R. Arrabal and E. Matykina, Corrosion Science 50 (2008) 780.
- [5] A. Pardo, M.C. Merino, A.E. Coy, F.Viejo, R. Arrabal and E. Matykina, Corrosion Science 50 (2008) 1796.
- [6] H. Baba, T. Kodama, and Y. Katada. Corrosion Science 44 (2002) 2393.
- [7] C. Lemaitre, A. A. Moneim, R. Djoudjou, B. Baroux and G. Beranger. Corrosion Science 34 (1993) 1913.
- [8] M. Kaneko, and H.S. Isaacs. Corrosion Science 44 (2002) 1825.
- [9] G. Berthomé, B. Malki, and B. Baroux, Corrosion Science 48 (2006) 2432.
- [10] C. Gabrielli, *Identification des processus électrochimiques par analyse de leur réponse en fréquence*, Paris, 1980.
- [11] A. H. Zimmerman, M. R. Martinelli, M. C. Janecki, C. C. Badcock. J. Electrochem. Soc. 129 (1982) 289.
- [12] P. Casson, N. A. Hampson, and M. K. Willars. J. Electroanal. Chem. 97 (1979) 21.
- [13] J. Mc Breen and E. Gannon. J. Electrochem. Soc. 130 (1983) 1667.
- [14] F. Mansfeld, M. W. Kendig, and S. Tsai. Corrosion Nace 38 (1982) 570.
- [15] M. U. Macdonald and D. D. Macdonald. J. Electrochem. Soc. 136 (1989) 961.
- [16] D. D. Macdonald, B. C. Syrett, and S. S. Wing. Corrosion Nace 35 (1979) 367.
- [17] X. Cheng, G. Li, E. A. Kneer, B. Vermeire, H. G. Parks, S. Raghavan, and J. S. Jeon. J. Electrochem. Soc. 145 (1998) 352.

- [18] I. Epelboin, M. Jousselein, and R. Wiart. *J. Electroanal. Chem.* 119 (1981) 61.
- [19] M. Chemla, V. Bertagna, R. Erre, F. Rouelle, S. Petitdidier, and D. Levy. *Electrochem. Solid State Let.* 6 (2003) G7.
- [20] J. F. McCann and S. P. S. Badwal. *J. Electrochem. Soc.* 129 (1982) 551.
- [21] M. F. Weber, L. C. Schumacher, and M. J. Dignam. *J. Electrochem. Soc.* 129 (1982) 2022.
- [22] J. Kittel, N. Celati, M. Keddami, and H. Takenouti. *Prog. Orga. Coat.* 46 (2003) 135.
- [23] J. Vogelsang and W. Strunz. *Electrochimica Acta* 46 (2001) 3817.
- [24] G. I. Goldstein, D. E. Newbury, P. Echlin, D. C. Joy, C. Fiori, and E. Lifshin, “*Scanning electron microscopy and x-ray microanalysis*”. New York: Plenum Press, (1981).
- [25] T. E. Everhart, and R. F. M. Thornley. “*Wide-band detector for micro-microampere low-energy electron currents. Journal of Scientific Instruments*” 37, (1960) 246.
- [26] C. Vittoz. “*Etude de l'acido-basicité des surfaces par mouillabilité et XPS. Application aux aciers inoxydables*”. Thèse - INPG, (1997).
- [27] K. Asami, and K. Hashimoto, *Corrosion Science* 17 (1977) 559.
- [28] E. DESIMONI, C. Malitesta, P. G. Zambonin, and A. D. Roberts *Surface and Interface Analysis* 13 (1988)173.
- [29] K. Petkov, V. Krastev, And T. Marinova. *Surface and Interface Analysis* 18 (1992) 487.
- [30] I. Grohmann, E. Kemnitz, A. Lippitz, and W.E.S. Unger. *Surface and Interface Analysis* 23 (1995) 887.
- [31] K. Asami, K. Hashimoto, and S. Shimodaira. *Corrosion Science* 16 (1976) 387.
- [32] K. Asami, K. Hashimoto, and S. Shimodaira. *Corrosion Science* 16 (1976) 35.
- [33] N. S. McIntyre, And D. G. Zetaruk. *Analytical Chemistry* 49 1(977) 1521.
- [34] M. MANTEL, and J.P. WIGHTMAN. *Surfaces and Interfaces Analysis* 21 (1994) 595.
- [35] D. Landolt. *J. Physics D: Appl. Phys.* 39 (2006) 1.
- [36] S. W. Watson, F. J. Friedersdorf, B. W. Madsen, and S. D. Cramer, *Wear* 181-183. (1995) 476.
- [37] K. Sasaki, G.T. Burstein. *Philosophical Magazine Letters* 80 (2000) 489.
- [38] D. Landolt, “*Corrosion and Surface Chemistry of Metals. EPFL Press*”, Lausanne Switzerland (2007) 227.

CHAPTER 3

***MO EFFECT ON PITTING
NUCLEATION AND
PROPAGATION – AN INDUSTRIAL
AND LABORATORY APPROACH***

OUTLINE

3. MO EFFECT ON PITTING NUCLEATION AND PROPAGATION – AN INDUSTRIAL AND LABORATORY APPROACH	82
3.1. INTRODUCTION	82
3.2. INFLUENCE OF Mo ADITION ON INDUSTRIAL SS	83
3.2.1. EFFECT OF Mo ADITION ON PITTING POTENTIAL OF INDUSTRIAL SS IN FUNCTION OF pH	83
3.2.2. Mo EFFECT ON METASTABLE PITS	88
3.3. EFFECT OF Mo ADITION ON PITTING POTENTIAL OF LABORATORY SS IN FUNCTION OF pH	90
3.4. INFLUENCE OF Mo ADDITION ON EACH PHASE OF DUPLEX STRUCTURE	97
3.5. CONCLUSION	103
3.6. REFERENCES	104

3. Mo EFFECT ON PITTING NUCLEATION AND PROPAGATION – AN INDUSTRIAL AND LABORATORY APPROACH

3.1. INTRODUCTION

In the last few years, strong fluctuations and a net increasing tendency of the price of several important alloying elements yielded much effort from the major stainless steel suppliers to propose new technological solutions that minimize the use or even eliminate those alloying elements (mainly nickel and molybdenum) in the composition of special grades. This at least partially explains the appearance of new less expensive alloys like lean duplex stainless steels on the market [1, 2]. In general the use of Mo-free or low Mo content alloys is now sometimes extended into service conditions for which formerly Mo-containing alloys would have been used. This development is mostly due to economic reasons inasmuch as the role of Mo is still not fully understood. The lack of scientific knowledge concerning the role of Mo can be illustrated by a fundamental disagreement in the literature as to whether Mo is a component of passive films [3-5] or not [6-10].

The consequences of a more widespread use of these alloys are difficult to predict. Indeed, it is true that the positive role of Mo in acidic media can be considered as generally accepted [11-14]. In the case of alkaline media, however, the role of Mo is much less studied. Some previous studies have pointed out that in certain conditions Mo has no beneficial effect on the pitting corrosion resistance of stainless steels [15-18], which could thus justify abandoning high Mo alloys for alkaline service conditions. It is worth noticing however that those results were limited to austenitic steels in some specific conditions [15] or were based upon preliminary laboratory observations [16].

In this chapter, the most important results about the molybdenum influence on pitting nucleation and propagation of industrial and laboratory SS will be discussed. The electrochemical measurements from acidic to alkaline environments (mainly in chloride alkaline media simulating concrete pore solutions) and also the surface characterization for three different families of SS (austenitic, ferritic and duplex) will be analyzed and interpreted in terms of presence or absence of Molybdenum on the bulk material composition.

Our research started with studies about commercial industrial materials of three different SS families, austenitic, duplex and ferritic. The aim of this first step was to

characterize the behavior of Mo-containing and Mo-free austenitic (AISI 316L and 304L), ferritic (AISI 434 and 430) and duplex (2205 and 2304) SS exposed to different chloride rich media, mainly at alkaline conditions. These conditions are particularly relevant to coastal or off shore rebar applications and also for paper and alkali industries. Furthermore, measurements with laboratory castings with highly controlled composition were also performed in order to have a better understanding of the Mo effect.

3.2. INFLUENCE OF Mo ADDITION ON INDUSTRIAL SS

3.2.1. EFFECT OF Mo ADDITION ON PITTING POTENTIAL OF INDUSTRIAL SS IN FUNCTION OF pH

Fig. 3.1 a), b), c) and d) show the typical polarization curves obtained for industrial 304L and 316L SS at pH 0.6, 7, 10 and 12.1, respectively. The Fig. 3.1 a) illustrates the huge positive effect of Mo on the corrosion resistance of austenitic grades in chloride acidic environments (pH 0.6), as the 304L SS shows no passivation and corrodes already at open circuit potential (E_{corr}) whilst 316L shows a passivation range and a pit potential (E_{pit}) around 280 mV_{sce}, which means that this acidic pH is lower than the depassivation pH for the 304L alloy. This positive effect of Mo for austenitic SS was also observed on chloride neutral condition as shown in Fig. 3.1 b). In this condition, both 316L and 304L present a passive plateau but the Mo-containing SS present a higher E_{pit} compared to the free Mo one (E_{pit} was about 80 mV higher for 316L). In the alkaline domain, however, an absence of positive role of Mo for austenitic SS was remarked for pH 10, as presented in Fig. 3.1 c). Moreover, if the pH is even higher (12.1), the 304L SS becomes more resistant than the 316L SS (E_{pit} for 316L < E_{pit} for 304L), as can be seen in Fig. 3.1 d) [19-21]. These results were found by using different industrial heats of these grades by 3 different researchers from CRU - UGITECH and LEPMI laboratory, which assure the reproducibility of these data.

The E_{pit} evolution of 316L and 304L SS as function of pH are clearly represented in Fig. 3.2. The increasing of the pitting corrosion resistance occasioned by Mo addition was detected in acidic and neutral chloride media. In alkaline media, however, the results are inverted which confirms the anomalous behavior already pointed out. It must be stressed that

polarization measurements were done at least 3 times and dispersion of E_{pit} values were, more and less, 30 mV.

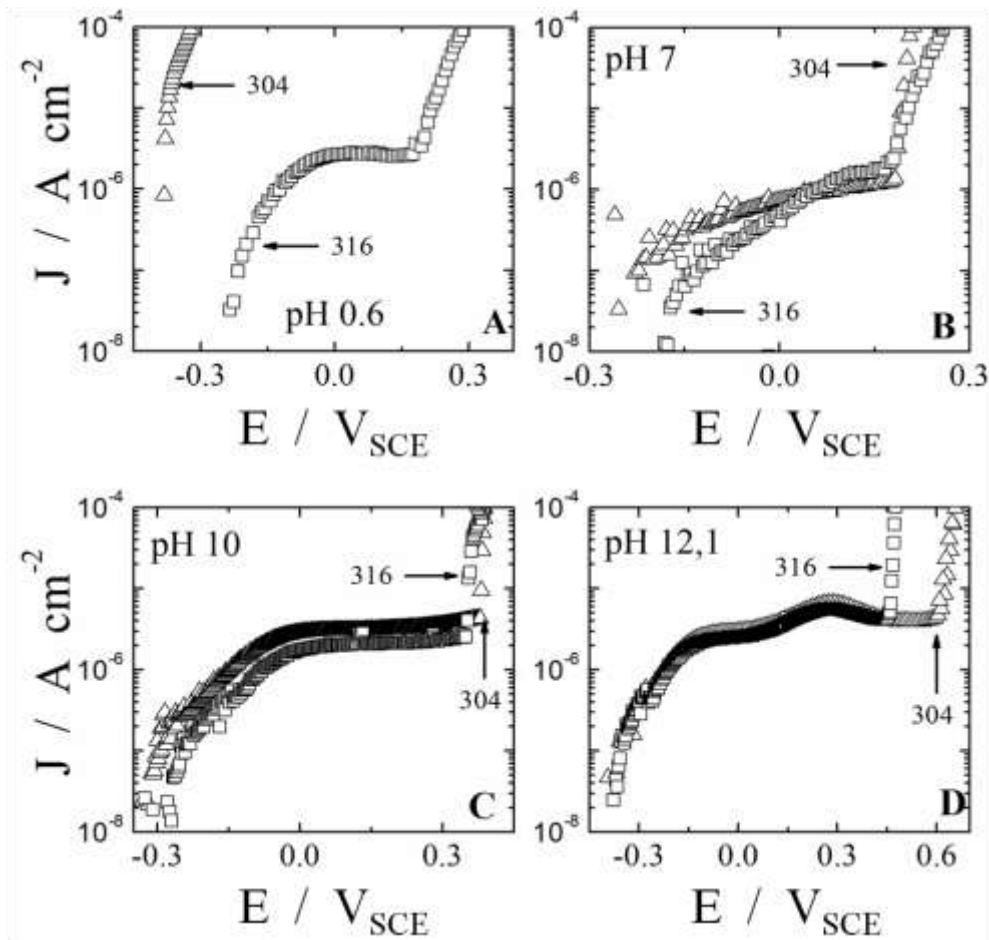


Figure 3.1 - Polarization curves obtained for 304L (Δ) and 316L (\square) austenitic SS in different pHs of chloride solution (**A:** pH 0.6; **B:** pH 7 **C:** pH 10 and **D:** pH 12.1) at 25°C.

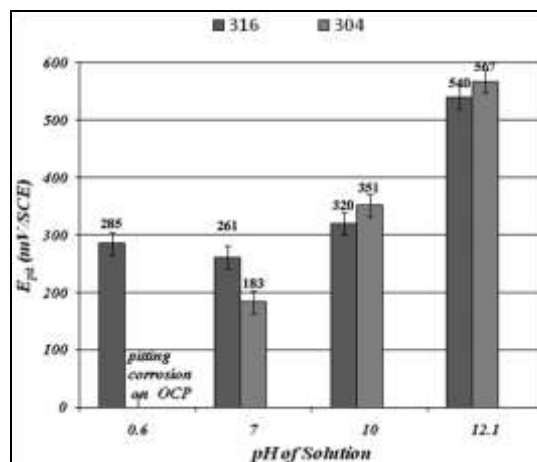


Figure 3.2 – E_{pit} Average of austenitic SS obtained in different pH of chloride solution. The unlike effect of Mo addition on pitting corrosion resistance is directly observed by the comparison between the E_{pit} values of AISI 316L and 304L on alkaline conditions.

It seems hence that, for these austenitic grades, there is a monotonic loss of Mo effect as the pH increases, which have not been reported by the literature yet. The $\Delta E_{pit\ 316 - 304}$ values mainly represents the Mo influence on pitting corrosion resistance of these materials as the presence of Mo on 316L SS increased in 5 points the PREn compared to the 304L SS. It is hence interesting to straightforwardly evaluate the evolution of the difference on the E_{pit} values from the 316L and 304L SS ($\Delta E_{pit\ 316 - 304}$) with pH as done in Fig. 3.3. The loss of Mo effect clearly appears since as the pH increases $\Delta E_{pit\ 316 - 304}$ falls from 450 mV (pH 0.6) to – 25 mV (pH 12) illustrating the mentioned inversion in the austenitic SS performances. This anomalous behavior could be related to the reaction mechanism associated to the effect of Mo, for instance a pH dependent state of charge that could allow Cl⁻ trapping by Mo cations in acidic solutions [22] but not in alkaline media. However, these mechanistic insights are still far from being fully researched and understood, as mentioned before on chapter 1.

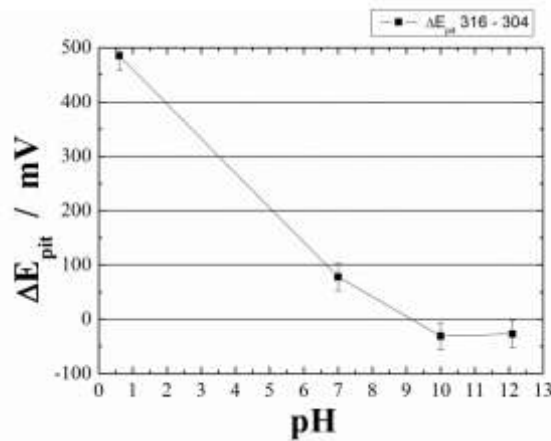


Figure 3.3 - E_{pit} difference ($\Delta E_{pit\ 316 - 304}$) between the 316L and 304L in function of the pH.

It has been argued that these unlike results previously detected were related to 316 SS having a higher amount of manganese than 304 [12, 23, 24]. In these cases, the SS usually exhibit an uncompleted dissolution of this element in the austenite phase, resulting in the formation of manganese-rich sulphide inclusions, which are not thermodynamically stable at the passivity region potentials. As a result, these inclusions tend to dissolve, starting a localized attack at the inclusion/austenitic matrix interfaces and consequently hide the protect Mo effect. However, our austenitic alloys have almost the same Mn contents (0,733 wt.% Mn and 0,599 wt.% Mn for AISI 316L and AISI 304L, respectively (see Table 2.1)) which eliminate the possibility of a higher MnS inclusion contents on 316L and then an undesirable E_{pit} reduction for this material in alkaline conditions. Furthermore, if this anomalous behavior of austenitic SS was associated with the a higher content of MnS on 316L grade, the 304L should have presented a greater pitting corrosion resistance in all pH conditions as the used

samples were exactly the same for all experiment solutions (acidic, neutral and alkaline media).

Another important remark concerns the fact that these SS are industrial heats with small composition differences in the other alloying elements that can also have a non-negligible effect on the overall corrosion resistance behavior. This exactly why we also worked with fully controlled lab heats for which Mo content was strictly the only difference. We will discuss about this results later. Before, it is worth noticing that, in a first glance, these first results seem to validate the idea that Mo is not functional in alkaline media, at least not with respect to localized corrosion resistance of austenitic SS. Moreover, since austenite is intrinsically more corrosion resistant than ferrite in most service conditions, it could be assumed, that the effect discussed from Fig. 3.1, 3.2 and 3.3 equally applies to ferritic and duplex SS. This hasty conclusion is however incorrect as we will see in the following results.

Fig. 3.4 shows the typical polarization curves of duplex alloys, AISI 2304 and 2205, in different pH media. The beneficial effect of Mo addition on pitting corrosion resistance (determined by the E_{pit}) for duplex SS can be clearly observed even at elevated pH such as 10. The 2205 duplex SS did not present pitting corrosion in any pH and at pH 12 both duplex grades showed no pit attack at all. Then, the current density increase for the 2205 SS observed in Fig. 3.4, is due to the oxygen evolution and not to a passivity breakdown. It means that the oxygen evolution of these solutions happen before the pitting attack of this steel. The oxygen evolution reaction can be described by:

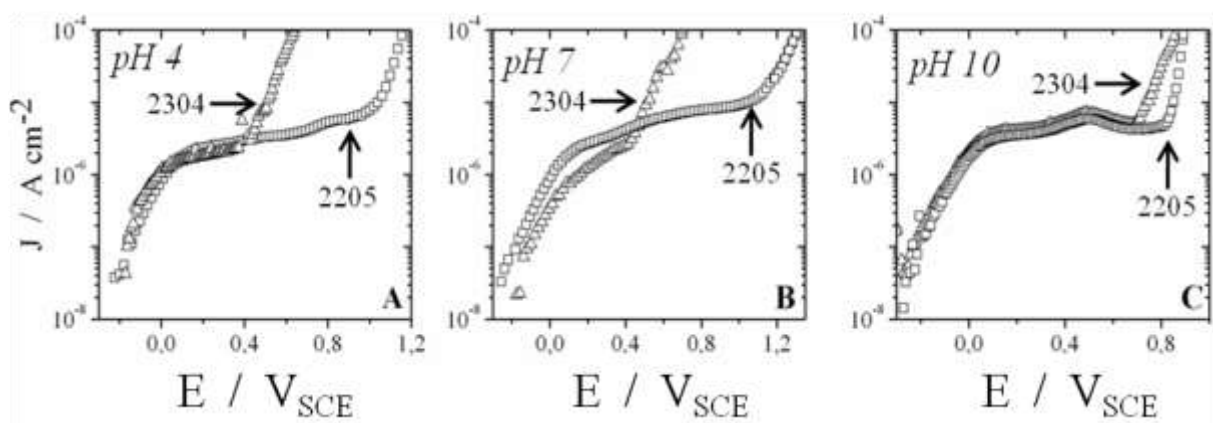
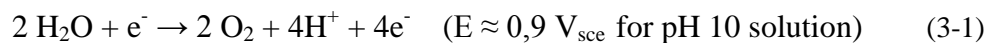


Figure 3.4 – Polarization curves obtained for 2304 (Δ) and 2205 (\square) duplex SS in different pH (A: pH 4; B: pH 7 and C: pH 10) at 25°C. The current increases up for the 2205 grade are due to oxygen evolution and not pitting corrosion.

The typical cyclic polarization curves of ferritic alloys, AISI 430 and 434, in different pH media are shown in Fig 3.5. As for the duplex, the beneficial effect of Mo addition on pitting corrosion resistance of ferritic SS can be easily observed. Indeed, at very acidic pH (pH 0.6), these SS corroded intensively, as did the 304L (Fig. 3.1). The main difference is that, for neutral and alkaline media, where the E_{pit} difference between the Mo-containing and the Mo-free ferritic grades does not decrease with increasing pH but oscillated between +20 and +90 mV in the pH range studied, whilst as mentioned before, the austenitic grade difference monotonically decreased. It is worth saying that all anodic polarization graphs presented in Figs. 3.1, 3.4 and 3.5 are just typical examples of a quite reproducible behavior.

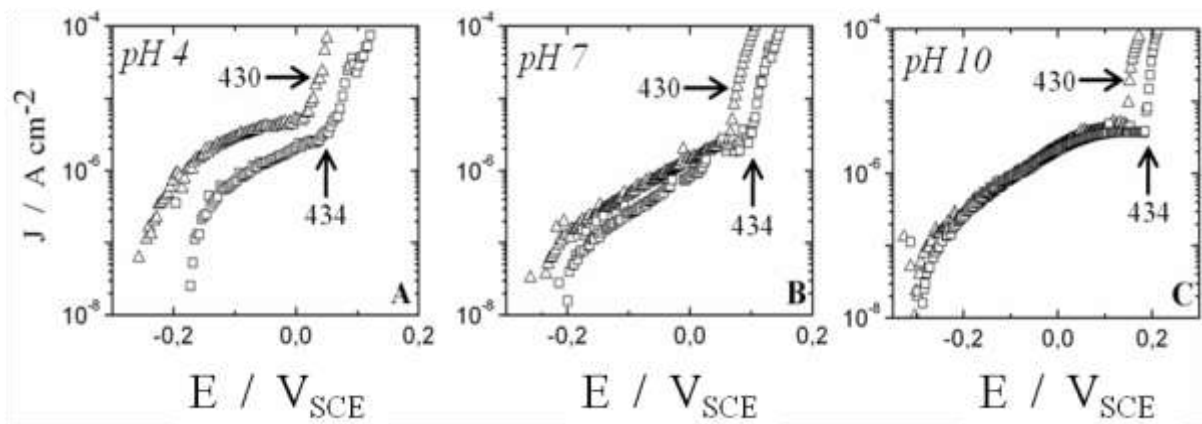


Figure 3.5 - Polarization curves obtained for 430 (Δ) and 434 (\square) ferritic SS in different pHs of chloride solution (A: pH 4; B: pH 7 and C: pH 10) at 25°C.

The beneficial effect of Mo on ferritic SS are resumed at Fig. 3.6 which presents the positive difference between the E_{pit} values for 434 and 430 ($\Delta E_{pit\ 434 - 430}$) in all three studied pH solutions.

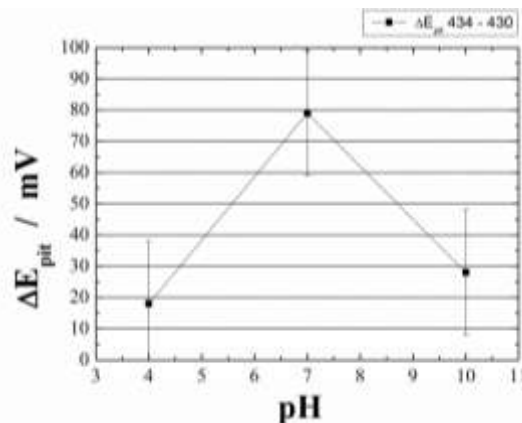


Figure 3.6 - E_{pit} difference ($\Delta E_{pit\ 434 - 430}$) between the 434 and 430 in function of pH.

Table 3.1 describes the E_{pit} and E_{corr} values for all industrial SS. The influence of Mo could be simply observed in this table by comparing the 2 grades for the same SS family and

at a similar pH. For example, at pH 7, Mo addition shifted E_{pit} values for more noble values, from 0.183 to 0.261 V_{sce} for austenitic SS, from 0.073 to 0.152V_{sce} for ferritic SS, and from 0.415 to more than 0.900V_{sce} for duplex ones. Moreover, at acidic and neutral media, Mo seems to have also a positive effect on the E_{corr} that increases whereas it has no effect in alkaline solutions. It is worth noticing that E_{corr} values are the average between 3 experimental results at least, and the standard error is about 28 mV_{sce}. The effect of Mo on the well known repassivation potential E_{rep} was not discussed here because of the irreproducibility in those values. This irreproducibility is probably due to the differences on pitting attack morphology (different amounts of pit or a variety on pits sizes) already explained in the experimental section. For example, a sample which presents a lot of big pits will never repassivates in the same way of a sample corroded by few small pits.

Table 3.1 - E_{pit} and E_{corr} values (mV_{sce}) for the industrial SS at different pH conditions.

Material	pH0.6		pH4		pH7		pH10		pH12.1	
	E_{corr}	E_{pit}								
304	-385	-300	X	X	-283	183	-292	351	-390	567
316	-215	285	X	X	-169	261	-315	320	-383	540
430	X	X	-241	10	-232	73	-238	155	X	X
434	X	X	-186	28	-203	152	-239	183	X	X
2304	X	X	-210	491	-207	415	-281	695	X	X
2205	X	X	-207	>1000	-266	>1000	-285	>1000	X	X

Summarizing these results from industrial SS, for austenitic grades, it clearly appears that Mo has not a positive effect in their corrosion resistance in alkaline environments. On the other hand, Mo does have a protective role for ferritic SS in alkaline media. Consequently, the pretty positive effect of Mo for duplex SS should be associated to the improvement of the ferrite pitting corrosion resistance instead of austenite in high pH solutions. This idea will be deeply discussed in the following sections.

3.2.2. Mo EFFECT ON METASTABLE PITS

The results presented above indicate that the Mo role should also encompass some prior-to-the-attack metallurgical effects, such as microstructures (austenite or ferrite) or the reinforcement of the passive film by Mo, besides post-attack interfacial kinetic processes, like

those related to Mo cations interactions with electrolyte anions [22, 25]. Indeed, if the Mo effect was related to chemical or electrochemical interactions of Mo cations with the electrolyte only, pH changes should have more or less the same impact regardless of the allotropic form, which is clearly not the case as presented before. Those later interfacial effects have been proposed to be at the origin of enhanced repassivation kinetics [26, 27], which can be expected to yield smaller time constants of the repassivation transient after a metastable pit initiation, for instance. Fig. 3.7 shows two typical current transients — shifted to have the same arbitrary time origin — associated to metastable pits taking place at 430 and 434 surfaces at pH 10 solution and polarized to +500 mV with respect to their open circuit potential. The repassivation (represented by the current decay after reaching a maximum) appears quite steep in both cases, thus illustrating equivalent repassivation kinetic in the absence and in the presence of Mo. On the other hand, the pit initiation (related to the current increase) seems to be slowed down in the presence of Mo, showing effectively a much less pronounced current increase profile (higher time constant) represented by a rise time up to the maximum of about 0.7s for the 430 and 2.3s for the 434 as well as a lower transient amplitude. This would effectively mean that the role of Mo should not be only related to the way it accelerates repassivation but mostly to how it inhibits pit initiation and the first steps of growth.

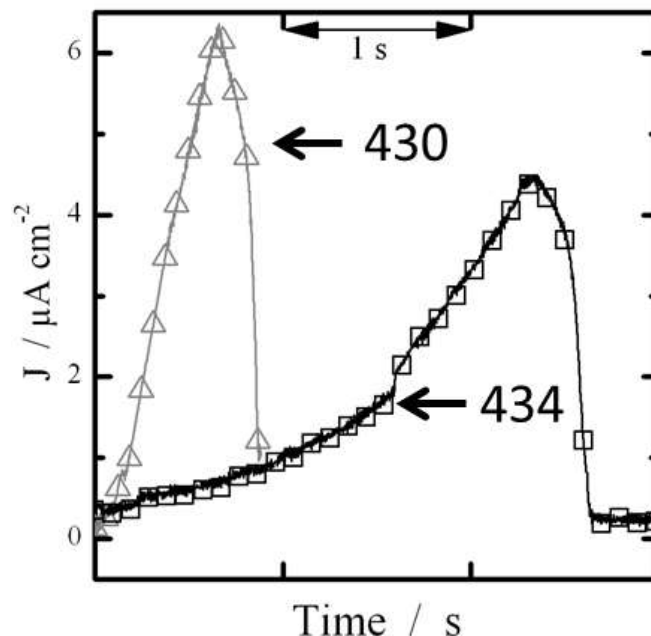


Figure 3.7 - Time records of metastable pit transients taking place at 430 (Δ , gray) and 434 (\square , black) grades at pH 10. Both samples polarized at +500 mV with respect to their open circuit potential. Transients were shifted so as to coincide their initiation at an arbitrary time origin. Sample frequency 1000 Hz [19].

From these results, we can conclude that Mo effect on pitting corrosion of ferritic SS is more likely due to a hindered pit initiation than due to kinetic aspects related to the modification of alkaline electrolyte composition as proposed in the case of acidic solutions as reported by the literature [25].

3.3. EFFECT OF Mo ADITION ON PITTING POTENTIAL OF LABORATORY SS IN FUNCTION OF pH

From a strict point of view, the concomitant differences of several alloying elements in the industrial heats preclude any unambiguous interpretation that could ascribe to Mo only the different behaviors described up to now. Thus, as previously mentioned, a full set of experiments has been performed with laboratory heats.

In this sense, as well as for the industrial materials, the role of Mo on the pitting corrosion resistance of lab heats was instigated from acidic to alkaline conditions in the presence of ions Cl⁻ by electrochemical polarization measurements. As said before, with these lab alloys, we will be capable of associated the corrosion behaviors of these SS with their Mo concentration only. Fig. 3.8 shows the typical polarization curves obtained for 18Cr12Ni, 18Cr12Ni1Mo, 18Cr12Ni2Mo and 18Cr12Ni3Mo SS in different pH conditions pH 2, 4, 7, 10, 12 and 12.6.

The polarization curves presented at Figs 3.8 a), b) and c) illustrate the huge positive effect of Mo on the pitting corrosion resistance of laboratory austenitic grades in acidic and neutral chloride environments (pH 2, 4 and 7). In these conditions, even with only 1% Mo addition on the austenitic matrix, the passive range and the E_{pit} substantially increased compared to 18Cr12Ni SS. For alkaline solutions, however, this positive effect of Mo was not so clear, as shown by Figs. 3.8 d), e) and f). For example at the pH 10 (Fig. 3.8 d)), the presence of Mo shifted the E_{pit} for noble values without changing the passivation plateau, so the breakdown passivity potential was almost the same for all lab austenitic SS in this condition. Moreover, in a higher pH 12, this beneficial influence of Mo on shifting the E_{pit} was very small even when 3% of Mo was added on the bulk composition (see Fig. 3.8 e)). Finally, at pH 12.6, any austenitic lab SS presented pitting attack, as the oxygen evolution of the solution happens before the corrosion attack.

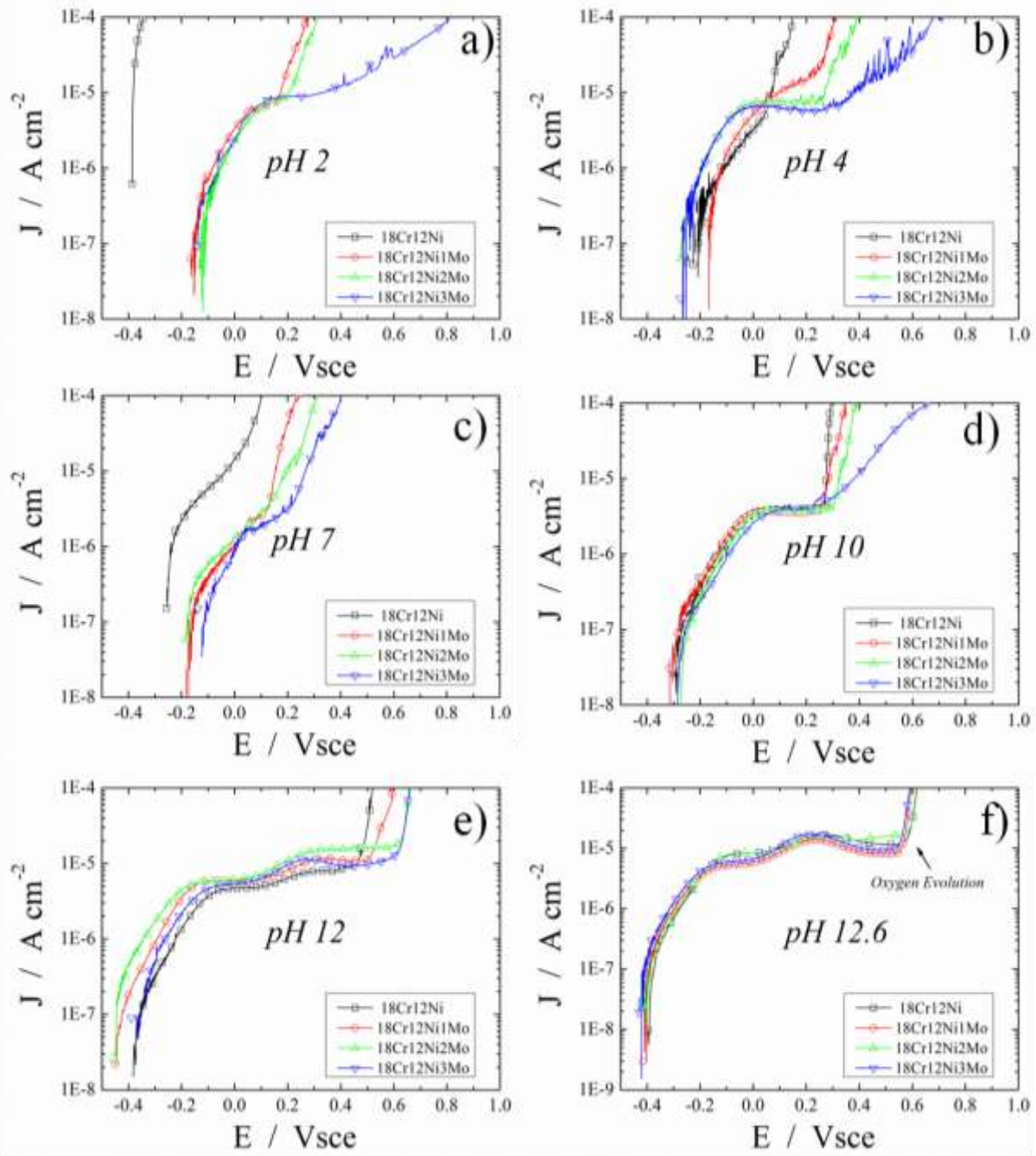


Figure 3.8 - Polarization curves obtained for lab austenitic at several media: **a)** pH 2; **b)** pH 4
c) pH 7, **d)** pH 10, **e)** pH 12 and **f)** pH 12.6 at 25°C.

The E_{pit} and E_{corr} values for all austenitic lab SS are summarized in Table 3.2. The influence of Mo could be simply observed in this table by comparing these values for the different Mo contents at a same pH. For example, at pH 4, Mo addition shifted E_{pit} values for more noble values, from 0.108 to 0.244 V_{sce} for 1%Mo addition, from 0.108 to 0.381V_{sce} for 2%Mo addition, and from 0.108 to more than 0.758V_{sce} for 3%Mo addition. Mo seems to have also a positive effect on the E_{corr} of austenitic lab SS at acidic and neutral media, because the Mo addition appears to increase the E_{corr} in these conditions whereas it has no

effect in alkaline solutions. As well as for the industrial materials, the repassivation potential E_{rep} was not reproducible for the lab alloys, so that the effect of Mo on those values was not discussed here. It is worth noticing that E_{corr} values are the average between 3 experimental results at least, and the standard error is about 40mVsc.

Table 3.2 - E_{pit} and E_{corr} values (mVsc) for the industrial SS at different pH conditions.

Material	pH2		pH4		pH7		pH10		pH12	
	E_{corr}	E_{pit}								
18Cr12Ni	-385	X	-211	108	-283	137	-298	320	-390	530
18Cr12Ni1Mo	-179	282	-192	244	-190	288	-308	371	-423	564
18Cr12Ni2Mo	-165	426	-241	381	-194	351	-283	398	-426	623
18Cr12Ni3Mo	-174	749	-239	758	-165	414	-285	624	-388	660

Fig. 3.9 shows the ΔE_{pit} ($\Delta E_{pit} = E_{pit} \text{ for Mo containing SS} - E_{pit} \text{ for Free Mo SS}$) for industrial and lab austenitic alloys in order to verify the role of Molybdenum in function of different pH conditions. Firstly, it is clear that Mo has more or less a beneficial influence in all media for the lab heats. However, it is worth noticing that the Mo effect, represented by ΔE_{pit} , decays with the pH increase, which confirms the general tendency observed for industrial heats discussed before. It is important to mention another time here that the E_{pit} values in the present work were computed as the potential value for which the current density reached $100 \mu\text{A cm}^{-2}$, which constitutes in an experimental protocol largely employed in the literature [12, 28-31].

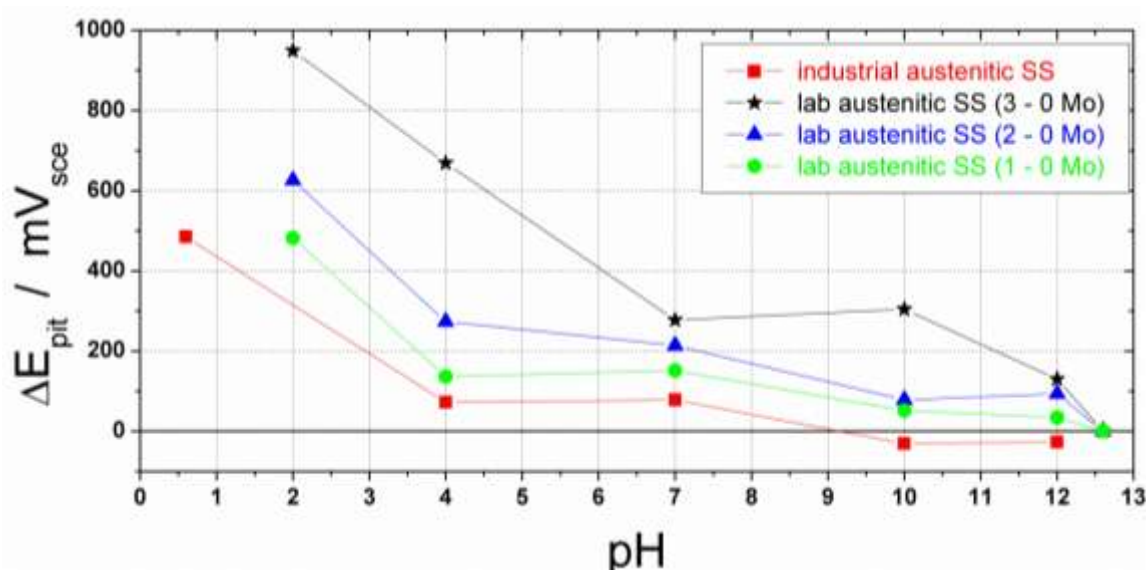


Figure 3.9 - E_{pit} difference (ΔE_{pit}) between Mo *containing* and Mo *Free* SS for the industrial and lab austenitic heats.

These results are in a good agreement with those found for the industrial austenitic grades as the Mo addition promotes a positive effect on acidic and neutral media but has mostly no or negligible effect in alkaline environments for both industrial and laboratory SS (cf Fig 3.9). The only difference between the industrial and lab heats is the fact that a “negative” effect of Mo was observed for industrial materials at alkaline conditions (inversion between 316 and 304SS at pH 10 and 12). This inversion which in fact indicate that the 304 behaves better than 316, could be explained by the fact that Mo effect is really small at alkaline conditions as shown in Fig 3.9, associated with the higher Cr content for the 304SS compared to 316SS in the case of industrial material (see Table 2.1). So, this difference in the Cr content on the chemical composition of industrial SS promotes a higher pitting corrosion resistance for the 304SS at alkaline media, where Mo has almost no effect.

Fig. 3.10 a) and b) present a MnS inclusion and the first step of pitting corrosion for the 18Cr12Ni3Mo SS at pH 10 solution, respectively.

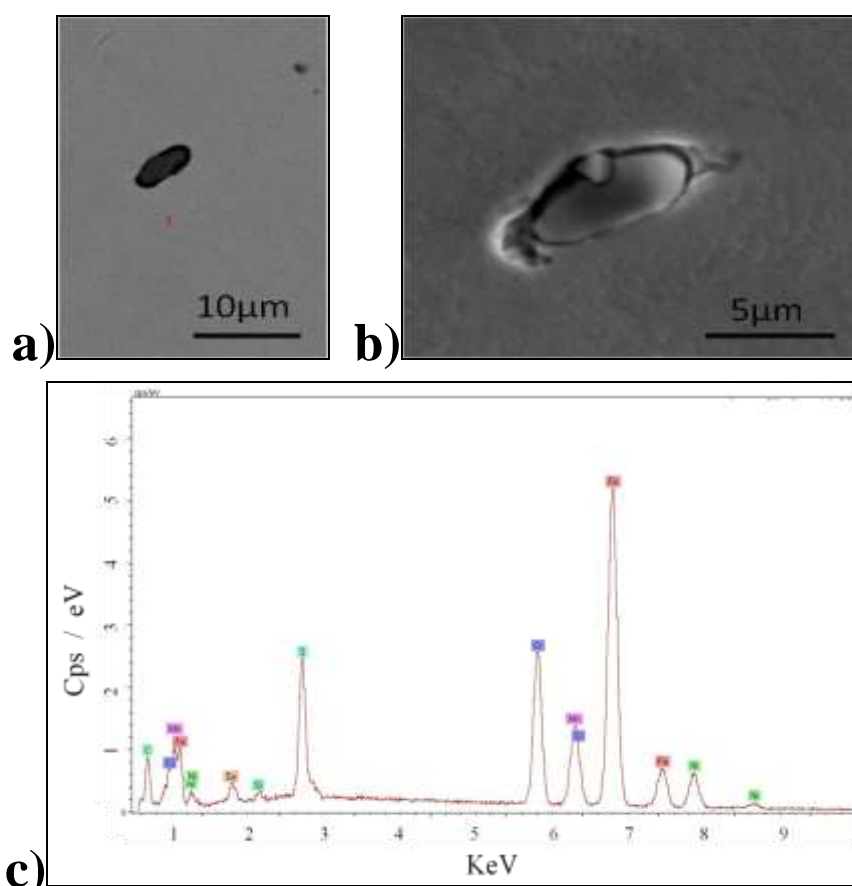


Figure 3.10 – a) MnS inclusion, b) the first step of pitting attack at pH 10 solution and c) EDX spectra of the MnS inclusion for the 18Cr12Ni3Mo SS.

These pictures show that pitting initiation for this material can also be triggered around the MnS inclusions, as already observed in acidic and neutral media [11, 12, 23, 24].

Moreover, some authors [24, 32-34] claimed for the alloying element influence on the inclusion composition (Mo could be trapped in the inclusion) and on its susceptibility to be dissolved in different solutions, but no trace of Mo was found in the sulphides inclusions for the austenitic lab SS, as shown by the EDX spectra illustrated on Fig 3.10 c). Therefore, Mo mechanism on pitting attack initiation can not be associated neither to a change of the inclusion composition nor to an increase of the inclusion stability in different pH.

Fig. 3.11 shows the anodic polarization measurements for ferritic lab grades at four different pH. From these experiments, we can clearly see the positive effect on the pitting corrosion of ferritic SS. The E_{pit} was more than 200mV_{sce} higher for the 18Cr3Mo SS compared to the 18Cr SS even at alkaline pH (pH 10) whereas the E_{corr} was almost the same in the presence or absence of Mo.

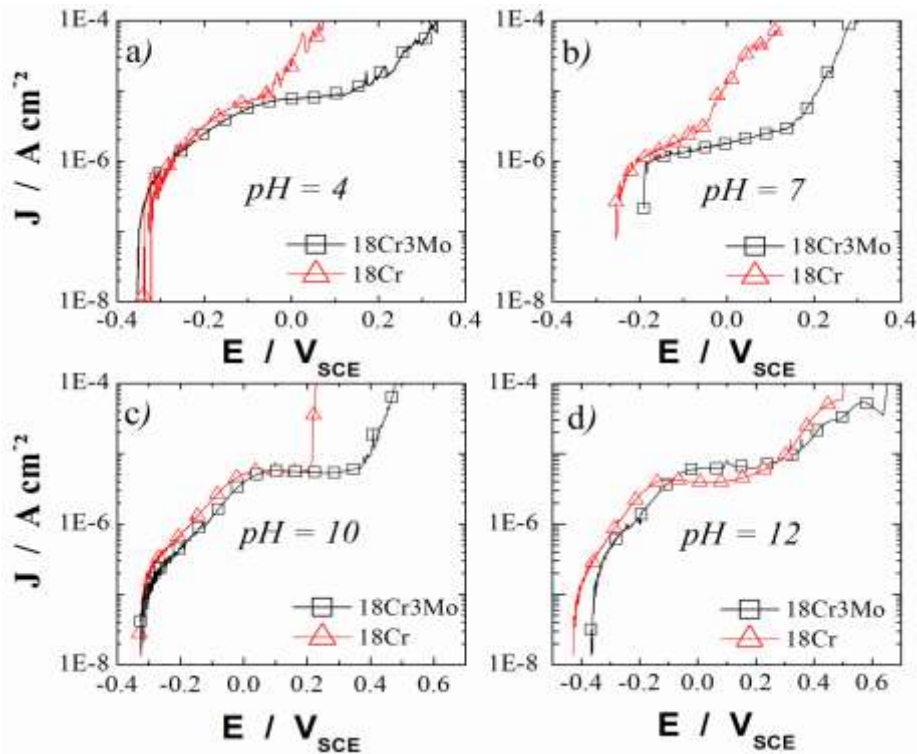


Figure 3.11 - Polarization curves obtained for 18Cr (red Δ) and 18Cr3Mo (black \square) heats in different pHs of chloride solution: **a)** pH 4; **b)** pH 7 **c)** pH 10 and **d)** pH 12 at 25°C.

For the ferritic SS, all results are just typical examples of a quite reproducible behavior between industrial and laboratory heats with respect of Mo role on the pitting corrosion resistance, which was always positive for any media for both materials. The influence of Mo was more evident on the results presented by the lab heats than those for industrial ones (see section 3.2). The E_{pit} difference between the Free Mo and Mo containing ferritic alloys was about 250mV_{sce} and about 50mV_{sce} for lab and industrial alloys,

respectively. These results could be easily associated with the higher Mo addition on lab heats (3%Mo) so that they presented a greater pitting corrosion resistance.

Fig. 3.12 a) and b) illustrate the pitting attack on the 18Cr SS and 18Cr3Mo SS after dynamic polarization experiment at pH 10 solution. The pit morphology is almost the same in the presence or absence of Mo on the bulk composition. The pits normally spread from the inclusions and propagate under the metal surface. In certain places, the attack will reach the surface giving rise to an irregular network, as shown in Fig 12, because of the passivity breakdown caused by the impoverishment of the passive layer around of the inclusions or precipitations [23].

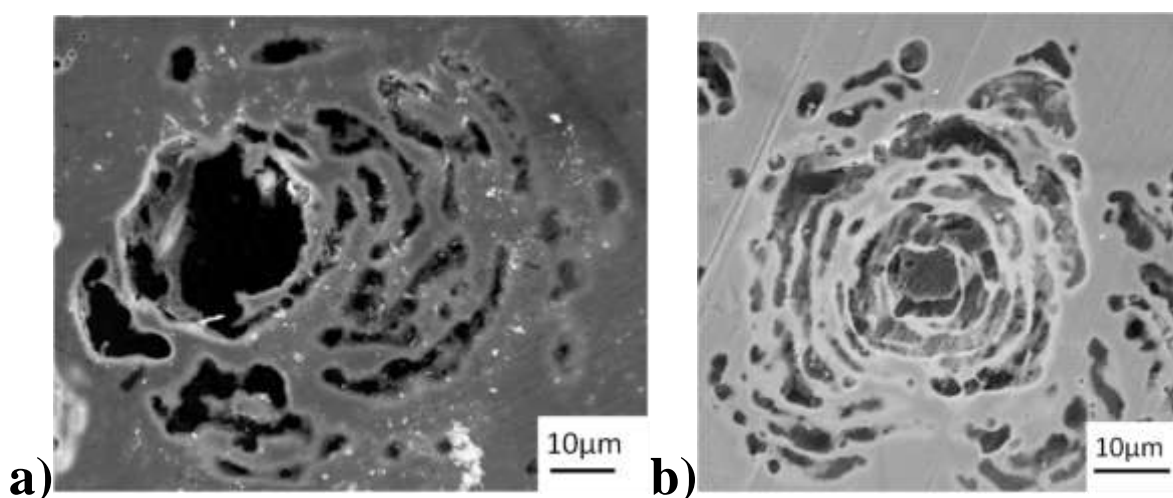


Figure 3.12 - Pitting attack morphology of the a) 18Cr SS and b) 18Cr3Mo after dynamic polarization experiment at pH 10 solution at 25°C.

As far as the corrosion resistance is concerned, the difference of Mo influence for austenitic (no effect) and ferritic SS (positive effect) at alkaline media is probably due to their crystalline structure. The austenitic SS has a Face Centered Cubic FCC structure whereas the ferritic SS has a Body-Centered Cubic BCC structure. Thus, in the FCC structure the atoms can pack closer together than they can in the BCC structure and consequently the atomic bonds are stronger for the FCC crystals [35], and in our case, for the austenitic SS. One possible explanation for the best results obtained with ferritic grade should hence be that Mo atoms could act easier for the ferritic SS than austenitic ones during all pitting corrosion steps by quickly passing to the passive layer or directly to the aggressive solution formed within a pit. Afterwards, it would trap Cl^- or precipitate as oxides as suggested in the literature [11, 12, 41].

The beneficial effect of Mo addition on pitting corrosion resistance was also detected for lab DSS as can be observed at Fig 3.13. For a fixed pH the presence of Mo shifted E_{pit} values to more noble values and increased the passive range. Taking the pH 10 electrolyte as an example, and noting that this is the one for which the Mo effect is less pronounced, E_{pit} is shifted from 0.510 to once again more than 0.830V_{SCE} (potential at which occurs the oxygen evolution), as shown in Fig. 3.13 c). In the high alkaline pH (pH 12), neither 23Cr4.6Ni SS nor 23Cr4.6Ni3Mo SS was attacked, so the current increase presented at Fig 3.13 d) is due to oxygen evolution.

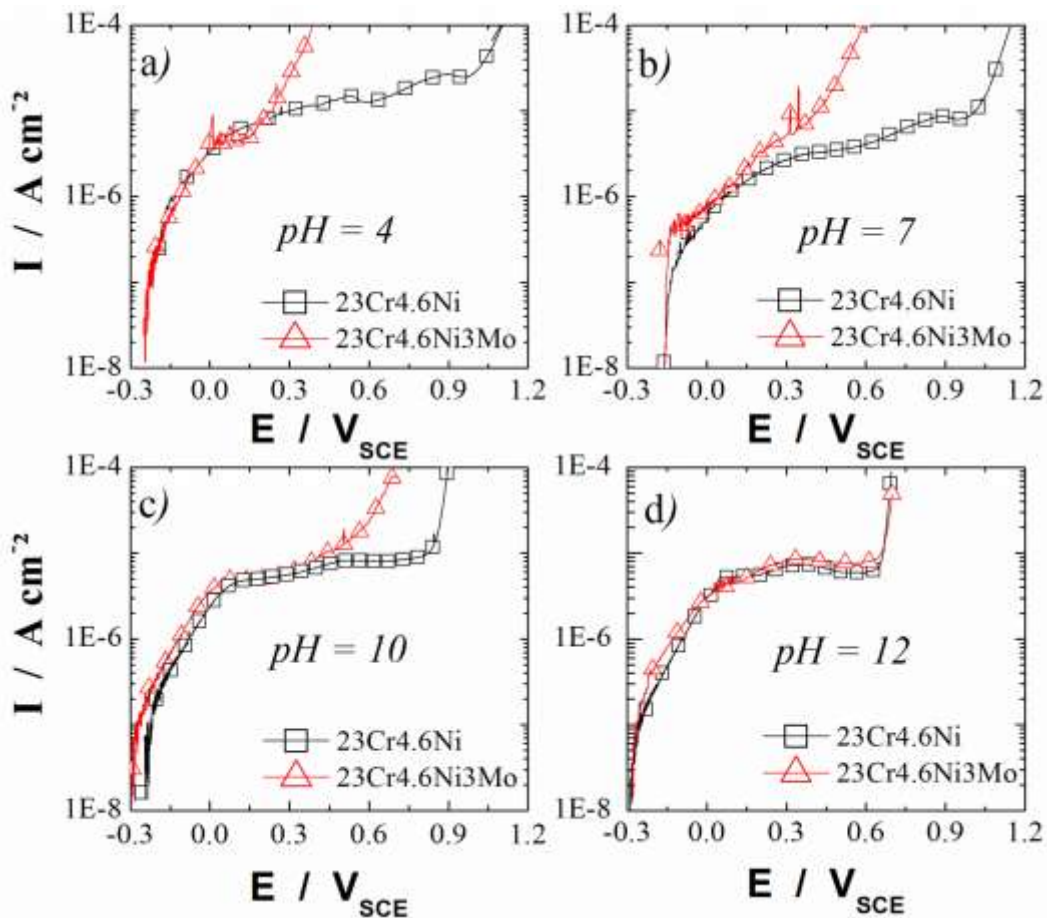


Figure 3.13 - Polarization curves obtained for 23Cr4.6Ni (red Δ) and 23Cr4.6Ni3Mo (black \square) duplex SS in different pHs of chloride solution: a) pH 4; b) pH 7 c) pH 10 and d) pH 12 at 25°C.

As far as the Mo addition on lab heats is concerned, it is clearly beneficial for the pitting corrosion resistance of all SS, except for the austenitic lab SS at alkaline pH. Moreover, these behaviors can not be associated with any metallurgical defects or another alloying element as the only difference between the lab grades of each SS family was the amount of molybdenum. Furthermore, the increase on the pitting corrosion resistance of

DSS containing Mo at alkaline conditions can be undirected associated with the ferrite phase pitting resistance since the positive effect of Mo was only reported to the pure ferritic lab SS and not for the austenitic one.

3.4. INFLUENCE OF Mo ADDITION ON EACH PHASE OF DUPLEX STRUCTURE

Fig. 3.14 shows SEM pictures of general and pit corrosion for Free-Mo and Mo containing industrial DSS under chloride acidic conditions at high temperature (pH 0.6 at 75°C) after polarization experiments until $40\mu\text{A cm}^{-2}$.

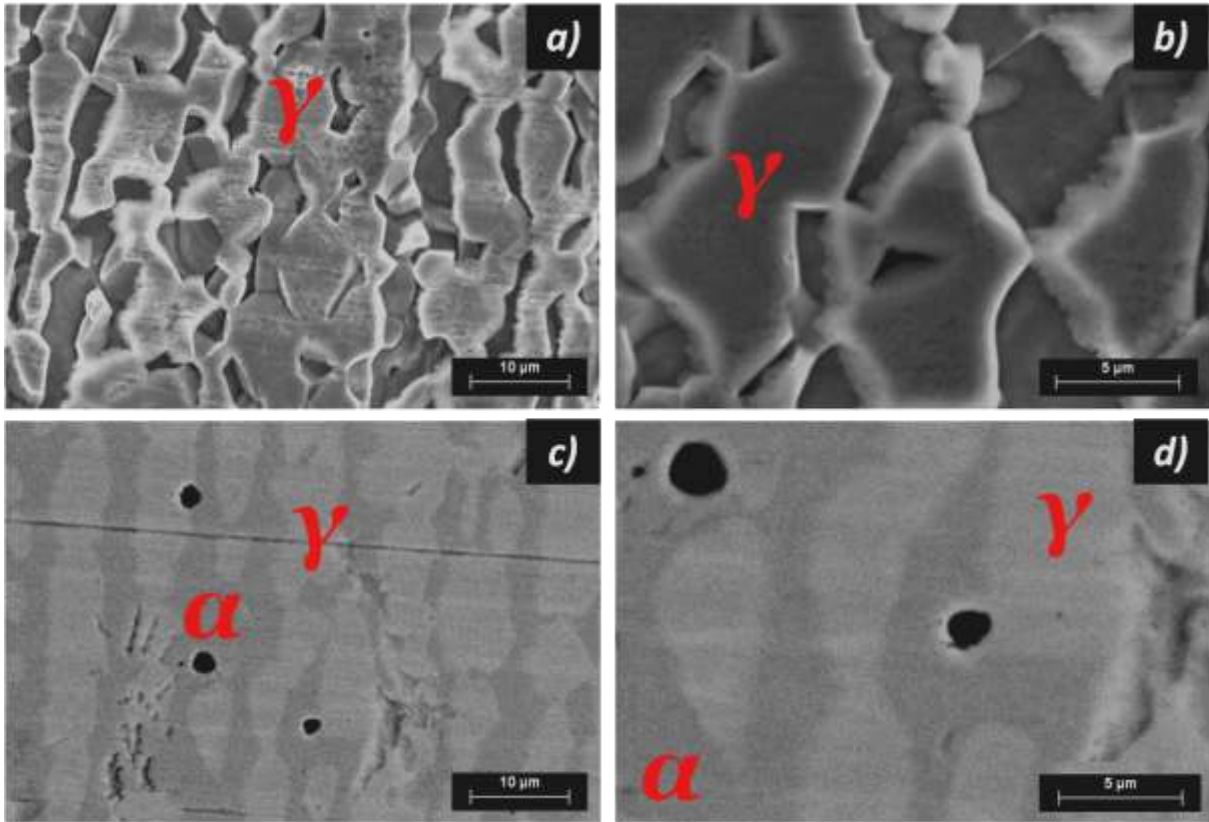


Figure 3.14 - Back scattered SEM images from corrosive attacks at chloride acidic conditions for different samples: **a)** 2000x and **b)** 5000x images of 2304 at pH 0.6 showing austenite grains (lighter gray) left after ferrite grains (darker gray) have been dissolved. : **c)** 2000x and **d)** 5000x images of 2205 at pH 0,6 showing pit initiation at the ferrite phase and also austenite.

The pictures 3.14 a) and b) show the general corrosion of the ferrite phase of the 2304 SS at this acidic medium (pH 0.6). The ferrite grains appeared to be completely dissolved whilst austenite grains remained much less attacked. For the 2205 SS, however, pit propagation is strongly hindered in the ferrite phase and then localized attack appeared to

split between the two phases (see Figs. 3.14 c) and d)). These results indicate a beneficial effect of Mo on both phases as the corrosion attack passes from general corrosion morphology for 2304 duplex SS to a localized corrosion morphology for 2205 duplex SS, even though the improvement is more representative for ferrite phase.

The same analyses were done with laboratory heats in order to confirm the results found out for the industrial DSS, as shown in Fig 3.15. The general corrosion for 23Cr4.6Ni and pit corrosion for 23Cr4.6Ni3Mo lab DSS under chloride acidic conditions at high temperature (pH 0.6 at 75°C) after polarization experiments until $40\mu\text{A cm}^{-2}$ can be easily observed. The picture 3.15 a) shows that the ferrite phase was totally corroded while austenitic grains remained much less attacked in the absence of Mo on the bulk composition. The general feature looks like corrosion of ferrite and only localized corrosion of austenite. If we go further with the analyses and we imagine the Fig. 3.15 a) in 3D dimensions, it seems that the corrosion attack propagated in the ferrite phase but when the corrosion front reached the austenite phase in subjacent grains of the duplex microstructure, the corrosion attack was stopped since this phase is much more resistant. However, for 23Cr4.6Ni3Mo, pit propagation is strongly hindered in the ferrite phase and then localized attack appeared to split between the two phases as shown in Fig. 3.15 b). These results for the lab DSS are exactly the same to those found for 2304 and 2205 SS in Figs. 3.14.

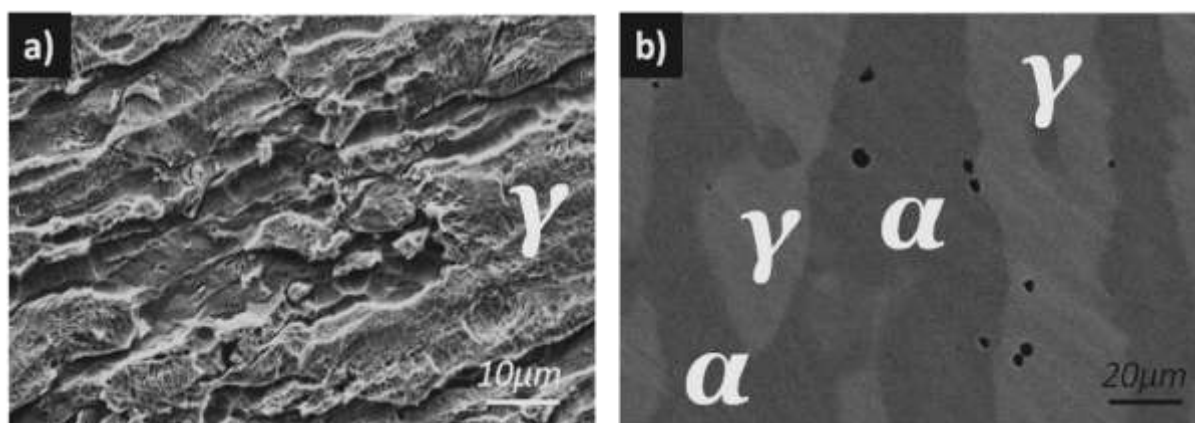


Figure 3.15 - Back scattered SEM images from corrosive attacks at chloride acidic conditions for different samples: **a)** 23Cr4.6Ni images and **b)** 23Cr4.6Ni 3Mo images at pH 0,6.

The SEM results are however even more pronounced in the pitting corrosion attack on alkaline media at 75°C after polarization experiment up to $40\mu\text{A cm}^{-2}$. For 2304 SS, pits are, as expected, initiated in the less resistant ferrite phase as shown by Figs. 3.16 a) and b). On the other hand, in the presence of Mo, the scenario is reversed. The ferrite becomes much

more resistant and pits were now almost exclusively located at the austenite grains, as can be seen in Figs. 3.16 c) and d). This kind of pits was more occluded with a dimension of $\approx 2\mu\text{m}$, which is consistent with the results found by *Deng et al.* [29].

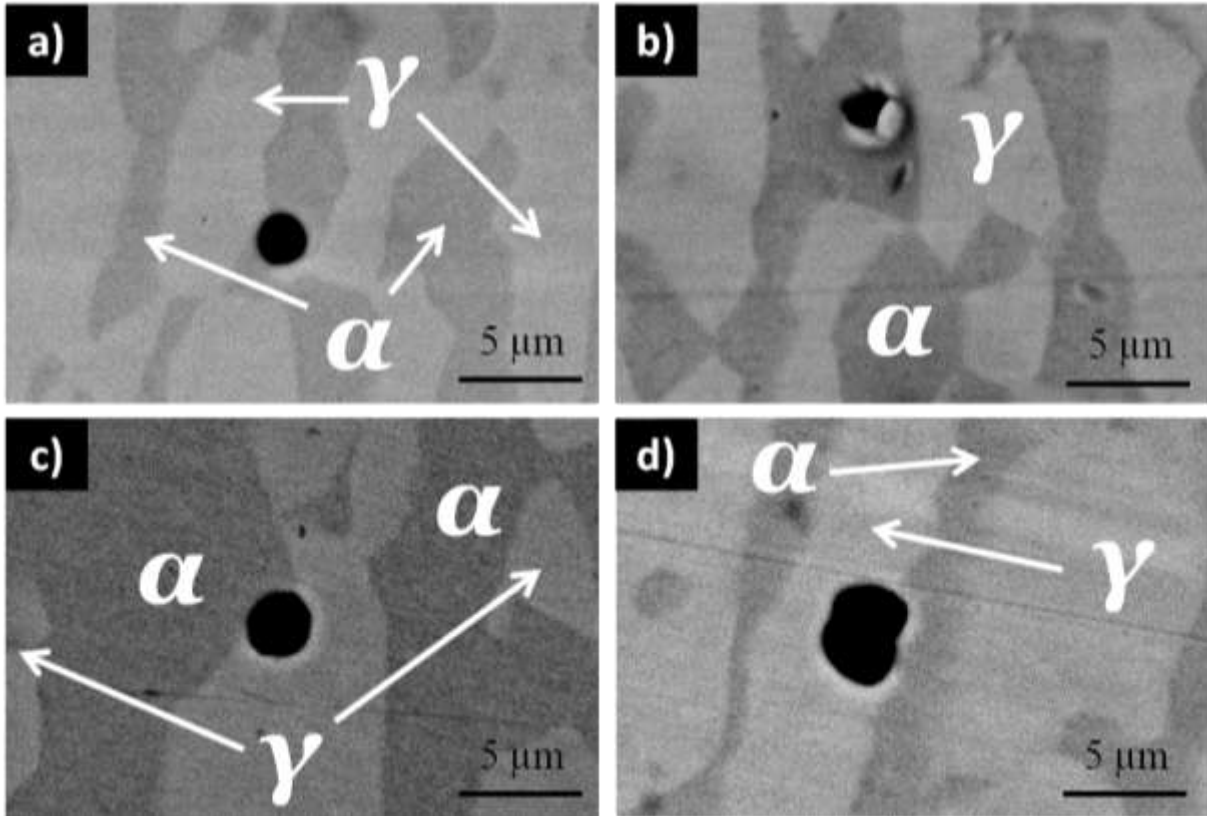


Figure 3.16 -. Back scattered SEM images from corrosive attacks at chloride alkaline conditions for different samples: pictures **a)** and **b)** of 2304 at pH 10 showing pit nucleation at ferrite; **c)** and **d)** of 2205 at pH 10 showing pit nucleation at austenite.

After continuing corrosion attack by making a polarization until $1000\mu\text{A cm}^{-2}$ at alkaline conditions, the ferrite phase definitely shows better corrosion resistance for the 2205 DSS as presented by Fig. 3.17. Indeed, the periphery of the big pit reveals an attack profile characterized by the preferential hammering of the austenite phase whilst the ferrite grains seem to locally pin down the pit propagation (Fig. 3.17 a)). On the more zoomed pictures of the pitting attack on the 2205 DSS (3.17 b) and c)), pit is not only initiated at the austenite but also propagates inside it before eventually eating into the adjacent ferrite. This scenario of enhanced ferrite phase corrosion resistance by addition of Mo on the bulk alloy can of course drastically change in the presence of sigma phase (δ) precipitates, as this precipitation is located at ferrite and impoverishes its Cr and Mo contents [36].

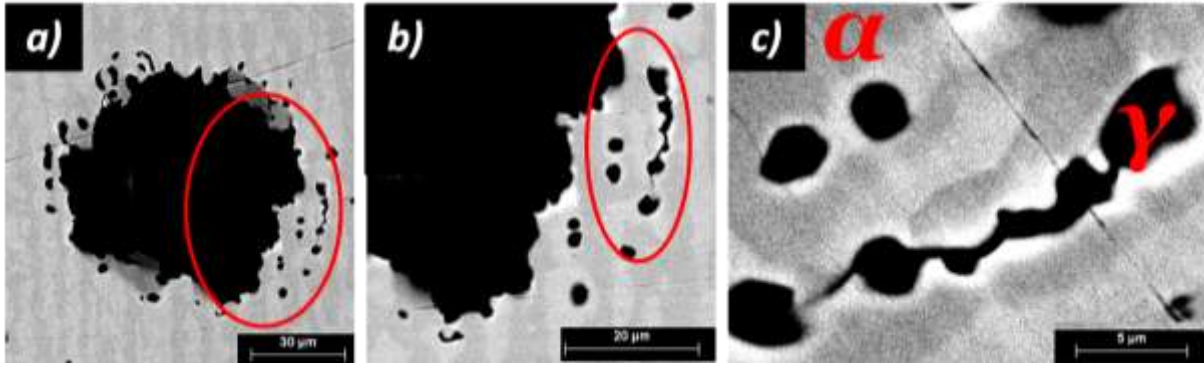


Figure 3.17 - Back scattered electrons SEM images from 2205 after polarization up to $1000\mu\text{A cm}^{-2}$ on pH 10 solution at 75°C . **a)** 700x , **b)** 1500x and **c)** 5000x images. The zoomed areas are marked with the red line in the images **a)** and **b)**).

These results were first obtained with industrial grades, but the same kind of experiments followed by SEM observations was reproduced with the laboratory samples for which the overall compositions were better controlled. Results fully confirmed the better ferrite resistance and the consequent shift of pit nucleation and propagation to austenitic grains. Fig. 3.18 shows SEM images of the etched surface of lab DSS after polarization experiments (up to $40\mu\text{A cm}^{-2}$) in simulated concrete pore solution at 75°C . For the 23Cr4.6Ni, pits are, as expected, preferentially nucleated in the usually less resistant ferrite phase as shown in Fig. 3.18 a). For the 23Cr4.6Ni3Mo, however, ferrite gets much more corrosion resistant so that it overtakes the usually more resistant austenitic phase. The pit nucleation is hence mostly shifted to the austenitic microstructure as seen in Fig. 3.18 b).

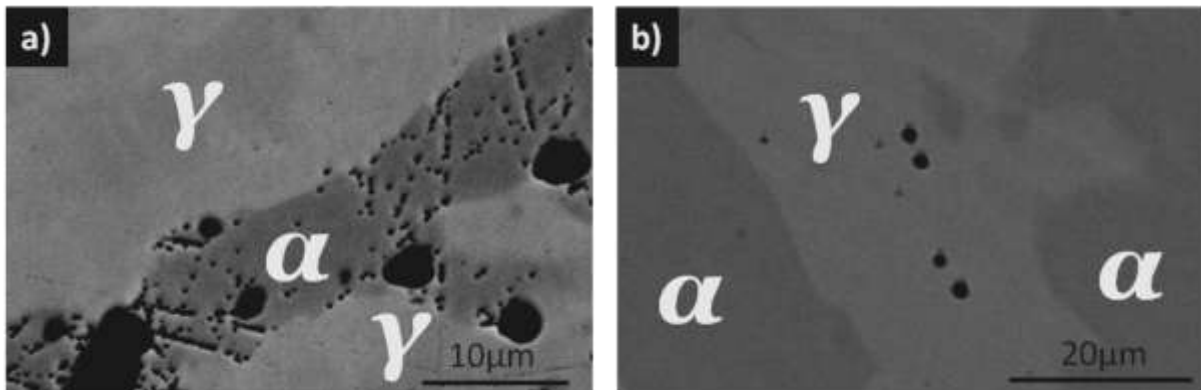


Figure 3.18 – Back scattered electrons SEM images from **a)** 23Cr4.6Ni and **b)** 23Cr4.6Ni3Mo DSS after polarization measurements in simulated concrete pore solution (pH 10) at 75°C up to $40\mu\text{A cm}^{-2}$. The major influence of Mo on the ferrite phase was clearly observed in these conditions.

Fig. 3.19 illustrates this issue with the help of more pronounced polarization protocols (up to $1000\mu\text{A cm}^{-2}$). It can be seen that in the absence of Mo (Fig. 3.19 a)), ferrite grains are

completely corroded whilst austenite grains remained intact. The addition of Mo induced the inversion of that scenario (Fig. 3.19 b)). Pits were now not only nucleated at the austenitic phase as seen in Fig. 3.19 b), but propagated throughout the austenitic grains, leaving the ferritic grains almost completely undamaged, hence confirming the results from industrial SS and highlighting the strong effect of Mo in the ferrite phase [19-21, 37].

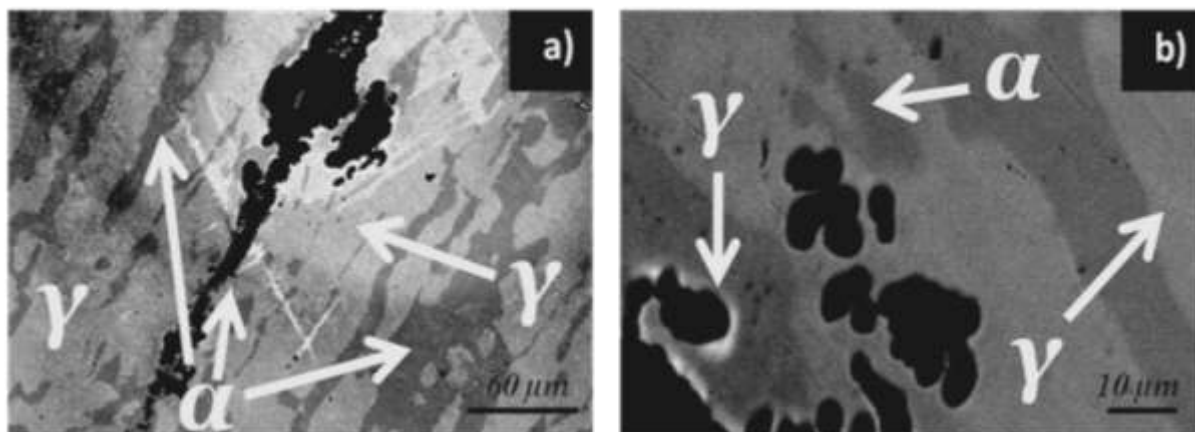


Figure 3.19 – Back scattered electrons SEM images from a) 23Cr4.6Ni and b) 23Cr4.6Ni3Mo lab DSS after polarization measurements in simulated concrete pore solution (pH 10) at 75°C up to 1000 $\mu\text{A cm}^{-2}$. The major influence of Mo on the ferrite phase was clearly observed in these conditions.

This indirect evidence of the role of Mo was confirmed by a metallurgical analysis. A calculation of each phase composition using Thermocalc[®] software confirmed that for the 2205 steel and 23Cr4.6Ni3Mo lab SS, Mo is preferentially dissolved into the ferrite phase (about 3.4%) that hence has its corrosion resistance improved compared to the austenite phase which contains less Mo (about 2.2%). More importantly, this better ferrite behavior cannot be ascribed to different Cr contents in free-Mo alloys and Mo-containing steel since their Cr contents were roughly the same (see Table 3.3). Results obtained from Thermocalc[®] have been complemented by wavelength-dispersive spectrometer (WDS) as seen in Table 3.3. WDS values are in full agreement with those obtained from theoretical estimations and confirm the preferential Mo dissolution in ferrite.

As mentioned before, PREn calculations should be handled carefully particularly in experimental conditions far from those from which the empiric expressions have been derived. At first glance, pitting potential results seem to be in good agreement with the bulk alloy PREn calculations, which are about 10 points higher in the presence of Mo for

industrial and laboratory heats, as shown in Table 2.1 and Table 2.2, respectively. It confirms the first idea of the positive effect of Mo on the pitting corrosion resistance given by PREn expression (1- 9). However, a sharper analysis of Table 3.3 results points out an important deviation from the PREn estimates. Indeed, comparing the PREn values for austenite and ferrite of each DSS, the α phase clearly has a higher PREn value in both cases: absence and presence of Mo. Taking only the PREn values into account, as done in Refs [2, 28-30, 38-40], pits would have to have initiated in the austenite for all DSS in all tested solutions and not only in the presence of Mo, as discussed before at Figs 3.16, 3.17, 3.18 and 3.19. Thus, as seen above, both microstructural and electrolyte variables are of major concern in the corrosion resistance of steels exposed to different media, although the PREn expression does not really reflect the same.

Table 3.3 – Thermocalc® calculations and WDS measurements of the Mo, Cr and N composition in austenite and ferrite for the industrial and lab DSS and also their PREn values.

	Material	Phase	Elements (wt. %)			
			Cr	Mo	N	PREn
Thermocalc	2304	α	25.19	0.356	0.031	26.86
		γ	20.41	0.226	0.216	24.61
	23Cr4.6Ni	α	26.09	0.020	0.033	26.68
		γ	21.38	0.012	0.249	25.41
	2205	α	25.32	3.395	0.028	36.97
		γ	20.34	2.162	0.283	31.99
	23Cr4.6Ni3Mo	α	24.34	3.582	0.036	36.73
		γ	21.30	2.300	0.369	34.80
WDS	2304	α	24.55	0.360	0.043	26.44
		γ	20.75	0.236	0.27	25.85
	23Cr4.6Ni	α	25.53	0.033	0.026	25.94
		γ	21.73	0.028	0.202	24.97
	2205	α	25.06	3.462	0.043	37.16
		γ	21.29	2.156	0.318	33.49
	23Cr4.6Ni3Mo	α	24.31	3.638	0.043	37.00
		γ	21.66	2.360	0.337	34.84

These results confirm the major role of Mo in DSS which can be used as rebar in severe conditions. As mentioned before, attention must be paid however to the deleterious effect related to the presence of sigma phase precipitates that can, since they preferentially precipitate at the ferrite microstructure, seriously compromise the beneficial role of Mo described above [18]. Sigma phase, therefore, has to be avoided through proper heat treatment.

Finally, both microstructural and electrolyte variables are of major concern in the late corrosion resistance of steels exposed to different media as seen above although the PREn expression does not encompass these factors.

3.5. CONCLUSION

For all alloys, there was a very good agreement between the laboratory and industrial heats with respect to Mo influence on pitting corrosion resistance in all pH conditions. The anomalous behavior of Mo addition found for austenitic SS was validated by the results from lab heats containing 0%, 1%, 2% and 3% of Mo on the bulk composition. This anomalous behavior has hence been confirmed to be due to a loss of Mo efficiency with pH for the austenitic grades so that eventual effects related to inclusions or other microstructural problems could be disregarded. The differences between the ferrite and austenite should be ascribed for instance to the fact that the less closed packed ferrite allows the Mo to be more easily released inside initiated pits or easily be incorporated to the passive film.

On the other hand, Mo presents a strong beneficial effect for both ferritic and duplex SS, which was totally confirmed by the results from the lab castings. It is shown that Mo has a strong positive influence on the pitting corrosion resistance of these SS in all studied chloride-rich media, especially in simulated concrete pore solutions. For the DSS, this beneficial effect is due to the huge increase of ferrite corrosion resistance thanks to Mo, as seen from SEM analyses for both industrial and also laboratory DSS. Indeed, in the absence of Mo the ferrite phase was attacked and in the presence of Mo, however, the austenite phase was corroded. This evidence of the stronger Mo effect on ferrite phase claimed by SEM observation was theoretically and experimentally confirmed by Thermocalc calculations and electron probe microanalyser (WDS) analyses, respectively. As a consequence, the overall corrosion resistance of Mo-containing DSS grades was increased. Thus, concerning the application of DSS as reinforcement bar in severe service conditions, the presence of Mo on the bulk composition has high beneficial and should not be neglected. Even though all these

results are indicating a better corrosion resistance of the ferrite phase in the presence of Mo during local depassivation of the duplex SS oxide layer caused by the Cl⁻ ions attack, the austenite phase plays a very important role on the DSS corrosion resistance when this material is submitted to friction and abrasion under aggressive corrosion situations. It's worth keeping this argument in mind as this point will be widely discussed by the SEM images and mainly by tribocorrosion experiments described in the next chapter.

As far as the Mo mechanism in alkaline solutions is concerned, this is more likely due to a hindered pit initiation than due to kinetic aspects related to the modification of electrolyte composition as proposed in the case of acidic solutions [25] and moreover it depends on the microstructure, ferrite (BCC) or austenite (FCC), as they have a high influence on the Mo ions diffusion [19-21, 37].

3.6. REFERENCES

- [1] G. Gedge, J. Construc. Steel Research. 64 (2008) 1194.
- [2] L. Zhang, Y. Jiang, B. Deng, W. Zhang, J. Xu and J. Li, Electrochimica Acta 54 (2009) 5387.
- [3] M.F. Montemor, A. Simões, M.G.S. Ferreira, M. Da Cunha Belo, Corros. Sci. 41 (1999) 17.
- [4] K. Sugimoto, and Y. Sawada, Corrosion Nace 32 (1976) 347.
- [5] K. Sugimoto, Y. Sawada, Corros. Sci. 17 (1977) 425.
- [6] D. Addari, B. Elsener and A. Rossi, Electrochimica Acta 53 (2008) 8078.
- [7] A. E. Yaniv, J. B. Lumsden., and R. W. Staehle. J. Electrochem. Soc. 124 (1977) 490.
- [8] H. Habazaki, A. Kawashima, K. Asami, and K.Hashimoto. Corrosion Science 33 (1992) 225.
- [9] K. Hashimoto, K. Asami, A. Kawashima, H. Habazaki, and E.Akiyama. Corrosion Science 49 (2007) 42.
- [10] M. W.Tan, E. Akiyama, H. Habazaki, A. Kawashima, k. Asami, and K. Hashimoto. Corrosion Science 39 (1997) 589.
- [11] A. Pardo, M.C. Merino, A.E. Coy, F.Viejo, R. Arrabal and E. Matykina, Corrosion Science 50 (2008) 780.
- [12] A. Pardo, M.C. Merino, A.E. Coy, F.Viejo, R. Arrabal and E. Matykina, Corrosion Science 50 (2008) 1796.
- [13] C. Lemaitre, A. A. Moneim, R. Djoudjou, B. Baroux and G.Beranger. Corrosion Science 34 (1993) 1913.
- [14] C. Lemaitre, B. Baroux, and G. Beranger. Corrosion Science 31 (1990) 585.
- [15] E. Chauveau, T. Sourisseau, B. Dermelin and M. Mantel, MEDACHS 08, International Conference in Coastal and Marine Environments (2008).

- [16] S.A.M Refaey, F. Taha, and A.M.A. El-Malak. *Applied Surface Science* 242 (2005) 114.
- [17] A. Bautista, G. Blanco and F. Velasco. *Cement and Concrete Research* 36 (2006) 1922.
- [18] A. Bautista, G. Blanco, F. Velasco, A. Gutiérrez, L. Soriano, F. J. Palomares and H. Takenouti. *Corrosion. Science* 51 (2009) 785.
- [19] T. J. Mesquita, E. Chauveau, M. Mantel, N. Kinsman and R.P. Nogueira. *Materials Chemistry and Physics*, 126 (2011) 602
- [20] T. J. Mesquita, E. Chauveau, M. Mantel, N. Kinsman and R. P. Nogueira. 10th Brazilian Stainless Steel Conference – International Edition., 2010.
- [21] T. J. Mesquita, E. Chauveau, M. Mantel, N. Kinsman and R. P. Nogueira. 61st Annual Meeting of the International Society of Electrochemistry, 2010.
- [22] V. Vignal, J.M. Olive, and D. Desjardins. *Corrosion Science* 41 (1999) 869.
- [23] G. S. Eklund. *J. Electrochem. Soc.* 121 (1974) 467.
- [24] B. Baroux. *Corrosion Science* 28 (1988) 969.
- [25] M. Kimura, M. Kaneko and N. Ohta, *ISIJ Int* 42 (2002). 1399.
- [26] M.H Moayed, and R.C. Newman. *Corrosion Science* 48 (2006) 1004.
- [27] W.J. Tobler, and S. Virtanen. *Corrosion Science* 48 (2006) 1585.
- [28] L. Zhang, Y. Jiang, B. Deng, W. Zhang and J. Xu, J. Li. *Materials Characterization* 60 (2009) 1522.
- [29] B. Deng, Y. Jiang, J. Gong, C. Zhong, J. Gao and J. Li, *Electrochimica Acta* 53 (2008) 5220.
- [30] B. Deng, Y. Jiang, J. Gong, C. Zhong, J. Gao and J. Li. *Electrochimica Acta*, 54 (2009) 2790.
- [31] M. Moreno, W. Morris, M. G. Alvarez, G.S. Duffó. *Corrosion Science* 46 (2004) 2681.
- [32] T. Sourisseau, E. Chauveau, and B. Baroux. *Corrosion Science* 47 (2005) 1097.
- [33] L. Sudesh, L. Wijesinghe and D. J. Blackwood. *Corrosion Science* 49 (2007) 1755.
- [34] D. E. Williams, M. R. Kilburn, J. Cliff, G. I. N. Waterhouse. *Corrosion Science*. 52 (2010) 3702.
- [35] W. D. Callister Jr. *Materials Science and Engineering - An Introduction*.
- [36] I. N. Bastos, S. M. Tavares, F. Dalard and R.P. Nogueira. *Scripta Materialia* 57 (2007) 913.
- [37] T. J. Mesquita, E. Chauveau, M. Mantel, N. Kinsman and R. P. Nogueira. Duplex World Conference, Baune 2010, 2010.
- [38] F. Zhang, J. Pan, and C. Lin. *Corrosion. Science* 51 (2009) 2130.
- [39] B. Deng, Y. Jiang, J. Gong, C. Zhong, J. Gao, L. Zhang, W. Zhang, and J. Li *Corrosion Science* 52(2010) 969.
- [40] B. Deng, Z. Wang, Y. Jiang, T. Sun, J. Xu, and J. Li. *Corrosion Science* 51 (2009) 2969.
- [41] V. Vignal, J.M. Olive, and D. Desjardins. *Corrosion Science* 41 (1999) 869.

CHAPTER 4

***THE INFLUENCE OF Mo ON
PITTING REPASSIVATION
PROCESS AND MOLYBDATE
INHIBITOR BEHAVIORS***

OUTLINE

4. THE INFLUENCE OF Mo ON PITTING REPASSIVATION PROCESS AND MOLYBDATE INHIBITOR BEHAVIORS	106
4.1. INTRODUCTION	106
4.2. A COMPARATIVE STUDY OF REPASSIVATION CURRENT TRANSIENTS	107
4.2.1. THE INFLUENCE OF Mo ADITION ON REPASSIVATION TRANSIENTS IN DIFFERENT pH	107
4.2.2. Mo EFFECT ON THE REPASSIVATION KINETICS	113
4.2.3. Mo EFFECT ON EACH PHASE OF DUPLEX SS AFTER MECHANICAL DEPASSIVATION	115
4.3. THE CORROSION INHIBITOR EFFECT OF MOLYBDATES IN FUNCTION OF pH	117
4.4. CONCLUSION	122
4.5. REFERENCES	123

4. THE INFLUENCE OF Mo ON PITTING REPASSIVATION PROCESS AND MOLYBDATE INHIBITOR BEHAVIORS

4.1. INTRODUCTION

It is well known that under the action of aggressive ions, i.e. chloride anion, local breakdown of passivity occurs, mainly at sites of local heterogeneities such as MnS inclusions, causing pitting corrosion [1-7]. The mechanism of pitting attack of stainless steel has been divided into four consecutive steps: initiation, metastable propagation, stable propagation, and repassivation of pits. The initiation step is mainly a local breakdown of the passivation oxide layer in presence of aggressive anions of the environment. The corrosion rate is increased by the fact that an even more aggressive environment is produced by the corrosion reaction itself. However, at the earlier stages of pit propagation, when the pits are still very small, they can be repassivated spontaneously. This stage is often referred as metastable pit growth. The stage of stable propagation is reached when spontaneous repassivation is no longer possible [3, 6, 8-10].

Molybdenum is considered as one of the principal alloying elements in stainless steels and its effect on corrosion resistance has been most thoroughly investigated. It is well known that Mo enhances the resistance to pitting corrosion and expands the passive region in neutral and acidic chloride solution [9, 11-22]. However, the complexity of the chemistry of molybdenum makes it rather difficult to determine the nature of its influence, mainly at alkaline conditions, where the data is not as available as in acidic media [23-26]. In these situations, Molybdenum presumably may have an effect on more than one step in a pitting event.

As far as the influence of Mo on repassivation kinetic of stainless steels is concerned, the main effect of Mo seems to be the decrease of the rate of dissolution in active zones by formation and retention of molybdenum oxyhydroxide or molybdates (MoO_4^{2-}) at these sites, as proposed by *Hashimoto et al.* [14, 15]. Furthermore, *Ogawa et al.* [27] suggested that Mo is first dissolved from the substrate, into the solution, and then oxidized to molybdate. In agreement with this, MoO_4^{2-} was detected in all passive films formed on Mo bearing alloys in acidic solutions [17, 28-30]. However, according to Pourbaix diagrams [31] (cf Fig 1.4), molybdate ions are thermodynamically unstable in acidic solutions, forming MoO_3 precipitate whereas MoO_4^{2-} is still stable in alkaline conditions.

Another alternative explanation for the effect of Mo on localized corrosion was provided by *Kimura et al. [32]*, who made direct *in-situ* measurements of the speciation of Mo in artificial corrosion pits using X-ray absorption spectroscopy. They measured the Mo K edge in pits grown in 1 M LiCl and 1 M LiBr and described the spectra as “quite similar to that of Na₂MoO₄ showing the formation of a complex similar to the network of [MoO₄(H₂O)₂]²⁻ “octahedra”, suggesting that the formation of such polymeric networks near the dissolving metal interface plays a significant role in the beneficial effect of Mo on the corrosion resistance of stainless steel.

In these contexts, the main objective of this chapter is to study the influence of Mo addition on the repassivation kinetics of different SS families under several chloride pH solutions, mainly in alkaline condition. For these studies, the tribocorrosion scratch test was employed for the different lab heats. A comparative analysis of the current transients, corresponding to the mechanical breakdown of the passive layer, was done in the absence and presence of Mo on the materials composition. Finally, the effect of Molybdates as a corrosion inhibitor in different pH solutions was discussed in order to have a better understand of the Mo mechanism in alkaline situations.

4.2.A COMPARATIVE STUDY OF REPASSIVATION CURRENT TRANSIENTS

4.2.1. THE INFLUENCE OF Mo ADITION ON REPASSIVATION TRANSIENTS IN DIFFERENT pH

In this section a comparison of the tribocorrosion results will be done as respect of the Mo role on the repassivation process of different SS. During the tribocorrosion tests, 20 mechanical depassivations were done and then the current peaks in the absence and presence of Mo were compared one by one.

Figs. 4.1 a) and b) illustrate the first and last current transients for the ferritic SS at acidic solution (pH4), respectively. From these Figs., a large beneficial effect of Mo addition on the repassivation for lab ferritic SS in acidic pH could be clearly observed. The role of Mo was very strong for these ferritic SS, firstly because of the difference on the initial and final current intensity during the first scratch test for 18Cr and 18Cr3Mo, which are about 70µA lower in the presence of Mo. Secondly, because the current intensity seems to decrease faster to 18Cr3Mo SS than to 18Cr SS.

Comparing Figs 4.1 a) and b), a higher I amplitude could be observed in the last peaks for both 18Cr and 18Cr3Mo materials, which is likely to be associated with the stronger wear of the surface at this late step of the tribocorrosion experiment. However, Mo played a positive role even in this high aggressive condition for the ferritic heats.

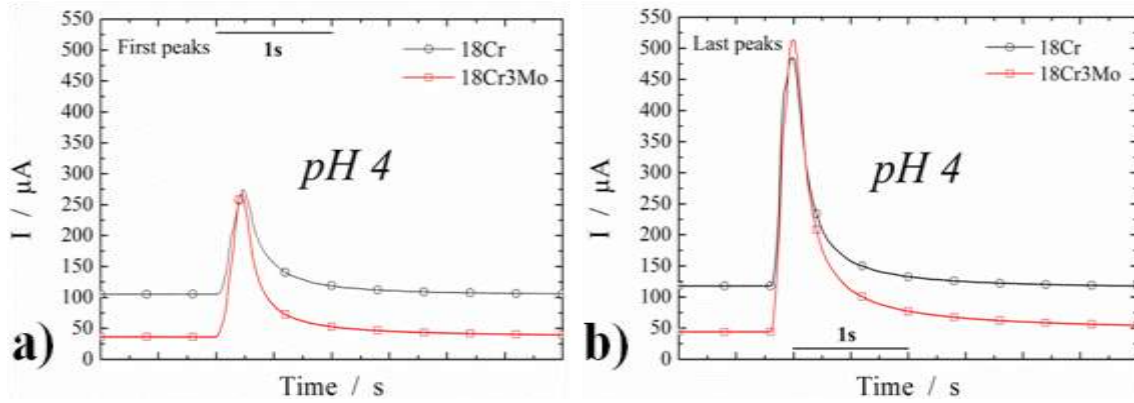


Figure 4.1 – Current transients of laboratory ferritic SS under acidic condition (pH 4) corresponding to the **a)** first and **b)** last scratch tests.

Mo addition also presented a positive effect on lab austenitic SS repassivation in this acidic medium (pH4). Figs. 4.2 a) and b) show the first and the last current transient corresponding to the mechanical depassivation of these alloys. Particularly, the 18Cr12Ni3Mo SS repassivation allows a final current intensity to be recovered compared to the 18Cr12Ni SS after both initial and final mechanical depassivations, which indicates a better repassivation tendency of austenitic in presence of Mo at acidic conditions.

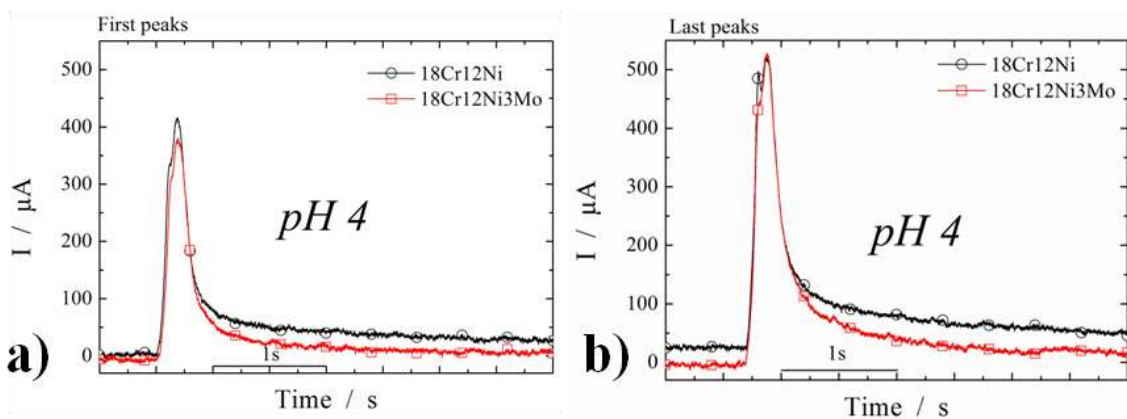


Figure 4.2 – Current transients of laboratory austenitic SS under acidic condition (pH 4) corresponding to the **a)** first and **b)** last scratch tests.

As said before for the ferritic SS, the maximum I values of last peaks were also higher than the first ones for austenitic samples. However, the difference between amplitudes of the

first and last peaks were more than 200 μ A for ferritic whereas it was about 100 μ A for the austenitic SS. This fact should be associated with the hardness of each SS family causing then a greater wear on the less hard (ferritic ones) after 20 tribocorrosion cycles. The Vickers hardness of each lab heat is given in Table 4.1. Mo clearly increased the hardness of all SS families

Table 4.1 – Vickers hardness of the lab heats.

Laboratory Material		Vickers Hardness
Austenitic	18Cr12Ni	866 HV
	18Cr12Ni3Mo	1066 HV
Ferritic	18Cr	717 HV
	18Cr3Mo	823 HV
Duplex	23Cr4.6Ni	1115 HV
	23Cr4.6Ni3Mo	1176 HV

The morphologies of the scratch trace for 18Cr12Ni and 18Cr12Ni3Mo after the tribocorrosion test are presented in Fig 4.3. SEM images of Figs. 4.3 a) and b) show the corrosion propagation inside the friction traces for the 18Cr12Ni SS at pH 4 condition whereas Figs. 4.3 c) and d) illustrated the much less attacked surface of the 18Cr12Ni3Mo.

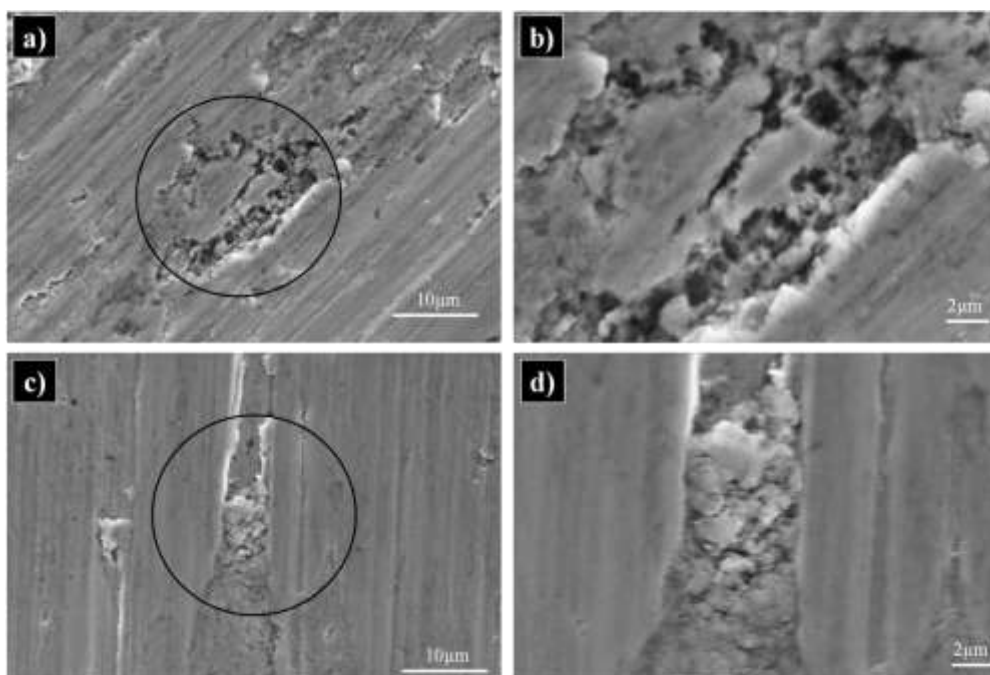


Figure 4.3 – SEM observation of: a) and b) 18Cr12Ni SS; c) and d) 18Cr12Ni3Mo SS after tribocorrosion experiment under acidic condition (pH 4).

Thus, the addition of Mo seems to have limited the pitting corrosion process after the mechanical depassivation, which was expected from the electrochemical results seen above. Moreover, in the presence of Mo, some products of the mechanical breakdown of the passivity (maybe Mo complex or molybdates) seem to be accumulated within the wear traces as clearly shown in Fig. 4.3 d). The deposition of these products in the cavities walls could have helped the repassivation of this material [3]. So, these SEM observations confirmed the positive effect of Mo on the repassivation process of austenitic SS at acidic conditions as illustrated by Fig. 4.2.

For the DSS, a positive influence of Mo on repassivation properties was also observed at pH 4 solution as illustrated by Fig. 4.4.

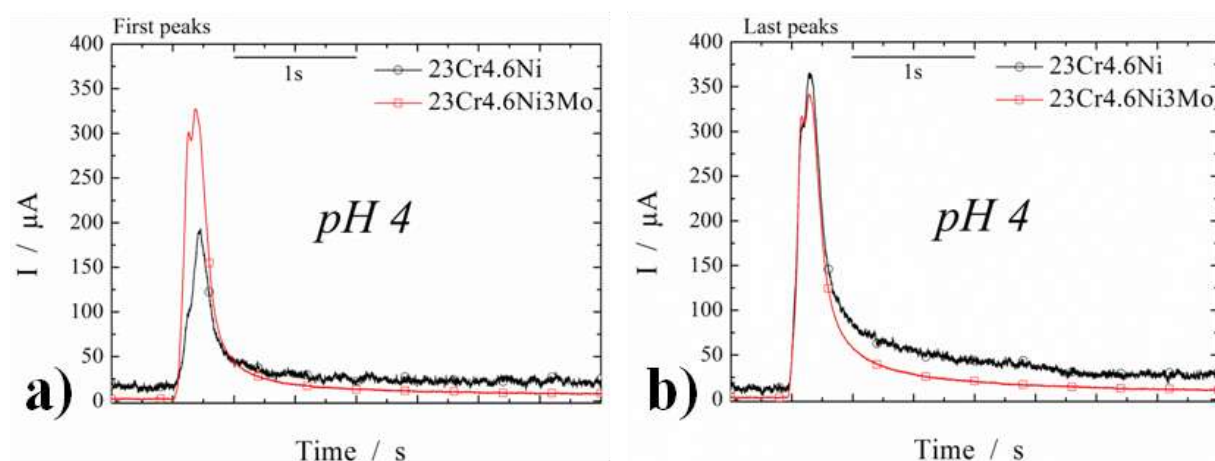


Figure 4.4 – Current transients of laboratory duplex SS under acidic condition (pH 4) corresponding to the a) first and b) last scratch tests.

The 23Cr4.6Ni3Mo SS repassivated until lower current intensities compared to 23Cr4.6Ni SS on both first and last current transients during the tribocorrosion tests. Moreover, the repassivation process seems to provide a more stable reconstruction of the passive layer in the presence of Mo since the maximum current intensities were almost the same at both the first and the last peaks for the 23Cr4.6Ni3Mo SS whereas this current intensity values increase more than 150 μA from the first to the last peak for the 23Cr4.6Ni SS.

The results presented in Figs. 4.1, 4.2, and 4.4 are in good agreement with some works about Mo mechanism in acidic environments reported by the literature [14, 15, 27, 32]. So, an hypothetical explanation for this positive role of Mo on the repassivation properties of SS at acidic media could be the following: - when the passivity of a Mo content SS is

mechanical broken down by the friction of the SS surface, a considerable quantity of Mo pass from the passive layer and also from the bulk material to the solution, creating then a high concentration of Mo ions within the wear's trace. These Mo ions might probably create molybdates or Mo complex in the solution [3, 33-37]. Consequently, a decrease on solution aggressiveness happens in the interface material/solution by the formation the complex such as MoO_3 or $[\text{MoO}_4(\text{H}_2\text{O})_2]^{2-}$, which promotes a quicker and more stable repassivation.

It is worth noticing that the Mo addition hardens the lab materials, as showed in Table 4.1. This difference on the mechanical properties of SS caused by Mo addition should certainly have an effect on the morphology of the wear trace after the scratch test. Normally, a softer material should present a larger trace. Consequently, a higher current intensity should be expected for the Mo-free SS due to a strong abrasion on their surfaces during the tribocorrosion measurement. However, this behavior was not found in our electrochemical results. For example, the 18Cr and 18Cr3Mo presented almost the same I amplitude in the first scratch test under acidic conditions (see Fig 4.1 a)), but if we only consider the Mo effect on the hardness, the 18Cr3Mo SS should have presented a smaller I compared to the 18Cr SS, which was not the case. So, for the interpretation of our tribocorrosion experiments, the corrosion properties of the materials seem to be predominant, which confirms our assumptions about the Mo effect on repassivation properties.

The Mo mechanism under acidic condition could be extended to chloride neutral solutions as the role of Mo at pH 7 condition was almost the same as those presented above for the pH 4 solution. Fig 4.5 shows the repassivation transients at pH7 solution for austenitic SS.

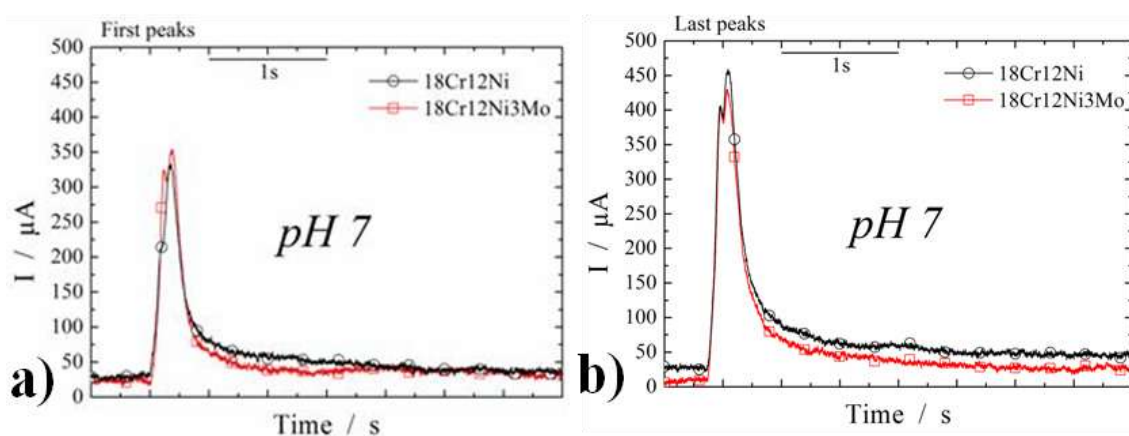


Figure 4.5 – Current transients of laboratory austenitic SS under neutral condition (pH 7) corresponding to the **a)** first and **b)** last scratch tests.

Fig. 4.5 illustrated once again that the repassivation transients reached lower I values in the presence of Mo for both first and last scratch test. However, this effect was much more evident for the experiments done under acidic conditions. This could be a new evidence of the monotonic loss of beneficial role of Mo for austenitic grades as the pH increases. The results from 18Cr, 18Cr3Mo, 23Cr12Ni, 23Cr12Ni3Mo in neutral conditions were very similar to those found for austenitic lab alloys so that they were not presented in this report.

As for the acidic and neutral conditions, the influence of Mo addition for the lab heats were also investigated at alkaline medium (pH 10). Firstly, the repassivation transients of 18Cr and 18Cr3Mo ferritic lab SS at this condition are shown in Fig. 4.6 and secondly those for the 18Cr12Ni and 18Cr12Ni3Mo austenitic lab SS are illustrated in Fig. 4.7. In these results from alkaline media, the positive effect of Mo seems to decrease and sometimes disappear for both materials.

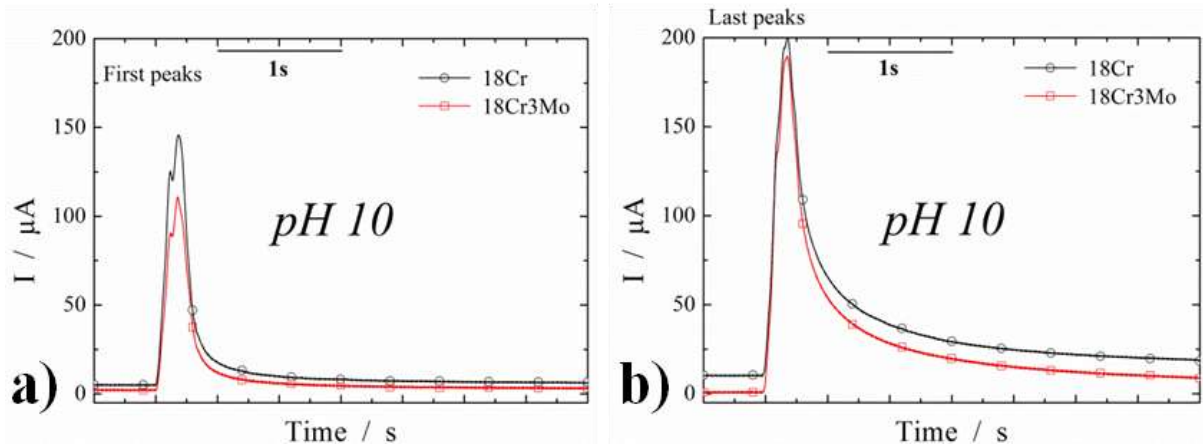


Figure 4.6 – Current transients of laboratory ferritic SS under alkaline condition (pH 10) corresponding to the **a)** first and **b)** last scratch tests.

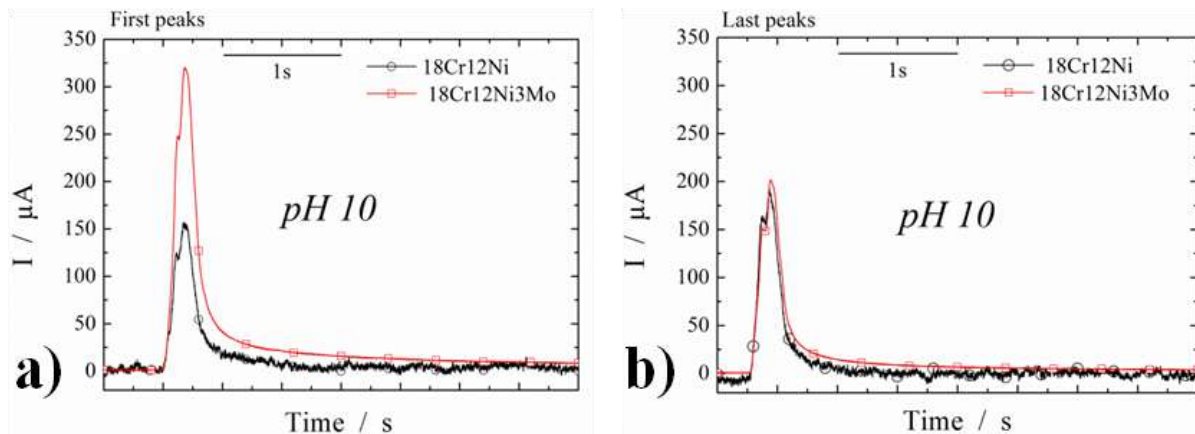


Figure 4.7 – Current transients of laboratory austenitic SS under alkaline condition (pH 10) corresponding to the **a)** first and **b)** last scratch tests.

From the Figs. presented above, it appears that the effect of Mo in ferritic grades is not as evident at pH 10 as at pH 4. This principal does not agree with the results discussed before (chapter 3) accounting for a clear positive effect of Mo to ferritic SS even at alkaline pH values. In fact this is likely to be related to the low aggressiveness of this electrolyte. Indeed, it's worth noticing that the peaks amplitudes for ferritic SS were lower at pH 10 than pH 7 and pH 4, which should be explained by the lower aggressiveness of the alkaline condition. This fact was also investigated by SEM images as illustrated in Fig. 4.8.

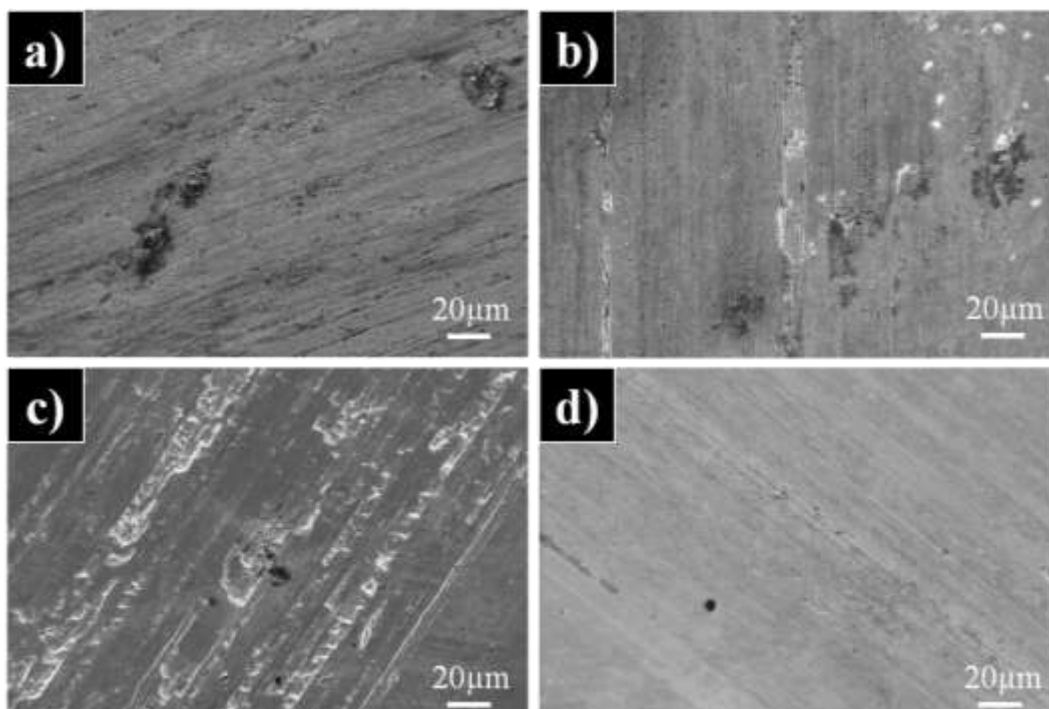


Figure 4.8 – SEM images of wear trace for 18Cr SS (pictures **a**) and **b**) and 18Cr3Mo SS (pictures **c**) and **d**) after tribocorrosion experiment under acidic and alkaline conditions, respectively.

Pictures 4.8 a) and b) shows the wear trace for 18Cr SS in acidic and alkaline conditions, respectively whereas the images 4.8 c) and d) represents the same conditions for 18Cr3Mo SS. Comparing Figs. 4.8 a) with b) or c) with d), the attack was more intense at pH 4 condition for both materials.

4.2.2. Mo EFFECT ON THE REPASSIVATION KINETICS

The low aggressiveness of the pH 10 solution and the fact that tribocorrosion experiments were performed under corrosion potential conditions can explain why Mo effect is not clearly seen in the main parameters of those small current transients for any SS grades. On the other hand, when the film is submitted to more severius conditions like those close to

the pitting potential, Mo can be more easily discerned, as discussed in the previous chapters. Anyway, a shaper analyzes of the ensemble of transients has been performed to proceed to a comparative evaluation of the transients in terms of repassivation rate. Trunkated linear slope, $I = - a t + b$, or a more generic exponential decay expression, $I = I_0 + A_1 \times \exp\left(\frac{-(t-t_0)}{t_1}\right)$, were used without given conclusive results for alkaline conditions. Nevertheless, the average repassivation charge Q of the ensemble of transients for each grade at each pH give interesting results as seen Table 4.2. Even if this results must be taken with care, the repassivation charge Q , that give us an idea of the energy spent by each material to reconstruct the passive layer, seems to confirm the beneficial effect of Mo in alkaline environments for ferritic grades even at corrosion potential conditions which is not seen for austenitic grades. Indeed, as can be seen in the Table 4.2, the repassivation charge Q was decreased by the addition of Mo in almost all studied circumstances even in the case of the ferritic SS at alkaline condition, where the linear approach and the exponential fits have indicated the contrary. This reduction of Q implies that a small energy was necessary to stop the corrosion attack and the repassivate for Mo containing SS in almost all condition. The only two cases, which this beneficial effect of Mo wasn't observed by the analyses of Q , were for austenitic and duplex SS at pH10, which was expected, as discussed above.

Table 4.2 – Spent charges for the repassivation process under different conditions.

Material	pH4		pH10	
	1°peak	20°peak	1°peak	20°peak
	Q ($10^{-5}A s^{-1}$)			
18Cr	16.1793	23.3332	3.8714	8.2183
18Cr3Mo	10.4757	20.0906	2.8048	7.0830
18Cr12Ni	12.8553	19.1089	4.0579	4.1301
18Cr12Ni3Mo	10.2189	17.1731	8.4174	5.0685
23Cr4.6Ni	6.2050	12.8657	2.7296	3.2935
23Cr4.6Ni3Mo	8.9616	10.6053	1.7648	4.8905

4.2.3. Mo EFFECT ON EACH PHASE OF DUPLEX SS AFTER MECHANICAL DEPASSIVATION

Figs. 4.9 and 4.10 shows SEM images of the morphology of the wear track on the surface of 23Cr4.6Ni and 23Cr4.6Ni3Mo DSS, respectively, after the scratch test in both acidic and alkaline media.

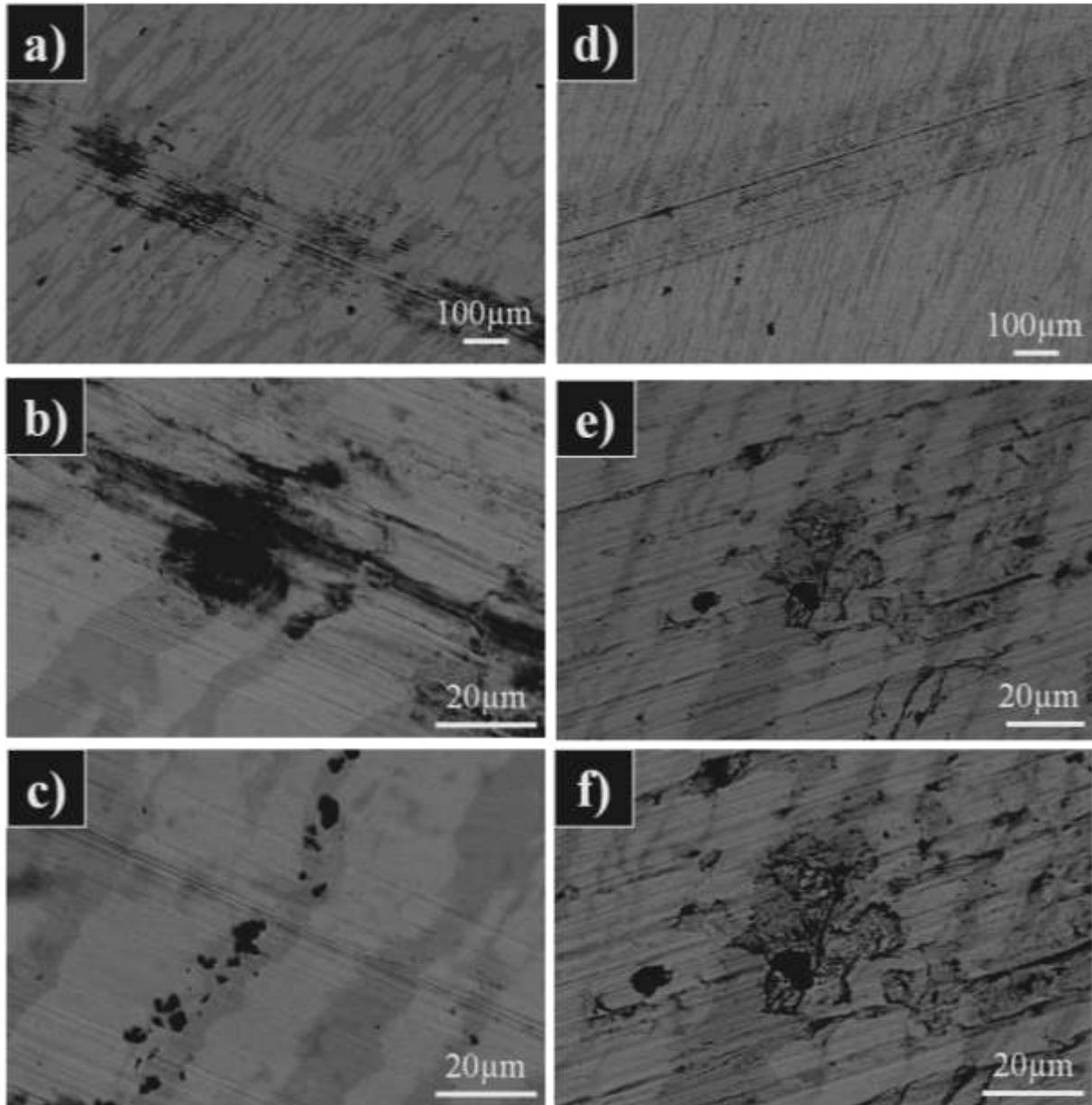


Figure 4.9 - SEM images of 23Cr4.6Ni SS surface after tribocorrosion experiments under acidic (pictures **a**), **b**) and **c**)) and alkaline (pictures **d**), **e**) and **f**)) conditions.

The high degradation of the ferrite phase caused by the mechanical passivity breakdown of the 23Cr4.6Ni alloy after the scratch test in acidic solution can be easily

observed in Figs 4.9 a) and b). Moreover and as expected, the preferential pitting attack of the ferrite in absence of Mo at the same condition was checked and is represented in Fig. 4.9 c). In the alkaline media, the corrosion of the 23Cr4.6Ni intensively occurred at the ferrite once more as illustrated in Figs. 4.9 d), e) and f), but thanks to the lower aggressiveness of the alkaline solution, the attack seem to have been less intense than in acidic medium. These results are in very good agreement with the SEM images presented in section 3.4 for the 23Cr4.6Ni SS as the ferrite was also the weaker phase in case of a passivity breakdown entailed by the Cl^- attack (see Figs. 3.14 and 3.15).

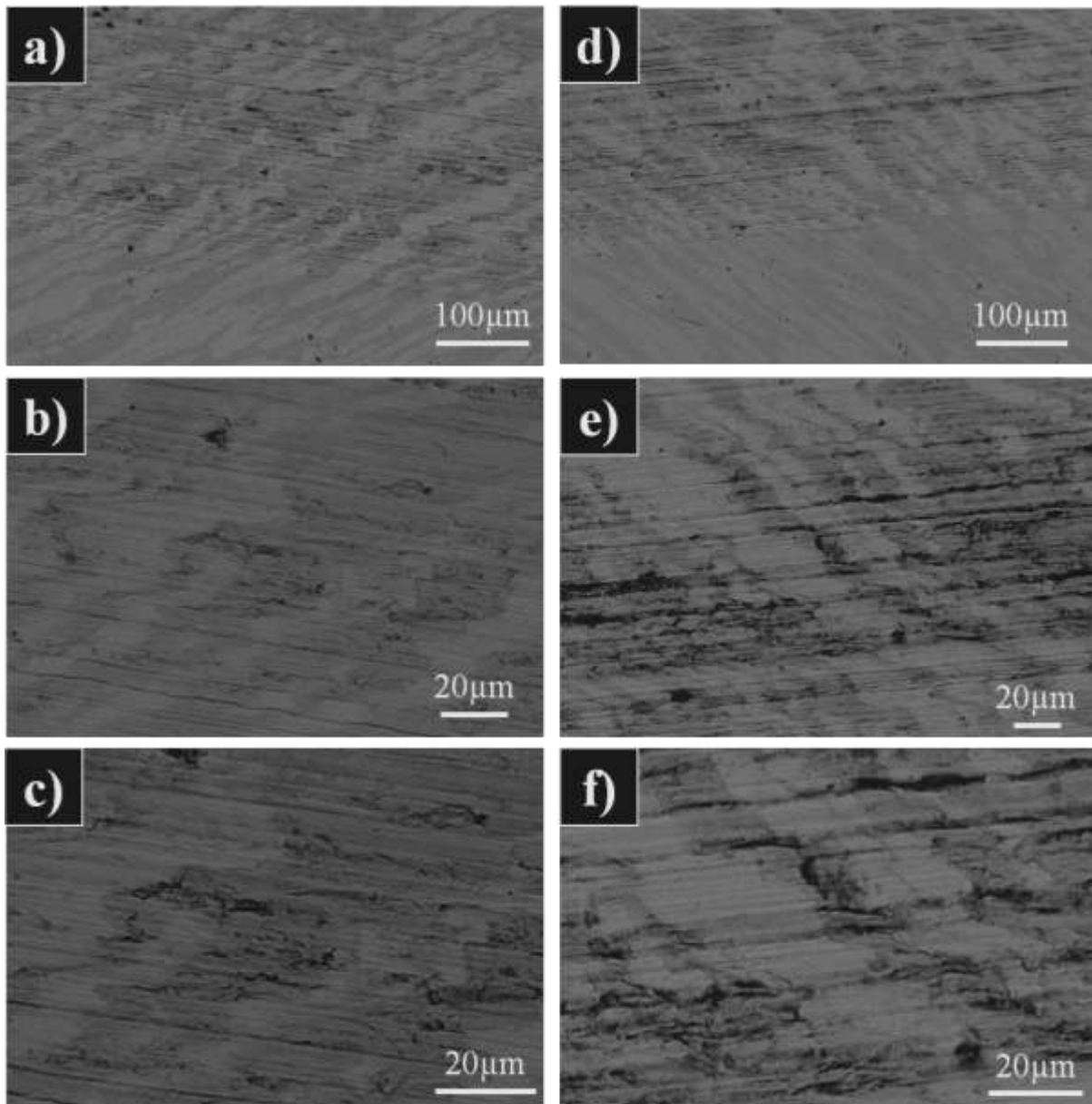


Figure 4.10 - SEM images of 23Cr4.6Ni3Mo SS surface after tribocorrosion experiments under acidic (pictures **a**), **b**) and **c**) and alkaline (pictures **d**), **e**) and **f**) conditions.

For the 23Cr4.6Ni3Mo SS, the ferrite phase was also more deteriorated than austenite as shown by Fig. 4.10 in both acidic (pictures a), b) and c)) and alkaline (pictures d) e) and f)) situations. This was a surprising result as in section 3.4 and in our papers [24, 41], we had confirmed that pitting nucleation and propagation passed from ferrite to austenite thanks to the Mo addition when the DSS were pitting attacked by the Cl^- . (see Figs 3.16, 3.17, 3.18 and 3.19)

A possible explanation for these unexpected results is related to the hypothesis that Mo role on the pitting corrosion resistance of SS should be due to its presence on the passive layer [42-45]. Then, in the case of DSS, the passive film formed on ferrite should contain a higher concentration of Mo as the ferrite chemical composition is Mo richer compared to the austenite composition (see Table 3.3). However, for the results presented in the Fig. 4.10, the 23Cr4.6Ni3Mo SS was mechanical depassivated by the scratch test, directly exposing the metallic surface of the DSS to the aggressive solutions hence annihilating the Mo effect, which is not the case in the pitting corrosion. Consequently, the Mo effect for ferrite phase after friction was not as strong as in the local pitting depassivation caused by Cl^- ions, where the presence of in the surrounding film ensure its better resistance.

A second alternative interpretation for these results, but not less important, is the fact that the ferrite phase is more susceptible to the abrasion attack than austenite. (ferritic SS are less harder than austenitic ones - see Table 4.1) Consequently, the increase of the amount of ferrite phase on the duplex microstructure due to the Mo addition should probably have increased the wear in this phase causing then its higher deterioration.

The final interesting observation from Fig. 4.10 is the fact that the ferrite of the 23Cr4.6Ni3Mo seems to have been more attacked in alkaline than in acidic condition (compare Figs. 4.10 a), b), c) with Figs. 4.10 d), e), f)). This behavior indicates over again the loss of Mo positive effect from the acidic to alkaline media.

4.3. THE CORROSION INHIBITOR EFFECT OF MOLYBDATES IN FUNCTION OF pH

The effect of Mo addition on SS in acidic and neutral media is often associated to decreasing dissolution rates in the highly aggressive solutions that develop within either metastable and stable pits, leading to the assertion that dissolution is blocked by a Mo-containing species enriching on the actively-dissolving surface [3, 12, 14, 18, 19, 46, 47],

such as $[\text{MoO}_4(\text{H}_2\text{O})_2]^{2-}$, which is very similar to the well-known corrosion inhibitor Na_2MoO_4 [32, 36, 48]. Moreover, the mechanism of Mo on the repassivation of SS after the pitting corrosion is mostly associated with the formation of Mo compounds, mainly molybdates (MoO_4^{2-}), in the aggressive solution within the pits cavity by the literature [25, 34, 36, 37]. Therefore, the influence of molybdates ions in different pH conditions will be investigated in this section.

For this investigation, 0.1 molar of sodium molybdate (Na_2MoO_4) was directly added in the salt media before the anodic polarization experiments. The aim of this addition was to roughly simulate the solution formed inside the pit during the pitting corrosion attack of Mo containing SS. The results from polarization measurements were discussed with respect to the effect of molybdates addition to the pitting potential E_{pit} of lab SS from acidic to alkaline solutions in presence or absence of molybdates.

Fig. 4.11 a), b), c) respectively show the typical polarization curves of Free Mo ferritic, austenitic and duplex lab SS on pH 4 solution and in a presence or absence of molybdate.

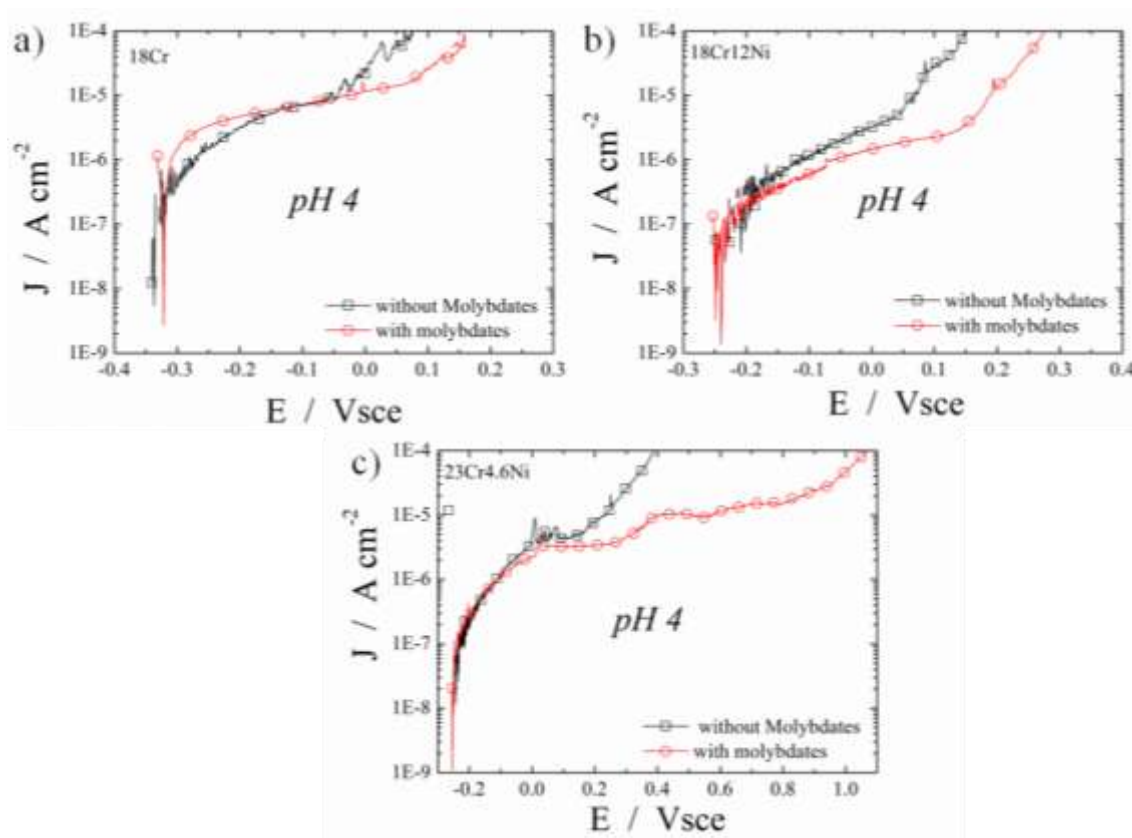


Figure 4.11 - Polarization curves obtained for a) 18Cr, b) 18Cr12Ni and c) 23Cr4.6Ni at the pH 4 solution in the absence (black \square) and presence (red \circ) of molybdates at 25°C.

The corrosion inhibitor effect of the molybdates can be clearly seen in these Figs., as its addition shifted the E_{pit} for noble values for the three different types of SS. In these conditions, the simple fact of adding 0.1 M Na_2MoO_4 on the chloride solution increased the E_{pit} more than 600 mV_{SCE} for 23Cr4.6Ni SS and more than 100 mV_{SCE} for 18Cr12Ni and 18Cr lab SS.

Similar results were previous reported by *Lemaitre et al.* [36] for austenitic and ferritic SS. Their explanation for these behavior was a competition between the adsorption of chloride or molybdate ions on the same active sites (metastable pits) of the passive film [49, 50]. These authors also suggested that the limiting step of this process depends on dissolved oxygen in the solution or that the adsorption of species at the passive film-medium interface could be modified by the presence of oxygen. Others authors [34] concluded that molybdates affects both the nucleation of pitting and metastable pitting by reducing the number and size of these events, which makes attainment of stable pit growth more difficult. Thus, in our case, the presence of molybdates in acidic media should have suppressed the pit nucleation and growth by its incorporation on the first atomic layer of the SS passive films [44] or the dissolved Mo from the passive film and substrate covered the pit walls and then helped the repassivation of Mo containing SS. This last interpretation is in the same way of the results from the tribocorrosion tests discussed above.

Under alkaline conditions, however, this dissolved molybdenum in the medium as molybdates ions did not improve the resistance to local breakdown of the passive film. Figs 4.12 a), b), c) respectively show the typical polarization curves of Free Mo ferritic, austenitic and duplex lab SS in pH 10 solution and in a presence or absence of molybdates. These results are in good agreement with *Pourbaix diagrams* (see Fig. 1.5) [31], as molybdate ions are thermodynamically unstable in acidic solutions, forming MoO_3 precipitate on the passive layer or in the pit walls. This Mo oxide would then slow down the pit attack at acidic conditions. On the other hand, MoO_4^{2-} ions are still stable in alkaline conditions and then are less adsorbed at the passive film-medium interface and hardly precipitates, which causes the loss of protective efficiency of Mo in this corrosion condition.

The ensemble of pitting potentials E_{pit} for Free-Mo stainless steels in four different pHs and in presence and absence of molybdates on the solution are summarized in Table 4.3. As can be seen in this Table, the presence of molybdates into the solution strongly affects the pitting corrosion resistance of SS under acidic and neutral media whereas its effect seems to

disappear in the alkaline domain. It is important to mention another time here that the E_{pit} values in the present work were computed as the potential value for which the current density reached $100 \mu\text{A cm}^{-2}$, which constitutes in an experimental protocol largely employed in the literature [3, 51-54].

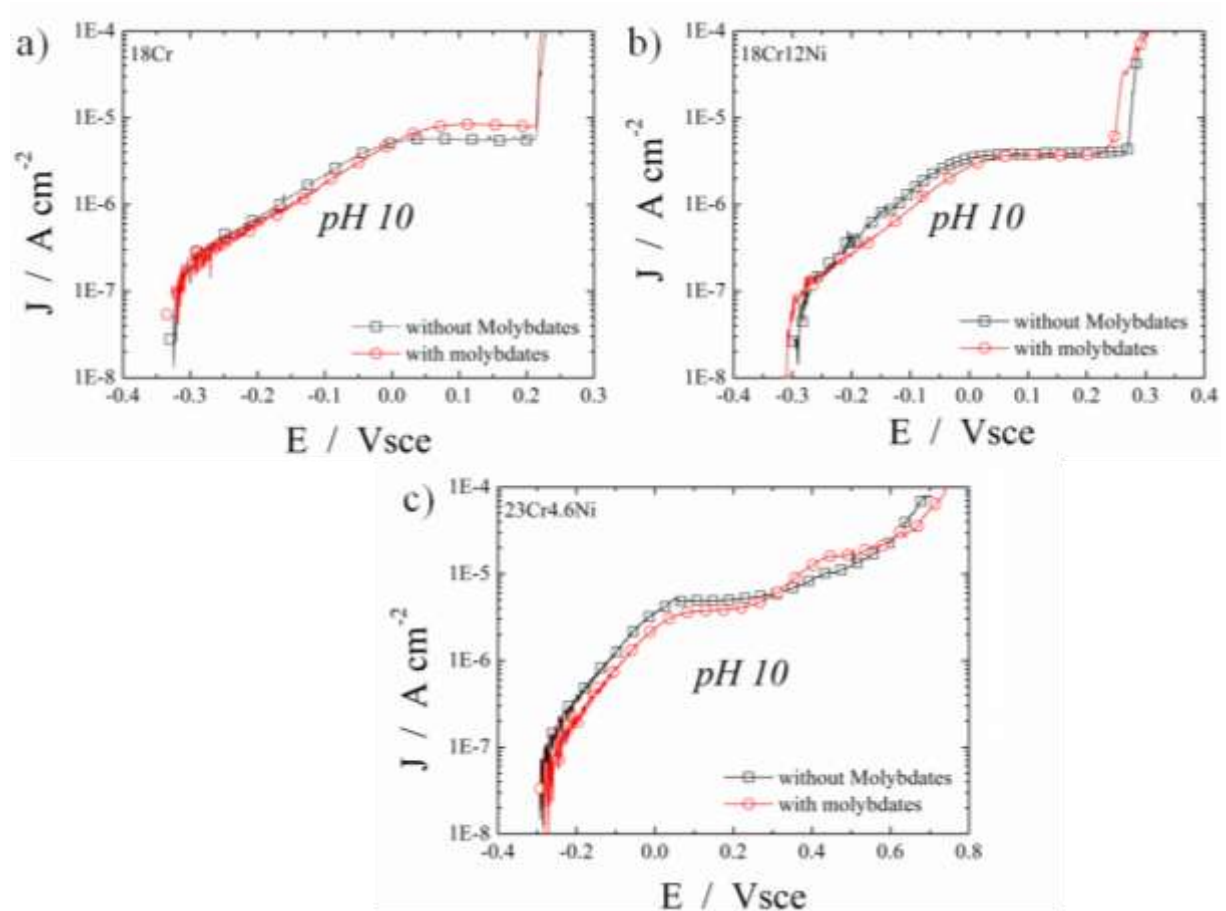


Figure 4.12 - Polarization curves obtained for a) 18Cr, b) 18Cr12Ni and c) 23Cr4.6Ni at the pH 10 solution in the absence (black \square) and presence (red \circ) of molybdates at 25°C.

Table 4.3 – Pitting potential (E_{pit} at $100\mu\text{A cm}^{-2}$) of Free – Mo SS in the presence or absence of molybdates into several different pH solutions.

PITTING POTENTIAL E_{pit} (mVsce)								
Material	pH4		pH7		pH10		pH12	
	With	Without	With	Without	With	Without	With	Without
18Cr	167	62	200	107	266	251	503	500
18Cr12Ni	312	108	293	137	356	320	538	530
23Cr4.6Ni	1067	390	1175	585	739	807	No pit	No pit

Fig. 4.13 shows the ΔE_{pit} ($\Delta E_{pit} = E_{pit}$ for Molybdate containing Solution – E_{pit} for Free Molybdate solution SS) for 18Cr, 18Cr12Ni and 23Cr4.6Ni lab alloys in different pH. In other words, this picture represents the corrosion inhibitor effect of the molybdates under different circumstances. So, as expected, the beneficial effect of molybdates addition on aggressive solutions to the pitting corrosion resistance of lab alloys was very high in acidic and neutral solutions (pH 4 and 7), whereas it didn't present any effect under alkaline conditions (pH 10 and 12), as clearly shown in Fig. 4.13.

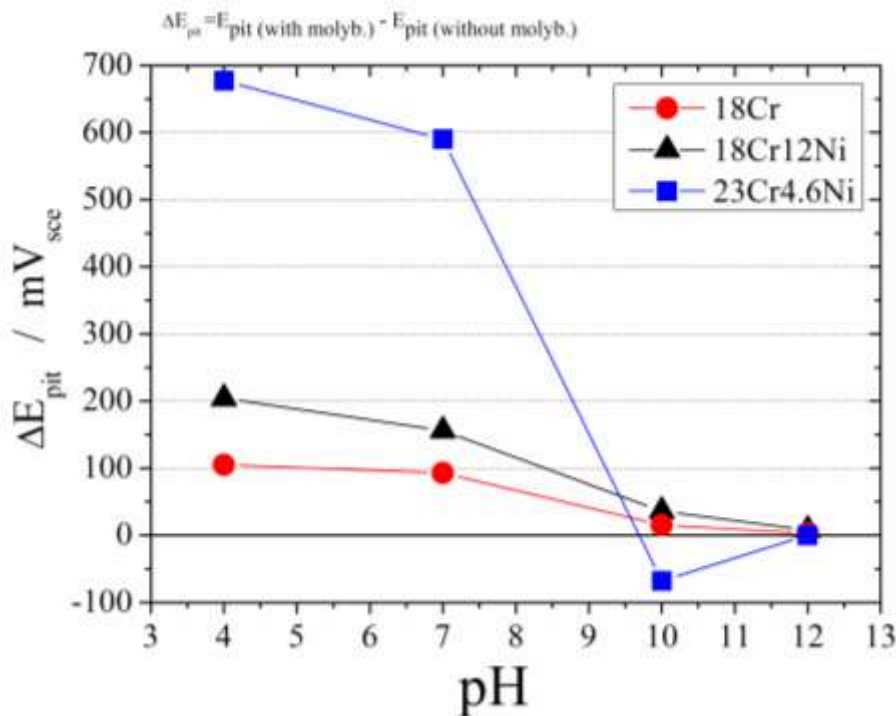


Figure 4.13 - ΔE_{pit} ($\Delta E_{pit} = E_{pit}$ for Molybdate containing Solution – E_{pit} for Free Molybdate solution SS) for 18Cr (black curve), 18Cr12Ni (red curve) and 23Cr4.6Ni (blue curve) lab alloys as a function of pH.

Indeed, if it is assumed that the molybdenum acts by its rapid dissolution and redeposition in the form of molybdate ions during the pitting attack, its performance should correspond to the inhibition behavior described by molybdate directly added in the solution. Then the same properties would roughly be expected for molybdenum alloyed in the SS or with molybdate directly added to the solution. In fact, this was only found for austenitic SS, as the same monotonic decrease of the effect Mo for the pitting corrosion resistance presented in chapter 3 (Fig 3.9) was also observed for the molybdate influence from acidic to alkaline conditions, as shown in Fig. 4.13. Therefore, a model where the alloyed molybdenum would act by its rapid dissolution followed by its redeposition (e.g. on MoO_4^{2-} a- form) does hold for austenitic SS only.

Nevertheless, Mo-containing Ferritic and Duplex grades did behave better than Mo-free alloys in these aggressive alkaline solutions as shown in chapter 3. So, for these materials, the results from Fig 4.13 seem to corroborate those already presented in Fig. 3.7 (chapter 3) [24]. In that Fig., hindered current increase profiles measured during pit initiation and repassivation indicated that Mo role should mostly be related to nucleation of pits through the passive layer rather than repassivation kinetics induced by Mo complex deposition on the pit walls. The results shown in Fig. 4.13 also go in this direction.

According to Fig. 4.13, if the role of Mo addition on SS was purely related to the electrolyte composition, all Mo containing lab SS heats should have presented about the same E_{pit} of Mo Free lab SS at alkaline media, which does not happen as discussed in previously. Thus, one tentative interpretation of Mo mechanism for SS under alkaline situations should be due to its presence in the passive layer as suggested by some authors [43-45, 55] rather than the formation of Mo-species on the aggressive solution within pit, as already published [3, 12, 15, 18, 19, 32, 34, 46] for acidic and neutral media. This discussion will be the subject of the following chapter.

4.4. CONCLUSION

In summary, it is shown that Mo has a slight influence on the repassivation mechanism in the alkaline media simulating concrete pore solutions, especially for austenitic alloys. This absence of a positive effect of Mo was also observed when molybdates were directly added in the aggressive media. The presence of Molybdates within the solutions promoted a high pitting corrosion inhibitor effect on acidic and neutral solutions whereas it has no influence on high alkaline conditions. These results were associated with the different species of Mo formed in each pH [26]. Therefore, Mo mechanism for SS under alkaline situations should mostly be due to its presence in the passive layer rather than the formation of Mo-species on the aggressive solution within the pit, which was also suggested in the chapter 3.

On the other hand, Mo has a stronger beneficial effect on the repassivation kinetics of all lab materials in acidic medium as its addition accelerates the current intensity decay after mechanical depassivation. This beneficial behavior was confirmed by the estimation of the charge used during the scratch transients. Thus, in this condition, Mo mechanism should be a mix of Mo presence into the passive layer and the formation of Mo complex within the pit

after a rapidly dissolution of Mo ions during the metastable or stable pitting corrosion, which is more favorable in the less close-packed ferrite phase (BCC crystalline structure).

The stronger Mo effect on ferrite phase of the DSS is limited to a local breakdown of thin passive films caused by Cl⁻. Nevertheless, the ferrite was the weaker phase during the tribocorrosion in the presence or absence of Mo in the bulk composition. These unexpected behaviors were experimental confirmed by SEM observation of the DSS structures after a mechanical depassivation. These results reinforce the hypotheses that Mo mechanism for DSS under alkaline situations should mostly be due to its presence in the passive layer rather than the formation of Mo-species on the aggressive solution within the pit.

Thus, when considering the use of SS in severe abrasive service conditions, the presence of Mo seems to be very beneficial and should not be neglected, mainly under acidic and neutral conditions.

4.5. REFERENCES

- [1] B. Baroux. Corrosion Science 28 (1988) 969.
- [2] G. S. Eklund. J. Electrochem. Soc. 121 (1974) 467.
- [3] A. Pardo, M.C. Merino, A.E. Coy, F.Viejo, R. Arrabal and E. Matykina, CorrosionScience 50 (2008) 1796.
- [4] T. Sourisseau, E. Chauveau, and B. Baroux. Corrosion Science 47 (2005) 1097.
- [5] J. Stewart, and D. E. Williams. Corrosion Science 33 (1992): 457-463, 465-474.
- [6] L. Sudesh, L.Wijesinghe and D. J. Blackwood. Corrosion Science 49 (2007) 1755.
- [7] D. E.Williams, M. R. Kilburn, J. Cliff, G. I. N. Waterhouse. Corrosion Science. 52 (2010) 3702.
- [8] R. Qvarfort, Corrosion Science 40. 40 (1998) 215.
- [9] G.O. Ilevbare, and G.T. Burstein. Corrosion Science 45 (2003) 1545.
- [10]N.J. Laycock, and R.C. Newman. Corrosion Science 39 (1997) 1771
- [11]E. Akiyama, A. Kawashima, K. Asami, K. Hashimoto. Corrosion Science 38 (1996) 1281.
- [12]A. J. Davenport, A. J. Dent, M. Monir, J. A. Hammons, S. M. Ghahari, P. D. Quinn and T. Raymentb. J. Electrochem. Soc. 158 (2011).
- [13]H. Habazaki, A. Kawashima, K. Asami, and K.Hashimoto. Corrosion Science 33 (1992) 225.

- [14] K. Hashimoto, K. Asami, A. Kawashima, H. Habazaki, and E. Akiyama. *Corrosion Science* 49 (2007) 42.
- [15] K. Hashimoto, K. Asami, and K. Teramoto. *Corrosion Science* 19 (1979) 3.
- [16] M. Kaneko, and H.S. Isaacs. *Corrosion Science* 44 (2002) 1825.
- [17] Y.C. Lu, and C.R. Clayton. *Corrosion Science* 29 (1989) 927.
- [18] R. C. Newman. *Corrosion Science* 25 (1985) 331.
- [19] R. C. Newman. *Corrosion Science* 25 (1985) 341.
- [20] M.K Umarakhunov, U.A. Sadykova, and G.A. Khodzhaeva. *Russian Journal of Physical Chemistry* 84 (2010). 889.
- [21] J.N. Wanklyn. *Corrosion Science* 21 (1981) 211.
- [22] Y. Wu, R. C. Ni, H. Z. Hua and A. Pourbaix. *Corrosion Science* 24 (1984) 691.
- [23] E. Chauveau, T. Sourisseau, B. Dermelin and M. Mantel, MEDACHS 08, International Conference in Coastal and Marine Environments (2008).
- [24] T. J. Mesquita, E. Chauveau, M. Mantel, N. Kinsman and R.P. Nogueira. *Materials Chemistry and Physics*, 126 (2011) 602
- [25] C.M. Abreu, M. J. Cristóbal, R. Losada, X. R. Nóvoa, G. Pena, M. C. Pérez. *Electrochimica Acta* 49 (2004) 3049.
- [26] W.A. Badawy and F.M. Al-Kharafi. *Electrochimica Acta* 44 (1998) 693.
- [27] H. Ogawa, H. Omata, I. Itoh, and H. Okada. *Corrosion* 34 (1978) 52.
- [28] C. R. Clayton and Y. C. Lu. *J. Electrochem. Soc.* 133 (1986) 2465.
- [29] C. R. Clayton and Y. C. Lu, *J. Electrochem. Soc.* 132 (1985) 2517.
- [30] A. R. Brooks, C. R. Clayton, K. Doss, and Y. C. Lu et al., *On J. Electrochem. Soc.* 133 (1986) 2459.
- [31] M. Pourbaix, *Atlas of Electrochemical Equilibria in Aqueous Solutions*. NACE, CEBELCOR, (1974).
- [32] M. Kimura, M. Kaneko and N. Ohta, *ISIJ Int* 42 (2002). 1399.
- [33] A. Anderko, N. Sridhar, M. A. Jakab, and G. Tormoen. *Corrosion Science* 50 (2008) 3629.
- [34] G.O. Ilevbare, and G.T. Burstein. *Corrosion Science* 45 (2003) 1545.
- [35] K. Hashimoto, K. Asami, and K. Teramoto. *Corrosion Science* 19 (1979) 3.

- [36] C. Lemaitre, A. A. Moneim, R. Djoudjou, B. Baroux and G. Beranger. *Corrosion Science* 34 (1993) 1913.
- [37] W.J. Tobler, and S. Virtanen. *Corrosion Science* 48 (2006) 1585.
- [38] A.A. Pozdeeva, E.I. Antonovskaya, and A.M. Sukhotin. *Corrosion Science* 6 (1966) 149.
- [39] W. D. Callister Jr. *Materials Science and Engineering - An Introduction*.
- [40] A. Collazo, X.R. Nóvoa, G. Pena, and M.C. Perez. *J. ASTM Int.* 3 (2006).
- [41] T. J. Mesquita, E. Chauveau, M. Mantel, N. Kinsman and R. P. Nogueira. *Duplex World Conference, Baune 2010, 2010*.
- [42] A. Pardo, M.C. Merino, A.E. Coy, F. Viejo, R. Arrabal and E. Matykina, *Corrosion Science* 50 (2008) 780.
- [43] M.F. Montemor, A. Simões, M.G.S. Ferreira, M. Da Cunha Belo, *Corros. Sci.* 41 (1999) 17.
- [44] K. Sugimoto, and Y. Sawada, *Corrosion Nace* 32 (1976) 347.
- [45] K. Sugimoto, Y. Sawada, *Corros. Sci.* 17 (1977) 425.
- [46] R. C. Newman, and E.M. Franz. *J. Electrochem. Soc.* 131 (1984) 223.
- [47] T. Rayment, A. J. Davenport, A. J. Dent, J. P. Tinnes, R. J. K. Wiltshire, C. Martin, G. Clark, P. Quinn, J. F. W. Mosselmans. *Electrochemistry Communications* 10 (2008) 855.
- [48] C. Lemaitre, B. Baroux, and G. Beranger. *Corrosion Science* 31 (1990) 585.
- [49] E. Maccafferty, 6th European Symp. on Corr. Inhibitors, Ferrara (It) 1985, *Ann. Univ. Ferrara, N.S., Sez V, Suppl. N.8*, 1 p. 533 (1985).
- [50] H.H. Strehblow and B. Titze. *Corrosion Science* 17 (1977) 461.
- [51] L. Zhang, Y. Jiang, B. Deng, W. Zhang and J. Xu, J. Li. *Materials Characterization* 60 (2009) 1522.
- [52] B. Deng, Y. Jiang, J. Gong, C. Zhong, J. Gao and J. Li, *Electrochimica Acta* 53 (2008) 5220.
- [53] B. Deng, Y. Jiang, J. Gong, C. Zhong, J. Gao and J. Li. *Electrochimica Acta*, 54 (2009) 2790.
- [54] M. Moreno, W. Morris, M. G. Alvarez, G.S. Duffó. *Corrosion Science* 46 (2004) 2681.
- [55] L. Freire, M. J. Carmezim, M. G. S. Ferreira, M. F. Montemor, *Electrochimica Acta* 55 (2010) 6174.

CHAPTER 5

***THE INFLUENCE OF M_o ON SS
PASSIVATION IN ALKALINE
“APPLICATIONS”***

OUTLINE

5. THE INFLUENCE OF M_0 ON SS PASSIVATION IN ALKALINE "APPLICATIONS"	126
5.1. INTRODUCTION	126
5.2. INFLUENCE OF M_0 ON THE PASSIVE FILM COMPOSITION - AN EX-SITU XPS STUDY IN AIR AND AT pH 7 AND 10 MEDIA	127
5.3. THE ROLE OF M_0 ON THE PASSIVE FILM STABILTY AT DIFFERENT pH	136
5.4. CONCLUSION	146
5.5. REFERENCES	147

5. THE INFLUENCE OF Mo ON SS PASSIVATION IN ALKALINE “APPLICATIONS”

5.1. INTRODUCTION

In this section, the effect of Mo on the SS passive layer formation will be discussed in terms of oxide film composition and stability. In the literature, the beneficial effect of Mo in the passivation of stainless steels has been attributed to several factors such as: an enrichment of Mo in the passive film [1-6] or in the alloy layer just below the passive film [3, 4], enrichment of Cr in the oxide layer [4] thickening of the passive film and stabilization of the Cr oxides by the presence of Mo^{6+} [7]. So, up to now, the mechanisms proposed for the Mo action seems to be related to its presence within the passive oxide film even if the presence of this alloying element in the oxide film of stainless steels is still debated in the literature [1-18].

Montemor et al. [3] have shown the presence of metallic Mo in the internal Cr rich layers (Cr_2O_3) and also in the Cr oxide/metal interface by using Auger and XPS experiments on austenitic SS at alkaline conditions. Thus, the presence of Mo in these regions could result in an enrichment of chromium in the inner layer of the film. *Olefford et al.* [7], based on XPS study of austenitic SS passivated in chloride solutions, suggested that the defects created by Fe^{2+} dissolution in the Cr oxide layer are cancelled by the creation of Mo^{4+} and Mo^{6+} oxides. These results are in a good agreement with *Pardo et al.* [14] whom have assigned the beneficial effect of Mo addition on austenitic SS at neutral condition to Mo^{6+} presence within the passive film, rendering it more stable against breakdown caused by attack of aggressive Cl^- ions, and also to the formation of Mo insoluble compounds (MoO_3 and FeMoO_4) in the aggressive pit environment facilitating the pit repassivation. Concerning the ferritic SS, *Doh et al.* [15] have described an increase of the amount of Mo with passivation time in passive film formed on 18Cr-2Mo alloy after *in-situ* XANES study. These last authors have mainly attributed this improvement of passivity to the substitution of Cr oxide by Mo oxide in the passive film.

As previously discussed in chapter 4, another alternative explanation for the effect of Mo on localized corrosion was provided by *Kimura et al.* [18] who made direct in situ measurements of the speciation of Mo in artificial corrosion pits using X-ray absorption spectroscopy. They measured the Mo K edge in pits grown in 1 M LiCl and 1 M LiBr and described the spectra as “quite similar to that of Na_2MoO_4 showing the formation of a

complex similar to the network of $[\text{MoO}_4(\text{H}_2\text{O})_2]_2$ octahedra", suggesting that the formation of such polymeric networks near the dissolving metal interface plays a significant role in the beneficial effect of Mo on the corrosion resistance of stainless steel. Nevertheless, these results are not consistent with a very recent work from *Davenport et al.* [10]. Those authors recorded the presence of Mo(III) species on the X-ray absorption Mo K-edge spectra (XANES experiments) of solutions inside 316L stainless steel artificial pits. It is worth noticing however that those results were limited to neutral and acidic media and also to some specific SS, mainly austenitic ones.

According to our previously studies [19-22] and as shown in the chapters above, a loss of beneficial Mo effect has been identified for conventional industrial austenitic SS (AISI 316L) under alkaline situations. Yet at these alkaline conditions, the Mo beneficial effect was nevertheless confirmed to yield a greater improvement of the ferrite phase pit corrosion resistance compared to austenite phase when Mo was added in the industrial and laboratory duplex SS (1.2205). So, the mechanism of Mo action should be better understood in these alkaline situations and also for the different microstructures of the SS.

Therefore, the aim of the present chapter is to characterize the passive film formed on free Mo (0wt% Mo) and Mo containing (3wt% Mo) laboratory SS heats to understand the real effect of Mo addition on the passivation behaviors of three different Stainless Steel families (austenitic, ferritic and duplex) by using X-ray photoelectron Spectroscopy (XPS) and Electrochemical Impedance Spectroscopy (EIS) techniques. A comparison between Mo containing heats and Free Mo ones was done under several pH conditions, mainly in a synthetic, Cl^- rich and carbonated solution simulating carbonated concrete pores environment (solution of pH10 with carbonates and chlorides ions). This condition is particularly relevant to coastal or off shore rebars applications or paper and alkali industries.

5.2. INFLUENCE OF Mo ON THE PASSIVE FILM COMPOSITION - AN EX-SITU XPS STUDY IN AIR AND AT pH 7 AND 10 MEDIA

In this section the results from the ex-situ XPS measurements of the austenitic, ferritic and duplex in different chloride solutions will be investigated. The chemical composition of the passive film formed in air and also at OCP condition in chloride solutions of pH, 10 and 7, was assessed by XPS measurements. Since the passive films formed on stainless steel are very thin (some tens of Angstrom) the XPS analysis gives a measure of the overall film

composition. Figs. 5.1 and 5.2 respectively show the Fe_{2p} , Cr_{2p} and $Mo_{3d_{3/2} - 3d_{5/2}}$ XPS spectra recorded at 90° for 18Cr12Ni3Mo and 18Cr12Ni lab SS in air, pH 7 and pH 10 conditions.

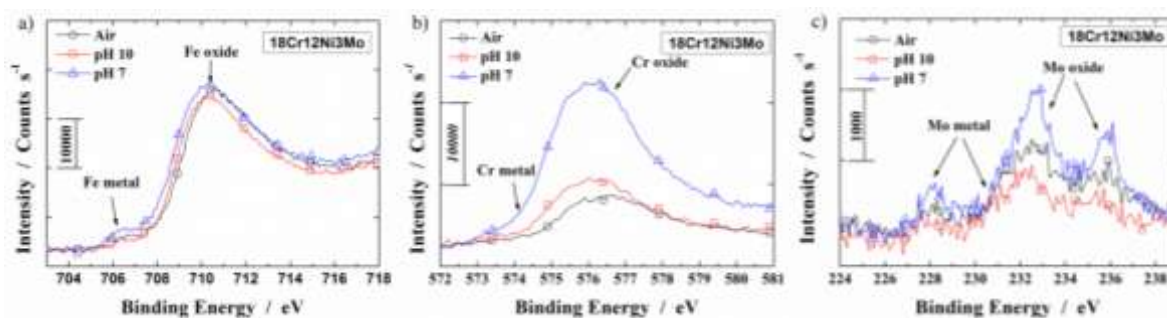


Figure 5.1 - XPS spectra at 90° for Fe_{2p} ionization (**left pictures**), Cr_{2p} ionization (**middle picture**) and $Mo_{3d_{3/2} - 3d_{5/2}}$ ionization (**right picture**) for the surface film formed on 18Cr12Ni3Mo lab SS under also at different aging conditions (air: black; pH 10: red and pH 7: blue curves).

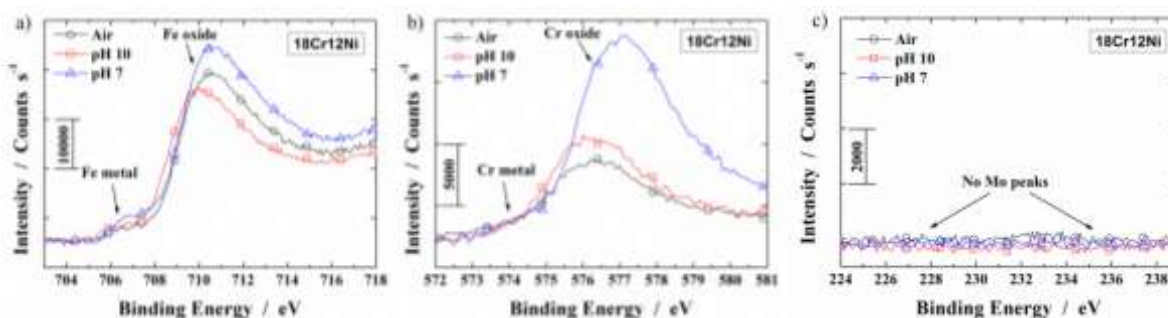


Figure 5.2 - XPS spectra at 90° for Fe_{2p} ionization (**left pictures**), Cr_{2p} ionization (**middle picture**) and $Mo_{3d_{3/2} - 3d_{5/2}}$ ionization (**right picture**) for the surface film formed on 18Cr12Ni lab SS under also at different aging conditions (air: black; pH 10: red and pH 7: blue curves).

These results show that the passive film on 18Cr12Ni3Mo and 18Cr12Ni is mainly composed of iron (Figs. 5.1 and 5.2 left), chromium (Figs. 5.1 and 2 middle) and molybdenum in the former case (Figs 5.1 right) in all experimental conditions studied. No traces of oxidized nickel were found under any circumstances. However, an enrichment of metallic Ni was observed in the metal/film interface.

The Fe_{2p} ionization was de-convoluted in two different contributions, Fe oxide and Fe metal. These contributions are assigned to the presence of Fe^0 (binding Energy (E_b) = 707.0 eV), and a group of Fe oxides such as Fe^{2+} oxides (E_b = 709.0–709.5 eV), Fe^{3+} oxide form (E_b = 710.5–711.5 eV) and also in the hydroxide form (E_b = 712.0–712.5 eV). As reported

elsewhere [23] the determination of Fe^{3+} contributions from Fe_2O_3 and Fe_3O_4 is a difficult task. Thus, the species detected in the range of binding energies from 710.5 to 711.5 eV could be generally assigned to Fe^{3+} oxides. In all Fe_{2p} spectra the dominant peak is the one associated with the presence of Fe^{3+} species, mainly oxides and hydroxides or oxihydroxides.

The Cr_{2p} ionizations (Figs. 5.1 and 5.2 middle) are characterized by the presence of a peak around 577.0 eV, related to the presence of Cr^{3+} oxides. The contribution of the metallic chromium was very small and could hardly be seen because of their low binding energies. An interesting result of the Cr ionizations for both austenitic SS is the fact that the Cr oxides peak increases from the air to aqueous solution. This effect is more remarkable when the pH decreases from pH 10 to pH 7, probably due to the stronger Fe dissolution in this environment. So, the more Fe dissolves into the electrolyte, the more Cr oxides will be formed in the oxide layer.

Oxidized Mo was also detected; but only for 18Cr12Ni3Mo as shown in Fig. 5.1 right. This effect was absolutely expected as the 18Cr12Ni has only a residual amount of Mo in its bulk composition (about 50ppm). Thus, $\text{Mo}_{3d_{3/2} - 3d_{5/2}}$ ionization for 18Cr12Ni3Mo is characterized by the presence of two peaks corresponding to Mo^{6+} oxides (MoO_3) around 232 - 236 eV mainly, as can be clearly seen on Fig. 1 c). Moreover, the small shoulder observed at low binding energies results from the contribution of the metallic molybdenum. The same behavior detected for Cr ionizations when the pH changes was found for Mo ones. So, the peak corresponding to Mo oxides is almost the same in neutral and alkaline conditions. It is important to notice that, even if many authors [3, 24, 25] did not observe Mo species in the surface film, they nevertheless suggested that Mo species also have an important effect in the defect structure of the inner chromium region and therefore on the electronic properties and corrosion resistance.

Figs. 5.3 a), b) and c) present the effect of Mo addition on $\text{Fe}/(\text{Mo}+\text{Cr}+\text{Fe})$, $\text{Cr}/(\text{Mo}+\text{Cr}+\text{Fe})$ and $\text{Mo}/(\text{Mo}+\text{Cr}+\text{Fe})$ ratios for different experimental conditions (different aging environments at the XPS measurement angle of 90° and 30°) for the lab austenitic SS. The atomic ratios for oxidized Fe, Cr and Mo were calculated using the results of oxides peaks deconvolutions and some specific tabulated values for each chemical element. The relative sensitivity factors are related with classical theories of XPS spectrometry and their values are reported in Table 5.1. This calculation procedure is better explained elsewhere [26, 27].

Table 5.1 - Relative sensitivity factors used for the XPS analysis.

Elements	C	O	Fe	Cr	Mo
100xS	1.63	4.3	15.41	11.12	7.44

Then, from Figs. 5.3 a) and b), it is worth seeing that the iron ratio ($\text{Fe}/(\text{Mo}+\text{Cr}+\text{Fe})$) decreased when the pH decrease meanwhile the chromium ratio ($\text{Cr}/(\text{Mo}+\text{Cr}+\text{Fe})$) increased. Moreover, the Mo addition in austenitic grades seems to enrich the passive film with Cr oxides in the air and at pH 7 whereas the Fe oxides contents were impoverished in both situations. In the pH 10, however, the Mo addition seems to decrease the Cr contents and slightly increase a little the Fe ratio on the passive layer.

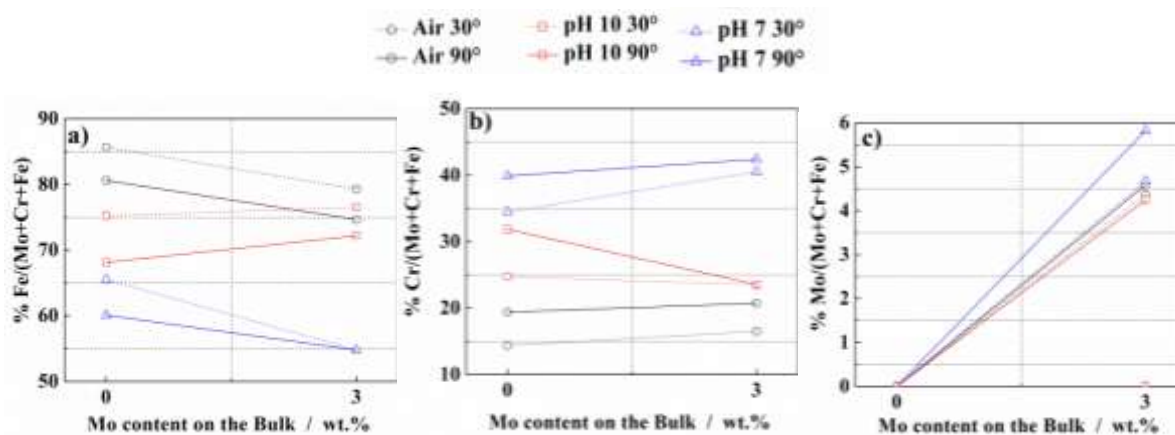


Figure 5.3 - Effect of Mo addition on the evolution of: **a)** $\% \text{Fe}/(\text{Mo}+\text{Cr}+\text{Fe})$, **b)** $\% \text{Cr}/(\text{Mo}+\text{Cr}+\text{Fe})$ and **c)** $\% \text{Mo}/(\text{Mo}+\text{Cr}+\text{Fe})$ ratios on the passive film formed at laboratory austenitic grades. These ratios were calculated from XPS spectra at 90° (solid trace) and 30° (dashed traces) and also at different aging conditions (air: black, pH 10: red and pH 7: blue).

Looking now to the results from the different analysis angles (90° and 30°), it is possible to have some information about the internal and external layers composition of the passive film. Thus, for these lab austenitic grades, the inner layers presented bigger amounts of oxidized Cr and Mo compared to the outer ones in almost all studied conditions. Oxidized Fe was hence more concentrated in the outer layer. However, the most interesting point of these results is the confirmation of Mo oxide presence into the passive layer of the 18Cr12Ni3Mo lab SS in all studied conditions, as shown in Fig. 3 c). Furthermore, it appears that oxidized Mo contents in the passive layer is lower in alkaline than in neutral media, decreasing from about 6 to 4%, which is such an important and beneficial change. This is in good agreement with the anomalous behavior of Mo pointed out in the chapter 3 which shows a loss of Mo efficiency in the corrosion resistance of conventional austenitic grades in alkaline conditions.

These passive film investigation was also carried out for the ferritic lab SS. The results from XPS measurements for 18Cr3Mo and 18Cr lab SS are described in Figs. 4 and 5, respectively.

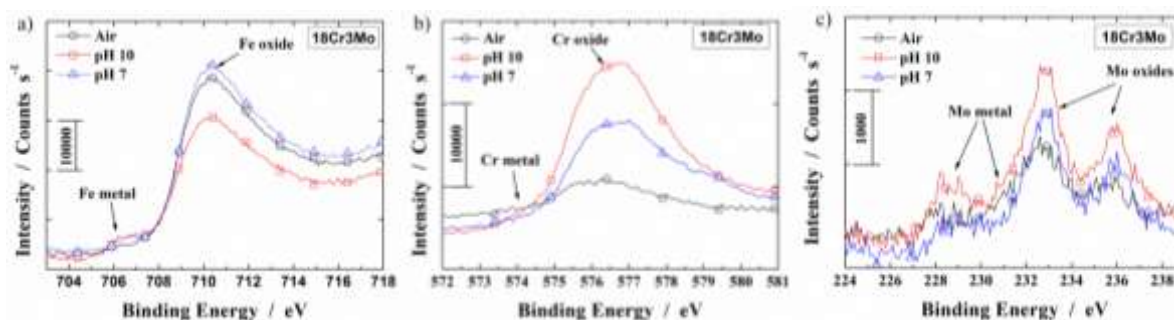


Figure 5.4 - XPS spectra at 90° for Fe_{2p} ionization (**left pictures**), Cr_{2p} ionization (**middle picture**) and Mo_{3d_{3/2}-3d_{5/2}} ionization (**right picture**) for the surface film formed on 18Cr3Mo lab SS under also at different aging conditions (air: black; pH 10: red and pH 7: blue curves).

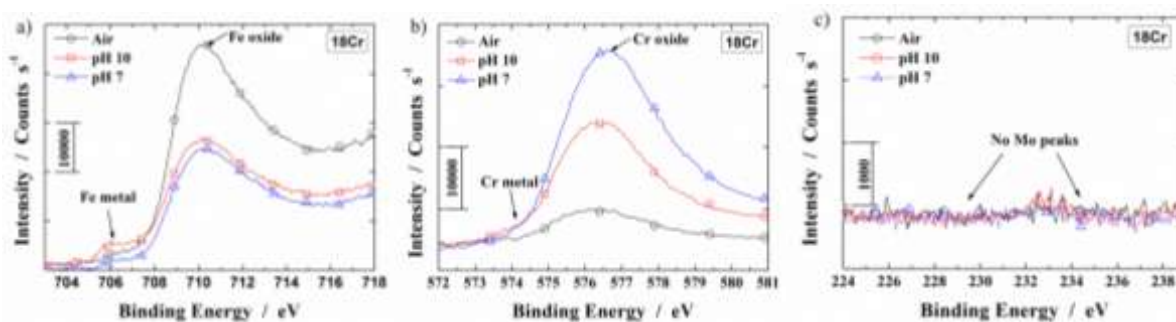


Figure 5.5 - XPS spectra at 90° for Fe_{2p} ionization (**left pictures**), Cr_{2p} ionization (**middle picture**) and Mo_{3d_{3/2}-3d_{5/2}} ionization (**right picture**) for the surface film formed on 18Cr lab SS under also at different aging conditions (air: black; pH 10: red and pH 7: blue curves).

As for austenitic lab SS, these XPS spectra show that the passive layer formed on ferritic lab alloys is mainly composed by Fe, Cr and Mo oxides. These XPS spectra indicated that Fe, Cr and Mo peaks have different intensities depending on the pH. For the 18Cr3Mo lab SS, the Cr peak (Fig. 5.4b)) is more intense in alkaline condition (pH 10) than in neutral conditions (pH 7). The same results were observed for the 18Cr lab SS as shown in the Fig. 5.5 b). The peaks corresponding to Mo oxides formed in alkaline medium (Fig 5.4 c) are stronger than in the others conditions for 18Cr3Mo SS, and as expected, no Mo peak was found for 18Cr SS.

The atomic ratios for oxidized Fe (Fe/(Mo+Cr+Fe)), Cr (Cr/(Mo+Cr+Fe)) and Mo (Mo/(Mo+Cr+Fe)) were calculated based on the XPS results from the lab ferritic heats, as

illustrated in Figs. 5.6 a), b) and c). For these alloys, the passive film always presented, as expected, a Fe-rich outer layer (Fig. 5.6 a)) and a Cr-rich inner layer (Fig. 5.6 b)). It is however interesting to notice that Mo addition seems to decrease the oxidized Cr content in the film, hence increasing the oxidized Fe, which is in good agreement with results from *Doh et al.* works [15]. According to them, the fact that Mo decreases the Cr content in the film, could be attributed to the substitution of Cr oxide by Mo oxide in the passive film. It is also worth noticing that the amount of oxidized Mo in the passive layer for 18Cr3Mo lab SS under alkaline solution shifted from about 5 % in air and neutral media to more than 6% for alkaline one as shown in Fig. 5.6 c).

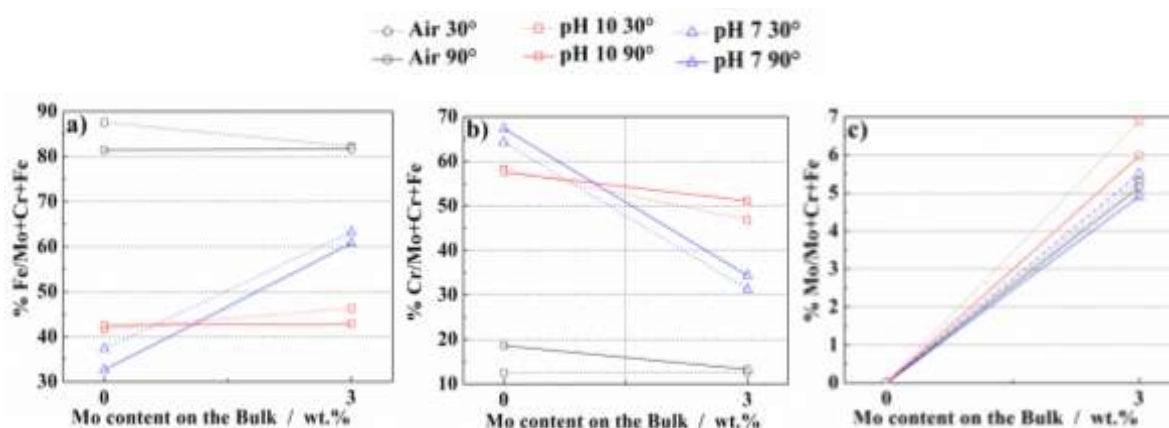


Figure 5.6 - Effect of Mo addition on the evolution of: **a)** %Fe/(Mo+Cr+Fe), **b)** %Cr/(Mo+Cr+Fe) and **c)** %Mo/(Mo+Cr+Fe) ratios on the passive film formed at laboratory ferritic grades. These ratios were calculated from XPS spectra at 90° (solid trace) and 30° (dashed traces) and also at different aging conditions (air: black, pH 10: red and pH 7: blue).

The lab duplex SS surfaces were also characterized in the same conditions by XPS, as presented in Fig. 5.7, which shows the atomic ratios for oxidized Fe, Cr and Mo. A decrease of Fe/(Mo+Cr+Fe) ratio in the oxide layer from about 80% in the air to less than 50% in pH 7 solution was clearly observed (see Fig. 5.7a)). On the other hand, Cr/(Mo+Cr+Fe) ratio shifted from less than 25% to more than 55%, in air and under pH 7, respectively, as shown in Fig. 7 b). Moreover, the Cr oxides contents decrease with the Mo addition in all experimental conditions which is probably due to the Mo incorporation in the film, as explained for the ferritic alloys. This incorporation of oxidized Mo in the film took place whatever the pH, but it is more evident at neutral condition, where its amount is about 7% (see Fig. 5.7 c)).

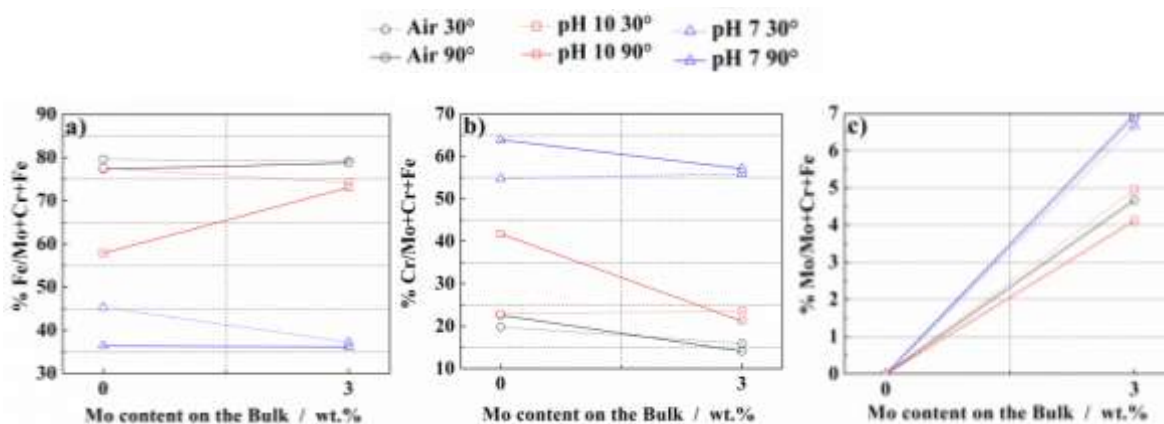


Figure 5.7 - Effect of Mo addition on the evolution of: **a)** %Fe/(Mo+Cr+Fe), **b)** %Cr/(Mo+Cr+Fe) and **c)** %Mo/(Mo+Cr+Fe) ratios on the passive film formed at laboratory duplex grades. Result from 90° experiments (solid trace) and 30° experiments (dashed traces) and also at different aging conditions (air: black, pH 10: red and pH 7: blue).

These XPS analysis did not reveal the presence of oxidized Ni in the surface film under any circumstances. However, *Freire et al.*[24] have reported the presence of Ni in the passive layer at alkaline conditions and a slight drop in Ni content as the pH decrease less alkaline. Moreover, they claimed that the presence of nickel might affect the chromium diffusion processes. According to *Abreu et al.* [28], the presence of nickel influences the chromium distribution across the passive film, determining the film growth and its corrosion resistance. Thus, the different influence of Mo addition for austenitic and ferritic SS with respect to Cr ratios (increase and decrease, respectively) could be associated to the presence of Ni in austenitic grades and its absence in ferritic ones; it hence seems that there is a synergy effect between molybdenum and nickel even if the presence of the latter on the passive layer has not been detected in the present study.

Another important result from the XPS measurements is Hydroxide/Oxide ratio (Hy/Ox) in both extreme internal and external layers of the passive film. These Hydroxide/Oxide ratio are summarized in Table 5.2. From this Table, it's possible to conclude that the passive film was mainly composed of oxides rather than hydroxides as all Hydroxide/Oxide ratio are inferior than 1. On the other hand, the passive film for all material and in all experimental conditions was, as expected, more hydrated in the outer layer than in inner one. For example, the 18Cr12Ni SS aged in air presented a Hydroxide/Oxide ratio of 0.809 in the 30° XPS measurement (inner layer) whilst this ratio was 0.725 in the 90° experiments (outer layer) under the same condition. The presence or absence of Mo did not

seem to have an influence on H_y/O_x values for the austenitic and duplex SS. Mo addition on ferritic lab SS, however, appears to decrease the H_y/O_x ratio when these materials are aged in the chloride media (pH7 and pH10 solutions). This result suggests that the 18Cr3Mo lab SS has a higher amount of oxides in its passive layer compared to the 18Cr lab SS.

Table 5.2 – Calculated Hydroxide/Oxide ratio (H_y/O_x) for the different lab SS after aging in the air, and pH7 and pH10 solutions.

Lab Materials		Hydroxide/Oxide ratio					
		air		pH 7		pH 10	
		30°	90°	30°	90°	30°	90°
austenitic	18Cr12Ni3Mo	0.746	0.750	0.456	0.343	0.531	0.461
	18Cr12Ni	0.809	0.725	0.445	0.331	0.589	0.484
ferritic	18Cr3Mo	0.715	0.543	0.379	0.282	0.511	0.405
	18Cr	0.553	0.425	0.816	0.699	0.744	0.502
duplex	23Cr4.6Ni3Mo	0.531	0.459	0.635	0.484	0.528	0.398
	23Cr4.6Ni	0.608	0.498	0.541	0.406	0.561	0.443

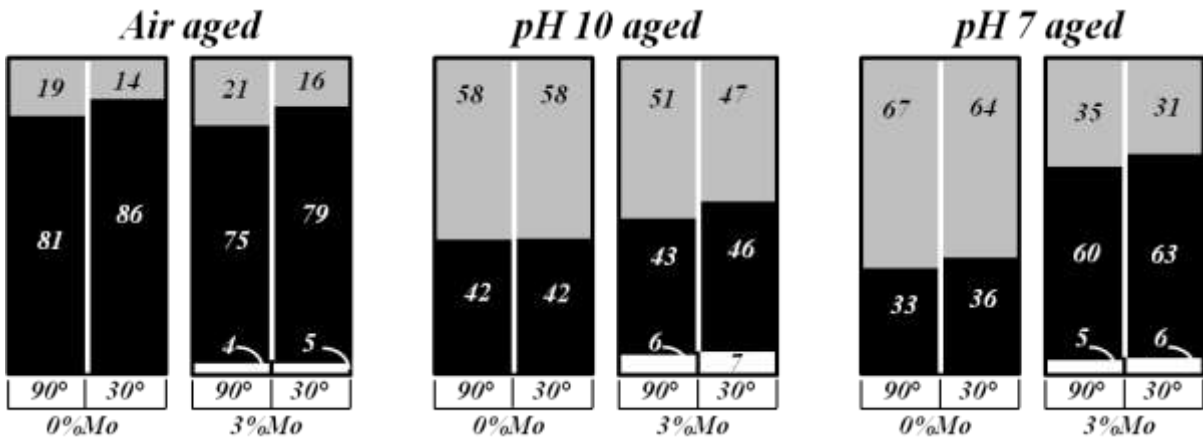
In order to have a better understanding of the passive film composition and its evolution with pH and mainly with Mo addition for three SS types, Fig. 5.8 illustrates a schematic representation of the oxide film evolution for each lab heat on different solutions in function of Mo presence or absence. The 30° and 90° angles are expected to bring information on the outer and inner layers, respectively, and the black, gray and white colors correspond to Fe, Cr, and Mo oxides ratio, respectively.

So, the outer layers are enriched in Mo and Fe oxides (30° results) whereas the inner layers are enriched in Cr oxides (90° results). However, the most interesting point of this representation is the presence of Mo oxide in studied conditions for all 3 SS families. At our knowledge, these strong changes on the Mo contents for austenitic, ferritic and mainly duplex SS passivation films under several different chloride conditions have not been reported in the literature yet, although the passivation processes for austenitic, ferritic and duplex SS have been widely studied in acidic media [3, 10, 15, 16, 23, 24, 29-32].

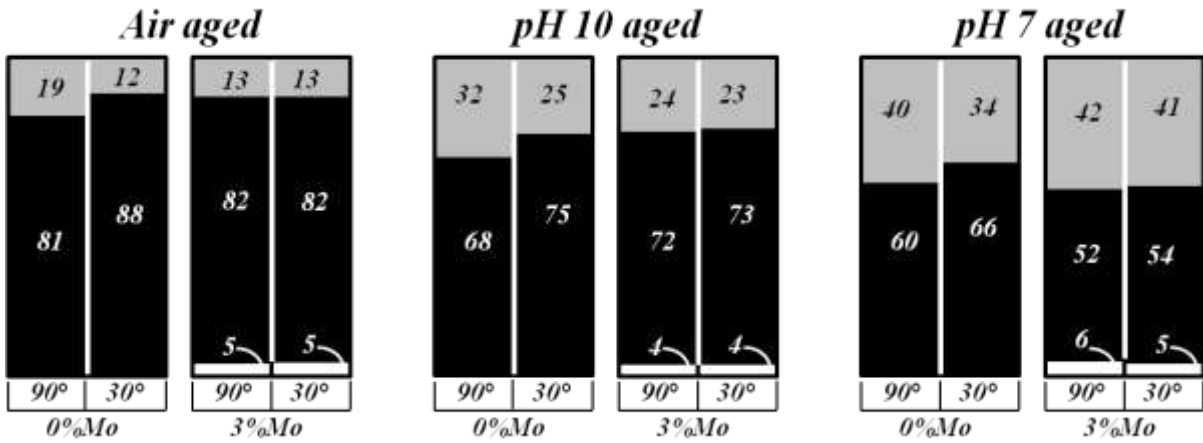
Another important detail that can be clearly observed in this Fig. is the higher Cr content in the passive layer formed on the ferritic lab SS than austenitic and duplex SS under

all studied conditions. This fact should be associated with a higher dissolution rate of iron ions from the ferritic microstructure than from austenitic or austeno-ferritic one.

- Ferritic Lab SS:



- Austenitic Lab SS:



- Duplex Lab SS:

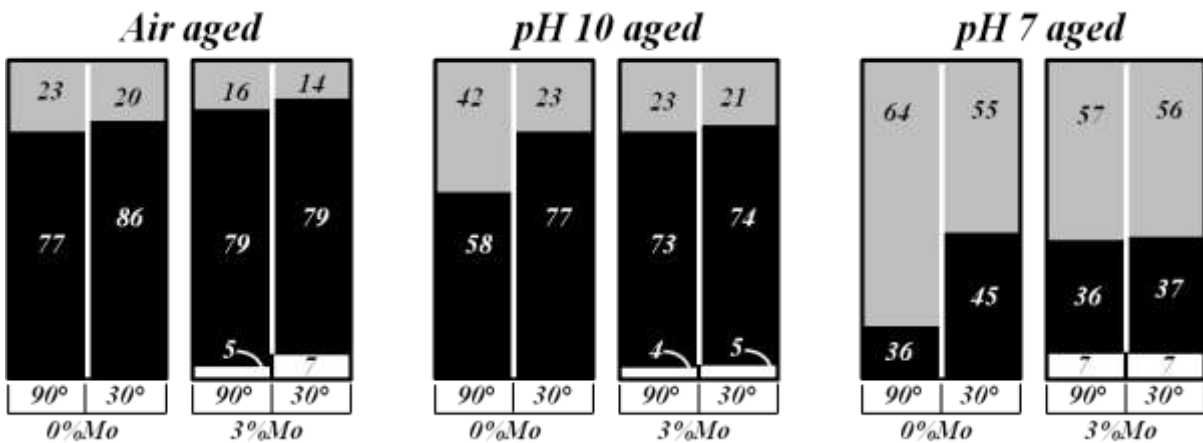


Figure 5.8 - Schematic representation of the passive film formed on laboratory SS in different conditions and in the presence or absence of Mo. The 90° and 30° angles are representing the inner outer layers, respectively. The gray, black and white colors correspond to Cr, Fe and Mo oxide ratio, respectively.

This ubiquitous presence of Mo can be taken as unexpected inasmuch as several authors claim that there is no Mo in the passive film. Even if Mo is also found in the air aged samples, it is probable that our sample preparation protocol favored the Mo incorporation in the film. Indeed, in the present case, we were interested in the study of SS in very aggressive alkaline conditions. In this sense, we made the option of working with “fresh” passive films, aged mostly directly in the aggressive solution, just one hour after polishing the surface. This certainly precluded the formation of thick stable films — as usually done — but fitted are aim of evaluating how these SS behave in such unfavorable conditions. Mo incorporation in the film should hence favor, unlikely to what happens in the case of thick stable films, for which Mo presence should be for instance strongly delayed. Anyway, we believe that our results clearly indicate that Mo presence in passive films is more than possible, probable, mainly in very aggressive conditions in which the film is exposed to strong interactions with the electrolyte.

5.3. THE ROLE OF Mo ON THE PASSIVE FILM STABILTY AT DIFFERENT pH

Additionally to the XPS measurements, EIS measurements were also carried out in different chloride solutions for all six lab SS. Fig. 5.9 shows typical results for EIS spectra (Nyquist plot) obtained for austenitic (Fig. 5.9 left), ferritic (Fig. 5.9 middle) and duplex (Fig. 5.9 right) after immersion in carbonated solution with 35g L^{-1} of NaCl (pH 10 solution) at open circuit potential (OCP) conditions. The beneficial Mo effect can be easily observed by comparing Mo containing (black curves) and Free-Mo heats (red curves). The impedance modulus are systematically greater for Mo containing grades, which point out at the low frequency limit extrapolation polarization resistances R_p giving higher values (and hence lower corrosion current densities) for all Mo containing grades. A deeper analysis of these circuits could be performed with the help of equivalent electric circuits (EEC), widely used in the literature to interpret EIS results.

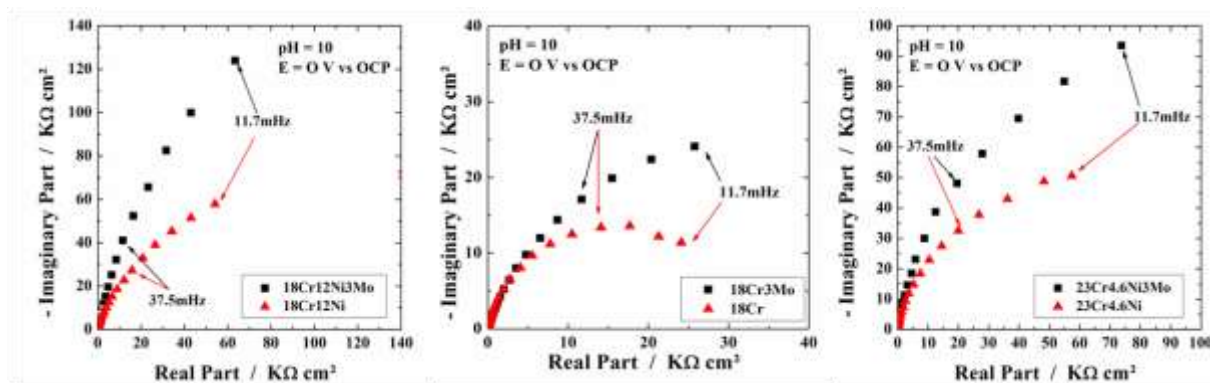


Figure 5.9 - Nyquist plot of EIS spectrum for lab materials: - **left**: austenitic, **middle**: ferritic and **right**: duplex SS after 1h in the pH 10 solution.

It must be stressed, however, that the huge availability of commercial software incorporated to virtually all the commercial devices for corrosion studies have made the EEC an easy to implement tool for fitting EIS curves. On the other hand, this easiness brings up the problem of a just-to-fit procedure that simply replaces an EIS diagram by an EEC, without gathering useful physical information. Also, there seems to be a tendency to favor the choice of those EEC that give the best curve adjustment than that having the more realistic physical sense. In what follows we will fully discuss the question on the basis of well-adjusting, but poorly physical supported EEC results found in the EEC analysis of our experiments. The attempt to get more liable results allowed us to open the way to a new research axis to better understand what is behind EEC and mainly what is the physical meaning and the limitations of constant phase elements (CPE) widely used in the adjustment of EIS curves by means of EEC.

In which concerns passive films, the literature proposes different models of equivalent circuits to interpret the impedance data on thin passive films formed on stainless steels. The simplest one consists in modeling the system with an equivalent circuit composed by one single time constant as proposed by *El-Agamy and Badaway* [33] to describe the behavior of 304 stainless steel in sodium sulfate solutions. This time constant was associated with the response of the passive film. However, this model could not fit the impedance data obtained in the present work and can hardly be associated to multiple step reaction mechanism involving charge transfer, faradaic processes and diffusion in the electrolyte and across the film. More realistic, the most common circuits are based on two time constants. A first two time-constants circuit, although not widely employed, was retained for the EIS results analysis. It has been proposed by *Blanco et al.* [34] and makes use of a series association of two R-CPE elements (circuit 1), as illustrated in Fig. 5.10 a) [10]. The second one is a cascade type two R-CPE elements circuit as shown in Figure 10 b) and is by far the most used one in the literature [5, 6, 10, 33, 35]. Indeed several authors found this circuit to yield the best fit for the behavior of passivation of carbon and stainless steels in different conditions, so that it was also held for a first attempt of EIS analysis in the present work and is referred to as circuit 2. These two models seem to be able to afford a coherent physical interpretation of the EIS results so that the corresponding results and interpretation are discussed in what follows.

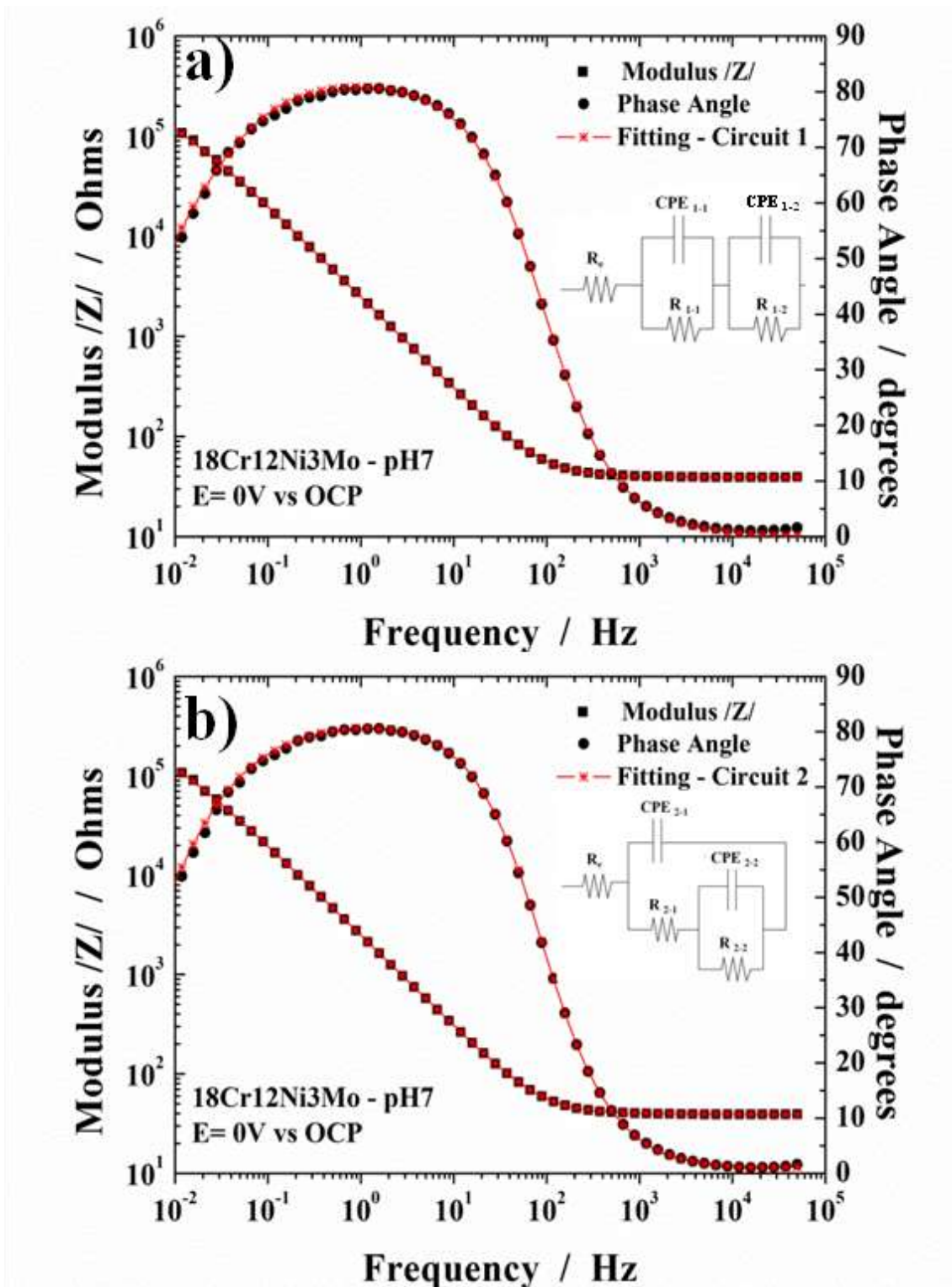


Figure 5.10 - Fitting results and equivalents circuits employed (a) circuit 1 and b) circuit 2) to simulate the experimental EIS data. In these examples, the result from 18Cr12Ni3Mo at pH7 solution was simulated.

The series arrangement of circuit 1 could be associated with a perfectly recovering passive film formation, splitting the interface in a first branch representing the film and a second one representing charge transfer processes on the material surface. Accordingly,

CPE₁₋₁ and R₁₋₁ elements should correspond to the capacitance and resistance of the charge transfer process taking place at the film-electrolyte interface while CPE₁₋₂ and R₁₋₂ should describe the passive layer capacitance and resistance, respectively.

Circuit 2 is usually associated with a porous passive film or with the presence of defects in the passive layer. The interpretation, as suggested by Freire *et al.* [10], is the following one: the fast time constant (high frequency response) can be correlated with the charge transfer process and it is composed by the charge transfer resistance at the metal-electrolyte interface (R₂₋₁) in parallel with the double layer capacitance (simulated by the admittance of CPE₂₋₁); the slow time constant (low frequency response), (R₂₋₂, CPE₂₋₂) has been associated with the redox processes taking place at the surface film, which are associated with the passive film stability [10]. A more detailed description of these parameters can be found elsewhere [36].

The fitting parameters R₁₋₁, R₂₋₁, CPE₁₋₁ and CPE₂₋₁ seem very close to the values expected for a double layer capacitances and resistances and are not discussed here. These results are directly associated with the passive films formed after 1-hour-immersion in solutions of pH 7 to 12 at OCP potential for all laboratory heats. Thus, Table 5.3 and 5.4 depict only the parameters related to the passive film provided by circuit 1 and 2, respectively.

Table 5.3 – CPE₁₋₂, R₁₋₂ and α₁₋₂ values from equivalent circuit 1 obtained after 1h-immersions in different pH solutions for all laboratory heats.

Lab Materials	pH 7			pH 10			pH 12			
	CPE ₁₋₂ (Ω ⁻¹ cm ⁻² s ⁻ⁿ)	R ₁₋₂ (KΩ)	α ₁₋₂	CPE ₁₋₂ (Ω ⁻¹ cm ⁻² s ⁻ⁿ)	R ₁₋₂ (KΩ)	α ₁₋₂	CPE ₁₋₂ (Ω ⁻¹ cm ⁻² s ⁻ⁿ)	R ₁₋₂ (KΩ)	α ₁₋₂	
austenitic	18Cr12Ni3Mo	2.51 x10 ⁻⁴	505	0.91	7.22 x10 ⁻⁵	646	0.88	6.07 x10 ⁻⁵	77.6	0.89
	18Cr12Ni	3.31 x10 ⁻⁴	23.8	0.9	1.64 x10 ⁻⁴	104	0.94	7.87 x10 ⁻⁵	121	0.93
ferritic	18Cr3Mo	1.12 x10 ⁻⁴	79.5	0.91	1.56 x10 ⁻⁴	76	0.86	1.05 x10 ⁻⁴	229	0.91
	18Cr	1.15 x10 ⁻⁴	32.1	0.91	1.19 x10 ⁻⁴	29.1	0.89	1.24 x10 ⁻⁴	148	0.93
duplex	23Cr4.6Ni3Mo	1.21 x10 ⁻⁴	118	0.93	6.79 x10 ⁻⁵	216	0.92	7.54 x10 ⁻⁵	189	0.93
	23Cr4.6Ni	1.14 x10 ⁻⁴	58.7	0.89	3.20 x10 ⁻⁴	339	0.98	1.41 x10 ⁻⁴	3.51	0.89

Concerning the evolution of passive layer stability with pH, both equivalent circuits presented the same tendency. The fitting parameters R_{1-2} , R_{2-2} , CPE_{1-2} and CPE_{2-2} were considerably affected by the Mo addition changes. R_{1-2} and R_{2-2} values suffered an important increase comparing free Mo lab heats and the Mo-containing ones, whereas CPE_{1-2} and CPE_{2-2} values decreased. These Tables could hence, in principle, highlight the influence of Mo addition on the oxide layer stability and also the effect of pH changes. This effect is, as mentioned before, already evident in the higher impedance modulus of Mo containing grades. What must be stressed here, however, is that the use of CPE elements (necessary to account to distorted diagrams), make the number of adjustable parameters of EEC large enough to almost always ensure a perfect adjustment regardless the circuit held. Fig. 5.10 perfectly illustrated this issue. Both circuits, although different and representing different interpretation strategies, convey an excellent fit, the results from which are depicted in Tables 5.3 and 5.4. This "always good" approach is obviously a matter of throwing doubt on the reliability and the robustness of the physical interpretation issuing from the results, but this is almost never considered.

Table 5.4 – CPE_{2-2} , R_{2-2} and α_{2-2} values from equivalent circuit 2 obtained after 1h-immersions in different pH solutions for all laboratory heats.

Lab Materials	pH 7			pH 10			pH 12			
	CPE_{2-2} ($\Omega^{-1} \text{cm}^{-2} \text{s}^{-n}$)	R_{2-2} ($\text{K}\Omega$)	α_{2-2}	CPE_{2-2} ($\Omega^{-1} \text{cm}^{-2} \text{s}^{-n}$)	R_{2-2} ($\text{K}\Omega$)	α_{2-2}	CPE_{2-2} ($\Omega^{-1} \text{cm}^{-2} \text{s}^{-n}$)	R_{2-2} ($\text{K}\Omega$)	α_{2-2}	
austenitic	18Cr12Ni3Mo	3.75×10^{-5}	131	0.86	1.01×10^{-5}	654	0.86	3.81×10^{-5}	105	0.94
	18Cr12Ni	4.95×10^{-5}	30.5	0.91	4.78×10^{-5}	194	0.88	5.42×10^{-5}	159	0.95
ferritic	18Cr3Mo	1.69×10^{-5}	160	0.92	1.74×10^{-5}	89	0.85	5.39×10^{-5}	162	0.91
	18Cr	10.8×10^{-5}	26.3	0.94	3.28×10^{-5}	29.4	0.91	5.77×10^{-5}	129	0.92
duplex	23Cr4.6Ni3Mo	7.28×10^{-5}	91.1	0.84	5.06×10^{-5}	23	0.87	4.19×10^{-5}	241	0.91
	23Cr4.6Ni	5.15×10^{-5}	60.4	0.88	7.13×10^{-5}	135	0.93	5.39×10^{-5}	123	0.98

Another sound evidence of an intrinsic problem on this fitting procedure comes from the deep analysis of the data consistency. Table 5.5 shows the errors related to the fitting parameters depicted in Tables 5.3 and 5.4, taking the pH 7 electrolyte at open circuit conditions for the 18Cr12Ni3Mo steel as an example.

Table 5.5 - The standard errors related to the fitting parameters depicted in circuit 1 and 2 for the 18Cr12Ni3Mo SS at pH 7 condition.

Fitted parameter	Error circuit 1 (%)	Error circuit 2 (%)
R_e	0.4	0.4
CPE_{x-1}	60	0.6
α_{x-1}	3	0.2
R_{x-1}	77	4
CPE_{x-2}	111	75
α_{x-2}	11	16
R_{x-2}	52	24

It clearly appears that several parameters are associated to very large uncertainties which undoubtedly compromise the model reliability. Indeed, large errors mean that the fitting is not sensible to the value of these parameters, or in other words: “they are not the good parameters” or “it is not the good model” in spite of the excellent curve adjustment shown in Fig. 5.10. So that it is a point of major importance. Indeed, if we have just retained the excellent fitting depicted in the Fig 5.10, we should have validated what it is now clearly seen as an inconsistent result. The inadequacy of these models do preclude in these conditions a deep analysis of the film stability based on EIS measurements.

However, before definitively ascribing this inconsistency to the inadequacy of the EECs proposed in the literature, it is also interesting to notice that the largest errors appear for the branches representing the passive film. This could be effectively due to the inadequacy of the model, as mentioned before, but also to the fact that the film is not long time aged. As in the case of XPS analysis, the sample preparation can also have an effect on the impedance behavior. To better understand this issue, we performed a new set of experiments with long time aged films. Furthermore, these results have been analyzed thanks to a deeper and strict mathematical description of CPE behavior we have developed recently [37]. We introduce here only the basic equations needed to analyze this issue. The complete paper is given in the annexes. Firstly we have obtained the CPE parameters from the analysis of the high frequency behavior ($f \gg$) of the imaginary component of the impedance Z_i [38]. The effective CPE exponent α_{eff} was calculated according to

$$\alpha_{\text{eff}}(f) = \left| \frac{d \log |Z_i(f)|_{f \gg}}{d \log f} \right|, \quad (5.1)$$

whereas the effective CPE parameter Q_{eff} was obtained from

$$Q_{\text{eff}}(f) = \sin \left[\frac{\alpha_{\text{eff}}(f) \pi}{2} \right] \frac{-1}{Z_i(f) (2\pi f)^{\alpha_{\text{eff}}(f)}}. \quad (5.2)$$

In this form both parameters appear as a function of frequency since they depend on the frequency at which the slope is evaluated. If we have a CPE behavior, for frequencies much larger than the characteristic frequency ω_0 of the high frequency capacitive loop, a power law of the form $Z_i \propto f^{-\alpha}$ is expected so the values obtained from (5.1) and (5.2) should converge to a constant value.

These expressions allow us to proceed to a more sharp simulation since, as seen before, the large number of adjustable parameters issuing from EEC almost always convey very good apparent adjustments even if the intrinsic consistency is poor. Figs. 5.11 illustrates the goodness of this treatment for a pH 7 long aged (3 days in air, 5 days in the electrolyte) 18Cr12Ni austenitic lab SS. It clearly shows a two time-constant related to two CPEs.

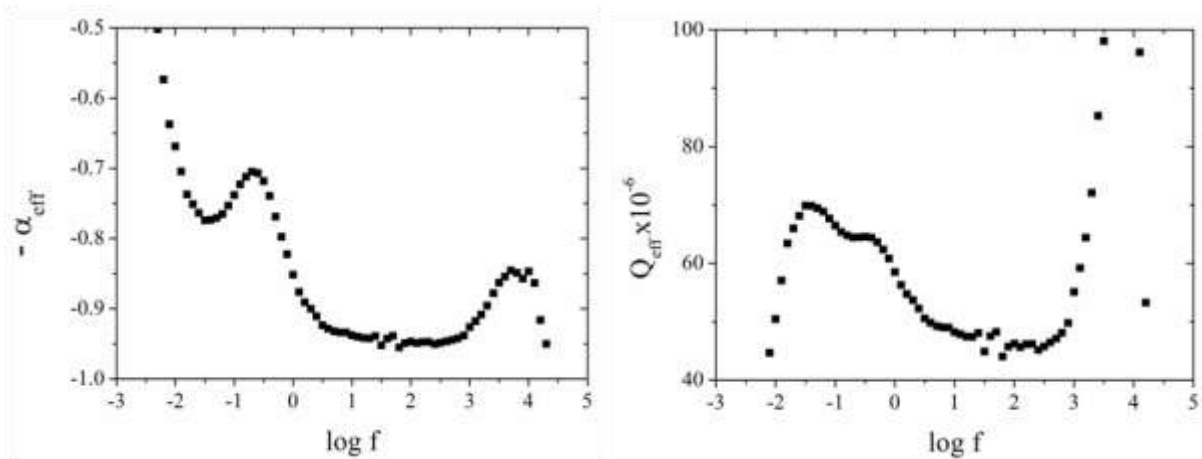


Figure 5.11 – CPE behavior for a long aged (3 days in air, 5 days in the electrolyte) 18Cr12Ni SS at pH 7 obtained from EIS measurements with the help of Equations (5.1) and (5.2). **Left:** $-\alpha_{\text{eff}}$, **right:** Q_{eff} .

As mentioned before, the behavior is very nice, showing two consecutive relaxations associated to both CPEs clearly observed for both α_{eff} and Q_{eff} . The high frequency ($f > 1$ kHz) wave is an artifact related to the geometry induced deviations as explained before.

Concerning the EEC fitting, Fig. 5.12 illustrates the fact that Circuit 1 does not succeed to simulate this behavior and can be disregarded, which should not be possible with the straightforward good EIS fitting as shown in Fig. 5.10. Indeed, this EEC does not capture the two relaxations of effective CPE parameters.

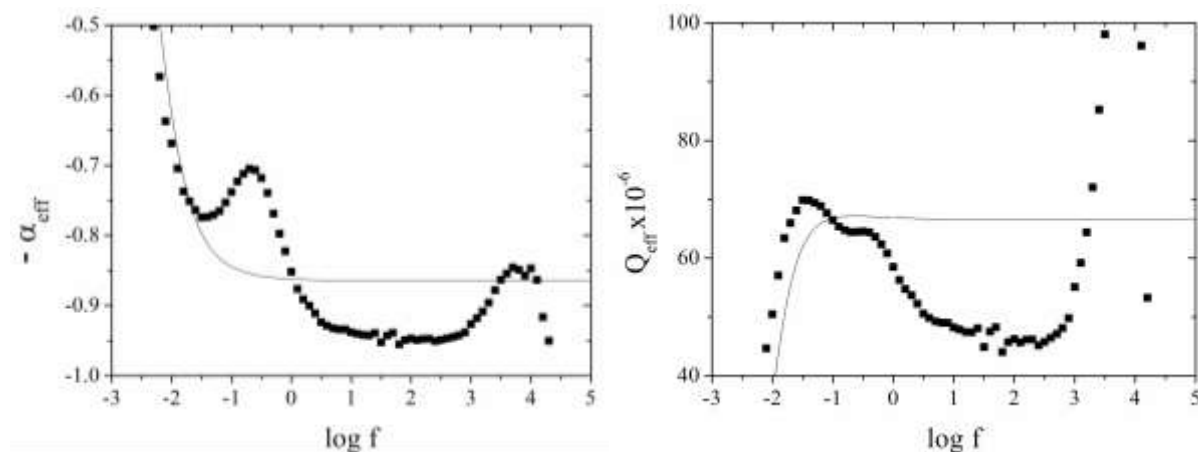


Figure 5.12 – CPE behavior for a long aged (3 days in air, 5 days in the electrolyte) 12Cr12Ni SS at pH 7 obtained from EIS measurements with the help of Equations (5.1) and (5.2). **Left:** $-\alpha_{eff}$, **right:** Q_{eff} . Point stand for experiments whereas solid lines corresponds to results from the fitting Circuit 1.

Results obtained with Circuit 2 were also not conclusive. On the other hand, a new circuit called Circuit 3 and depicted in Figure 5.13 allowed very nice results to be obtained.

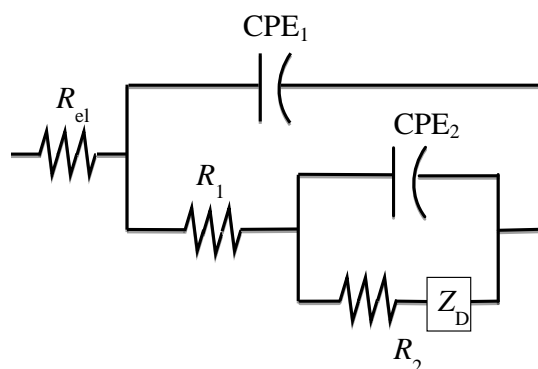


Figure 5.13 – Circuit 3, the one having provided the best results for EEC - EIS modeling.

This circuit is the equivalent to Circuit 2 to which we added a new mass transfer element which seemed to be mandatory for the best results of the ensemble of EIS diagrams measured. Since the cascade branch is often related to redox processes taking place at the film-electrolyte interface, its presence and the better results it convey should indicate that

these processes are at least partially under mass transfer control. It allowed the CPEs behavior to be very well emulated with two time constants as can be seen in Fig. 5.14 below:

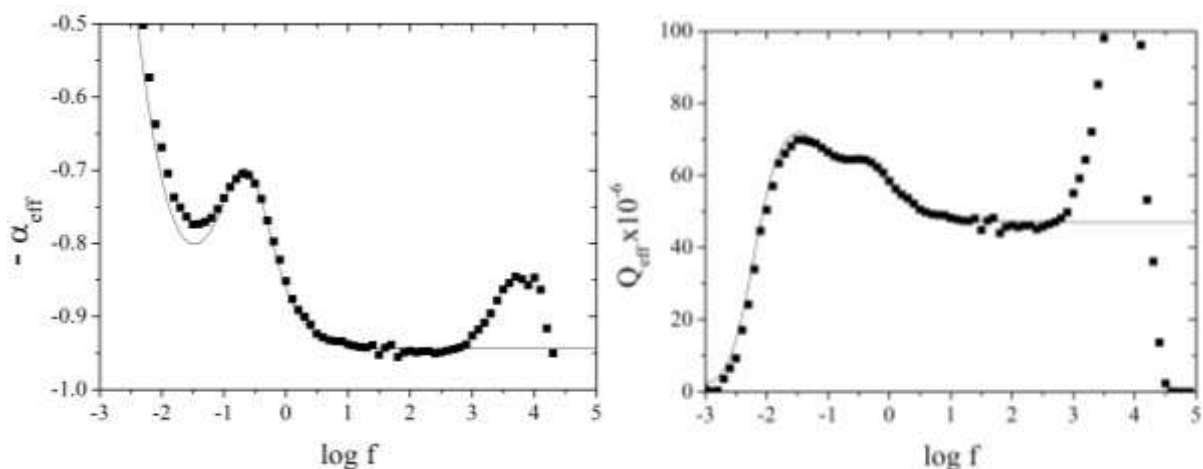


Figure 5.14 – CPE behavior for a long aged (3 days in air, 5 days in the electrolyte) 12Cr12Ni SS at pH 7 obtained from EIS measurements with the help of Equations (5.1) and (5.2). **Left:** $-\alpha_{eff}$, **right:** Q_{eff} . Point stand for experiments whereas solid lines corresponds to results from the fitting Circuit 3.

Circuit 3 was thus held for the comparison between 18Cr12Ni and 18Cr12Ni3Mo lab heats since it gave the better results in terms of smallest values of standard errors of fitted parameters and the best capture of CPE behavior. Fig. 5.15 shows the results obtained for pH 7 long aged (3 days in air, 5 days in the electrolyte) 18Cr12Ni3Mo SS superimposed to those from 18Cr12Ni SS (cf Fig. 5.11). Unlikely to 18Cr12Ni, the two time constants are not so clearly discernable.

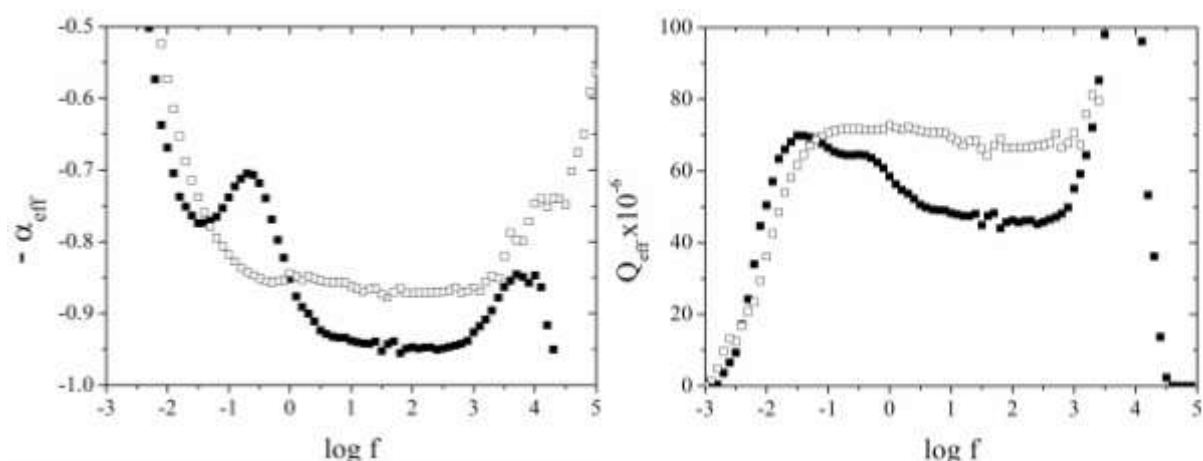


Figure 5.15 – CPE behavior for long aged (3 days in air, 5 days in the electrolyte) 18Cr12Ni SS (solid symbols) and 18Cr12Ni3Mo SS (open symbols) at pH 7 obtained from EIS measurements with the help of Equations (5.1) and (5.2). **Left:** $-\alpha_{eff}$, **right:** Q_{eff} .

Circuit 3 has also succeeded to fit the CPE behavior for the 18Cr12Ni3Mo samples, as seen in Fig. 5.16. The modeling is good enough to capture the two time constants evolution (see the curve inflexion at ca $f = 10$ Hz).

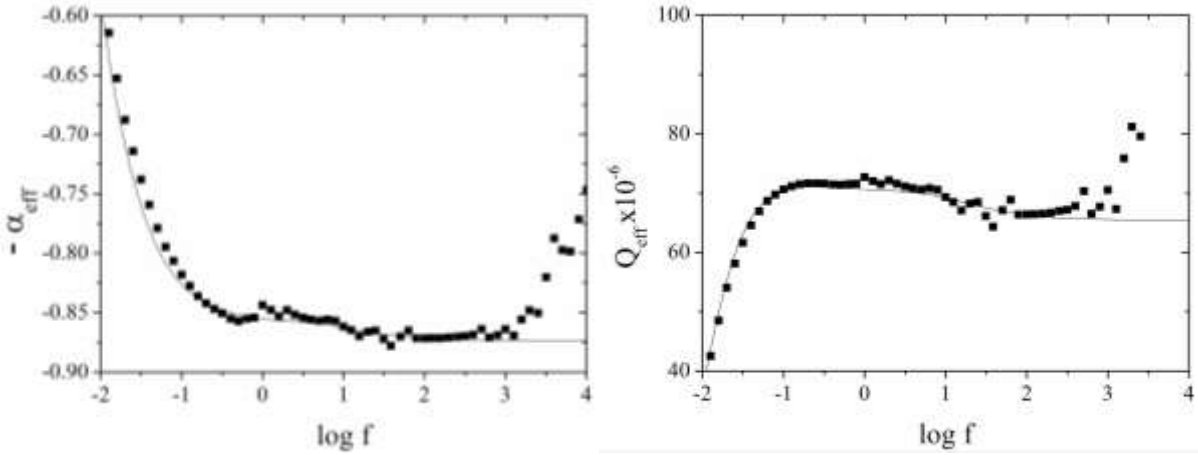


Figure 5.16 – CPE behavior for a long aged (3 days in air, 5 days in the electrolyte) 12Cr12Ni3Mo SS at pH 7 obtained from EIS measurements with the help of Equations (5.1) and (5.2). **Left:** $-\alpha_{eff}$, **right:** Q_{eff} . Point stand for experiments whereas solid lines corresponds to results from the fitting Circuit 3.

In spite of the drawbacks of EEC interpretation presented in the last paragraphs it appears that the analytical treatment detailed in the annexes, coupled to circuit 3, allowed robust and confident results to be gathered. The last step is hence to quantify and evaluate the role of Mo based on these results. The first effect of Mo is to merge the two relaxations. Indeed, in the absence of Mo (18Cr12Ni), the characteristic frequencies are largely different

$$f_1 = \frac{1}{2\pi} (Q_1 R_1)^{-1/\alpha_1} = 0.1314 \text{ Hz} ; f_2 = \frac{1}{2\pi} (Q_2 R_2)^{-1/\alpha_2} = 0.00435 \text{ Hz}$$

Whilst they become much closer in the presence of Mo (18Cr12Ni3Mo lab SS)

$$f_1 = \frac{1}{2\pi} (Q_1 R_1)^{-1/\alpha_1} = 0.1813 \text{ Hz} ; f_2 = \frac{1}{2\pi} (Q_2 R_2)^{-1/\alpha_2} = 0.0606 \text{ Hz}$$

These results indicate that the Mo effect is to strongly boost the characteristic frequency of the second branch in Fig. 5.13, that means, the internal cascade element attributed to redox processes taking place in the film – electrolyte interface, which can be seen as a first indirect evidence of the presence of Mo in the film for the Mo containing grades as it was also established by XPS. The capacitance estimation can help to corroborate

this hypothesis. To achieve this we take advantage of previous studies of Brug [39] so as to estimate the actual capacitance values according to the following expressions:

$$C_1 = \left[Q_1 (R_{el}^{-1} + R_1^{-1})^{(\alpha_1-1)} \right]^{1/\alpha_1} / S_0 = 13.34 \mu\text{F cm}^{-2} \text{ for 18Cr12Ni and } 7.28 \mu\text{F cm}^{-2} \text{ for 18Cr12Ni3Mo}$$

$$C_2 = \left[Q_2 \left((R_{el} + R_1)^{-1} + R_2^{-1} \right)^{(\alpha_2-1)} \right]^{1/\alpha_2} / S_0 = 23.09 \mu\text{F cm}^{-2} \text{ for 18Cr12Ni and } 0.87 \mu\text{F cm}^{-2} \text{ for 18Cr12Ni3Mo}$$

It clearly appears that Mo has a net effect on the results obtained from EIS measurements. The capacitance of the circuit branch assimilated to the film (C_1) for the Mo-containing grades is roughly half of that in the absence of Mo, which is expected for less reactive or permissive films that are hence supposed to ensure better corrosion resistance. Here again, this can be seen as an electrochemical indirect sign of the presence of Mo in the film, which would also stand for the huge decrease of the capacitance associated to the redox processes at the film – electrolyte interface. This ensemble of results claim for a positive effect of Mo and its presence in the passive film, which is in good agreement with XPS analysis at pH 7 condition presented above.

5.4. CONCLUSION

The Mo addition in austenitic grades has enriched the passive film with Cr ions whereas the Fe contents were impoverished. However, for ferritic and duplex SS, Mo addition decreases the oxidized Cr content in the film by incorporating oxidized Mo within it. Moreover, for all materials, the inner layers were always enriched by Cr oxide whereas the outer are generally enriched by Fe and Mo oxides.

As far as the pH changes are concerned, the amount of Mo in the passive layer raises from alkaline to neutral medium, about 5 to 7 % for all lab SS, which is an important shifting. Furthermore, oxidized Cr content in passive layer increases a lot passing from air to aqueous environments and also increasing the pH, which was associated with the Fe dissolution in the different media.

EIS results have shown to be hardly exploitable due to an intrinsic problem of EEC analysis with CPE elements that convey a number of adjustable parameters that almost always allow a good fitting to be obtained regardless the EEC details. A more complete mathematical treatment allowed us to get some relevant information on the Mo role that goes in the sense of confirming XPS measurements, that is, are in good agreement with the idea of

Mo presence in the passive film and hence an improvement in its corrosion resistance properties.

5.5. REFERENCES

- [1] Y.C. Lu, and C.R. Clayton. Corrosion Science 29 (1989) 927.
- [2] G.O. Ilevbare, and G.T. Burstein, Corrosion Science 43 (2001) 485.
- [3] M.F. Montemor, A. Simões, M.G.S. Ferreira, M. Da Cunha Belo, Corros. Sci. 41 (1999) 17.
- [4] V. Vignal, J.M. Olive, and D. Desjardins. Corrosion Science 45 (1999) 869.
- [5] C.M. Abreu, M. J. Cristóbal, R. Losada, X. R. Nóvoa, G. Pena, M. C. Pérez. Electrochimica Acta 49 (2004) 3049.
- [6] K. Sugimoto, Y. Sawada, Corros. Sci. 17 (1977) 425.
- [7] I. Olefjord, B. Brox, and A. U. Jelvestam. J. Electrochem. Soc. 132 (1985) 2854.
- [8] I. Betova, M. Bojinov, T. Laitinen, K. Mäkelä, P. Pohjanne and T. Saario, Corrosion Science 44 (2002) 2675.
- [9] I. Betova, M. Bojinov, T. Laitinen, K. Mäkelä, P. Pohjanne and T. Saario. Corrosion Science 44 (2002) 2699.
- [10] A. J. Davenport, A. J. Dent, M. Monir, J. A. Hammons, S. M. Ghahari, P. D. Quinn and T. Raymentb. J. Electrochem. Soc. 158 (2011).
- [11] R. C. Newman. Corrosion Science 25 (1985) 331.
- [12] R. C. Newman. Corrosion Science 25 (1985) 341.
- [13] A. Pardo, M.C. Merino, A.E. Coy, F.Viejo, R. Arrabal and E. Matykina, Corrosion Science 50 (2008) 780.
- [14] A. Pardo, M.C. Merino, A.E. Coy, F.Viejo, R. Arrabal and E. Matykina, Corrosion Science 50 (2008) 1796.
- [15] S. J. Doh, J. H. Je, J. S. Kim, K. Y. Kim, H. S. Kim, Y. D. Lee, J. M. Lee and Y. Hwu. Nuclear Instruments and Methods in Physics Research Section B: Beam Interactions with Materials and Atoms 199 (2003) 211.
- [16] V. Vignal, O. Delrue, O. Heintz and J. Peultier. Electrochimica Acta 55, 7118-7125.
- [17] R. Qvarfort, Corrosion Science 40. 40 (1998) 215.
- [18] M. Kimura, M.Kaneko and N. Ohta, ISIJ Int 42 (2002). 1399.

- [19] T. J. Mesquita, E. Chauveau, M. Mantel, N. Kinsman and R.P. Nogueira. *Materials Chemistry and Physics*, 126 (2011) 602
- [20] T. J. Mesquita, E. Chauveau, M. Mantel, N. Kinsman and R. P. Nogueira. 10th Brazilian Stainless Steel Conference – International Edition., 2010.
- [21] T. J. Mesquita, E. Chauveau, M. Mantel, N. Kinsman and R. P. Nogueira. 61st Annual Meeting of the International Society of Electrochemistry, 2010.
- [22] T. J. Mesquita, E. Chauveau, M. Mantel, N. Kinsman and R.P. Nogueira. *Revue de Métallurgie* (2011).
- [23] L. Freire, X. R. Nóvoa, M. F. Montemor and M. J. Carmezim, *Materials Chemistry and Physics* 114 (2009) 962.
- [24] L. Freire, M. J. Carmezim, M. G. S. Ferreira, M. F. Montemor, *Electrochimica Acta* 55 (2010) 6174.
- [25] C. O. A. Olsson and D. Landolt. *Electrochimica Acta* 48 (2003) 1093.
- [26] M. Houmard, G. Berthomé, L. Boulangé and J. C. Joud. *Corrosion Science* 49 (2007) 2602.
- [27] M. Mantel, And J.P. Wightman. *Surfaces and Interfaces Analysis* 21 (1994) 595.
- [28] C. M. Abreu, M. J. Cristóbal, R. Losada, X. R. Nóvoa, G. Pena and M. C. Pérez, *Electrochimica Acta* 51 (2006) 2991.
- [29] A. Bautista, G. Blanco, F. Velasco, A. Gutiérrez, L. Soriano, F. J. Palomares and H. Takenouti. *Corrosion. Science* 51 (2009) 785.
- [30] N. P. N. Ramasubramanian, and R. D. Davidson. *J. Electrochem. Soc.* 132 (1985) 793.
- [31] V. Guiñón-Pina, A. Igual-Muñoz and J. García-Antón, *Corrosion Science* 53, 575-581.
- [32] A. Alamr, D. F. Bahr and M. Jacroux, *Corrosion Science* 48 (2006), 48, 925.
- [33] S. S. El-Egamy and A. W. A. Badaway, *Journal of Applied Electrochemistry* 34 (2004) 1153.
- [34] G. Blanco, A. Bautista, and H. Takenouti. *Cement and Concrete Composites* 28 (2006) 212.
- [35] M. Sánchez, J. Gregori, C. Alonso, J. J. García-Jareño, H. Takenouti and F. Vicente, *Electrochimica Acta* 52 (2007) 7634.
- [36] S. Joiret, M. Keddou, X. R. Nóvoa, M. C. Pérez, C. Rangel and H. Takenouti, *Cement and Concrete Composites* 24 (2002) 7.

- [37] P. Córdoba-Torresa, T.J. Mesquita, R.P. Nogueira. *Electrochimica Acta*, submitted. (see annex 3)
- [38] M.E. Orazem, N. Pébère, B. Tribollet, J. *Electrochem. Soc.* 153 (2006) B129.
- [39] G.J. Brug, A.L.G. Van Den Eeden, M. Sluyters-Rehbach, J.H. Sluyters, J. *Electroanal. Chem.* 176 (1984) 275.

***GENERAL
CONCLUSION***

6. GENERAL CONCLUSION

Although widely used as an increasing corrosion resistance element in acidic environments, the influence of Mo addition on pitting corrosion resistance of stainless steels is not very clear in alkaline media. The alkaline condition is an important environment for stainless steels applications, such as petrochemical, chemical and paper industries and also the concrete reinforcement. Thus, understanding Mo action on corrosion resistance in these media is hence of major importance, particularly for new lean grades with low nickel and molybdenum contents which present a good balance between the properties required in these applications and the final cost of the material. The main objective of this thesis was to analyse of the role of Mo addition in austenitic, ferritic and duplex SS in several pH conditions. We focused on getting some new insights on the mechanisms of Mo on the pitting corrosion resistance of different SS in chloride solutions from acidic to alkaline pH and providing a possible scenario for Mo role in a environment simulating the concrete reinforcement application.

A first remark concerns the fact that analysis of Mo effect for austenitic SS indicated an unexpected behavior in alkaline media: - the positive influence of Mo on the pitting corrosion resistance of austenitic SS decreased from acidic to alkaline media. Moreover, an absence of the positive role of Mo on the pitting repassivation was noticed during the tribocorrosion measurements of austenitic SS in pH 10 condition. In acidic solution, however, Mo addition accelerates the repassivation kinetics of this material.

Thanks to XPS experiments, oxidized Mo was found in the passive layer of the 18Cr12Ni3Mo, and an enrichment of Mo and Ni was also detected at the passive film/substrate interface in all studied conditions. These results allowed the following mechanism to be proposed for the Mo effect on pitting corrosion of austenitic SS in alkaline pH:

- 1) In acidic media, the addition of Mo in austenitic SS enriches the passive film with stable Mo oxides increasing then its corrosion protection and retarding the pitting nucleation. On the other hand, in alkaline media, this small amount of Mo in the passive layer (see Fig. 6 a)) is not sufficient to increase the corrosion resistance of the passive layer because the Mo-oxides in alkaline media are not as stable as they are in acidic ones. According to the Pourbaix diagram of Mo (see Fig 1.5), MoO_3 is stable in low pH whereas the MoO_4^{2-} is stable in alkaline domain. Thus, the stable anionic form of the Mo species in

alkaline media (MoO_4^{2-}) should not prevent the Cl^- ions attack. We can hence conclude that pit nucleation happens in the same way for Free and Mo containing austenitic SS under alkaline media. This fact is in good agreement with monotonic decrease of Mo effect when the pH increases.

- 2) Mo cations are usually dissolved from the material to the solution when the pitting attack takes places. In the case of alkaline solution, these Mo ions should be MoO_4^{2-} and could not stop the Cl^- Ions attack. However, at the bottom of the pits where the pH significantly decreases and the MoO_3 becomes stable, the penetration of Cl^- would be blocked by the presence of Mo. So, the repassivation process could be slightly favored, as shown in Fig. 6.1 b). This assumption is in good agreement with the results found in electrochemical and tribocorrosion experiments for the austenitic SS.

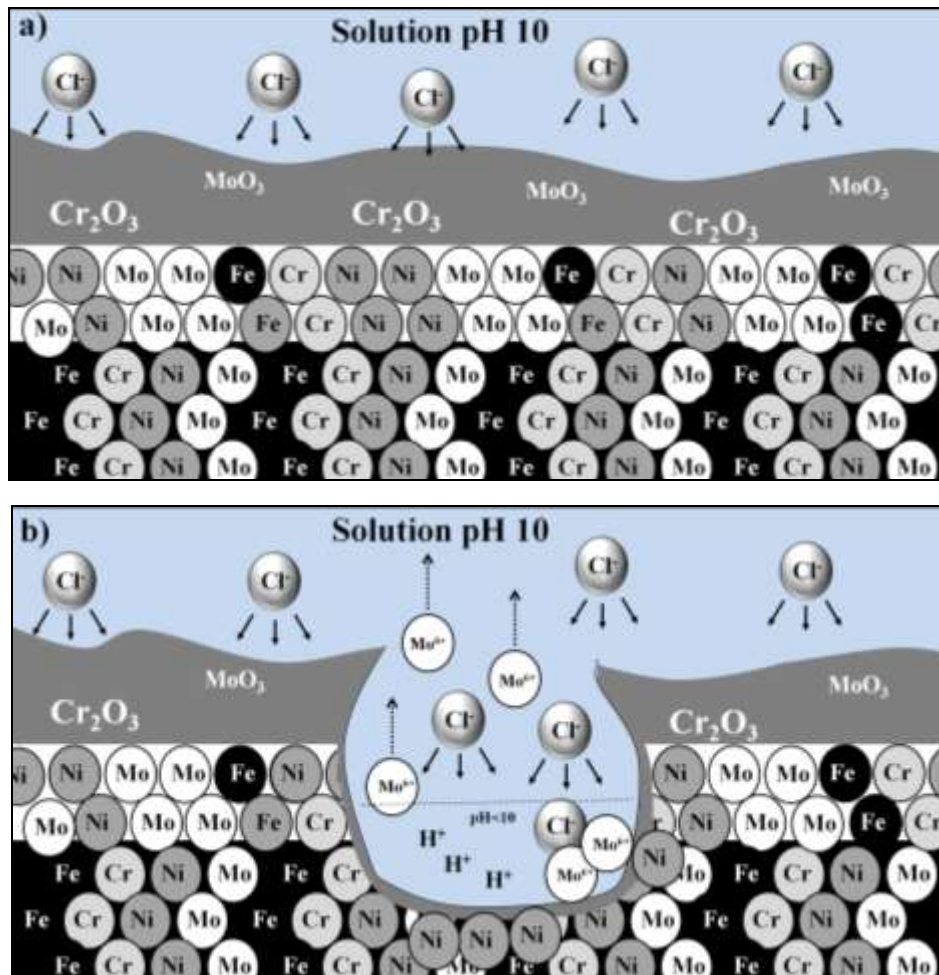


Figure 6.1 – Schematic illustration of a) the passive film formed in the 18Cr12Ni3Mo austenitic SS and b) the small effect of Mo on the pitting corrosion of austenitic SS under alkaline media. It's worth noticing the presence of Mo oxides in the passive layer and also the enrichment of Mo and Ni in the passive film/substrate interface

- 3) Another important detail about this proposed mechanism for austenitic SS is the fact that a high amount of metallic Ni in the passive film/substrate interface was found for both 18Cr12Ni and 18Cr12Ni3Mo materials. According to some authors, this Ni enrichment plays a fundamental role in the repassivation process. Consequently, the influence of Mo on the pitting corrosion under alkaline conditions could be masked by the presence of Ni in the bulk composition and in the passive film/substrate interface. This hypothesis is also in good agreement with all results presented above.

For the ferritic alloys, there was a very good agreement between the results from laboratory and industrial heats with respect to the Mo influence on pitting corrosion resistance in all pH condition. In others words, Mo addition always increased the pitting corrosion resistance for the ferritic SS. The Mo effect for this type of SS under aggressive alkaline solutions was not only associated to a hindered pit initiation (as shown by the ZRA results in Fig. 3.7), but also due to kinetic aspects related to the modification of electrolyte composition within the pits as shown by the tribocorrosion results. So, our proposal for the Mo mechanism of ferritic SS under alkaline conditions is the following:

- 1) As for austenitic SS, a small presence of Mo oxides was also detected into the passive layer of the ferritic SS in alkaline doomain. However, for 18Cr3Mo SS, a high Mo concentration was observed in the film/substrate interface as illustrated in Fig. 6.2 a). Thus, this region could be a source of Mo ions to balance the Cr vacancies, when this last is attacked by the Cl⁻ ions.
- 2) Moreover, this large amount of Mo in the passive layer/bulk material interface could also stop the pitting propagation and then accelerate the repassivation. Firstly, because a high quantity of Mo would be dissolved within the pit and secondly because of the absence of Ni that would mask the Mo positive effect. A schematic illustration of the Mo mechanism on the repassivation is described in Fig. 6.2 b).

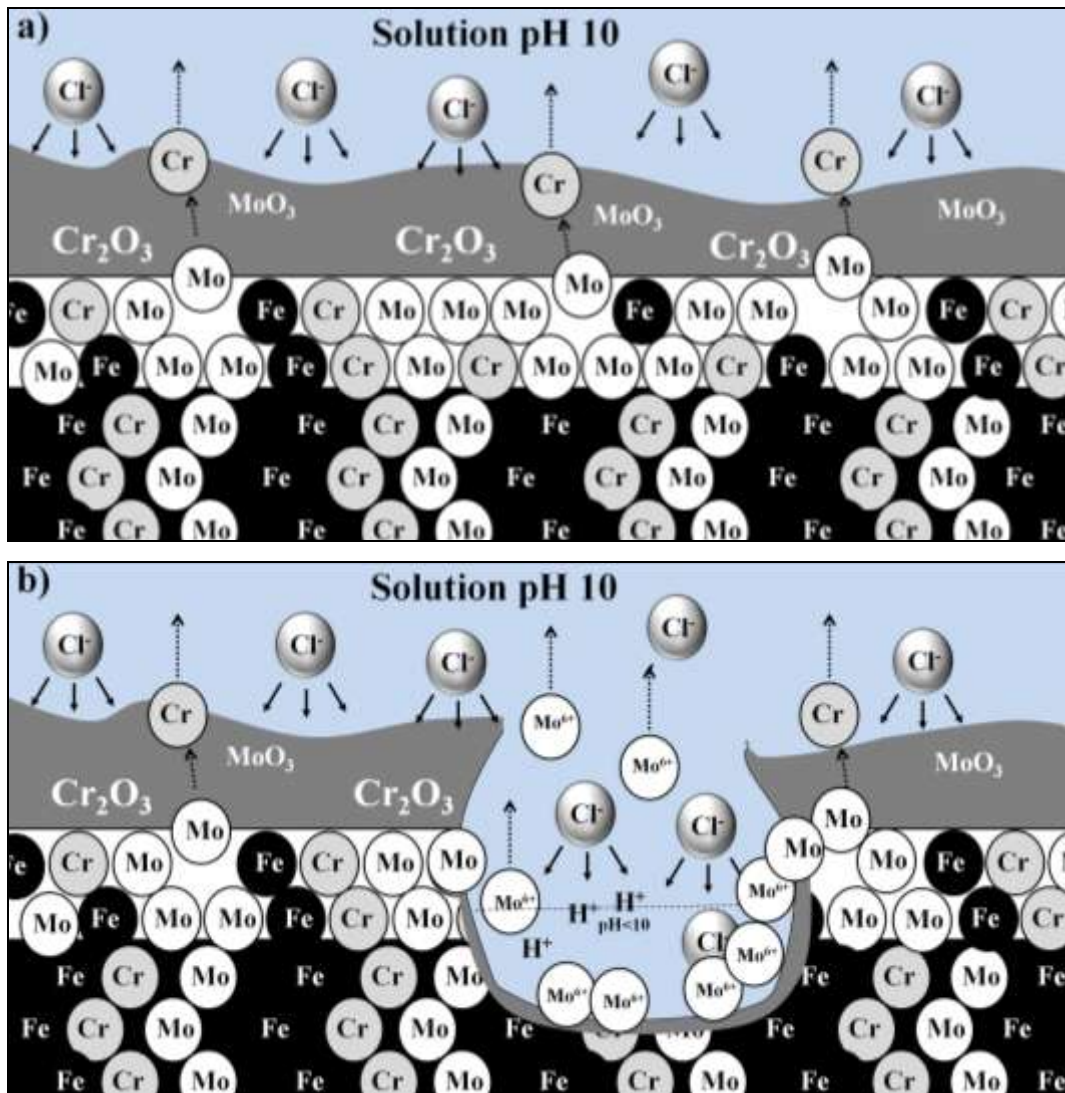


Figure 6.2 – Schematic illustration of a) the passive film formed in the 18Cr3Mo austenitic SS and b) Mo effect on inhibiting the pitting propagation of ferritic SS under alkaline media.

The Mo effect on the corrosion resistance of duplex SS is very complex as the microstructure of this material is composed by both austenite and ferrite. So, when the 23Cr4.6Ni3Mo SS is attacked by the Cl^- ions from the alkaline media, Mo has a stronger beneficial effect on the corrosion resistance of ferrite compared to austenite, consequently, the austenite phase is preferentially corroded. Therefore, we simply associated both the Mo mechanism for the austenitic SS and for the pure ferritic SS to better understand the Mo role for the duplex. Thus, the higher concentration of Mo in the ferrite phase would enrich its pitting corrosion resistance. Then, the Mo-rich ferrite would become more resistant than the austenite. Therefore, the pit would nucleate in the austenite phase, even if this phase contains a higher Ni contents, as shown in Fig. 6.3.

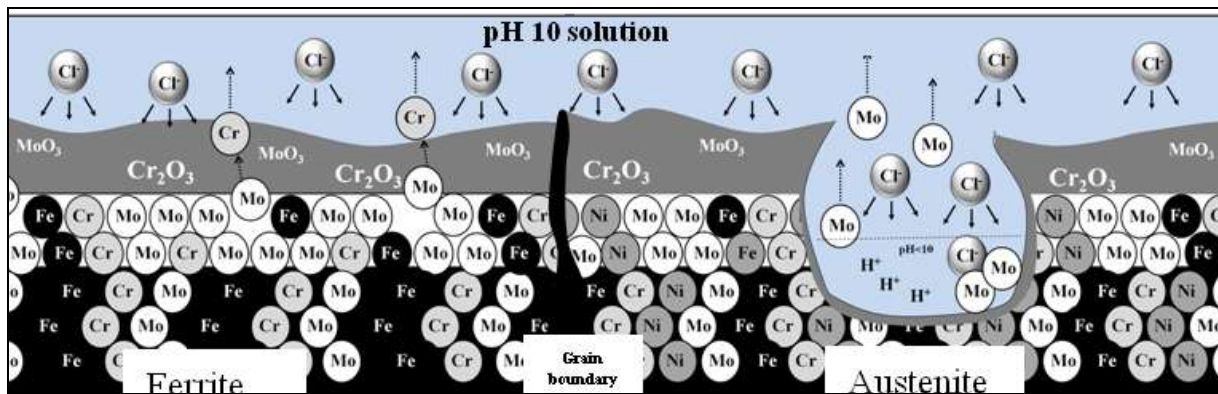


Figure 6.3 – Schematic illustration of the Mo mechanism for duplex SS. The pitting corrosion occurs preferentially in the austenite phase.

Careful examination of all results brought us to these innovative conclusions about the Mo mechanism on the pitting corrosion of austenitic, ferritic and duplex SS in alkaline media. However, these conclusions must be strengthened by further investigations as will be described in the following perspective section.

PERSPECTIVES

OUTLINE

7. PERSPECTIVES	155
7.1. INTRODUCTION	155
7.2 AN IN-SITU STUDY OF THE ROLE OF MOLYBDENUM ON PASSIVATION OF STAINLESS STEELS	155
7.3. SS PITTING CORROSION RESISTANCE - THE STUDY OF Mo AND N SYNERGY	156
7.4. IDEAS FOR DIRECT EXPERIMENTS ON THE POROUS CONCRETE ENVIRONMENT	159

7. PERSPECTIVES

7.1. INTRODUCTION

In this short chapter, some ideas for further works are going to be introduced which could bring out some perspectives with respect to an even better comprehension of Mo mechanism on pitting corrosion resistance of SS.

Firstly, we submitted a proposal to the ESRF (European Synchrotron Radiation Facility) which will be presented bellow. Secondly, a new hypothesis about a possible synergy between Mo and N will be briefly discussed based in some preliminary results. Finally, some ideas for a further collaboration with the IPT – Instituto de Pesquisas Tecnológicas – Sao Paulo – Brazil about direct measurements of concrete reinforcement corrosion will be commented.

7.2 AN IN-SITU STUDY OF THE ROLE OF MOLYBDENUM ON PASSIVATION OF STAINLESS STEELS

The major perspective of this work remains in the possibility of using the Synchrotron energy to complement our investigation about the role of Mo on the passivation of SS in several different pH. A project was submitted to the European Synchrotron Radiation Facility requesting the Beam Time for our *in-situ* experiments. The main objective of our proposal was to probe the chemical environment around the Mo ions in the protective oxide layer formed on austenitic, ferritic and duplex SS under different pH and potential conditions by in situ experiments. XAS is the most suitable technique for such kind of investigations and will supply the structural information about Mo local environment. Moreover, this study will permit to assess the presence of Mo and the way it is chemically bonded in the passive film during film formation. This will be achieved by in situ time spaced spectra obtained at different electrochemical potentials starting from a film-free surface and surveying the film formation and growth as the potential is anodically shifted up. More details about this project can be found in the annex 2.

The ensemble of results provided by XAS experiments will yield fundamental information about the film composition and evolution. This would represent a major advance in the understanding of SS film properties.

7.3. SS PITTING CORROSION RESISTANCE - THE STUDY OF Mo AND N SYNERGY

During this PhD work, preliminary investigations about the possible synergy between Mo and N were done. To do so, new laboratory heats containing different amount of Mo and N were provided by UGITECH Company, as can be seen in the Table 7.1. The details of lab alloy manufacturing process could be found in the annex 1.

Table 7.1 - Chemical composition of laboratory austenitic and austenitic LN stainless steels elaborated by UGITECH research center.

Laboratory Material		C	Si	Mn	Ni	Cr	Mo	N	Al	S*	PREn
Austenitic	18Cr12Ni	0.025	0.594	1.012	12.067	17.999	0.004	0.023	0.0033	13	18.38
	18Cr12Ni3Mo	0.028	0.571	1.018	11.995	18.003	2.989	0.029	0.0036	15	28.33
Austenitic LN	18Cr12Ni0.1N	0.025	0.502	1.074	11.77	18.06	0.007	0.115	0.001	11	19.92
	18Cr12Ni3Mo0.1N	0.025	0.510	1.011	12.09	17.88	2.952	0.107	0.001	17	29.33

As it was done in chapter 3 for the study of Mo effect on the pitting corrosion resistance, the synergy between Mo and N was investigated from acidic to alkaline conditions in the presence of Cl⁻ ions by electrochemical polarization measurements. Fig. 7.1 shows the typical polarization curves obtained for 18Cr12Ni, 18Cr12Ni0.1N, 18Cr12Ni3Mo, and 18Cr12Ni3Mo0.1N in different pH conditions pH 2, 4, 7, 10, 12 and 12.6.

The only difference between these lab heats is the presence or absence of Mo and N as described in Table 7.1. Therefore, we could associate the corrosion behaviors to their Mo and/or N concentration as well as to the Mo+N synergy. The effect of Mo on austenitic SS pitting corrosion resistance of austenitic SS in absence of N have already been investigated in chapter 3 by comparing the polarization curves for the 18Cr12Ni, 18Cr12Ni1Mo, 18Cr12Ni2Mo and 18Cr12Ni3Mo in different pH conditions as presented in Figs 3.8. A huge positive effect of Mo on the pitting corrosion resistance of laboratory austenitic grades was

detected in acidic and neutral chloride environments (pH 2, 4 and 7) whereas this positive effect of Mo was not so clear in the alkaline domain.

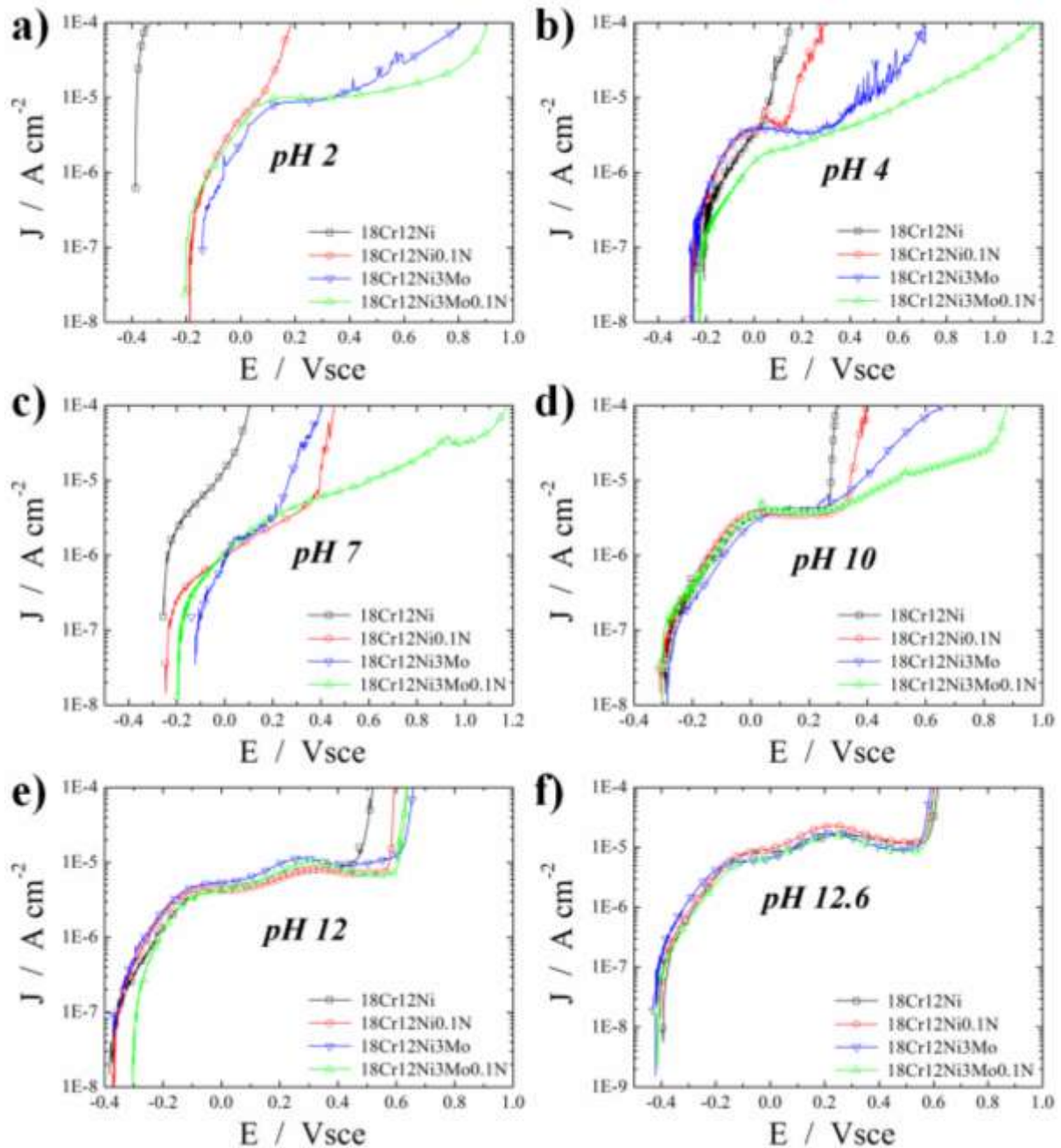


Figure 7.1 - Polarization curves obtained for lab austenitic and austenitic LN SS in several media: **a)** pH 2; **b)** pH 4 **c)** pH 7, **d)** pH 10, **e)** pH 12 and **f)** pH 12.6 at 25°C.

In Fig. 7.1, however, we were interested in the effect of N in the presence or absence of Mo and in their relationship concerning the SS pitting corrosion. So, comparing the polarization curves for 18Cr12Ni and 18Cr12Ni0.1N in Fig. 7.1, the addition of 0.1% of N shifted the E_{pit} to more noble values and increased the passivation plateau in all different pH in the absence of Mo. On the other hand, in the presence of Mo, the addition of 0.1N seems to

have an effect on enhancing the E_{pit} without changing the passivation plateau. (for E_{pit} take in at $100\mu\text{A cm}^{-2}$)

The effect of N on the E_{pit} of austenitic SS in presence or absence of Mo as a function of pH is shown in Fig. 7.2. This Fig. presents the difference ΔE_{pit} between 18Cr12Ni0.1N and 18Cr12Ni lab SS or 18Cr12Ni3Mo0.1N and 18Cr12Ni3Mo. From this Fig., the positive effect of N on the pitting corrosion resistance of austenitic LN was confirmed in both presence and absence of Mo for almost all pH. Moreover, this investigation showed a synergy between N and Mo since the N effect was significantly intensified in the presence of Mo from pH 3 to more than pH 11 as described in Fig. 7.1.

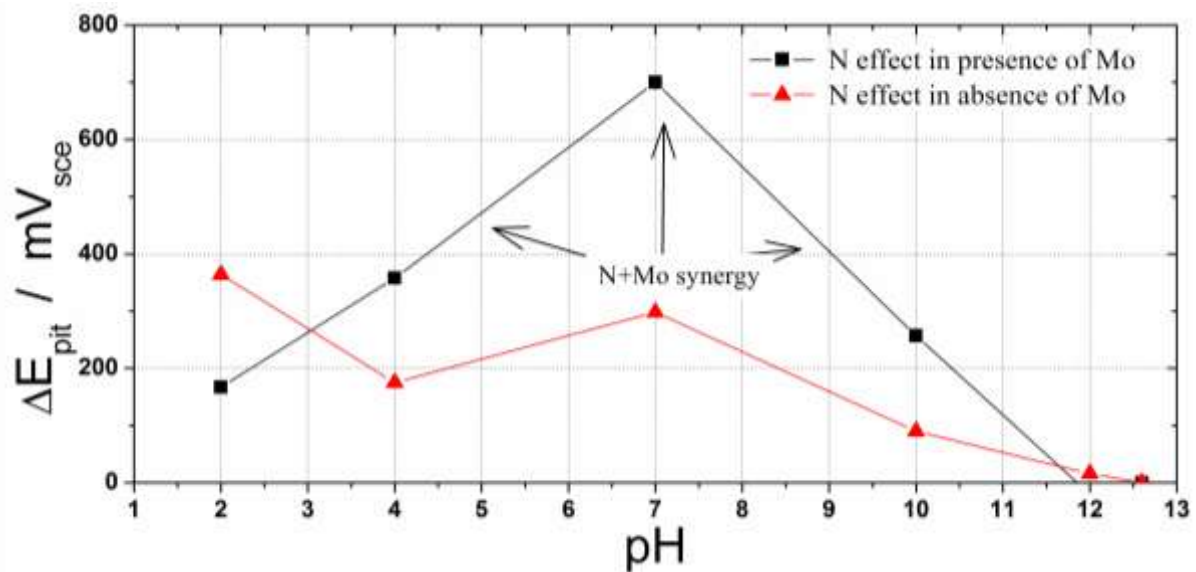


Figure 7.2 – N effect on lab austenitic SS in presence or absence of Mo. E_{pit} difference (ΔE_{pit}) between N *containing and N-Free SS* and also in presence or absence of Mo for lab austenitic heats. The N + Mo synergy is indicated by the gray arrows

This synergy between N and Mo could also be observed by studying the Mo effect on the pitting corrosion of austenitic SS in several different pH in absence or presence of N as shown in Fig. 7.3. This Fig. not only compare the E_{pit} difference (ΔE_{pit}) between 18Cr12Ni3Mo and 18Cr12Ni lab SS as was done before in Fig. 3.9 to show the Mo effect in absence of N, but also the ΔE_{pit} between 18Cr12Ni3Mo0.1N and 18Cr12Ni0.1N materials in order to highlight the Mo effect in the presence of N. In both cases, the only difference between the two compared materials is the amount of Mo, so a monotonic decay of the positive effect of Mo was observed from the acidic to alkaline media as expected. (see curves red and black in Fig. 7.3). Nevertheless, the synergy between Mo and N was once again clearly identified from pH 3 to more than 11. In this pH range, the addition of 3% Mo on the

Free-N lab austenitic heats increased a lot the its pitting corrosion resistance (red curve), however, this effect of Mo addition was even more protective when the austenitic SS content 0.1% N (black curve), as clearly shown in Fig. 7.3.

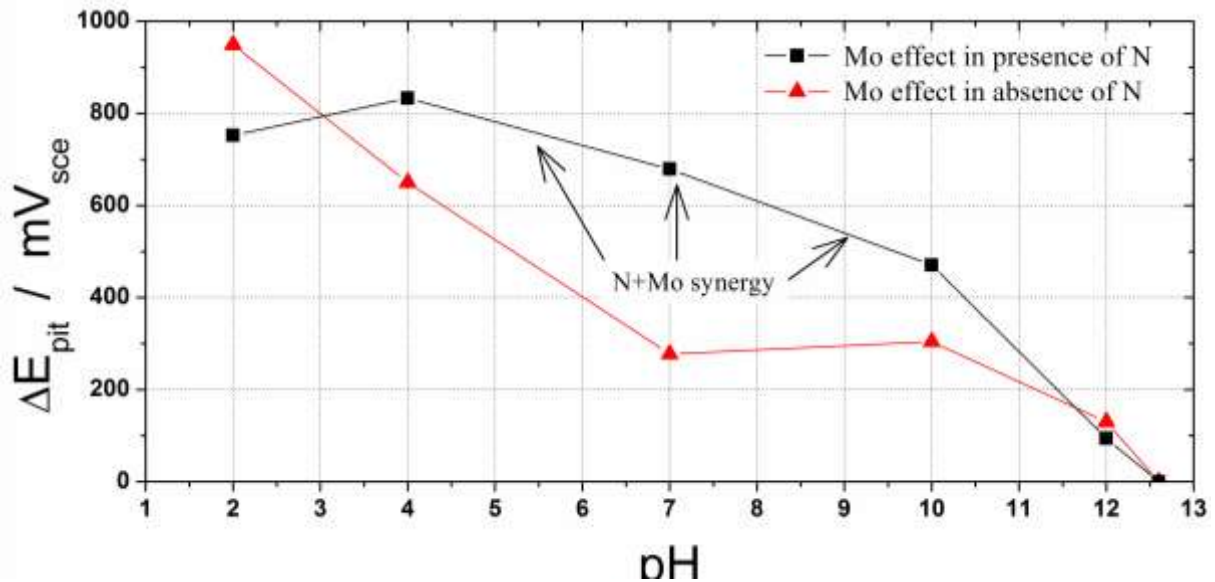


Figure 7.3 – Mo effect on lab austenitic SS in presence or absence of N. E_{pit} difference (ΔE_{pit}) between *Mo containing and Mo-Free SS* and also in presence or absence of N for lab austenitic heats. The N + Mo synergy is indicated by the gray arrows.

Summarizing these preliminaries results, the existence of a synergy between Mo and N has been clearly identified, which is such a promising and innovation conclusion. Therefore, further investigations are needed to determine a mechanism for both alloying elements together.

7.4. IDEAS FOR DIRECT EXPERIMENTS ON THE POROUS CONCRETE ENVIRONMENT

Some preliminaries studies will be conducted with chloride-contaminated porous concrete samples in order to simulate a high aggressive application of concrete for off shore constructions. For these measurements, the lab heats presented in Table 2.1(chapter 2) was prepared with a real concrete followed by its immersion in a chloride containing medium (35 g L^{-1} of NaCl), which approximately corresponds to the sea water chloride concentration. Moreover, all samples have passed by a carbonation chamber before the electrochemical measurements to contaminate the concrete with CO_2 and consequently reduce its pH. The

samples preparation during the concreting process and the carbonation chamber are illustrated in Figs. 7.4 a) and b), respectively.

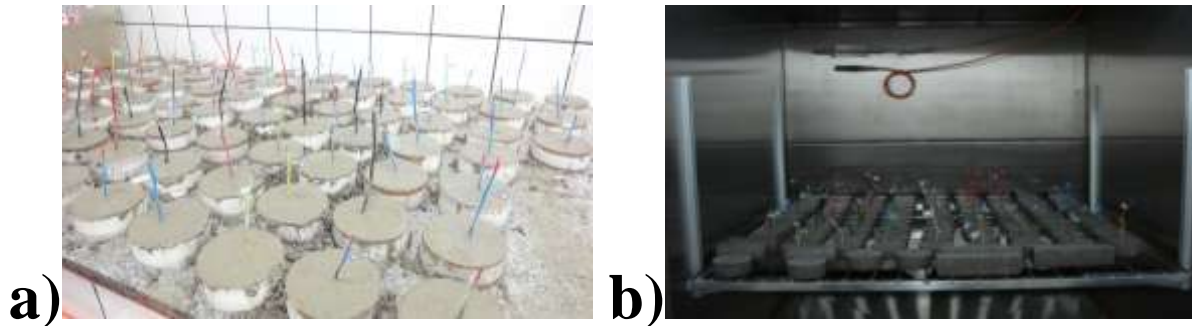


Fig. 7.4 – a) Laboratory SS concreting preparation and b) carbonation chamber.

For each lab material composition, 10 specimens will be prepared in order to assure the reproducibility of the experiments. This large number of samples will be used because the contaminated cement environment is such a complex electrolyte for accurate electrochemical measurements. Fig. 7.5 illustrates the E_{corr} measurement for one of our samples.

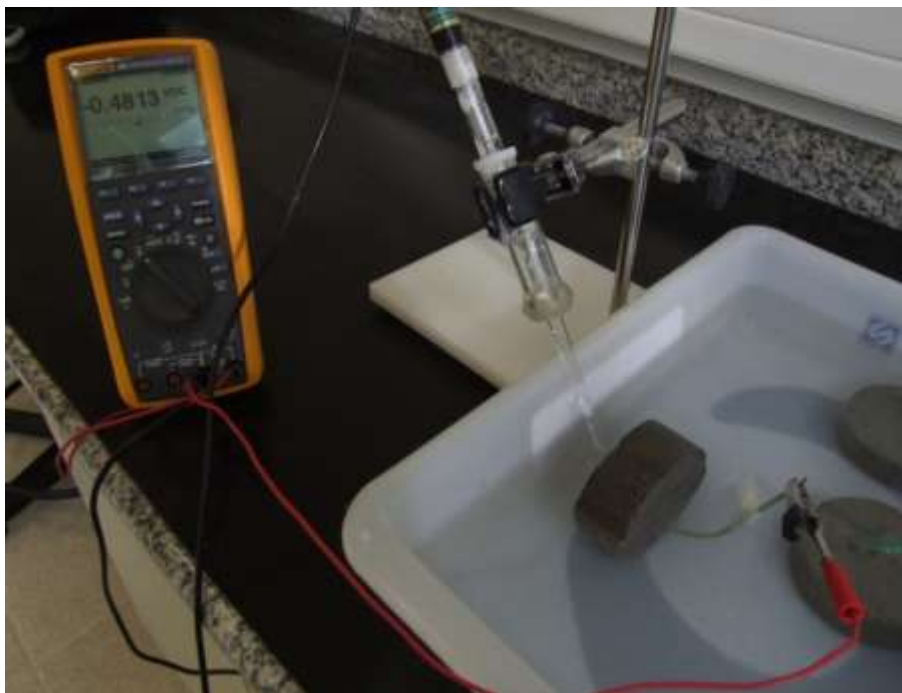


Fig. 7.5 – Laboratory SS under corrosion measurement in a chloride contaminated concrete.

These preliminaries experiments of SS simulating the real application conditions of the contaminated concrete will help us to a better understanding of this complex environment. Therefore, we should go further with these investigations and try to develop an optimized protocol to perform this kind of measurements. A following plan of

electrochemical experiments has been programmed to be done in 2012, which will bring up some new ideas to study of concrete reinforcement research.

During this PhD works, several new ideas appeared as stainless steels development is such a vast domain of the metallurgy. In the sections 7.2, 7.3 and 7.4 presented above, we highlighted three of our major perspectives for further works. These subjects are a mix of scientific and industrial interest, which deserve then our special attention.

***RESUME EN
FRANÇAIS***

***"ACIERS INOXYDABLES ET
CORROSION LOCALISEE:
LE ROLE DU MOLYBDENE"***

OUTLINE

8. RESUME EN FRANÇAIS	162
8.1. RESUME	162
8.2. INTRODUCTION	163
8.3. EFFECT DE L'ADDITION DU MO DANS LA RESISTANCE A LA CORROSION PAR PIQUES DES ACIERS INOXYDABLES EN FONCTION DU pH	166
8.4. INFLUENCE DU MO SUR LA CINETIQUE DE REPASSIVATION DES ACIERS INOX	171
8.5. ROLE DU MO SUR LA PASSIVATION DES ACIERS INOX EN MILIEUX ALCALINS	174
8.6. CONCLUSION	176
8.7. REFERENCES	179

8. RESUME EN FRANÇAIS

8.1. RESUME

Les aciers inoxydables sont de plus en plus utilisés comme renfort du béton dans les constructions marines et côtières, afin de prévenir la corrosion induite par les ions chlorures qui pénètrent dans le béton poreux. Dans ces milieux très agressifs, les aciers inoxydables commencent à être largement employés en raison de leur résistance à la corrosion très élevée et de leur tenue mécanique. L'ajout de molybdène dans les aciers inox contribue à augmenter leur résistance à la corrosion par piqure lorsqu'ils sont utilisés dans des environnements acides et neutres. Cependant, le rôle du Mo sur la corrosion par piqûre des aciers en milieu alcalin chloruré reste à ce jour flou et peu étudié. Par conséquent, la compréhension de l'action du Mo dans la résistance à la corrosion en milieu alcalin est donc d'une importance majeure. Cela permettra l'optimisation de la composition finale des alliages inoxydables en vue des applications potentielles comme renfort dans le béton. Ainsi, cette thèse vise à étudier l'effet de l'addition du Mo sur les propriétés de corrosion par piqûre des aciers inoxydables austénitiques, ferritiques et surtout lean duplex en milieu alcalin. Dans cette étude, plusieurs techniques électrochimiques telles que le suivi du potentiel en circuit ouvert (OCP), la polarisation dynamique, l'ampèremètre de résistance nulle (ZRA), et la spectroscopie d'impédance électrochimique (EIS) ont été largement utilisées, ainsi que de nombreuses méthodes de caractérisations de matériaux telles que la microscopie électronique à balayage (SEM), microanalyse X (EDX), des simulations avec le logiciel termocalc[®] et la spectroscopie photo-électronique des rayons-X (XPS). Les résultats ont été discutés à l'égard de l'influence du Mo sur la corrosion localisée d'aciers inoxydables industriels (AISI 316, 304, 434, 430 et 1.2205 et 1.2304) et également sur des coulées spécifiques dites de laboratoire. Ces alliages "laboratoires" ont été produits avec une composition chimique bien définie. Finalement, la seule différence entre différentes nuances de "laboratoire" est la concentration en Mo. Le rôle du Mo sur les aciers inoxydables a été discuté en termes de leur résistance à la corrosion localisée, cinétique de repassivation et propriétés de passivation dans plusieurs milieux agressifs, mais surtout dans une solution chlorurée synthétique qui simule les environnements poreux du béton (solution de pH10 avec des ions carbonates et chlorures).

Mots-clés: Aciers inoxydables, Molybdène, Corrosion par piqûre, Propriétés de passivation et Renfort du béton.

8.2. INTRODUCTION

Les matériaux utilisés dans le béton armé sont généralement des aciers au carbone ou aciers doux étant donné la faible agressivité de l'environnement et surtout leur bas coût. Les aciers inoxydables quant à eux n'ont jamais été largement utilisés comme matériaux de structure pour les bâtiments ces dernières années malgré leur bonne résistance à la corrosion [1]. Selon l'endroit où le béton armé est placé (milieu marin, lieu soumis à du sel de déglacage ou de la pollution routière), certains éléments chimiques tels que les chlorures et le dioxyde de carbone pénètrent et diffusent à travers le béton poreux vers l'armature en acier, entraînant une diminution significative du pH et par conséquent une augmentation de l'agressivité du milieu [2].

La corrosion des armatures induite par ces ions qui pénètrent dans le ciment est la cause principale d'endommagement des structures en béton armé [3]. Afin de prévenir la corrosion de ces armatures métalliques de renforcement du béton dans les environnements fortement agressifs, l'utilisation des aciers inoxydables tend à se développer pour la construction civile aux Etats-Unis, au Canada, en Australie et dans certains pays européens pour un large éventail d'applications [4]. Par ailleurs, les études dans des conditions alcalines agressives ne correspondent pas seulement aux armatures du béton, mais aussi à d'autres applications telles que la pétrochimie, les industries chimiques, la fabrication du papier, la transformation des aliments, etc...

Le coût des aciers inoxydables explique leur faible utilisation dans les applications structurelles. Le prix de ces aciers est directement associé aux prix des éléments d'alliage, surtout du nickel, chrome et molybdène. Par conséquent, les évolutions dans le domaine des matériaux au cours des 10 dernières années pourraient offrir désormais une nouvelle opportunité pour ces aciers inoxydables. En effet, la technologie métallurgique récente a vu l'introduction des aciers faiblement alliés comme les aciers inoxydables duplex (DSS), souvent désignés comme aciers inoxydables lean duplex. Ces nuances duplex présentent une faible teneur en nickel et molybdène et donc un impact économique réduit sur les structures en béton [1, 5]. Ces aciers inox lean Duplex sont caractérisés par une résistance mécanique équivalente à celle des nuances duplex traditionnelles, mais une résistance à la corrosion localisée supérieure ou bien comparable à celle des aciers austénitiques AISI 304 et 316, largement utilisés dans les milieux alcalins [1].

La résistance à la corrosion localisée des aciers inoxydables est généralement associée à des éléments d'alliage telles que Cr, Mo et N, tandis que Ni agit principalement pour stabiliser la phase austénitique [6, 7]. Une expression couramment utilisée pour estimer la résistance à la corrosion des aciers inox est le PREn (pitting resistance equivalent number) [8]. Le PREn est lié à la teneur des trois principaux éléments chimiques (Cr, Mo et N) chargés d'augmenter la résistance à la corrosion localisée des aciers, chacun d'eux pondérés en fonction de son influence sur la tendance à la piquration [8, 9] selon l'expression suivante:

$$PREn = \%Cr + 3.3 \times \%Mo + 16 \times \%N \quad (1)$$

Même si sans aucun doute les éléments d'alliage jouent effectivement un rôle extrêmement important dans la résistance à la corrosion par piqûre, nous ne devons pas oublier que le PREn reste une expression empirique élaborée à partir d'un inventaire de résultats expérimentaux obtenus dans certaines conditions spécifiques, principalement dans des solutions avec une concentration en chlorures fixe [10]. Il faut donc noter que son utilisation dans d'autres environnements doit se faire avec précaution, surtout quand il s'agit de milieux alcalins, comme ceux liés aux structures en béton. À titre d'exemple, certaines études récentes [11-14] ont souligné quelques résultats inattendus dans lesquels l'ajout de Mo n'a pas amélioré la résistance à la corrosion localisée des aciers austénitiques dans des conditions alcalines, en dépit du fait que le PREn prédit une meilleure performance de ces nuances avec Mo. Cela illustre l'absence de connaissances sur le mécanisme par lequel le Mo affecte la résistance à la corrosion des aciers inoxydables. La compréhension de ce mécanisme surtout en milieu alcalin est donc une préoccupation majeure pour l'optimisation de la composition chimique des alliages afin obtenir un bon équilibre entre les propriétés requises dans ces applications et leur coût final [12].

Dans ce contexte, l'objectif de ce doctorat est d'étudier l'influence de l'ajout de Mo sur toutes les étapes de la corrosion par piqûres (passivation, amorçage, propagation et repassivation) pour les différentes familles d'aciers inoxydables industriels, les traditionnels aciers austénitiques et ferritiques et également les nouveaux alliages lean DSS. Dans ce travail, plusieurs techniques différentes ont été utilisées telles que des mesures électrochimiques, la microscopie électronique à balayage (MEB), microanalyse X (EDX), des simulations avec le logiciel termocalc[®] et aussi la spectroscopie de photoélectrons X (XPS).

Le mémoire de thèse s'articule en 5 parties. Tout d'abord, une synthèse bibliographique sur l'effet du Mo sur la corrosion par piqure des aciers inox et sur les méthodes expérimentales a été réalisée dans les chapitres 1 et 2, respectivement. Ces travaux ont commencé avec une investigation préliminaire sur l'influence du Mo sur la résistance à la corrosion localisée de deux nuances austénitiques traditionnelles (AISI 316 et 304) et également sur les nouvelles nuances austéno-ferritiques (1.2205 et 1.2304), comme détaillé dans le chapitre 3. Les résultats préliminaires ont été discutés sur la base des mesures de potentiel de piqure E_{pit} dans des milieux synthétiques et à plusieurs pH. Comme nous le verrons dans le chapitre 3, les résultats ont indiqué une absence de l'effet bénéfique du Mo dans le cas des nuances austénitiques en milieu alcalin et au contraire la présence de Mo favorise la résistance à la corrosion localisée des nuances duplex [11] et nous ont permis d'avancer l'hypothèse selon laquelle le Mo aurait une influence plus marquée sur la phase ferrite que sur la phase austénite dans le DSS.

Nous avons donc décidé de tester les aciers ferritiques (AISI 430 et 434) afin de vérifier d'abord l'effet du Mo dans la corrosion pour chaque microstructure séparément (austénitique et ferritique) et ainsi mieux comprendre son effet quand ces deux structures sont associées dans le même matériau (acier duplex austéno-ferritique). Les résultats ont montré un effet positif du Mo pour les alliages ferritiques même dans le milieu alcalin (pH 10) à haute température (75°C). Le suivi par MEB et l'utilisation du logiciel Thermocalc, ont confirmé notre hypothèse selon laquelle le Mo agit principalement sur la phase ferrite dans les aciers duplex [11].

Ces résultats concernent des coulées industrielles qui présentent des différences dans leurs compositions chimiques (pas uniquement une teneur différente en Mo). Malgré l'intérêt des résultats et leur caractère innovant, il n'a donc pas été possible de déterminer le mécanisme du Mo sur la corrosion localisée dans des solutions alcalines en utilisant ces échantillons industriels. Par conséquent, nous avons décidé de préparer de nouvelles coulées dites de "laboratoire" avec pour unique différence la composition la teneur en Mo de 0% et 3%, afin d'étudier uniquement l'effet du Mo sur la résistance à la corrosion par piqure.

Dans le chapitre 4, certaines hypothèses sur l'effet du Mo dans la repassivation des piqures indiquées dans la littérature [15-18] ont pu être étudiées grâce à ces coulées

"laboratoires" par des expériences de tribocorrosion. Les résultats de cette étude ont montré une cinétique de repassivation plus rapide pour les aciers contenant du Mo en condition acide. Ce rôle bénéfique du Mo n'est pas si évident en milieu alcalin. Une étude complémentaire aux mesures de tribocorrosion a également été réalisée en ajoutant directement des ions molybdates en solution à différents pH, comme inhibiteur de corrosion. Encore une fois, l'influence du Mo a diminué avec l'augmentation de l'alcalinité de la solution chlorurée. Ces résultats ont confirmé le comportement atypique du molybdène. L'interprétation de ces données a soulevé l'idée de la présence du Mo dans la couche passive lorsque les aciers inox sont exposés à des milieux alcalins, plutôt que la formation d'espèces Mo dans la solution, comme publié [15-22] pour des milieux acides et neutres.

Pour cette raison, la technique de spectroscopie de photoélectrons X (XPS) a été utilisée pour caractériser la couche de passivation formée sur les surfaces des coulées laboratoires dans différentes conditions de pH, comme détaillé dans le chapitre 5. L'objectif de ces analyses XPS était d'observer la présence ou l'absence du Mo oxydé dans ce film protecteur d'oxydes. Par ailleurs, la technique de spectroscopie d'impédance électrochimique (EIS) a été également employée afin de démontrer le rôle du Mo sur la stabilité de ce film passif.

Finalement, tous ces résultats concernant le rôle du Mo sur les propriétés de passivation, résistance à la corrosion localisée et cinétique de repassivation d'aciers inox vont être repris dans ce résumé en langue française.

8.3. EFFET DE L'ADDITION DU MO DANS LA RESISTANCE A LA CORROSION PAR PIQURE DES ACIERS INOXYDABLES EN FONCTION DU pH

Dans une première série d'expériences, plusieurs coulées industrielles d'acier inoxydable ont été étudiées: 2 austénitiques (304 et 316), 2 ferritiques (430 et 434) et 2 duplex (2304 et 2205). La différence majeure entre les deux nuances de chaque famille d'acier est la teneur en Mo (0,21 et 2,17 % pour les nuances austénitiques, 0,05 et 0,92 % pour les ferritiques et 0,28 et 2,78.% pour les duplex). Leurs compositions nominales sont données dans le Tableau 8.1.

Tableau 8.1 - Composition chimique des aciers inoxydables industriels fournis par UGITECH.

Coulées Industrielles		Eléments d'alliage (poids. %)										
		C	Si	Mn	Ni	Cr	Mo	Cu	N	Co	S *	PREn
Austénitiques	304L	0.02	0.49	0.60	11.12	18.29	0.21	0.31	0.03	0.00	9	19.46
	316L	0.01	0.49	0.73	11.08	16.89	2.17	0.48	0.03	0.25	10	24.53
Ferritiques	430	0.01	0.31	0.30	0.29	16.16	0.05	0.10	0.03	0.02	5	16.80
	434	0.03	0.39	0.39	0.45	16.17	0.92	0.12	0.05	0.03	23	20.01
Duplex	2304	0.02	0.41	1.09	4.02	22.30	0.28	0.30	0.15	0.13	4	25.62
	2205	0.02	0.4	1.61	5.45	22.91	2.78	0.22	0.15	0.07	3	34.48

*S ppm

Les résultats les plus importants obtenus avec les aciers industriels sont :

- 1) l'absence d'effet positif du Mo sur la résistance à la corrosion par pique des aciers inoxydables austénitiques dans les milieux alcalins. Les Fig. 8.1 a), b), c) et d) montrent les courbes de polarisation obtenues avec les aciers industriels 304 et 316 à pH 0,6, 7, 10 et 12,1, respectivement. Dans cette Figure nous avons pu constater un effet très positif du Mo sur le potentiel de pique (E_{pit}) des aciers austénitiques dans les pH acide et neutre. Par contre, dans les pH basiques, cet effet disparaît.

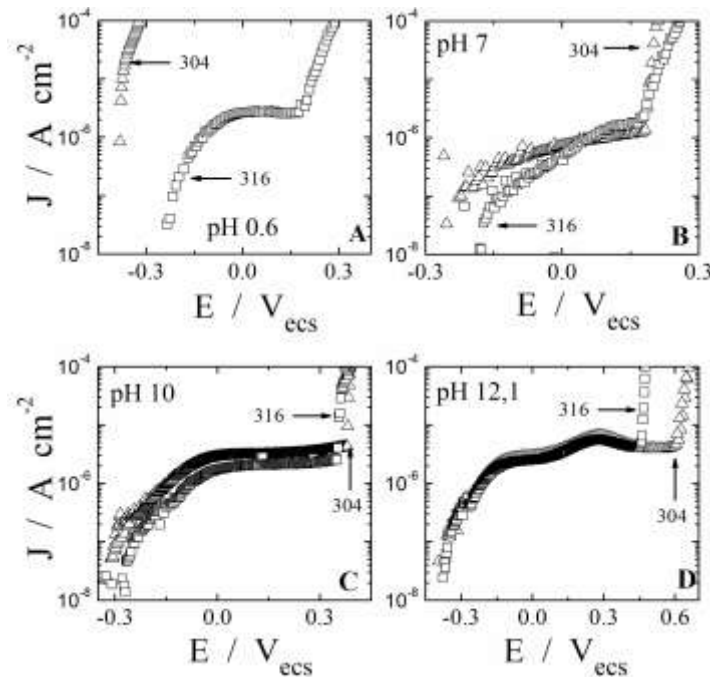


Figure 8.1 - Courbes de polarisations anodiques obtenues avec les aciers austénitiques 304 (Δ) and 316 (\square) dans des solutions chlorurées à différents pH (A: pH 0,6; B: pH 7 C: pH 10 et D: pH 12,1) à 25°C.

D'autre part, les courbes de polarisation d'aciers ferritiques et duplex ont montré que l'influence du Mo sur la résistance à la corrosion par piqures est toujours positive pour ces 2 matériaux. Donc, l'ensemble des résultats de polarisations électrochimiques, nous permet de penser que pour un acier duplex, le rôle du Mo est surtout lié à la phase ferritique.

2) Cette hypothèse théorique d'un effet majeur du Mo sur la phase ferritique a été confirmée par des investigations MEB, Thermocalc et WDS. Pour l'acier 2304, comme prévu, les piqures sont amorcées dans la phase la moins résistante (ferrite). Les Fig. 8.2 a) et b) illustrent les piqures dans la ferrite pour un acier 2304. D'autre part, en présence de Mo, le scénario est inversé, car la ferrite devient beaucoup plus résistante. Dans ce cas, les piqures sont presque exclusivement situées dans les grains austénitiques d'acier 2205. (voir les Fig. 8.2 c) et d)).

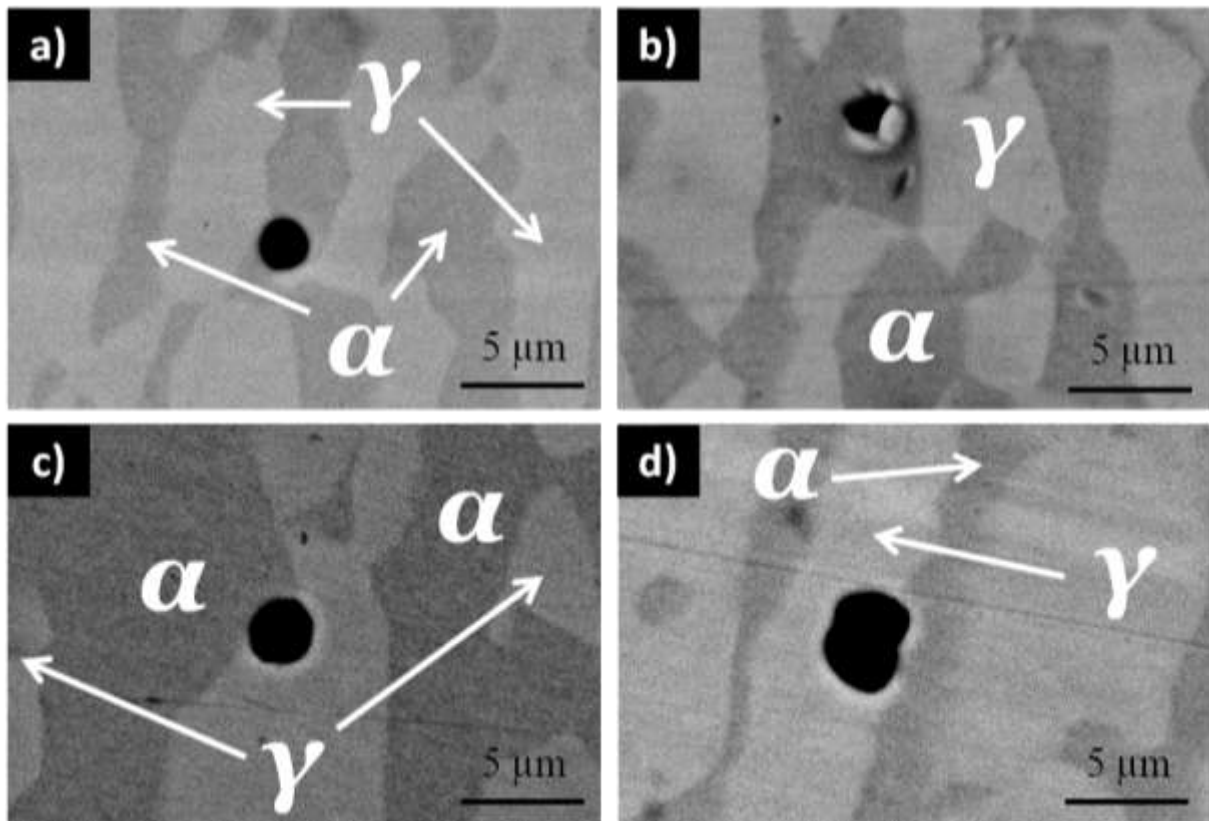


Figure 8.2 - MEB images montrant la nucléation des piqures sur la phase ferritique d'un acier a) et b) 2304, dans l'austénite pour l'acier c) et d) 2205 après les essais électrochimiques à pH 10 et 75°C.

Le calcul de la composition chimique de chaque phase a été fait théoriquement par thermocalc et expérimentalement par WDS. Ces résultats ont confirmé pour un acier 2205 une dissolution préférentielle du Mo dans la phase ferrite (3,2%) contre 2% dans la phase

austénite. Donc, la présence de Mo dans la ferrite a améliorée sa résistance à la corrosion par piqure.

3) Le rôle du Mo a été également étudié grâce aux transitoires de courant provenant des analyses ZRA. Nous pouvons observer dans la Fig. 8.3 que l'initiation de la piqure métastable (liée à l'augmentation du courant) semble être ralentie en présence de Mo (courbe d'acier 434). Le transitoire pour l'acier 434 montre effectivement une augmentation beaucoup moins prononcée ainsi qu'une faible amplitude. Le temps de montée jusqu'à un J maximum est d'environ 0,7 s pour l'acier 430 et 2,3 s pour l'acier 434. Cela signifierait que le rôle de Mo ne devrait pas être lié à la façon dont il accélère la repassivation des aciers inox mais surtout à la façon dont il inhibe l'initiation et la propagation des piqures.

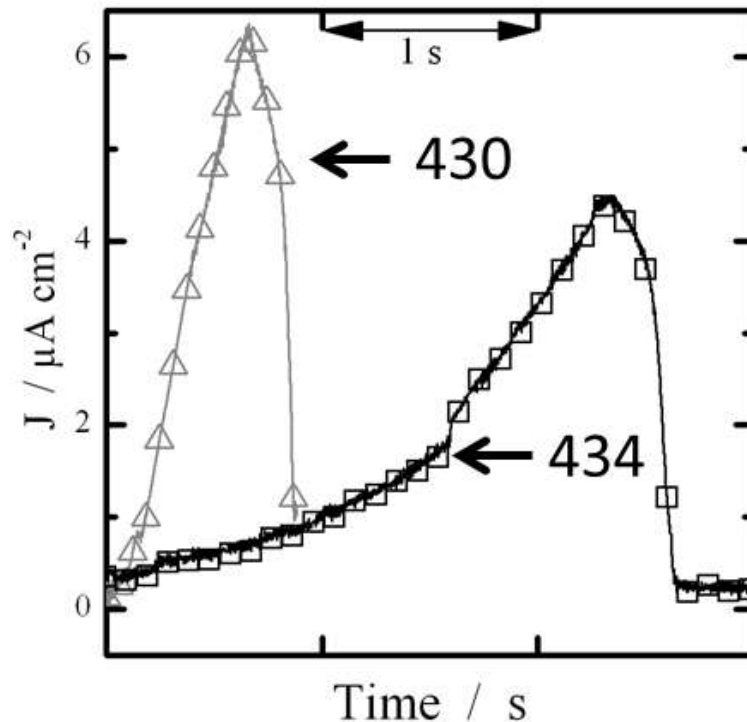


Figure 8.3 - Transitoires de courant provenant des piqures métastable à la surfaces des nuances 430 (\triangle , gris) et 434 (\square , noir) pendant les manipulations ZRA à pH 10.

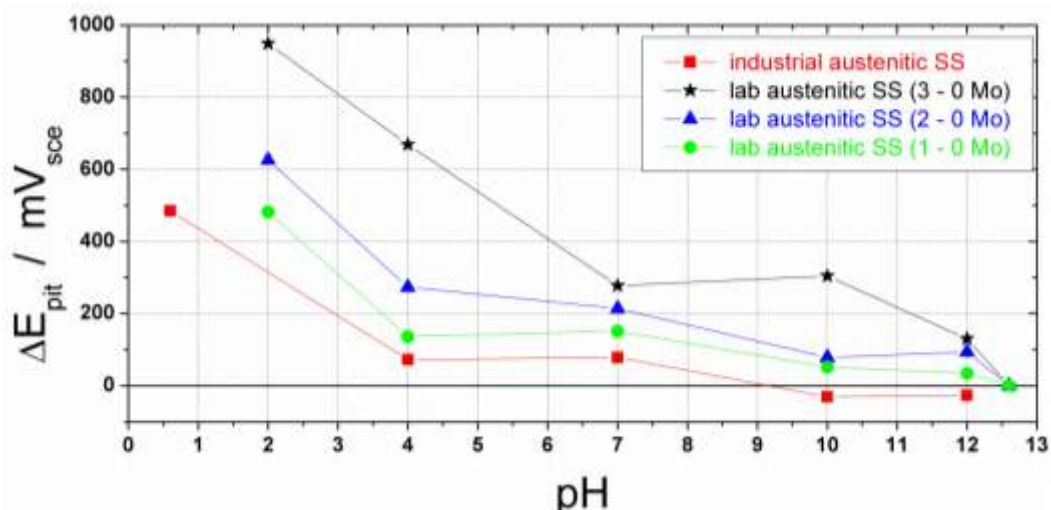
Cependant, la teneur des autres éléments d'alliage est légèrement différente pour ces aciers inoxydables industriels. Donc pour renforcer ces résultats basés sur la présence ou l'absence du Mo, nous avons décidé d'étudier également des coulées "laboratoires" pour lesquels la seule variation est strictement la concentration en Mo. La composition chimique de ces nuances "laboratoires" est indiquée dans le Tableau 8.2.

Tableau 8.2 - Composition chimique des coulées laboratoires fournis par UGITECH.

	Coulées Laboratoires										
		C	Si	Mn	Ni	Cr	Mo	N	Al	S*	PREn
Austénitiques	18Cr12Ni	0.025	0.594	1.012	12.067	17.999	0.004	0.023	0.0033	13	18.38
	18Cr12Ni1Mo	0.028	0.513	0.990	12.060	17.859	1.000	0.024	0.0031	13	21.54
	18Cr12Ni2Mo	0.020	0.515	1.048	12.080	17.879	1.968	0.019	0.0032	12	24.68
	18Cr12Ni3Mo	0.028	0.571	1.018	11.995	18.003	2.989	0.029	0.0036	15	28.33
Ferrit.	18Cr	0.028	0.492	1.056	0.003	18.108	0.004	0.029	0.0024	15	18.59
	18Cr3Mo	0.029	0.533	1.076	0.005	18.018	3.01	0.028	0.0023	14	28.399
Duplex	23Cr4.6Ni	0.029	0.58	1.031	4.569	22.968	0.015	0.175	0.0024	12	25.82
	23Cr4.6Ni3Mo	0.029	0.559	0.981	4.56	22.97	3.004	0.186	0.003	13	35.86

*S ppm

La perte d'effet positif du Mo avec l'augmentation du pH a été confirmée par les expérimentations électrochimiques faites avec les coulées "laboratoires" d'aciers austénitiques. La Fig. 8.4 présente le ΔE_{pit} les alliages austénitiques industrielles et laboratoires afin de vérifier le rôle de molybdène en fonction des différentes conditions de pH. ($\Delta E_{\text{pit}} = E_{\text{pit}}$ pour l'acier contenant Mo - E_{pit} pour l'acier sans Mo). Premièrement, il est clair que le Mo a une influence bénéfique dans tous les milieux pour les coulées laboratoires. Cependant, il est intéressant de remarquer que cet effet, représenté par ΔE_{pit} , diminue avec l'augmentation du pH. Cela prouve le comportement étrange du Mo dans des conditions expérimentales alcalines.

Figure 8.4 - ΔE_{pit} des alliages austénitiques industrielles et laboratoires.

Les courbes de polarisations des coulées "laboratoires" ferritiques et duplex ont confirmé l'influence positive du Mo sur la corrosion par piqure dans tous les pH. L'addition de 3% Mo dans la composition chimique de ces deux familles d'acier a augmenté leurs E_{pit} dans toutes les conditions étudiées.

Finalement, l'effet majeur du Mo sur la phase ferritique d'un acier duplex a été également confirmé par microscopie avec les coulées "laboratoires". Sur la Fig. 8.5 a), nous avons pu constater que pour l'alliage 23Cr4.6Ni, les piqures sont amorcées dans la phase ferritique exactement comme pour l'acier 2304 (voir Fig. 8.2 a) et b)). D'autre part, pour la nuance 23Cr4.6Ni3Mo (Fig. 8.5 b)), la ferrite devient beaucoup plus résistante et donc les piqures sont exclusivement amorcées dans l'austénite. Ce résultat confirme donc les résultats obtenus auparavant avec les coulées industrielles 2205. (Voir Fig. 8.2 c) et d)).

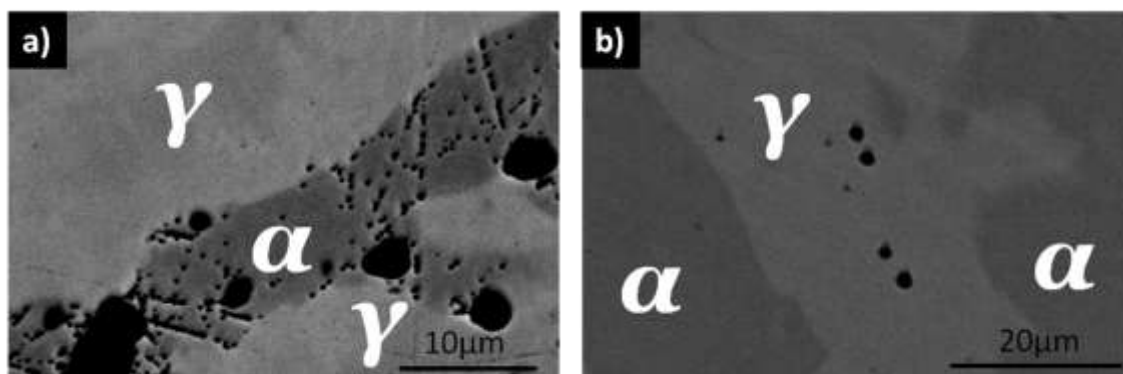


Figure 8.5 - Images MEB montrant l'amorçage des piqures sur les coulées labo a) 23Cr4.6Ni et b) 23Cr4.6Ni3Mo après les essais électrochimiques à pH 10 et 75°C.

Nous avons donc pu conclure qu'il y a un très bon accord entre les résultats des coulées laboratoires et industrielles en ce qui concerne l'influence du Mo sur résistance à la corrosion par piqure. Ces résultats ont également montré que le mécanisme d'addition Mo dans des solutions alcalines est plutôt lié à l'amorçage des piqures (film de passivation) qu'aux aspects de cinétique de repassivation. De plus, le rôle du Mo sur la corrosion localisée a montré une dépendance de la microstructure des aciers, ferritique ou austénitique, en milieu alcalin.

8.4. INFLUENCE DU MO SUR LA CINÉTIQUE DE REPASSIVATION DES ACIERS INOX

Dans cette section, l'influence de l'addition Mo sur la cinétique repassivation a été étudiée pour toutes les coulées et pour plusieurs pH. Pour ces études, la technique tribocorrosion ("scratch test") a été utilisée et donc une analyse comparative des transitoires

de courant est proposée. Ces transitoires correspondent à la rupture mécanique de la couche passive. Tous ces résultats ont été interprétés à l'égard de l'absence et la présence de Mo dans la composition des matériaux. Finalement, l'effet des molybdates, bien connus comme inhibiteur de corrosion, a été également discuté afin de mieux comprendre le mécanisme d'action du Mo sur la corrosion des aciers inox dans les conditions alcalines.

Les résultats les plus intéressants de cette partie sont :

1) En milieu acide (pH 4), la cinétique de repassivation est accélérée par l'addition du Mo indépendamment de la microstructure l'acier inoxydable (austénitique, ferritique ou duplex). Cependant, cet effet positif du Mo n'est pas observé pour les aciers austénitiques en milieu alcalin. La Fig. 8.6 présente les transitoires de courant des aciers 18Cr12Ni et 18Cr12Ni3Mo en milieux acides et alcalins, respectivement. Dans la Fig. 8.6 a), nous pouvons clairement observer l'effet positif du Mo dans la cinétique de repassivation en pH 4. Cependant, à pH 10, cet effet disparaît (voir Fig. 8.6 b)) : ainsi en solutions alcalines comme détaillé précédemment l'addition du Mo influence davantage l'amorçage des piqûres et n'a pas d'effet sur la cinétique de repassivation.

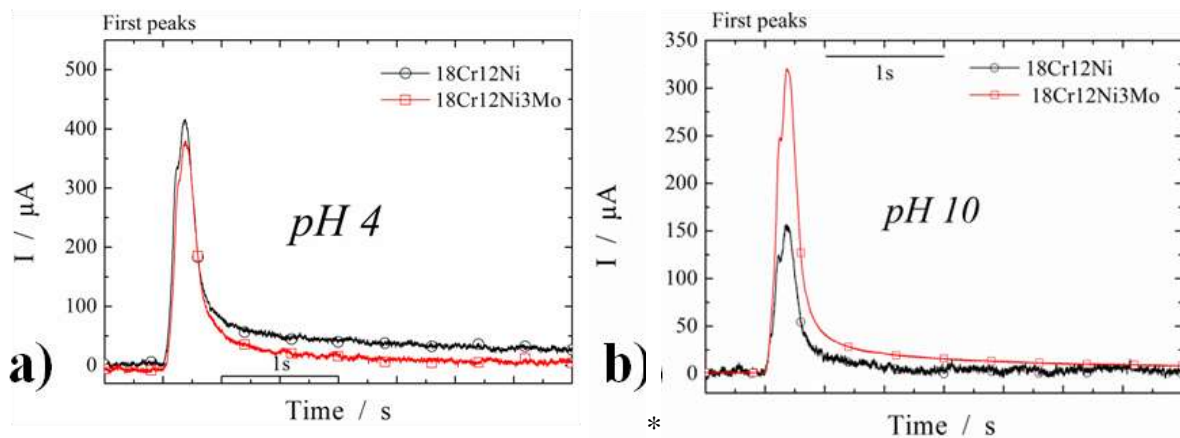


Figure 8.6 – Transitoires de courant correspondant à une depassivation mécanique des aciers inox austénitiques 18Cr12Ni et 18Cr12Ni3Mo dans les **a)** pH 4 et **b)** pH 10.

2) Malgré l'influence majeure du Mo sur la résistance à la corrosion par piqûre de la phase ferrite, une forte dégradation de cette phase ferrite dans l'alliage 23Cr4.6Ni3Mo a été observée après les essais tribocorrosion. Cette attaque préférentielle de la phase ferritique peut être observée sur la Fig. 8.7. Ces résultats sont simplement expliqués par le fait que la phase ferritique soit beaucoup plus sensible à l'abrasion que la phase austénitique. (ferrite

plus "mole" que l'austénite). Donc, l'effet positif du Mo sur la corrosion localisée de la phase ferritique peut être "caché" lorsque ce matériau subi une rupture mécanique de la passivité.

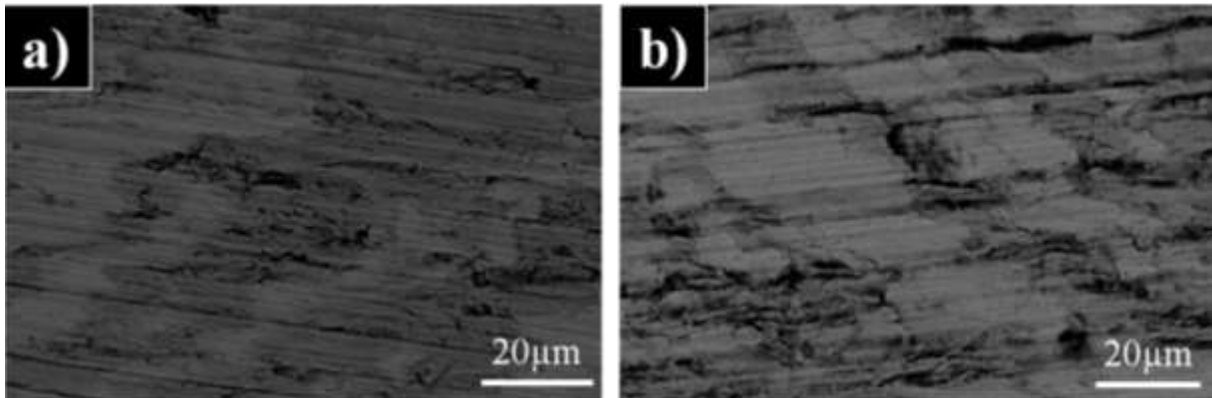


Figure 8.7 - Images MEB montrant la trace d'usure les coulées labo 23Cr4.6Ni3Mo après les essais tribocorrosion à **a)** pH 4 et **b)** pH10.

3) Finalement, les résultats des manipulations de tribocorrosion ont été complétés par des essais électrochimiques dans des solutions de plusieurs pH et en présence des ions molybdates. La Fig. 8.8 montre l'effet inhibiteur des molybdates en fonction du pH pour les alliages 18Cr, 18Cr12Ni et 23Cr4.6Ni. Le rôle des molybdates sur la résistance corrosion par piqûre est prononcé dans les solutions de pH acides et neutres. Cependant, l'ajout de molybdates dans des conditions alcalines ne présente aucun effet sur les propriétés de corrosion localisée de ces aciers.

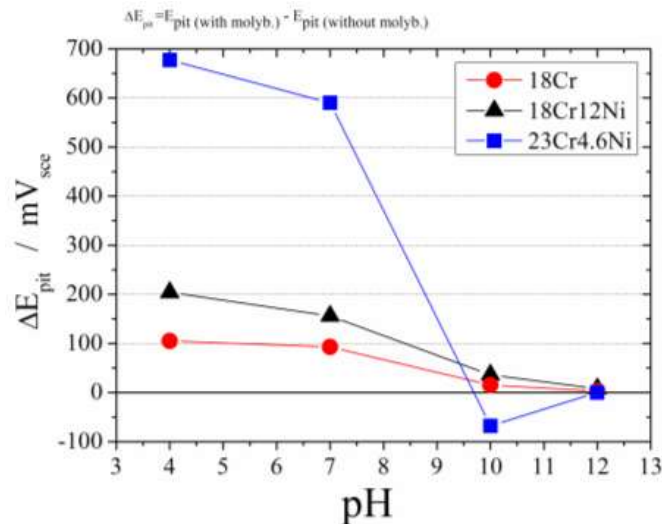


Figure 8.8 - L'effet inhibiteur de corrosion des ions molybdates en fonction du pH pour les alliages 18Cr, 18Cr12Ni et 23Cr4.6Ni.

L'ensemble des résultats de cette deuxième partie de la thèse a renforcé notre hypothèse sur la présence de Mo dans la couche passive des aciers [23-25]. La discussion sur la présence du Mo dans la composition du film passif sera l'objet de la section suivante.

8.5. ROLE DU MO SUR LA PASSIVATION DES ACIERS INOX EN MILIEUX ALCALINS

Dans le cinquième chapitre de cette thèse, l'influence de l'addition du Mo sur la composition et la stabilité de la couche passive a été étudiée. Les alliages "laboratoires" ont subi une période de vieillissement pendant 3 semaines dans l'air ainsi que dans des solutions chlorurées de plusieurs pH (10 et 7). Pour cette étude, la technique de spectroscopie photoélectronique des rayons-X (XPS) nous a permis de comparer la composition chimique du film passif sur les différents alliages. Les résultats XPS ont été discutés à l'égard du mécanisme de Mo sur la corrosion des aciers inox, surtout dans les conditions alcalines.

Sur les Figs. 8.9, 8.10 et 8.11, nous pouvons observer l'effet de l'addition de Mo sur les rapports $(Fe / (Mo + Cr + Fe))$, $(Cr / (Cr + Mo + Fe))$ et $(Mo / (Cr + Mo + Fe))$ pour plusieurs conditions de vieillissement pour les trois familles d'aciers inox (austénitique, ferritique et duplex, respectivement).

Le rapport $(Fe / (Mo + Cr + Fe))$ décroît lorsque l'alcalinité du milieu diminue pour tous les alliages. D'autre part, le rapport $(Cr / (Mo + Cr + Fe))$ a augmenté dans les mêmes conditions.

Par ailleurs, l'ajout de molybdène dans les aciers austénitiques semble enrichir le film passif avec des oxydes de Cr dans les conditions air et à pH 7 alors que les teneurs en oxydes de Fe diminuent dans ces deux milieux. Cependant, dans le pH 10, l'ajout de Mo semble diminuer la teneur en Cr et augmenter la teneur en Fe dans la couche passive. (voir Fig. 8.9)

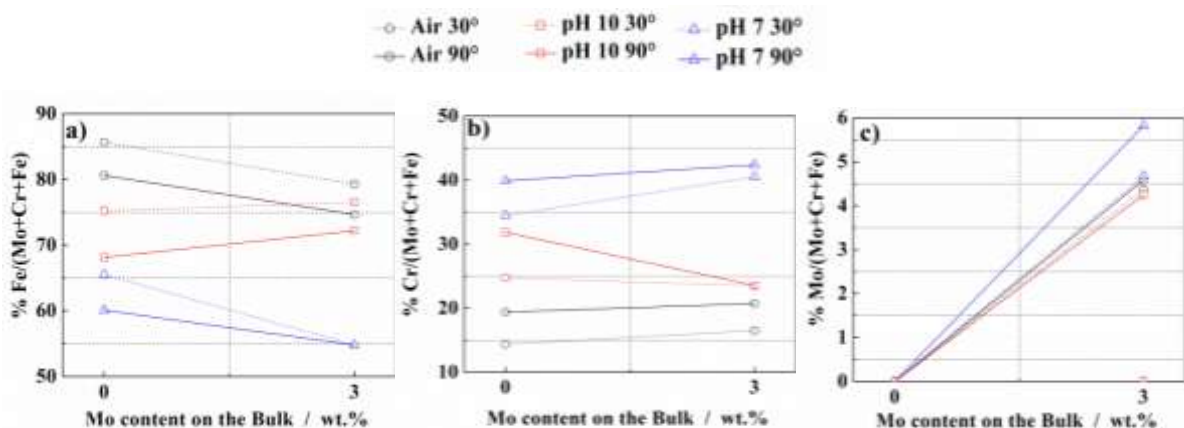


Figure 8.9 - Effet de l'addition du Mo sur l'évolution de la composition chimique (rapports **a**) $\% Fe / (Mo + Cr + Fe)$, **b**) $\%$ de $Cr / (Cr + Mo + Fe)$ et **c**) $\% Mo / (Mo + Cr + Fe)$) du film passif formé sur les nuances austénitiques. Résultats des manipulations XPS faites à 90° (lignes solides) et à 30° (traces en pointillées) et aussi à différentes conditions de vieillissement (air: noires, pH 10: rouges et pH 7: bleues).

Les rapports atomiques d'oxydes de Fe ($\text{Fe}/(\text{Mo}+\text{Cr}+\text{Fe})$), Cr ($\text{Cr}/(\text{Cr}+\text{Mo}+\text{Fe})$) et Mo ($\text{Mo}/(\text{Mo}+\text{Cr}+\text{Fe})$) ont été également calculés à l'aide des résultats XPS pour les coulées laboratoires des aciers ferritiques, comme illustré dans les Figs. 8.10 a), b) et c). Comme prévu pour ces alliages, le film passif a toujours présenté une couche externe riche en Fe (Fig. 8.10 a)) et une couche interne riche en Cr (Fig. 8.10 b)). Il est cependant intéressant de remarquer que l'ajout Mo semble diminuer la teneur en Cr oxydé dans le film passif. Par contre, la teneur en Fe et en Mo oxydé a augmenté.

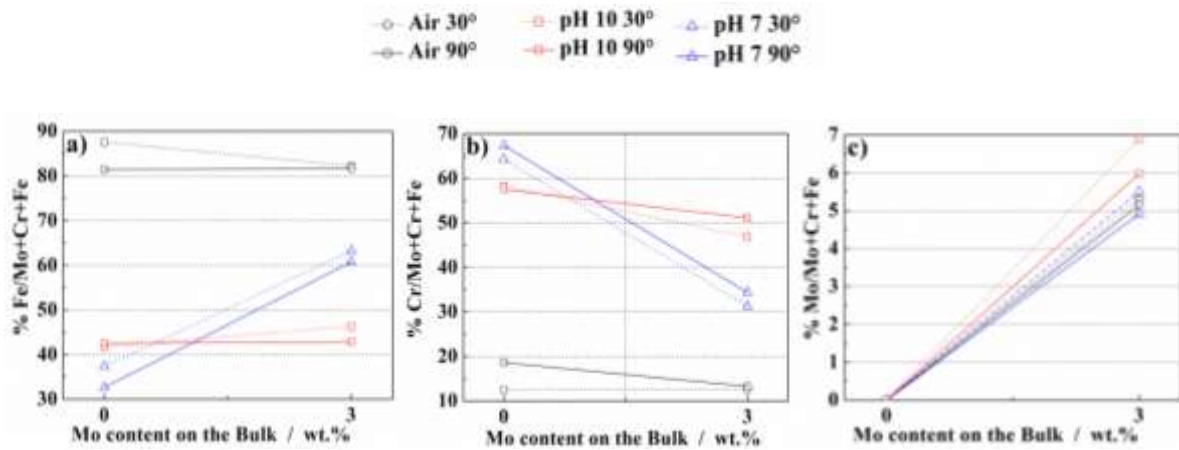


Figure 8.10 - Effet de l'addition du Mo sur l'évolution de la composition chimique (rapports **a)** $\% \text{Fe} / (\text{Mo} + \text{Cr} + \text{Fe})$, **b)** $\%$ de $\text{Cr} / (\text{Cr} + \text{Mo} + \text{Fe})$ et **c)** $\% \text{Mo} / (\text{Mo} + \text{Cr} + \text{Fe})$) du film passif formé sur les nuances ferritiques. Résultats des manipulations XPS faites à 90° (lignes solides) et à 30° (traces en pointillées) et aussi à différentes conditions de vieillissement (air: noires, pH 10: rouges et pH 7: bleues).

Finalement, la surface des coulées laboratoires duplex a été également caractérisée. Les Fig. 8.11 a), b) et c) montrent les rapports de composition atomiques pour le Fe, Cr et Mo oxydé, respectivement. Une diminution du rapport $\text{Fe}/(\text{Mo}+\text{Cr}+\text{Fe})$ a été observé entre les vieillissements dans l'air et dans les solutions chlorurées. D'autre part, le rapport $\text{Cr}/(\text{Cr}+\text{Mo}+\text{Fe})$ est passé de moins de 25% dans l'air à plus de 50% dans la solution de pH 7, comme indiqué dans la Fig. 8.11 b). Par ailleurs, la quantité de Cr oxydes semble diminuer avec l'ajout de Mo dans toutes les conditions expérimentales. Ce résultat est probablement dû à l'incorporation de Mo dans le film. Cette incorporation de Mo oxydé dans le film a eu lieu à tous les pH, mais surtout dans la condition de pH neutre, où la teneur en Mo oxydé dans le film passif est d'environ 7% (voir fig. 7 c)).

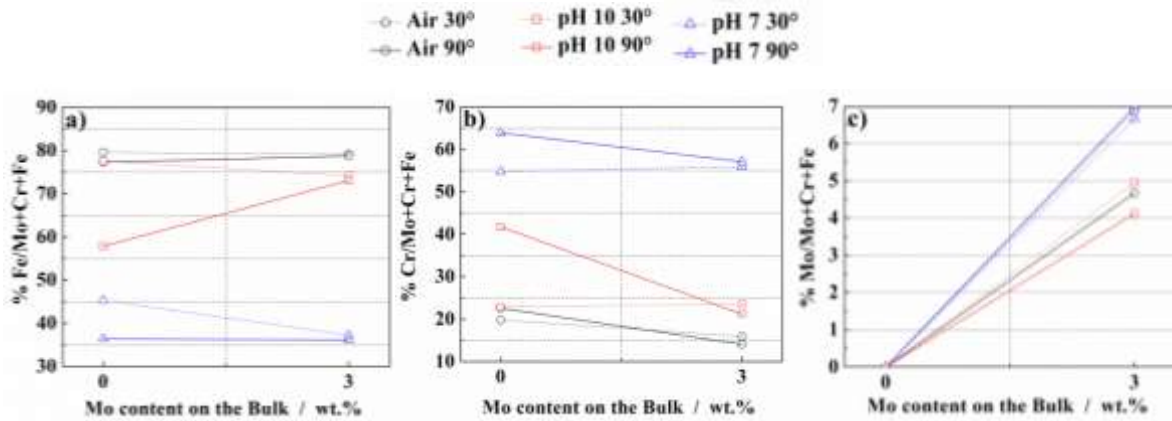


Figure 8.11 - Effet de l'addition du Mo sur l'évolution de la composition chimique (rapports **a**) % Fe / (Mo + Cr + Fe), **b**) % de Cr / (Cr + Mo + Fe) et **c**) % Mo / (Mo + Cr + Fe)) du film passif formé sur les nuances duplex. Résultats des manipulations XPS faites à 90° (lignes solides) et à 30° (traces en pointillées) et aussi à différentes conditions de vieillissement (air: noires, pH 10: rouges et pH 7: bleues).

Les analyses XPS n'ont pas révélé la présence de Ni oxydé dans la couche passive d'aucun acier, mais un enrichissement de Ni métallique dans l'interface film/substrat. Cependant, *Freire et al.* [26] ont indiqué la présence de nickel oxydé dans la couche passive à des conditions alcalines et aussi une diminution de cette teneur en Ni avec la diminution de l'alcalinité de la solution. Ces auteurs ont affirmé que la présence de Ni pourrait affecter le processus de diffusion du chrome sur le film passif. La présence de nickel influe sur la distribution du chrome dans le film passif selon *Abreu et al.* [27]. Donc, le Ni semble avoir un effet sur la croissance et la résistance à la corrosion du film créé dans des solutions alcalines.

Ainsi, l'influence majeure du Mo pour les aciers ferritiques que pour les austénitiques pourrait être associée à la présence de Nickel dans les nuances austénitiques et son absence dans les ferritiques. Finalement, il semble qu'il y a une compétition entre ces éléments d'alliage (molybdène et nickel), même si la présence ce dernier dans la couche de passivation n'a pas été détecté.

8.6. CONCLUSION

Les conclusions de la thèse sont établies pour chaque famille d'acier inox.

- En milieu acide, l'ajout de Mo dans les aciers austénitiques semble provoquer un enrichissement du film passif avec les oxydes de Mo qui sont très stables dans ces conditions. Ainsi, la présence du Mo a augmenté la protection contre la corrosion en retardant l'amorçage des piqûres. Cependant, cette présence de Mo dans la couche d'oxyde n'augmente pas la résistance à la corrosion des aciers austénitiques en milieux alcalins car les oxydes de Mo n'étant pas stables dans ces conditions.

- De plus, les ions Mo dissous à partir du matériau par la solution lors de la corrosion par piqûre, deviennent normalement MoO_4^{2-} . Ces ions MoO_4^{2-} ne peuvent pas arrêter l'attaque des ions Cl^- . Toutefois, dans le fond des piqures (où le pH diminue), la pénétration de Cl^- sera bloquée par la présence Mo qui assure l'électro-neutralité. Dans ces conditions le MoO_3 est sensiblement stable. Ce mécanisme proposé pour expliquer l'action du Mo sur les propriétés de résistance à la corrosion par piqure des aciers austénitiques en milieu alcalin est schématiquement illustré sur la Fig. 8.12.

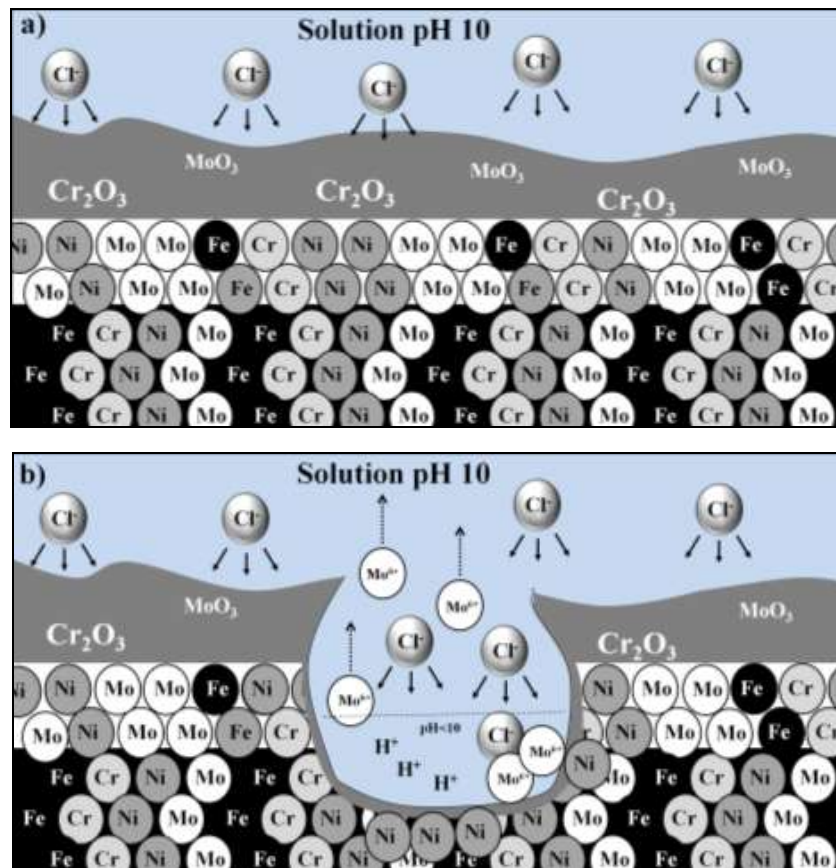


Figure 8.12 - Schéma a) du film passif formé dans l'acier austénitique 18Cr12Ni3Mo et b) du faible effet de Mo sur la corrosion par piqûres d'aciers austénitiques en milieux alcalins. Il est important de noter la présence d'oxydes de molybdène dans la couche passive et aussi l'enrichissement de Mo et Ni dans l'interface film passif/substrat.

Un autre détail très important à propos de ce mécanisme est la présence d'une grande quantité de Ni métal à l'interface film passif/substrat. Selon certains auteurs [26, 27], cet enrichissement de Ni joue un rôle fondamental dans le processus de repassivation. Par conséquent, l'influence du Mo sur la corrosion par piqûre dans des conditions alcalines est peut-être "cachée" par la présence de nickel.

Comme pour les aciers austénitiques, une petite présence d'oxydes de Mo a été également détectée dans la couche passive des aciers ferritiques. Cependant, pour la coulée 18Cr3Mo, une grande concentration de Mo a été observée à l'interface substrat/film. Ainsi, cette région servira comme une source d'ions Mo qui vont substituer les postes vacants du Cr, quand ce dernier sera attaqué par les ions Cl^- . Une illustration du film passif formé sur la coulée "laboratoire" 18Cr3Mo est proposée dans la Fig. 8.13 a).

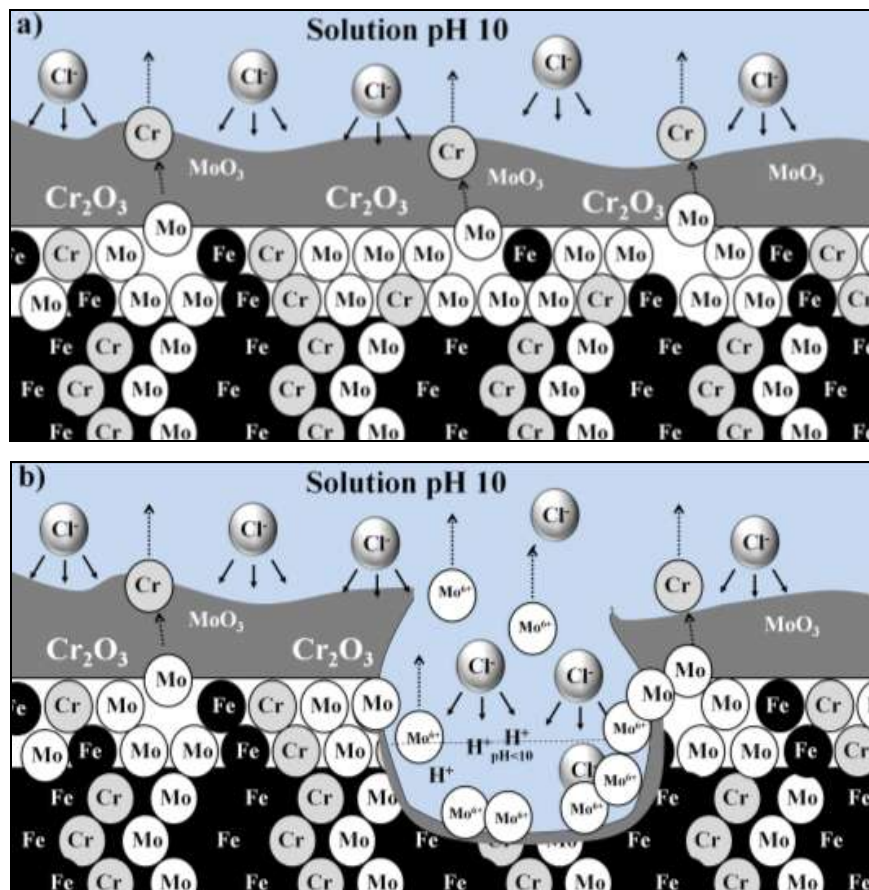


Figure 8.13 - Schéma a) du film passif formé dans l'acier ferritique 18Cr3Mo et b) du effet de Mo sur la corrosion par piqûres d'aciers ferritiques sous les milieux alcalins.

De plus, la grande quantité de Mo à l'interface couche de passivation/substrat va également jouer un rôle important sur la propagation des piqûres en accélérant la repassivation des aciers ferritiques. Premièrement, parce que une grande quantité de Mo sera

dissous dans les piqûres. Deuxièmement, en raison de l'absence de Ni qui masque l'effet positif du Mo. Une représentation schématique du mécanisme de Mo sur la corrosion par piqûre des aciers ferritiques est décrite dans la Fig. 8.13 b).

Finalement, la compréhension de l'effet du Mo sur la résistance à la corrosion d'aciers duplex a été très complexe parce que la microstructure de ces matériaux est composée à la fois de l'austénite et de la ferrite. Pour ces alliages duplex, nous avons vu que l'addition du Mo a eu un effet très bénéfique sur la résistance à la corrosion de la ferrite. Par conséquent, la phase austénite a été préférentiellement corrodée. Finalement, pour mieux comprendre le mécanisme de Mo pour les aciers duplex, nous avons associé le mécanisme proposé pour les aciers 100% austénitiques avec celui des aciers 100% ferritiques.

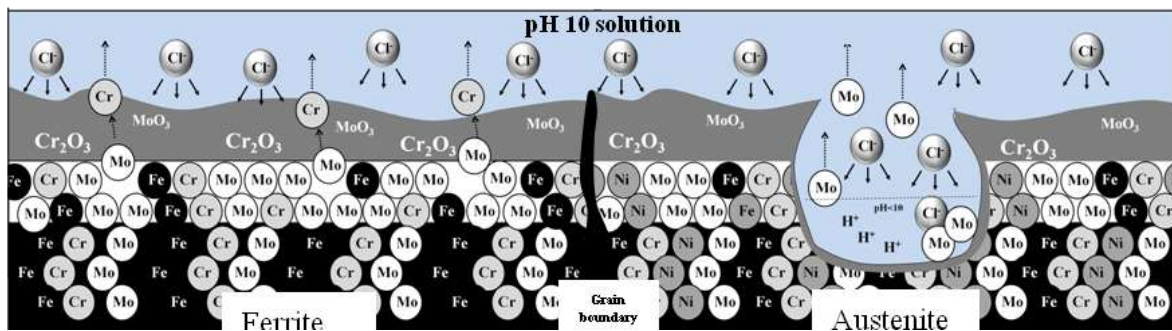


Figure 8.13 - Schéma du mécanisme du Mo sur la résistance à la corrosion localisée des aciers inoxydables duplex (23Cr4.6Ni3Mo) dans les milieux alcalins.

Ainsi, une concentration de Mo plus importante dans la phase ferrite va enrichir sa résistance à la corrosion par piqûres. Ensuite, la ferrite, riche en Mo, devient plus résistante que l'austénite de telle sorte que les piqûres vont amorcer dans la phase austénitique, même si cette phase est riche en Ni. Un schéma du rôle du Mo pour les aciers duplex dans des milieux alcalins est indiqué dans la Fig. 8.13.

8.7. REFERENCES

- [1] E. Chauveau, T. Sourisseau, B. Dermelin and M. Mantel, MEDACHS 08, International Conference in Coastal and Marine Environments (2008).
- [2] D. Addari, B. Elsener and A. Rossi, *Electrochimica Acta* 53 (2008) 8078
- [3] C. J. Abbott, *Concrete* 31 (1997) 28.
- [4] G. Gedge, *J. Construc. Steel Research*. 64 (2008) 1194.

- [5] Guidance on the use of stainless steel reinforcement, The Concrete Society, Technical Report 51 (1998).
- [6] F. Zhang, J. Pan, and C. Lin. Corrosion. Science 51 (2009) 2130.
- [7] L. Zhang, Y. Jiang, B. Deng, W. Zhang and J. Xu, J. Li. Materials Characterization 60 (2009) 1522.
- [8] R.N. Gunn. Abington Publishing, Cambridge England (1999).
- [9] L.F. Garfias-Mesias, J.M. Sykes and C.D.S. Tuck. Corrosion. Science 38 (1996) 1319.
- [10] ASTM G48 - 03(2009) - Standard Test Methods for Pitting and Crevice Corrosion Resistance of Stainless Steels and Related Alloys by Use of Ferric Chloride Solution
- [11] T. J. Mesquita, E. Chauveau, M. Mantel, N. Kinsman and R.P. Nogueira. Materials Chemistry and Physics, 126 (2011) 602
- [12] A. Bautista, G. Blanco and F. Velasco. Cement and Concrete Research 36 (2006) 1922.
- [13] A. Bautista, G. Blanco, F. Velasco, A. Gutiérrez, L. Soriano, F. J. Palomares and H. Takenouti. Corrosion. Science 51 (2009) 785.
- [14] W.A. Badawy and F.M. Al-Kharafi. Electrochimica Acta 44 (1998) 693.
- [15] K. Hashimoto, K. Asami, and K. Teramoto. Corrosion Science 19 (1979) 3.
- [16] G.O. Ilevbare, and G.T. Burstein. Corrosion Science 45 (2003) 1545.
- [17] M. Kimura, M. Kaneko and N. Ohta, ISIJ Int 42 (2002). 1399.
- [18] A. J. Davenport, A. J. Dent, M. Monir, J. A. Hammons, S. M. Ghahari, P. D. Quinn and T. Rayment. J. Electrochem. Soc. 158 (2011).
- [19] A. Pardo, M.C. Merino, A.E. Coy, F. Viejo, R. Arrabal and E. Matykina, Corrosion Science 50 (2008) 1796.
- [20] R. C. Newman. Corrosion Science 25 (1985) 331.
- [21] R. C. Newman. Corrosion Science 25 (1985) 341.
- [22] R. C. Newman, and E.M. Franz. J. Electrochem. Soc. 131 (1984) 223.

- [23] M.F. Montemor, A. Simões, M.G.S. Ferreira, M. Da Cunha Belo, *Corros. Sci.* 41 (1999) 17.
- [24] K. Sugimoto, and Y. Sawada, *Corrosion Nace* 32 (1976) 347.
- [25] K. Sugimoto, Y. Sawada, *Corros. Sci.* 17 (1977) 425.
- [26] L. Freire, M. J. Carmezim, M. G. S. Ferreira, M. F. Montemor, *Electrochimica Acta* 56 (2011) 5280.
- [27] C.M. Abreu, M. J. Cristóbal, R. Losada, X. R. Nóvoa, G. Pena, M. C. Pérez. *Electrochimica Acta* 49 (2004) 3049.

ANNEXES

9.1. ANNEX 1 – MANUFACTURING OF LABORATORY SS

In this annex, the details of the manufacturing process for the lab SS used during this PhD works will be described. Firstly, the chemical compositions of the SS were well defined in order to have 8 different lab samples: 4 austenitic SS, 2 ferritic SS and 2 duplex SS. The only difference between the grades of the same SS family was the Mo contents, as shown in Table 2.2. Thus, a 40-kilo heat was produced for each defined lab alloy.

Secondly, the lab casting passed to thermo-mechanical deformation. The first step of this process were the forging, where all heats were deformed until a dimension of 50x50 mm at temperature between 1250 – 950°C, as shown in the Fig. 9.1 below. All castings were air quenched after forging.

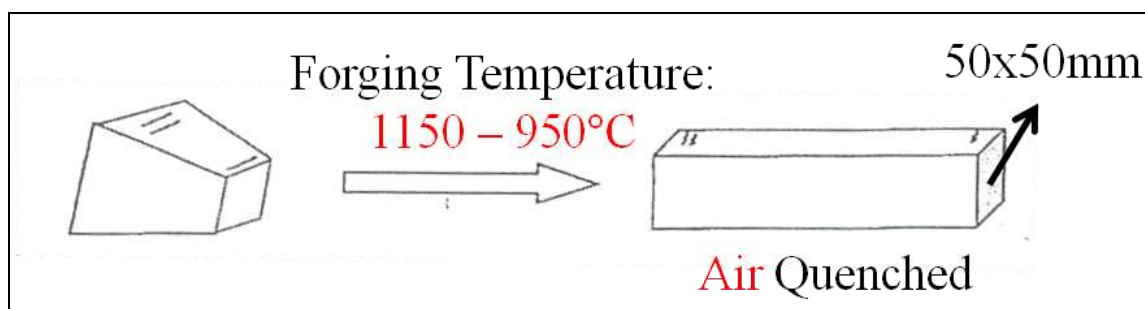


Figure 9.1 – Schematic Illustration of the lab SS forging process.

The next step was the hot rolling of the samples between 1200 – 1150°C in order to drastically reduce the thickness of the lab SS plaque. The final dimension of the laminated sheet samples after the hot rolling was about 4mm.

Finally, all lab samples were heat-treated and quenched in water. The annealing of the lab SS was carried out during 1-2 hour at 1060 or 820°C depending on the SS type. This process was followed by the stripping of all materials. The final mechanical treatment of the lab heats was the cold rolling, which decrease the thickness of the SS sheets from 4mm until 2 mm.

The specimens were sampled from the laboratory cold rolling boards after the heat-treatment in the pastille form (thickness 2mm x diameter 15mm), as presented in the chapter 2.

9.2. ANNEX 2– SYNCHROTRON PROJECT

Aims of the experiment and scientific background

Stainless Steels (SS) are increasingly used not only for structural needs¹ but also for medical devices such as metallic implants or prostheses² for which the presence and eventual release of toxic elements is a matter of major concern. The addition of Mo in SS is supposed to play a key role for their corrosion resistance, but a clear understanding of the mechanism behind this positive effect is still lacking. Several mechanisms have been proposed based on the SS intrinsic matrix microstructure (austenitic, ferritic, ...) or on the controversial presence of Mo in the passive film. In this sense, we have started the studies of the effect of Mo addition on three different SS families (austenitic, ferritic and austenoferritic duplex SS) in alkaline chloride rich media (much less studied than acidic ones) by electrochemical and microscopy techniques.^{3,4} It was shown that, under certain conditions, Mo containing grades can be even less corrosion resistant than Mo free ones.³ This anomalous behavior seems to be related to the austenite phase whereas for ferritic and duplex SS results clearly showed its beneficial effect.⁴ The protective passive film growth processes of these metals under different pH were studied by using *ex situ* XPS measurements⁵ in order to investigate the influence of Mo on oxide film composition for these three SS types. The XPS spectra for Mo containing austenitic SS (Figure 1) not only clearly shows a strong dependence of the film composition with pH solution, but also that Mo is really present within the passive layer which straightforwardly accounts for the high corrosion resistance of Mo-containing grades.³⁻⁵ On the other hand, this is still a matter of controversy in the literature as some authors^{6,7} reported that the Mo mechanism for austenitic SS should be mostly related to the formation of cationic Mo-species in the aggressive solution inside the pits.

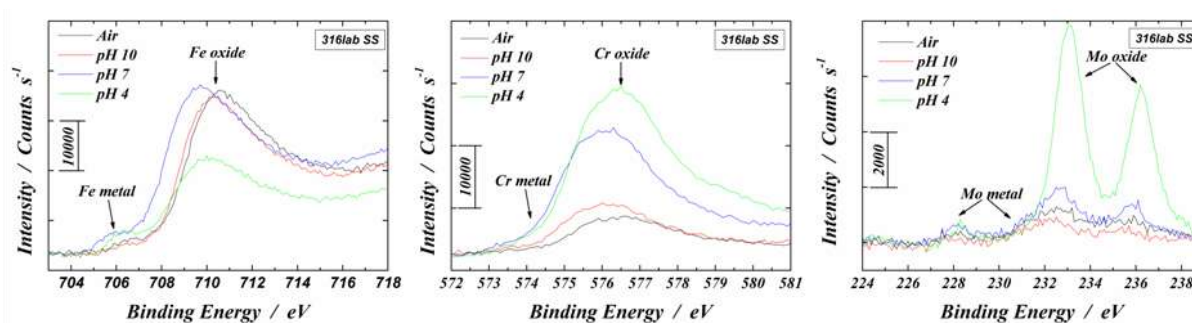


Figure 1 - XPS spectra at 90° for *Fe 2p* (left), *Cr 2p* (middle) and *Mo 3d_{3/2} - 3d_{5/2}* (right) ionizations at the surface film formed on Mo containing austenitic SS (316lab) at different aging conditions (air: black; pH 10: red; pH 7: blue and finally pH 4 green curves).⁵

It seems then clear that no major step forward will be done unless the actual composition and structure of passive films be deeply investigated. In particular, X-ray absorption studies are needed in order to understand the **Mo role in corrosion resistance of SS and this for different microstructures and under different pH conditions**. By now, the literature is scarce about this subject. Kimura et al.⁶ reported XAS measurements at the Mo K edge in pits grown in 1 M LiCl and 1 M LiBr and that showed the appearance of a complex similar to the network of $[\text{MoO}_4(\text{H}_2\text{O})_2]_2$ octahedra; they suggested that the formation of such polymeric networks near the corroding metal interface plays a significant role in the beneficial effect of Mo on the corrosion resistance of SS. Nevertheless, these results are still controversial and not consistent with a very recent XANES study from Davenport et al.⁷, who recorded the presence of Mo(III) species in the solution inside artificial pits formed on an austenitic Mo containing SS (316L). It is worth noticing that those results were limited to acidic media and also to austenitic SS type, so that **the goal of our proposal is to investigate, for the first time with in situ XAS measurements, the role of Mo addition at different pHs and microstructures under several potentials (applied potential inducing passivation process)**.

Objectives

The objective of this proposal is to probe the chemical environment around the Mo ions in the protective oxide layer formed on austenitic, ferritic and duplex SS under different pH and potential conditions by in situ experiments. XAS is the best suitable technique for such kind of investigations and will allow obtaining the structural information about Mo local environment. This study will permit to assess the presence of Mo and the way it is chemically bonded in the passive film during the film formation. This will be achieved by in situ time spaced spectra obtained at different electrochemical potentials starting from a film-free surface and surveying the film formation and growth as the potential is anodically shifted up.

The ensemble of results provided by XAS experiments will yield fundamental information about the film composition and evolution. This would represent a major advance in the understanding of SS film properties and their impact on the stability and eventual release of toxic elements in the case of medical uses of passive alloys.

Experimental method

We will use the *ad hoc* designed electrochemical cell for *in situ* experiments (SXRD, XAS)^{8,9} allowing grazing incident angle XAS measurements, necessary in order to minimize the bulk contribution. Only a few tens of microns of electrolyte will be in front of the SS electrode. The

XAS spectra at the Mo K edge (20 keV) will be recorded in fluorescence mode for each type of SS electrode (austenitic, ferritic and austenoferritic duplex) at different potential values (the potential will be applied during the whole experiment). This will permit us to follow the corrosion process and the induced structural modifications. If necessary, we will provide the cell with an electrolyte continuous flow, allowing the elimination of the corrosion products at the interface solution/ electrode. The XAS measurements will also be done for different pH values.

Expected Results:

This set of *in situ* experiments will allow us to determine the *Mo mechanism on both the pitting corrosion resistance and the passivation behaviour as function of the pH solution and also of the SS microstructures*. We will also be able to establish the exact *correlation between electrochemical characterizations in different pH and the Mo presence on the passive layer*.

Moreover, we will highlight the effect of the substrate and of the electrolytic solution on the Mo neighbouring species.

Beam time requested justification:

Such *in situ* XAS measurements are only possible with the high brilliance beam available at the synchrotron radiation sources. Moreover, in order to work at the high Mo K edge energy (20 keV), the ESRF and in particular the BM32B FAME BL is the best suitable XAS spectrometer. The 30 elements solid state detector available at FAME BL will allow the measurements of the very low signal expected from the passivation film.

References

- [1] D.Addari, B.Elsener, A.Rossi *Electrochim.Acta* 53 (2008) 8078.
- [2] Handbook of Materials for Medical Devices, ASM Publication(2003),Edited by J.R. Davis ISBN : 0-87170-790-X
- [3]T. J. Mesquita, E. Chauveau, M. Mantel, N. Kinsman and R.P. Nogueira. *Mat. Chem. and Phys.*, 126 (2011) 602
- [4]T. J. Mesquita, E. Chauveau, M. Mantel, N. Kinsman, V. Roche and R.P. Nogueira. Submitted to *Mat. Chem. and Phys*
- [5] T. J. Mesquita, E. Chauveau, M. Mantel, N. Kinsman, V. Roche and R.P. Nogueira. Submitted to *Electrochim. Acta*
- [6]M. Kimura, M.K., and N. Ohta, *ISIJ Int.* 42 (2002) 1399.
- [7]A. J. Davenport,A. J. Dent, M. Monir, J. A. Hammons, S. M. Ghahari, P. D. Quinn and T. Raymentb. *J. Electr.. Soc.* 158 (2011)
- [8] Y. Soldo-Olivier, M. C. Lafouresse, M. De Santis, C. Lebouin, M. de Boissieu, and E. Sibert *J. Phys. Chem. C*, 115(24) (2011) 12041
- [9] C. Lebouin, Y. Soldo-Olivier, E. Sibert, M. De Santis, F. Maillard, R. Faure, *Langmuir* 25 (8) (2009) 4251

9.3. ANNEX 3 – IMPEDANCE AND CPE DISCUSSION

Apparent potential-dependent CPE behavior caused by geometry-induced current and potential distributions

P. Córdoba-Torres^a, T.J. Mesquita^b, R.P. Nogueira^b

^a*Departamento de Física Matemática y de Fluidos, Facultad de Ciencias, UNED,*

Senda del Rey 9, Madrid 28040, Spain

^b*LEPMI UMR 5279 CNRS - Grenoble INP - Uds - UJF*

BP 75, 38402 St Martin d'Hères, France

Abstract

In this work we show how the influence of geometry-induced current and potential distributions imposes a restriction to the experimental frequency range employed in EIS analysis imposed that may lead to a misleading apparent dependence of the CPE behavior on the electrode potential, as it is often reported in the literature. When corrections due to this effect are properly taken into account, our results show that CPE exponent α and characteristic capacitance C_0 are independent magnitudes of the interface, i.e. they are intrinsic properties of the interface that do not depend on the experimental variables. This conclusion is along the line of some proposed theories on the origin of CPE.

Keywords: Electrochemical impedance; Constant-phase element; Geometry-induced current and potential distributions; Equivalent electrical circuit; Double-layer capacitance.

1. Introduction

Impedance response of solid electrode/electrolyte interfaces often reveal a frequency dispersion that is commonly modeled by a constant-phase element (CPE) with the following impedance [1,2]:

$$Z_{\text{CPE}} = \frac{1}{Q(i\omega)^\alpha}, \quad (1)$$

where α is known as the CPE exponent and Q ($\text{F cm}^{-2} \text{s}^{-(1-\alpha)}$ or $\Omega^{-1} \text{cm}^{-2} \text{s}^\alpha$) the CPE parameter. CPE –or apparent CPE– behavior is generally believed to reflect a distribution of reactivity originated from interface inhomogeneity. It has been attributed, for example, to surface disorder and roughness [3-12], to electrode porosity [12-16], to specific anion adsorption [17], to electrode geometry [18-21] and to normal-to surface distributions of properties in oxide layers, passive films and coatings [22,23]. It has then been concluded that in all cases it seems to result from a 2D (variation of properties along the surface of the electrode) or 3D (variation of properties also in the direction normal to the electrode surface) time constant distribution [18]. In this sense, it has been proposed that a 3D distribution should yield a local impedance CPE behavior [18,20].

An important issue that has focused the interest of many researchers concerns to the physical meaning of the CPE parameters and the information we can get from them about interface features such as the double-layer capacitance. Brug *et al.* [24] proposed a simple model to explain CPE behavior based on the idea of a double-layer capacity distribution along the interface caused by surface inhomogeneity, hence yielding a 2D time constant distribution. In their treatment they obtained the analytical expression of the distribution that exactly results in a CPE behavior. This distribution was characterized by two parameters: α , related to the dispersion of the distribution, and C_0 , a characteristic capacitance that is not exactly the mean capacitance –which becomes infinite in their model– but given by $\langle \ln C \rangle = \ln C_0$. In spite of this, C_0 was there suggested to represent the double-layer capacitance C_{DL} and found to be related with the model parameters through

$$C_0 = \left[Q \left(R_e^{-1} + R_{ct}^{-1} \right)^{(\alpha-1)} \right]^{1/\alpha}, \quad (2)$$

where R_e and R_{ct} are the electrolyte and charge-transfer resistances respectively. This equation was obtained for systems with faradaic reactions; the extension to ideally polarizable electrodes is straightforward by considering $R_{ct}^{-1} = 0$. An important idea derived from Brug and co-workers's theory is that CPE could not be a double-layer property *per se*

but instead be coupled to the interface magnitudes as in (2). Some experimental results [25] and theoretical analyses [6,7] pointed into that direction.

Although relationship in (2) was firstly derived from a model in which CPE behavior was attributed to a 2D capacitance distribution [24], it has been lately generalized for any system since it can be directly obtained from the characteristic time constant of the admittance [26] or, equivalently, from the frequency that maximizes the imaginary part of the admittance [27]. The use of the admittance instead of the impedance has been legitimized in the fact that in the case of a 2D surface time-constant distribution, it is the global admittance response of the electrode which includes additive contributions from each part of the electrode surface [26]. For that reason it has been argued that Eq. (2) should be used to estimate effective capacitance from CPE parameters in the case of 2D surface distributions. The same argument of additivity applied to systems displaying normal distributions leads to consider the global impedance response instead of the admittance, and then it is the Hsu and Mansfeld expression [28] $C_0 = Q(\omega_{Z''_{\max}})^{\alpha-1}$ which should be considered [26].

Equation (2) has been widely used to extract effective capacitance values –and by extension active surface area values– from CPE parameters. As examples of this we cite: scale electrodeposition on partially blocked electrodes [29], powdered electrodes in cavity electrodes [30], hydrogen evolution [31-34], porous electrodes [35], hydrogen adsorption in metals [36,37], oxygen evolution [38], polymer films [39], passive films [40,41], self-assembled monolayers [42,43] and studies on double layers [44-48]. Despite the apparent reliability of (2) in estimating the double-layer capacitance, there are not concluding evidences of it. In this sense, in a theoretical treatment of planar disk electrodes with faradaic reactions and uniform interfacial capacitance [21], the comparison with other capacitance estimators tested in the work led the authors to the conclusion that (2) provides the best means for estimating interfacial capacitance when frequency dispersion is significant, with errors that were less than 20% for all the experimental conditions investigated.

In any case, independently of the exact physical meaning of the characteristic capacitance C_0 in (2), what seems to be clear is that there must be some sort of coupling between CPE parameters and interface quantities, and that relationship in (2) represents a good candidate to it, as it has been shown in a recent work [27]. Furthermore, following the arguing presented by Brug in terms of distributions, and the results obtained in [27], it is

reasonable to think that parameters α and C_0 , which determine the time constant-distribution in Brug model, might be intrinsic properties of the interface, and thus independent of experimental magnitudes such as the electrode potential, contrarily to what is frequently found in the literature. In that case, CPE parameter Q would then be a dependent parameter, without any physical meaning, and related to the relevant interface quantities through (2). The aim of this paper is to provide some evidences of it.

Our claim here is that CPE parameters estimate is generally not taken with the attention and analysis that it deserves, and that there are important frequency range restrictions that, when not properly considered in the EIS data analysis, may hide the underlying actual CPE behavior thus leading to erroneous conclusions. In fact, in a series of papers Huang et al. have theoretically explored the role of geometry-induced current and potential distributions on the global and local impedance responses of ideally polarizable blocking disk electrodes with local ideally capacitive behavior [19], with local CPE behavior [20], and for disk electrodes with a faradaic reaction [21]. Among the very interesting conclusions they get from their numerical analysis, they showed that this influence affects the impedance response above a critical frequency, inducing an apparent pseudo-CPE behavior in those cases for which local capacitive behavior is ideal. This characteristic frequency can be well within the range of experimental measurements, thus representing an upper bound to the experimental frequency range to be considered in EIS data analysis if we want to characterize the real underlying behavior.

In this paper we present an accurate and quantitative analysis of the potential dependence of the CPE behavior of a monocrystalline pure Fe electrode with two levels of surface roughness in 1M NaOH + 0.1M $K_3[Fe(CN)_6]$ electrolyte. We show how the proximity of the characteristic frequency of the underlying CPE relaxation to the above critical frequency precludes the correct estimate of the CPE parameters. The distance between these two characteristic frequencies is monitored by the potential, yielding an apparent potential dependence of CPE parameters. We show that when proper corrections taking this effect into account are considered in the model, independent constant values for α and C_0 are obtained.

2. Experimental

The experiments were carried out with pure monocrystalline iron (99.99%) in a conventional three-electrode cell: the working electrode (WE) consisted of a rod of 19.635

mm² cross-sectional area embedded in epoxy resin; a Pt grid was used as counter electrode and the reference was a mercurous sulfate electrode (SSE).

Two types of electrode surface have been considered: polished and rough. To get the polished surface, sample surface was grounded down to P2400 grade followed by diamond compounds (6, 3 and 1 μm) and alumina 0.5 μm grade polishing; finally it was rinsed in distilled ethanol in an ultrasonic bath and dried in warm air. Rough surface were prepared by submitting the polished surface to electrodisolution in 0.5 M H₂SO₄ electrolyte (25°C) at $I = 5.093 \text{ mA cm}^{-2}$ during 40 min.

Samples thus generated were washed with distilled water, dried with nitrogen, and investigated by EIS. To avoid further dissolution during the EIS experiments, measurements were carried out in non-aggressive conditions: 1M NaOH + 0.1M K₃[Fe(CN)₆] at 25°C. Frequency was swept from 50 kHz until 0.4 Hz and a 10 mV r.m.s. perturbation signal was applied. Impedance data was obtained at different cathodic polarization potentials ranging from -0.6 to -0.025 V_{sse}, and at a rotation rate of 3000 rpm. For each polarization EIS measurements were repeated three times after different stabilization times to have reproducibility control. All the electrochemical measurements were performed with a potentiostat/galvanostat, ref. 600 from Gamry instruments.

3. Results and discussion

Impedance data obtained from the experiments described above were analyzed according to the following procedure. Firstly we have obtained the CPE parameters from the analysis of the high frequency behavior ($f \gg$) of the imaginary component of the impedance Z_i [49]. The effective CPE exponent α_{eff} was calculated according to

$$\alpha_{\text{eff}}(f) = \left| \frac{d \log |Z_i(f)|_{f \gg}}{d \log f} \right|, \quad (3)$$

whereas the effective CPE parameter Q_{eff} was obtained from

$$Q_{\text{eff}}(f) = \sin \left[\frac{\alpha_{\text{eff}}(f) \pi}{2} \right] \frac{-1}{Z_i(f) (2\pi f)^{\alpha_{\text{eff}}(f)}}. \quad (4)$$

In this form both parameters appear as a function of frequency since they depend on the frequency at which the slope is evaluated. If we have CPE behavior, for frequencies much

larger than the characteristic frequency ω_0 of the high frequency capacitive loop, a power law of the form $Z_i \propto f^{-\alpha}$ is expected so the values obtained from (3) and (4) should converge to a constant value. The procedure and a representative case of the behavior observed in EIS data have been illustrated in Figs. 1 and 2.

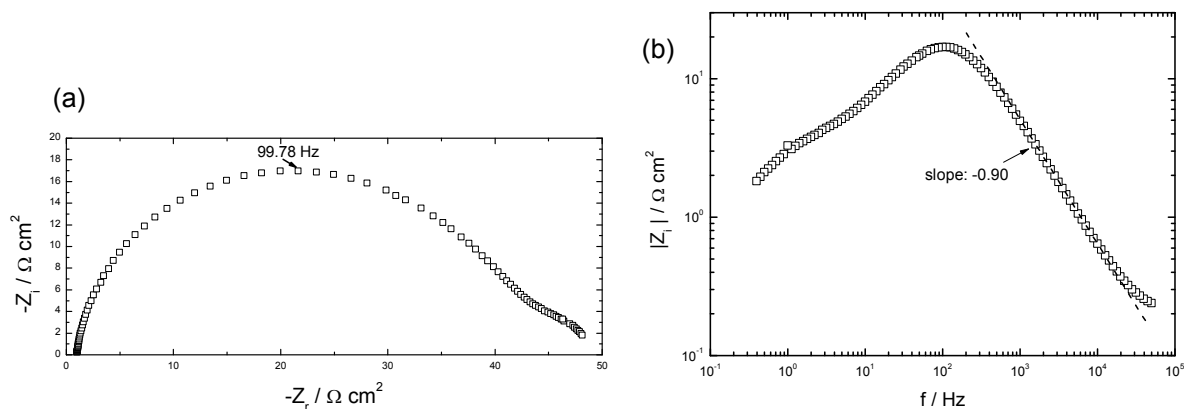


Fig. 1. Experimental impedance data obtained with the rough monocrystal Fe rotating disk electrode (3000 rpm) in 1M NaOH + 0.1M $K_3[Fe(CN)_6]$ at 25° under cathodic polarization at -0.25 V_{sse}. (a) Nyquist plot; (b) imaginary part of the impedance as a function of frequency. Asymptotic CPE behavior has been indicated with the broken line.

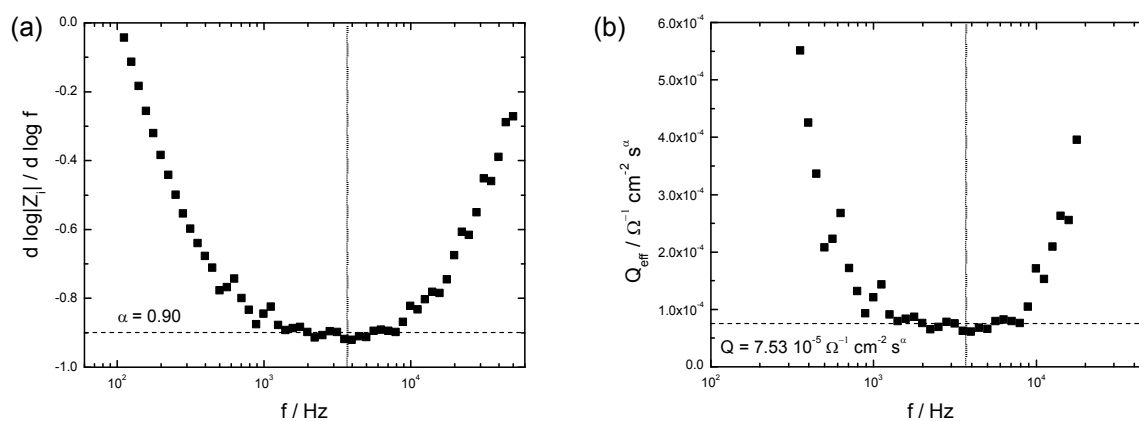


Fig. 2. Derivative of the logarithm of the magnitude of the imaginary part of the impedance with respect to the logarithm of frequency (a) and effective CPE parameter (b) as function of frequency, calculated from EIS data displayed in Figure 1 by using Eqs. (3) and (4) respectively. Horizontal dashed lines indicate the saturation mean values considered for α and Q . Vertical dotted lines indicate the frequency at which $K = 1$.

The complex plane plot of experimental impedance data displayed in Fig. 1a has, as expected [50,51], two time constants. The high frequency capacitive-like loop is attributed to the charge transfer of the Fe^{3+} reduction, in this case with a characteristic frequency of about 100 Hz, followed by a finite Warburg behavior in the low frequency domain that characterizes the diffusion process of Fe^{3+} . On the other hand, the imaginary part of the impedance, shown in Fig. 1b, decays in the high frequency domain with a slope that departs from -1, thus revealing a CPE-like behavior. This CPE behavior has been characterized in Fig. 2a, in which $-\alpha_{\text{eff}}$ has been represented as function of frequency according to (3). It can be seen that the derivative seems to reach a constant mean value one decade of frequency beyond the characteristic frequency, and that it lasts roughly constant one decade further. We have then considered that α is well-defined by the mean value in this frequency range, indicated with the horizontal dashed line. A similar reasoning has been used in Fig. 2b, in which Q_{eff} calculated from (4) is represented as function of frequency, to estimate the CPE parameter Q .

After saturation a high-frequency feature is evident in both figures. This anomalous behavior can be attributed to the influence of surface distribution caused by non-uniform current and potential distributions. Huang et al. [19-21] have shown that disk electrodes yield geometry-induced potential and current distributions that induce a high-frequency pseudo-CPE behavior. This behavior seems to appear for $K > 1$, where K is a characteristic dimensionless frequency that takes different forms depending on the local behavior. If it is ideal, i.e. double layer behaves locally as a perfect capacitance, then K has the form $K = \omega C_{DL} r_0 / \kappa$ [19,21], where C_{DL} is the interfacial capacitance, r_0 the disk radius and κ the conductivity of the electrolyte. On the contrary, if interface behaves locally as a CPE with parameters α and Q , then we have to consider $K = Q \omega^\alpha r_0 / \kappa$ [20]. Thus, a correct analysis of the influence of geometry-induced potential and current distributions implies a certain knowledge on the origin of the underlying CPE behavior. If it arises from a 2D distribution of properties along the surface of the electrode, then it is reasonable to assume an ideal local behavior [18,20,22]. However, if CPE behavior is caused from a variation of properties in the normal-to-surface direction (as in oxide layers, passive films, protective coatings, corrosion inhibitors, porosity), it is said to arise from a 3D distribution which should yield a local impedance CPE behavior [18,20,22]. Local impedance measurements will probably answer this question, but previous similar results [27] clearly point to the 2D distribution hypothesis.

Nevertheless, we have not found significant differences from the two approaches, so for the purpose of the present paper we have assume that our CPE behavior has an origin in a surface distribution and that the critical angular frequency ω_{\max} at which the current distribution influences the impedance response is consequently expressed as

$$\omega_{\max} = \frac{\kappa}{C_{DL}r_0}. \quad (5)$$

For the case displayed in Figs. 1 and 2, with a electrolyte conductivity of $0.127 \Omega^{-1} \text{cm}^{-1}$ and an interfacial capacitance estimated from (2) –see below– of $C_{DL} = 22 \mu\text{F cm}^{-2}$, in good agreement with expected metal | electrolyte interfaces double layer capacitance values, the critical value $K = 1$ corresponds to a frequency of $f_{\max} = 3.675 \text{ kHz}$ ($f_{\max} = \omega_{\max} / 2\pi$), indicated in Fig. 2 with the vertical dotted line. It can be seen that it lies in the frequency range considered for the estimate of α and Q , so it is then reasonable to effectively attribute the anomalous behavior observed for higher frequencies to this effect. This is also consistent with our results: larger is the interfacial capacitance –as in the case of the rough electrode– lower is the maximum frequency ω_{\max} . For the purpose of the present work this highest frequency part of the spectra has been disregarded. This is as much important as this frequency restriction for the actual CPE behavior to hold is hardly visible in Fig. 1b, which is however usually employed to estimate \square values. Indeed, for the bare eye, Fig. 1b can indicate a \square constant behavior between ca 400 and 20 kHz, largely beyond the actual constant range depicted in Fig. 2a. This can mislead the experimenter who will ascribe a wide spread CPE behavior where there is only a frequency restrained one.

Our analysis of experimental data has been complemented for comparison by another usual evaluation procedure: the nonlinear fitting of impedance values to an equivalent electric circuit (EEC). The EEC used in this work has been displayed in Fig. 3, with the CPE impedance given in (1) and the convective diffusion impedance $Z_D(f)$ given by the expression for a finite stationary diffusion layer, i.e. $Z_D(\omega) = Z_D(0) \tanh(\sqrt{i\omega\tau_d}) / \sqrt{i\omega\tau_d}$. The impedance of this interface model is then given by:

$$Z(\omega) = R_e + \frac{R_{ct} + Z_D(\omega)}{1 + (i\omega)^\alpha Q [R_{ct} + Z_D(\omega)]}. \quad (6)$$

The same range of highest frequencies disregarded in the previous analysis was consistently disregarded here as well.

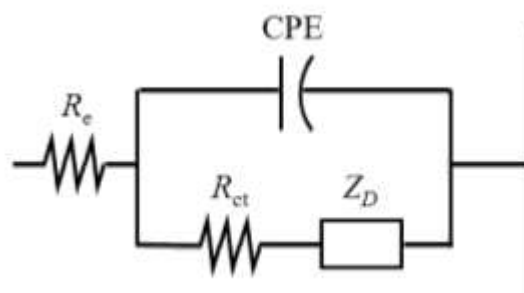


Fig 3. Equivalent electric circuit used to fit EIS data.

As described in the experimental part, the cathodic polarization potential used in the impedance measurements was swept from $-0.6 V_{sse}$ to $-0.025 V_{sse}$ with steps of $0.05 V_{sse}$. The electrode potential was not monotonously changed to avoid any possible bias in the results, and several impedance measurements were carried out after different stabilization times for each polarization. Impedance data was analyzed as described above, and the results have been displayed in Fig. 4 for the rough electrode. Figure 4a shows the value of the CPE exponent, obtained both from the analysis of the high frequency behavior of the imaginary component of the impedance and from the EEC fitting, as function of the charge transfer resistance obtained from the ECC fitting. Figure 4b displays the same but for the characteristic capacitance calculated from (2). It should be stressed out that in both analyses the values of R_e and R_{ct} were those obtained from the ECC fitting.

Similar qualitative behaviors are observed in the two analyses for both parameters. There is a very rapid and significant variation of their magnitudes for low values of R_{ct} , followed by a slow saturation as long as the charge transfer resistance increases. The most significant difference appears for the behavior of α : whereas for the results obtained from the $Z_i(j)$ analysis the CPE exponent seems to reach the saturation value at $R_{ct} \approx 100 \Omega \text{ cm}^2$, the results obtained from the ECC show a very slow and continuous decay that move away both estimates. This comparison was aimed to show that a characterization of CPE behavior should involve a deeper analysis than a simple fit to an EEC. As we show in this work, the analysis of Z_i makes possible a detailed characterization of the impedance response as

function of the frequency range, thus allowing a better identification of the real underlying CPE behavior.

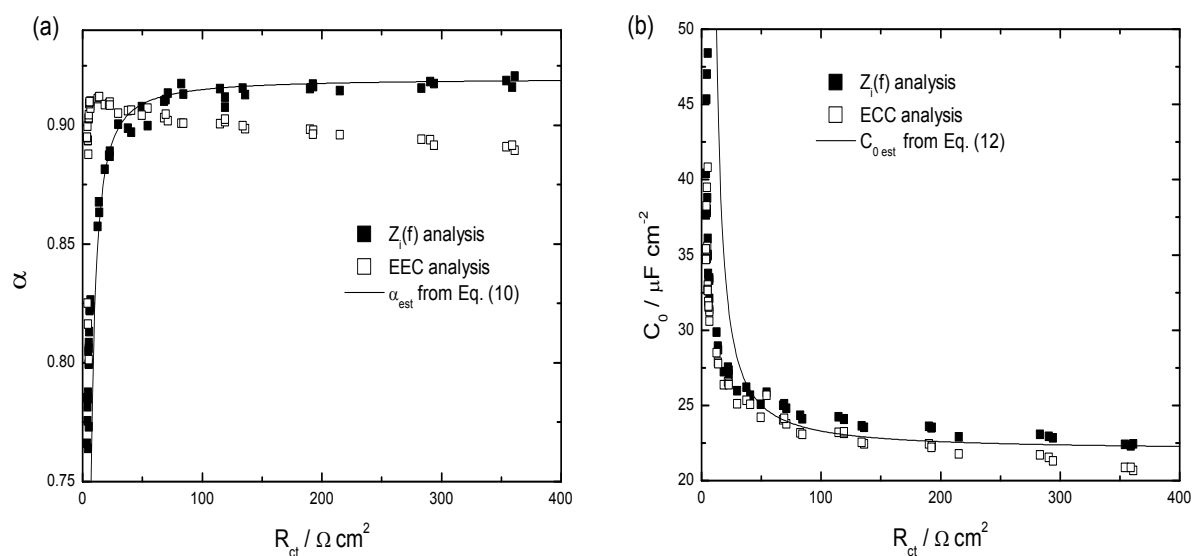


Fig. 4. CPE exponent α (a) and characteristic capacitance C_0 (b) as function of the charge transfer resistance. Symbols correspond to results from EIS data analyses: (solid) $Z_i(f)$ analysis; (open) ECC fitting. Equation (2) was used in both cases to calculate C_0 . Experimental impedance data was obtained with a rough Fe rotating disk electrode (3000 rpm) in 1M NaOH + 0.1M $K_3[Fe(CN)_6]$ at 25° by varying the cathodic polarization from -0.6 to -0.025 V_{sse} . Continuous lines stand for the analytical estimates given in Eqs. (10) and (12) respectively.

The behavior displayed in Fig. 4 can be understood by analyzing the behavior of Z_i in the high frequency domain, in which the influence of mass transport vanishes. From (6) we obtain

$$|Z_i(\omega)|_{\omega \gg} = R_{ct} \frac{\sin(\alpha\pi/2)}{(\omega/\omega_0)^\alpha + (\omega/\omega_0)^{-\alpha} + 2\cos(\alpha\pi/2)}, \quad (7)$$

where

$$\omega_0 = (QR_{ct})^{-1/\alpha} \quad (8)$$

is the characteristic frequency maximizing Z_i directly related to the time constant of the mass transfer process. Notice that expected CPE power law $Z_i \propto \omega^{-\alpha}$ is attained in (7) for

frequencies much larger than ω_0 . We can now calculate the derivative involved in (3) for the calculus of α_{eff}

$$\left| \frac{d \log |Z_i(\omega)|_{\omega \gg}}{d \log \omega} \right| = \frac{\alpha \left[1 - (\omega/\omega_0)^{-2\alpha} \right]}{1 + (\omega/\omega_0)^{-2\alpha} + 2(\omega/\omega_0)^{-\alpha} \cos(\alpha\pi/2)}, \quad (9)$$

which shows how α_{eff} deviates from actual α value when frequency is not sufficiently larger than ω_0 .

As discussed above, the range of frequencies in which CPE behavior is not perturbed by the influence of geometry is limited by the condition $K = 1$, which establishes the upper bound given in (5). From a practical point of view, the experimental frequency range is therefore constrained to $\omega_0 \ll \omega < \omega_{\text{max}}$. In our experiments, this range narrows as long as the electrode potential increases since charge transfer resistance diminishes, thus yielding a raising of ω_0 , whereas ω_{max} is kept constant. What we claim here is that this constriction precludes the observation of the actual CPE behavior, resulting in the under prediction of α for small values of R_{ct} displayed in Fig. 4a. To illustrate this point we have displayed in Fig. 5 the variation of $-\alpha_{\text{eff}}$ with the frequency for different overpotentials considered in this work. Again, the critical frequency f_{max} has been represented by the vertical broken line. The behavior is quite similar in all cases: the effective CPE decreases with frequency reaching a minimum value around of which α is estimated for each potential, and then quickly raises in the highest frequency domain. However, for many potentials, saturation of $-\alpha_{\text{eff}}$ occurs in frequency regime dominated by the effects of geometry. Furthermore, the range of frequencies of the plateau shortens with the increasing potential and this happens at smaller values of α_{eff} . Only for very small values of the potential we observe large plateaus in a frequency range well before f_{max} , in which we can affirm that α is well estimate by α_{eff} . In this form the saturation values seem to vary monotonously with the potential within the range of values –indicated in the figure with dotted horizontal lines– limited by $\alpha = 0.78$, which has been theoretically found to characterize the pseudo-CPE behavior induced by the effect of geometry [21], and $\alpha = 0.92$, which corresponds to the apparent asymptotic value reached by α in Fig. 4a. From the figure we can conclude that the proximity between the two

characteristic frequencies precludes the decreasing value of $-\alpha_{\text{eff}}$ to reach its saturation real CPE value. In consequence, the apparent saturation displayed for large potentials is due to the crossover towards the highest geometry-ruled frequency regimen, so it does not reveal the real CPE behavior.

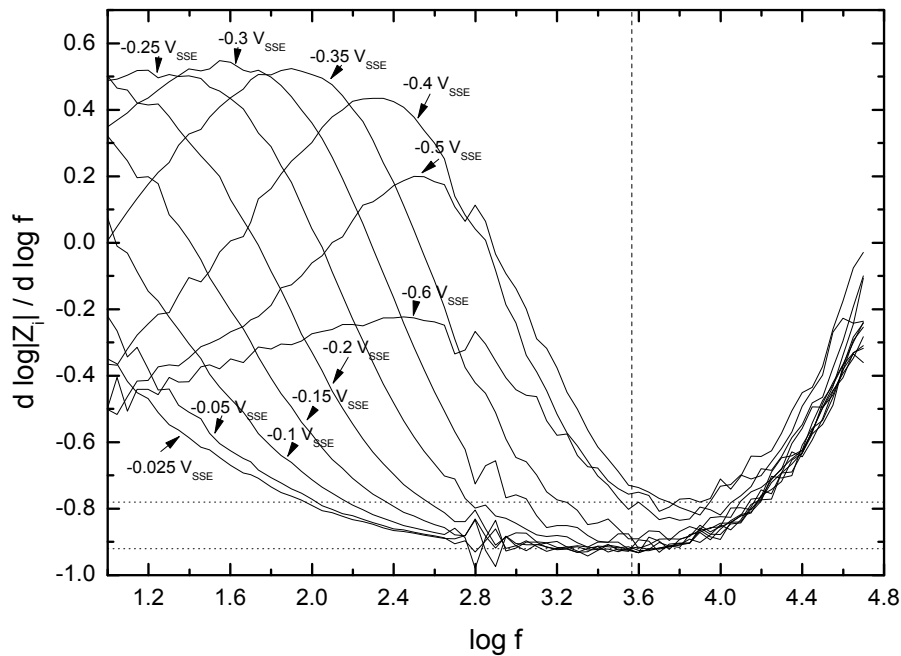


Fig. 5. Behavior of $-\alpha_{\text{eff}}$ as function of the logarithm of frequency for different cathodic overpotentials. The results have been calculated from EIS data obtained with a rough Fe rotating disk electrode (3000 rpm) in 1M NaOH + 0.1M $\text{K}_3[\text{Fe}(\text{CN})_6]$ at 25°. Vertical dashed line indicate the frequency at which $K=1$. Horizontal dotted lines indicates the values $\alpha = 0.78$ and $\alpha = 0.92$.

We can easily recover the behavior of Fig. 4 from the hypothesis that both α and C_0 are constant independent variables in our system, given by their saturation values displayed in Fig. 4: $\alpha \approx 0.92$ and $C_0 \approx 22 \mu\text{F cm}^{-2}$, and that CPE exponent α is obtained from (9) at the maximum frequency “available” ω_{max} , thus having the following estimate

$$\alpha_{\text{est}} = \frac{\alpha \left[1 - (\omega_{\text{max}}/\omega_0)^{-2\alpha} \right]}{1 + (\omega_{\text{max}}/\omega_0)^{-2\alpha} + 2(\omega_{\text{max}}/\omega_0)^{-\alpha} \cos(\alpha\pi/2)}, \quad (10)$$

in which ω_0 has the form

$$\omega_0 = C_0^{-1} \left(R_{ct} \left(R_e^{-1} + R_{ct}^{-1} \right)^{(1-\alpha)} \right)^{-1/\alpha}, \quad (11)$$

which is obtained by considering (2) in (8). Since the ohmic resistance is roughly constant in the experiments ($R_e \approx 0.946 \Omega \text{ cm}^2$), CPE exponent estimated from (10) appears as a function of the charge transfer resistance. Behavior predicted from (10) has been represented with continuous line in Fig. 4a. It clearly appears that α_{est} perfectly emulates the collapse of “measurable” α values for small R_{ct} values.

We can applied a similar reasoning to the characteristic capacitance in (2) and consider

$$C_{0 \text{ est}} = \left[Q_{\text{est}}(\omega_{\text{max}}) \left[R_e^{-1} + R_{ct}^{-1} \right]^{(\alpha_{\text{est}}-1)} \right]^{1/\alpha_{\text{est}}}, \quad (12)$$

where $Q_{\text{est}}(\omega_{\text{max}})$ is the result of the evaluation of (4) at frequency ω_{max} taking into account the corrections given in α_{est} :

$$Q_{\text{est}}(\omega_{\text{max}}) = \sin \left[\frac{\alpha_{\text{est}} \pi}{2} \right] \frac{-1}{Z_i(\omega_{\text{max}}) \omega_{\text{max}}^{\alpha_{\text{est}}}}. \quad (13)$$

To calculate $Z_i(\omega_{\text{max}})$ we can consider that in the high frequency domain our interface behaves as a perfect CPE with impedance:

$$Z_i(\omega_{\text{max}}) = R_{ct} \frac{-\sin(\alpha\pi/2)}{\left(\omega_{\text{max}}/\omega_0 \right)^{-\alpha} + \left(\omega_{\text{max}}/\omega_0 \right)^{\alpha} + 2 \cos(\alpha\pi/2)}. \quad (14)$$

In this form we obtain again an analytic expression of $C_{0 \text{ est}}$ as function of R_{ct} . The comparison of this estimate –continuous line in Fig. 4b– with experimental data does not show the so good agreement displayed in Fig. 4a, probably due to the approximations done in (13) and (14). It is worth to remind that the only hypothesis considered here is that our interface behaves as a perfect CPE with independent parameters α and C_0 .

The same behavior has been observed for electrodes with different levels of roughness. In Figure 6 we compare the results displayed in Fig. 4 with those obtained for the polished electrode. Whereas the qualitative behavior is the same, quantitative differences

appear. The asymptotic CPE exponent value seems to be a bit smaller (above 0.91), but the differences in the capacitance values are much more significant, reflecting the different degrees of roughness and thus of active surface area. The increasing of f_{\max} in the polished electrode, with a value of 9000 Hz estimated from a similar analysis to that displayed in Fig. 5, is in perfect agreement with the smaller asymptotic saturation value of the capacitance $C_0 \approx 9.0 \mu\text{F cm}^{-2}$ displayed in Fig. 6. This gives a relation between the roughness factors of both surfaces of 2.4.

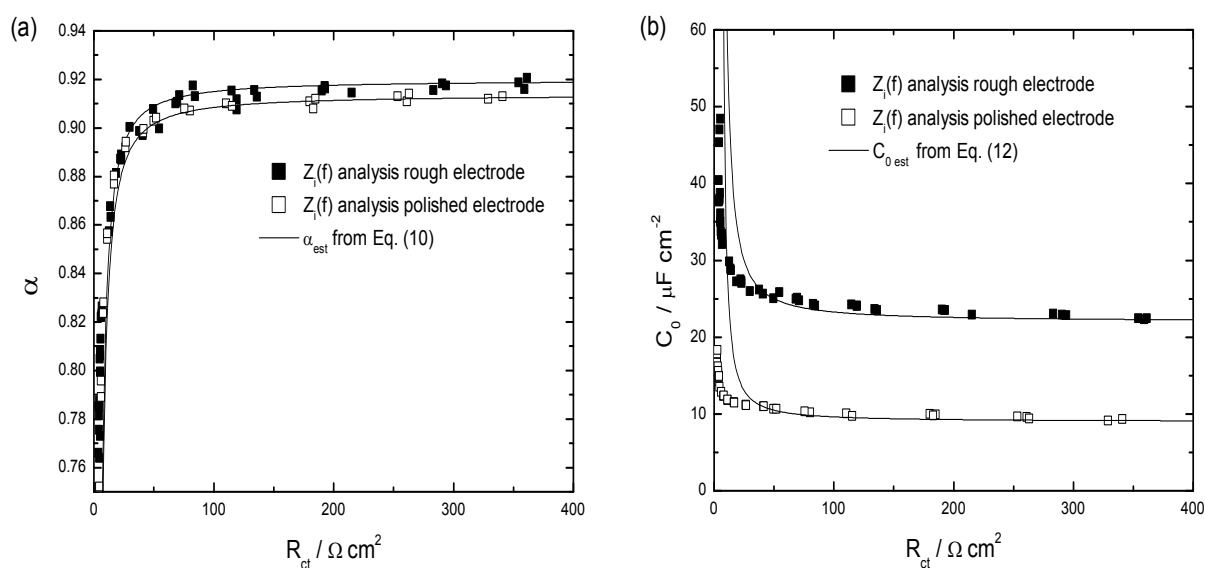


Fig. 6. CPE exponent α (a) and characteristic capacitance C_0 (b) as function of the charge transfer resistance. Symbols correspond to results from $Z_i(f)$ data analyses: (solid) rough electrode; (open) polished electrode. Equation (2) was used in both cases to calculate C_0 . Continuous lines stand for the analytical estimates given in Eqs. (10) and (12) respectively.

The results obtained here are consistent with numerical simulations of the impedance response of disk electrode subject to faradaic reactions [21]. In that case there was no underlying CPE behavior (ideally capacitive behavior) and the only distributions taking into account were those of current and potential induced by the electrode geometry. It was shown –see Fig. 5a in the reference– that for small values of the dimensionless current density $J = 4R_e / \pi R_{ct}$, the frequency-dependent CPE exponent α approached unity at dimensionless frequencies K well below the critical value $K=1$, thus revealing the perfectly ideal capacitive underlying behavior. For larger values of J , α reached asymptotic values near 0.78, which characterizes the quasi-CPE behavior induced by geometry. In our experiments, J is

directly related with the applied electrode potential. Small values of J are obtained for low (cathodic) overpotentials, and in that case we have seen that impedance data reveals the real underlying CPE behavior in a frequency range much smaller than the critical frequency f_{\max} . As long as the overpotential increases, the relaxation of α with frequency is disturbed by the proximity of f_{\max} and the effects of geometry, this resulting in an underestimate of α . For very large overpotentials we obtain values of α very close to that reported (0.78), even smaller. The behavior that follows for higher frequencies does not match with the numerical analysis and it should be attributed to other effects that are presently under study.

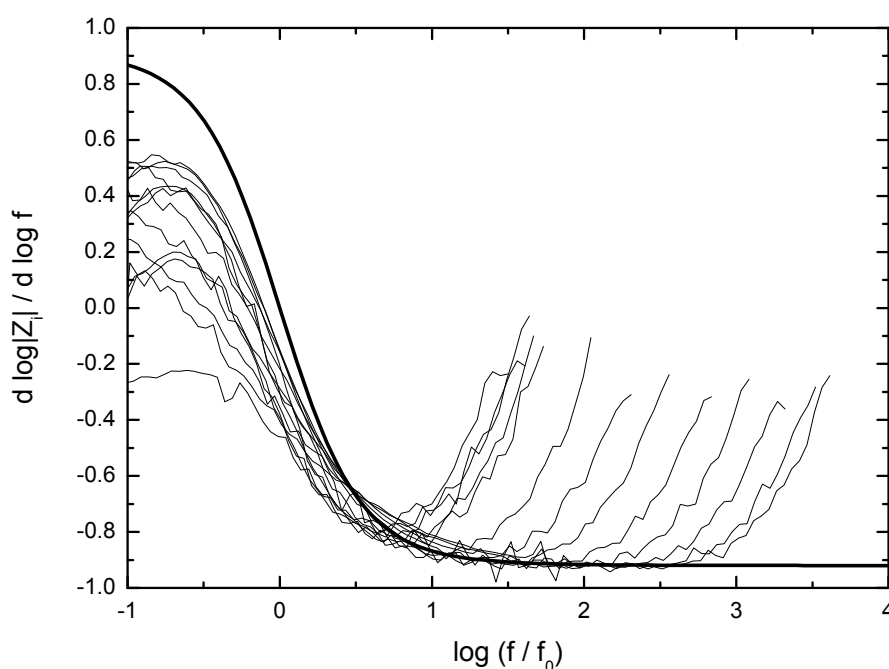


Fig. 7. Variation of $-\alpha_{\text{eff}}$ as function of rescaled frequency for different cathodic overpotentials. Thick line corresponds to the expected behavior of a pure CPE given from (9) in which $\alpha = 0.92$ has been considered.

The consistency of our analysis with the numerical treatment presented in [21] is illustrated by the collapse of the results displayed in Fig. 5 when plotted against the dimensionless frequency f/f_0 , as shown in Fig. 7, in which f_0 has been calculated from (11). This figure should be compared with Fig. 5b in Ref. [21] provided that $K/J = f/f_0$. In our case the collapse is not complete, probably as a consequence of the errors in the values for charge-transfer resistance estimated from impedance data due to geometry-induced frequency dispersion. We have also displayed in the figure, just for illustration, the theoretical

behavior expected from (9) for a pure CPE, i.e. a CPE behavior without the effects of mass transport in the low frequency domain, nor the high frequency effects such as those imposed by the electrode geometry.

Finally, one important remark intended for future works should be done in relation to those theoretical results and the conclusions of our analysis. As mentioned there, there are two characteristic frequencies involved: $K/J=1$, equivalent in our analysis to the characteristic frequency of the charge-transfer process $f = f_0$, and $K=1$, equivalent to $f = f_{\max}$ at which geometry-induced effects become significant. However, from the point of view of a correct measure of the underlying behavior it is the relationship ω_{\max} / ω_0 which becomes crucial. A simple algebra gives $\omega_{\max} / \omega_0 = J^{-1}$, indicating that it is the dimensionless current J the important magnitude with the critical value given at $J=1$. A value of J equal or larger than 1 indicates that the highest frequency behavior of the impedance is completely dominated by the effect of geometry, so it is impossible to get any information about any other process. Only for values $J < 1$ we will be able to observe the effect of the primary process, the information of which will be more precise as long as J decreases.

4. Conclusions

There are two important conclusions in this work, one concerning to the methodology employed in CPE analysis and characterization, and a second one providing fundamental insights on the CPE behavior nature. From the methodological point of view we have shown that the characterization of CPE behavior should involve a deeper analysis, much clearer than the obscure fits to equivalent electric circuits usual found in the literature, and more precise than the also usual direct fit of the high frequency behavior of the imaginary part of the impedance to a power law. A detailed characterization of the impedance response must be done taking into account important effects that can occur within the frequency range of the experimental measurements. When the suitable corrections due to these effects are not taken into account, the results can lead to erroneous conclusions. This is the case of the effect analyzed here: when the influence of geometry-induced potential and current distributions is not properly considered, the CPE behavior shows very significant variations with the applied electrode potential.

With regard to the fundamental knowledge about CPEs, we have obtained evidences pointing to the idea that the physically meaningful parameters of a CPE are the CPE exponent α and the characteristic capacitance C_0 . Interestingly, both quantities completely determine the distribution function when CPE is caused by a capacitance surface distribution [24], with α related to the variance and C_0 being a characteristic mean value of the distribution. In our experiments this apparent distribution did not vary with the electrode potential since these quantities appeared to have a constant value when extra effects beyond the CPE origin were considered in the EIS experimental data analysis.

References

- [1] J.R. Macdonald, *Impedance Spectroscopy: Emphasizing Solid Materials and Systems*, John Wiley & Sons, New York, 1987.
- [2] A. Lasia, in: R.E. White, B.E. Conway, J.O.M. Bockris (Eds.), *Modern Aspects of Electro-chemistry*, vol. 32, Plenum Press, New York, 1999, p. 143.
- [3] Z. Kerner, T. Pajkossy, *J. Electroanal. Chem.* 448 (1998) 139.
- [4] C.-H. Kim, S.-I. Pyun, J.H. Kim, *Electrochim. Acta* 48 (2003) 3455.
- [5] Z. Kerner, T. Pajkossy, *Electrochim. Acta* 46 (2000) 207.
- [6] L. Nyikos, T. Pajkossy, *Electrochim. Acta* 30 (1985) 1533.
- [7] B. Sapoval, R. Gutfraind, P. Meakin, M. Keddad, H. Takenouti, *Phys. Rev. E* 48 (1993) 3333.
- [8] T. Pajkossy, *Heterogeneous Chem. Rev.* 2 (1995) 143.
- [9] J.B. Bates, Y.T. Chu, W.T. Stribling, *Phys. Rev. Lett.* 60 (1988) 627.
- [10] U. Rammelt, G. Reinhard, *Electrochim. Acta* 35 (1990) 1045.
- [11] E.D. Bidóia, L.O.S. Bulhoes, R.C. Rocha-Filho, *Electrochim. Acta* 39 (1994) 763.
- [12] R. de Levie, *Electrochim. Acta* 10 (1965) 113.
- [13] R. de Levie, in: P. Delahay, Ch.W. Tobias (Eds.), *Advances in Electrochemistry Electrochemical Engineering*, vol. 6, Wiley, New York, 1967, p. 329.
- [14] A. Lasia, *J. Electroanal. Chem.* 397 (1995) 27.
- [15] C. Hitz, A. Lasia, *J. Electroanal. Chem.* 500 (2001) 213.
- [16] H.-K. Song, H.-Y. Hwang, K.-H. Lee, L.H. Dao, *Electrochim. Acta* 45 (2000) 2257.
- [17] T. Pajkossy, T. Wandlowski, D.M. Kolb, *J. Electroanal. Chem.* 414 (1996) 2093.
- [18] J.-B. Jorcin, M.E. Orazem, N. Pébère, B. Tribollet, *Electrochim. Acta* 51 (2006) 1473.
- [19] V. M.-W. Huang, V. Vivier, M. E. Orazem, N. Pébère, B. Tribollet, *J. Electrochem. Soc.* 154 (2007) C81.
- [20] V. M.-W. Huang, V. Vivier, M. E. Orazem, N. Pébère, B. Tribollet, *J. Electrochem. Soc.* 154 (2007) C89.
- [21] V. M.-W. Huang, V. Vivier, M. E. Orazem, N. Pébère, B. Tribollet, *J. Electrochem. Soc.* 154 (2007) C99.
- [22] B. Hirschorn, M.E. Orazem, B. Tribollet, V. Vivier, I. Frateur, M. Musiani, *J. Electrochem. Soc.* 157 (2010) C452.

- [23] B. Hirschorn, M.E. Orazem, B. Tribollet, V. Vivier, I. Frateur, M. Musiani, J. Electrochem. Soc. 157 (2010) C458.
- [24] G.J. Brug, A.L.G. Van Den Eeden, M. Sluyters-Rehbach, J.H. Sluyters, J. Electroanal. Chem. **176** (1984) 275.
- [25] W. Scheider, J. Phys. Chem. 79 (1975) 127.
- [26] B. Hirschorn, M.E. Orazem, B. Tribollet, V. Vivier, I. Frateur, M. Musiani, Electrochim. Acta 55 (2010) 6218.
- [27] P. Córdoba-Torres, T.J. Mesquita, R.P. Nogueira, Electrochim. Acta (submitted).
- [28] C.H. Hsu, F. Mansfeld, Corrosion 57 (2001) 747.
- [29] O. Devos, C. Gabrielli, B. Tribollet, Electrochim. Acta 51 (2006) 1413.
- [30] M.-L. Tremblay, M.H. Martin, C. Lebouin, A. Lasia, D. Guay, Electrochim. Acta 55 (2010) 6283.
- [31] I. Herraiz-Cardona, E. Ortega, V. Pérez-Herranz, Electrochim. Acta 56 (2011) 1308.
- [32] N.R. Elezović, V.D. Jović, N.V. Krstajić, Electrochim. Acta 50 (2005) 5594.
- [33] L. Vázquez-Gómez, S. Cattarin, P. Guerriero, M. Musiani, Electrochim. Acta 52 (2007) 8055.
- [34] S.M.A. Shibli, V.S. Dilimon, Int. J. Hydrogen Energy 33 (2008) 1104.
- [35] R. Jurczakowski, C. Hitz, A. Lasia, J. Electroanal. Chem. 572 (2004) 355.
- [36] C. Gabrielli, P.P. Grand, A. Lasia, H. Perrot, J. Electrochem. Soc. 151 (2004) A1943.
- [37] M.H. Martin, A. Lasia, Electrochim. Acta 54 (2009) 5292.
- [38] V.A. Alves, L.A. da Silva, J.F.C. Boodts, Electrochim. Acta 44 (1998) 1525.
- [39] T. Zalewska, A. Lisowska-Oleksiak, S. Biallozor, V. Jasulaitiene, Electrochim. Acta 45 (2000) 4031.
- [40] S.P. Harrington, T.M. Devine, J. Electrochem. Soc. 155 (2008) C381.
- [41] S.P. Harrington, T.M. Devine, J. Electrochem. Soc. 156 (2009) C154.
- [42] J.M. Campiña, A. Martins, F. Silva, J. Phys. Chem. C 111 (2007) 5351.
- [43] J.M. Campiña, A. Martins, F. Silva, J. Phys. Chem. C 113 (2009) 2405.
- [44] W.G. Pell, A. Zolfaghari, B.E. Conway, J. Electroanal. Chem. 532 (2002) 13.
- [45] V.D. Jović, B.M. Jović, J. Electroanal. Chem. 541 (2003) 1.
- [46] V.D. Jović, B.M. Jović, J. Electroanal. Chem. 541 (2003) 13.
- [47] P.S. Germain, W.G. Pell, B.E. Conway, Electrochim. Acta 49 (2004) 1775.
- [48] M. Figueiredo, C. Gomes, R. Costa, A. Martins, C.M. Pereira, F. Silva, Electrochim. Acta 54 (2009) 2630.
- [49] M.E. Orazem, N. Pébère, B. Tribollet, J. Electrochem. Soc. 153 (2006) B129.
- [50] A.J. Bard, L.R. Faulkner, Electrochemical Methods: Fundamentals and applications, 2nd Ed., John Wiley and Sons, Hoboken, NJ, 2001.
- [51] C. Gabrielli, F. Huet, R. P. Nogueira, Electrochim. Acta 47 (2002) 2043.

ABSTRACT

The use of stainless steels (SS) as concrete reinforcement is becoming increasingly popular in coastal and marine constructions in order to prevent corrosion induced by chloride ions penetrating into the concrete. However, the influence of Mo addition on pitting corrosion resistance of these steels is not fully understood in alkaline chloride conditions although this element is widely associated to an increasing corrosion resistance in acidic and neutral environments. Therefore, understanding Mo mechanism on corrosion resistance in alkaline conditions is hence of major importance for the setting of optimized alloy composition. This PhD work aims to study the effect of Mo addition on pitting corrosion properties of austenitic, ferritic and mainly lean duplex stainless steels in alkaline media, which simulates the concrete environment. As far as the role of Mo is concerned, it will be discussed in terms of, pitting corrosion resistance, repassivation kinetics, and passivation properties from acidic to alkaline conditions.

Keywords: Stainless Steels, Molybdenum, Pitting Corrosion, Passivation properties, and Concrete Reinforcement.

RESUME

Les aciers inoxydables sont de plus en plus utilisés comme renfort du béton dans les constructions marines et côtières, afin de prévenir la corrosion induite par les ions chlorures qui pénètrent dans le béton poreux. L'ajout de molybdène dans les aciers inox contribue à augmenter leur résistance à la corrosion par piqure lorsqu'ils sont utilisés dans des environnements acides et neutres. Cependant, le rôle du Mo sur la corrosion par piqûre des aciers en milieu alcalin chloruré reste à ce jour flou et peu étudié. Par conséquent, la compréhension de l'action du Mo dans la résistance à la corrosion en milieu alcalin est donc d'une importance majeure. Cela permettra l'optimisation de la composition finale des alliages inoxydables en vue des applications potentiels comme renfort dans le béton. Ainsi, cette thèse vise à étudier l'effet de l'addition du Mo sur les propriétés de corrosion par piqûre des aciers inoxydables austénitiques, ferritiques et surtout lean duplex en milieu alcalin. Finalement, le rôle du Mo sur les aciers inoxydables a été discuté en termes de leur résistance à la corrosion localisée, cinétique de repassivation et propriétés de passivation dans plusieurs milieux agressifs, mais surtout dans une solution chlorurée synthétique qui simule les environnements poreux du béton (solution de pH10 avec des ions carbonates et chlorures).

Mots-clés: Aciers inoxydables, Molybdène, Corrosion par piqûre, Propriétés de passivation et Renfort du béton.

